AXIAL SOIL-PIPELINE INTERACTION UNDER DIFFERENT SOIL MOISTURE CONDITIONS: PHYSICAL AND DEM MODELLING

GUO CHANG

PhD

The Hong Kong Polytechnic University

2025

The Hong Kong Polytechnic University

Department of Civil and Environmental Engineering

Axial Soil-pipeline Interaction under Different Soil Moisture Conditions: Physical and DEM Modelling

GUO Chang

A thesis submitted in partial fulfilment of the requirements for the degree of Doctor of Philosophy

February 2025

Certificate of Originality

I hereby declare that this thesis is my own work and that, to the best of my knowledge and belief, it reproduces no material previously published or written, nor material that has been accepted for the award of any other degree or diploma, except where due acknowledgement has been made in the text.

_____ (Signed)

GUO Chang (Name of student)

Abstract

Buried pipelines are called lifelines due to their critical role in economically and efficiently transporting natural resources. Soil-pipe relative displacements caused by landslides, earthquakes and thermal expansion/contraction can impose significant loads on pipeline systems, inducing the risk of failures. A thorough understanding of soil-pipe interaction behaviour is crucial for accurately predicting these loads. This study focuses on the axial soil-pipeline interaction (ASPI). Current design guidelines and previous research have not fully addressed three key factors of ASPI, potentially underestimating soil loads or pipe deformations. Firstly, surface roughness and coating hardness are critical determinants of soil-interface shearing behaviours, including friction angle and dilatancy, but the dilatancy effect on axial resistance hasn't been fully considered. Secondly, pipelines carrying hot fluids are frequently subjected to cyclic displacement relative to the surrounding soil due to thermal variations. This cyclic loading can significantly affect axial resistance on pipes during and after loading. Thirdly, pipelines are often buried in partially saturated soils with negative water pressure (matric suction). Matric suction can make unsaturated soils stiffer and stronger, increasing the interface shearing strength, dilatancy and, thus, axial resistance.

To enhance the understanding of ASPI, this study aims to (i) investigate how surface roughness, coating hardness and cyclic displacement amplitude affect axial resistance of pipes buried in dry soils through physical modelling; (ii) reveal how matric suction and water content affect axial resistance of pipe buried in unsaturated soils through physical modelling; (iii) uncover the mechanisms of ASPI by developing a new code using Discrete Element Method (DEM); and (iv) develop a new method for predicting the axial resistance of buried pipes.

This study developed a large-scale physical modelling system to explore ASPI. A single-point-type tactile pressure sensor was developed to measure interface contact and earth pressures. Twenty-seven large-scale physical modelling tests were conducted at varying

moisture conditions, roughness and coatings, and numbers and amplitudes of cyclic loading. An advanced 3D DEM code was developed to provide microscopic insights into ASPI. The pipe is modelled as a clump of overlapping particles to simulate roughness. A scaling factor for the surface tension coefficient, equalling to that for particle size, is used in calculating capillary forces, addressing particle size scaling effects in the unsaturated soil simulation. Based on the results of physical and DEM modelling, the major conclusions are as follows:

Roughness and hardness are decisive for ASPI. The monotonic axial resistance of rough pipes in dry sand is 2.70~2.85 times that of smooth pipes. 72~79% of this increase is due to the interface friction coefficient increasing with the roughness increasing. The remaining is due to the interface contact pressure increase induced by constrained dilation and negative soil arching, as evidenced by soil particle movement and strong force chains developed from the pipe crown and invert in the DEM simulation. A critical hardness was observed (around 35 HRA). Pipes with lower hardness behave like rough pipes due to equivalent roughness from particle embedding.

With the cyclic loading, axial resistance degrades with increasing cycles and stabilises at 32~62% of the monotonic resistance. This is mainly because ongoing pipe settlement translates negative soil arching to positive soil arching, reducing interface contact pressure at the crown and shoulders and thus lowering the average interface contact pressure as predicted. The post-cyclic resistance exceeds the monotonic resistance when the cyclic displacement is smaller than 5 mm due to cyclic loading-induced soil densification.

The axial resistance at unsaturated conditions increases with matric suction under constant nominal pressure. At a suction of 70.2 kPa, the resistance was 1.69 times greater than in the saturated condition. 68% of this increment is attributed to the additional interface contact pressure induced by interface capillary forces. The remaining is related to net interface contact

pressure increase due to higher constrained dilation under unsaturated conditions, as evidenced by larger particle displacements and stronger force chains in the DEM simulation.

Finally, a new and simple equation was proposed to predict axial resistance by considering roughness effects on the interface friction angle, constrained dilation effects on interface contact pressure, and suction effects on Bishop's interface contact pressure and constrained dilation. The new equation successfully predicts results from previous and current studies.

Publications Arising from the Thesis

(1) **Guo, C**. & Zhou, C.* (2025) Axial Behaviour of Steel Pipelines Buried in Sand: Effects of Surface Roughness and Hardness. *Géotechnique* **75,** No. 6, 800-813.

(2) **Guo, C**. & Zhou, C.* (2025) Novel Single-Point-Type Tactile Pressure Sensors for Earth and Soil-Structure Interface Contact Pressures Measurement. *Geotechnical Testing Journal*, Published online, 1-19.

(3) **Guo, C**., Zhou, C.* & Meguid, M. (2025) Discrete Element Modeling of Axial Interaction Between Sand and Pipeline with Different Roughness Conditions. *Computers and Geotechnics* (Accepted)

(4) **Guo, C**. & Zhou, C.* (2025) Axial Behaviour of Steel Pipeline Buried in Unsaturated Soils. *Tunnelling and Underground Space Technology* (Accepted)

(5) **Guo, C**., Zhou, C.* & Meguid, M. (2025) Cyclic and Post-cyclic Axial Behaviors of Steel Pipelines Buried in Dense Sand. *Acta Geotechnica* (Under review)

(6) **Guo, C**., Zhou, C.*, Meguid, M. & Tai, P. (2025) Micro-mechanical Analysis of the Axial Behaviour of Underground Pipelines Buried in Unsaturated Coarse-grained Soils. *Tunnelling and Underground Space Technology* (Submitted)

Acknowledgements

During my PhD journey, the person who had the most profound impact on my development was undoubtedly my supervisor, Dr. ZHOU, Chao. His unwavering encouragement, patience with students, immense enthusiasm for research and extensive knowledge of soil mechanics have been crucial to my growth. I consider myself incredibly fortunate to have such a supervisor.

I am deeply grateful to Prof. YIN, Jian-Hua, my co-supervisor, for his exceptional academic influence within the global geotechnical community and for providing top experimental facilities in the soil mechanics lab. I extend my heartfelt thanks to Prof. Mohamed A. Meguid for facilitating a pivotal six-month academic visit to McGill University. His expertise in buried pipeline engineering and DEM simulation greatly complemented Dr. ZHOU's research team, enriching my thesis. I am also thankful to Dr. Jérôme Duriez from the National Research Institute for Agriculture, Food and Environment in France for offering invaluable one-on-one training on using the capillary model and modifying the YADE source code.

My sincere appreciation goes to Prof. WU, Wei from the University of Natural Resources and Life Sciences, Prof. NI, Peng-peng from Sun Yat-sen University and Dr. Andy Y. F. Leung from PolyU for their valuable time and efforts as examiners and the committee chairman, which significantly enhanced the quality of my thesis.

I am grateful to all my research colleagues for their insightful questions and constructive suggestions, which strengthened my PhD thesis and academic skills. Special thanks to the technical technicians, including Mr. YAO, Gang from Deqing Xingyu Automation Technology Co., Ltd., and Mr. David Leung, Mr. C. K. Leung, and Mr. Raymond Leung from CEE, PolyU, for their essential technical assistance with my experiments.

Lastly, my deepest gratitude goes to my parents for their unconditional love, which has given me strength and resilience, and to my wife for her unwavering love, support and encouragement throughout this journey.

Table of Contents

Certificate of Originality ..... **iii**

Abstract ..... **iv**

Publications Arising from the Thesis ..... **vii**

Acknowledgements ..... **viii**

Table of Contents ..... **ix**

List of Tables ..... **xvi**

List of Figures ..... **xviii**

List of Abbreviations ..... **xxviii**

List of Notations ..... **xxix**

CHAPTER 1 INTRODUCTION ..... **- 1 -**

1.1 Background of the research ..... **- 1 -**

1.2 Research objectives and strategies ..... **- 5 -**

1.3 Structure of the thesis ..... **- 7 -**

CHAPTER 2 LITERATURE REVIEW ..... **- 9 -**

2.1 Engineering practices for buried pipeline systems ..... **- 9 -**

2.1.1 Applications and construction for buried pipeline engineering ..... - 9 -

2.1.2 Pipe material, size and surface treatment ..... - 11 -

2.1.3 Loads on buried pipelines ..... - 13 -

2.1.4 Calculation of axial resistance in guidelines ..... - 14 -

2.2 Physical modelling and field tests on axial soil-pipe interaction ..... **- 18 -**

2.2.1 Axial behaviour of pipes subjected to monotonic loading ..... - 18 -

2.2.2 Axial behaviour of pipes subjected to cyclic loading ..... - 20 -

2.2.3 Unsaturated effect on axial soil-pipe interaction ..... - 24 -
2.2.4 Measuring earth pressure and soil-structure interface contact pressure using tactile pressure sensors ..... - 24 -
2.3 Analytical and numerical simulation on axial soil-pipe interaction ..... - 27 -
2.3.1 Analytical solution on axial force during pipe pullout ..... - 27 -
2.3.2 Numerical modelling on axial soil-pipe interaction ..... - 28 -
2.4 Soil-interface shear behaviour ..... - 33 -
2.4.1 Effects of surface roughness and hardness on soil-interface shear behaviour ..- 33 -
2.4.2 Cyclic effects on soil-interface shear behaviour ..... - 36 -
2.4.3 Interface shear behaviour of unsaturated soils ..... - 37 -
2.5 Discrete element method ..... - 39 -
2.5.1 Basic knowledge ..... - 39 -
2.5.2 DEM simulation of unsaturated soil ..... - 43 -
2.5.3 DEM simulation of soil-pipe interaction subjected to lateral and vertical loading ..... - 47 -
2.6 Summary ..... - 49 -
CHAPTER 3 EXPERIMENTAL SYSTEM, INSTRUMENTATION, MATERIALS AND PROCEDURES OF PHYSICAL MODELLING TESTS ..... - 52 -
3.1 A new large-scale system for axial soil-pipe interaction physical modelling tests. ..... - 52 -
3.1.1 Steel box for simulating pipeline trench ..... - 52 -
3.1.2 Axial actuation subsystem for pipeline pullout ..... - 54 -
3.1.3 Vertical loading subsystem for controlling nominal pressure ..... - 55 -
3.1.4 Instrumentation ..... - 56 -
3.1.5 Evaluation of boundary effects ..... - 57 -

3.2 Measurement of soil-pipe interface contact pressure and earth pressure around the pipe using tactile pressure sensors (TPS) ..... - 59 -

3.2.1 Design of thin TPS-EPS and curved surface-fitted TPS-ICPT ..... - 59 -

3.2.2 Multi-channel measurement ..... - 62 -

3.2.3 Post-installation calibration of TPS-EPC and TPS-ICPT ..... - 64 -

3.2.4 Non-linear signal conversion ..... - 70 -

3.2.5 Comparison between traditional EPC and TPS-based EPC ..... - 71 -

3.2.6 Specific application in physical modelling of this study ..... - 77 -

3.3 Pipes with different surface roughness and hardness ..... - 77 -

3.4 Soil materials ..... - 78 -

3.4.1 Fujian medium sand (FJM sand) ..... - 78 -

3.4.2 Completely decomposed granite (CDG) ..... - 79 -

3.5 Model preparation and test procedures ..... - 86 -

CHAPTER 4 PHYSICAL MODELLING ON AXIAL BEHAVIOUR OF BURIED PIPES SUBJECTED TO MONOTONIC LOADING ..... - 90 -

4.1 Introduction ..... - 90 -

4.2 Testing programme ..... - 90 -

4.3 Experimental results and discussion ..... - 91 -

4.3.1 Roughness effects on pullout force-displacement relationship and pullout resistance ..... - 91 -

4.3.2 Roughness effects on interface contact pressures distribution and evolution ..... - 95 -

4.3.3 Effects of soil arching and constrained dilatancy on pipe pullout mechanism ..... - 98 -

4.3.4 Roughness effects on stress path ..... - 100 -

4.3.5 Coating hardness effects on pullout behaviour ..... - 103 -

4.4 Development of a new method for calculating pipe pullout resistance ..... - 105 -

4.5 Summary ..... - 110 -

CHAPTER 5 PHYSICAL MODELLING ON AXIAL BEHAVIOUR OF BURIED PIPES SUBJECTED TO CYCLIC LOADING ..... - 113 -

5.1 Introduction ..... - 113 -

5.2 Testing programme ..... - 113 -

5.3 Experimental results and discussion ..... - 114 -

5.3.1 Effects of roughness and nominal overburden pressure on cyclic ASPI ..... - 114 -

5.3.2 Evolution of interface contact pressures during cyclic loading ..... - 120 -

5.3.3 Pipe settlement behaviour during cyclic loading ..... - 123 -

5.3.4 Soil arching effects on cyclic ASPI ..... - 126 -

5.3.5 Effects of cyclic displacement amplitude on ASPI ..... - 129 -

5.3.6 Post-cyclic pullout behaviour ..... - 139 -

5.4 Summary ..... - 141 -

CHAPTER 6 PHYSICAL MODELLING ON AXIAL BEHAVIOUR OF BURIED PIPES BURIED IN UNSATURATED SOILS ..... - 143 -

6.1 Introduction ..... - 143 -

6.2 Testing programme ..... - 143 -

6.3 Prediction of interface shear strength ..... - 145 -

6.4 Experimental results and discussion ..... - 145 -

6.4.1 Axial behaviour of steel pipe buried in saturated and unsaturated soils ..... - 145 -

6.4.2 Effects of suction and buried pressure on pullout resistance ..... - 147 -

6.4.3 Suction effects on interface contact pressures distribution and evolution ..... - 152 -

6.4.4 Suction effects on stress path ..... - 154 -

6.5 Development of a new method for calculating the pullout resistance of pipe buried in unsaturated soils ..... - 155 -

6.6 Summary ..... - 158 -

CHAPTER 7 DEM SIMULATION OF AXIAL BEHAVIOUR OF PIPES BURIED IN DRY SOILS ..... - 161 -

7.1 Introduction ..... - 161 -

7.2 Numerical model and boundary conditions ..... - 161 -

7.3 Soil particles and contact model ..... - 164 -

7.4 Modelling of pipe with various roughness conditions ..... - 169 -

7.5 Effectiveness of the periodic boundary and determination of periodic domain thickness ..... - 170 -

7.6 Sample generation and simulation procedures ..... - 174 -

7.7 Validation of the DEM model and analysis of the macro-behaviour ..... - 175 -

7.7.1 Comparisons between the measured and computed pullout force and vertical displacement ..... - 175 -

7.7.2 Comparisons between the measured and computed interface contact pressure at the soil-pipe interface ..... - 177 -

7.7.3 Comparisons between the measured and computed stress path at the soil-pipe interface ..... - 182 -

7.8 Micro-mechanical analysis of axial soil-pipe interaction ..... - 185 -

7.8.1 Soil-pipe interface shear band ..... - 185 -

7.8.2 Soil particle displacement field in the *x-z* plane ..... - 187 -

7.8.3 Force chain evolution ..... - 189 -

7.8.4 Earth pressure evolution around the pipe ..... - 193 -

7.9 Parametric studies ..... - 193 -

7.9.1 Relationship between axial resistance and surface roughness ..... - 193 -

7.9.2 Effect of pipe outer diameter ..... - 195 -

7.10 Summary ..... - 197 -

CHAPTER 8 DEM SIMULATION OF AXIAL BEHAVIOUR OF PIPES BURIED IN UNSATURATED SOILS ..... - 199 -

8.1 Introduction ..... - 199 -

8.2 Numerical model, boundary conditions and pipe generation ..... - 199 -

8.3 Inter-particle contact model with capillary force ..... - 200 -

8.4 Derivation and verification of scaling law for capillary force ..... - 203 -

8.5 Soil particles and parameters calibration ..... - 208 -

8.6 Simulation procedures ..... - 211 -

8.7 Interpretations of the simulation results ..... - 212 -

8.7.1 Comparison between the measured and computed axial behaviours at the unsaturated condition ..... - 212 -

8.7.2 Matric suction and buried pressure effects on axial behaviours ..... - 214 -

8.7.3 Interface contact pressure at the soil-pipe interface ..... - 220 -

8.7.4 Stress path at the soil-pipe interface ..... - 221 -

8.7.5 Soil particle displacement around the pipe ..... - 223 -

8.7.6 Inter-particle normal contact force chain evolution ..... - 227 -

8.7.7 Earth pressure evolution ..... - 228 -

8.8 Summary ..... - 230 -

CHAPTER 9 CONCLUSIONS AND SUGGESTIONS FOR FUTURE RESEARCH ..... - 233 -

9.1 Summary and major conclusions ..... - 233 -

9.1.1 A novel single-point-type tactile pressure sensor for earth and soil-structure interface contact pressure measurement ..... - 233 -

9.1.2 A new experimental system for physical modelling of ASPI ..... - 233 -

9.1.3 An advanced DEM code to simulate ASPI under unsaturated conditions .....- 234 -
9.1.4 Surface roughness and hardness effects on ASPI subjected to the monotonic loading .....- 234 -
9.1.5 Cyclic and post-cyclic ASPI behaviour.....- 235 -
9.1.6 Matric suction effect on ASPI behaviour .....- 236 -
9.1.7 A new design equation to predict axial resistance for soils with varying water contents .....- 237 -
9.2 Recommendation for further work..... - 237 -
9.2.1 DEM simulation of ASPI under a higher degree of saturation.....- 237 -
9.2.2 Thermal effects on ASPI .....- 238 -
9.2.3 Soil-pipe interaction behaviour under multidirectional loading.....- 238 -
9.2.4 Suction effect on lateral earth pressure.....- 239 -
9.2.5 Influence of surface roughness, hardness and hydrophilicity on unsaturated soil-interface shear behaviour .....- 239 -
References ..... - 240 -

List of Tables

Table 2.1 Minimum trench width with varying nominal diameters (DN) (BSI BS EN 1610, 2015) ..... - 11 -

Table 2.2 Minimum trench width with varying trench depths (BSI BS EN 1610, 2015) ... - 11 -

Table 2.3 Common materials and sizes of water mains in Hong Kong (WSD, 2020) ..... - 12 -

Table 2.4 Interface friction angle factor with different pipe coating (ALA, 2001) ..... - 16 -

Table 2.5 Summary of physical modelling and field tests on ASPI ..... - 17 -

Table 2.6 Summary of typical DEM unsaturation simulation methods ..... - 45 -

Table 3.1 Parameters in DEM simulation of earth pressure cell thickness effect ..... - 72 -

Table 3.2 Pipe properties ..... - 80 -

Table 3.3 Pipe surface conditions ..... - 80 -

Table 3.4 Properties of Fujian medium (FJM) sand ..... - 82 -

Table 3.5 Friction angle between FJM sand and steel pipe interface ..... - 82 -

Table 3.6 Properties of CDG ..... - 85 -

Table 3.7 Shear strength between unsaturated CDG and steel pipe interface with R_{max} = 0.08 and R_n = 1.02 ..... - 85 -

Table 4.1 Testing program of surface roughness and coating hardness effects on ASPI subjected to monotonic loading ..... - 91 -

Table 4.2 Parameters for the new equation of dry sands ..... - 112 -

Table 5.1 Testing program of cyclic and post-cyclic effects on ASPI ..... - 115 -

Table 6.1 Testing program of ASPI in the unsaturated condition ..... - 143 -

Table 6.2 Measurement of matric suction and water content around pipe before pullout - 144 -

Table 6.3 Parameters for the new equation of unsaturated soils ..... - 160 -

Table 7.1. Scaling factor for soil particle size, minimum thickness and particle number of each zone ..... - 164 -

Table 7.2. DEM model parameters of ASPI at the dry condition..... - 165 -

Table 8.1 DEM model parameters of ASPI at the unsaturated condition.....- 211 -

List of Figures

Figure 1.1 Landslide-caused pipeline rupture: (a) Shenzhen, December 2015; (b) West Virginia, USA, December 2012; (c) schematic diagram of soil-pipe axial displacement (Al-Khazaali & Vanapalli, 2019) ..... - 2 -

Figure 1.2 Technical route of this thesis..... - 6 -

Figure 2.1 Typical pipeline construction sequence (Rizkalla & Read, 2019)..... - 9 -

Figure 2.2 Idealisation of soil forces on buried pipe (ASCE, 1984): (a) idealised 3D soil loads with discrete springs in three dimensions; (b) bi-linear spring representing the relationship between axial force (t) and relative displacement (u) ..... - 14 -

Figure 2.3 Recommended bounds for adhesion factor (PRCI, 2009) ..... - 16 -

Figure 2.4 Interface contact pressure evolution during pipe pullout (Wijewickreme *et al.*, 2009) ..... - 19 -

Figure 2.5 Cyclic degradation of axial resistance dependent on relative density (D_r) (Weidlich & Achmus, 2006) ..... - 21 -

Figure 2.6 Experiment details of Sheil *et al.* (2018): (a) schematic diagram of the experimental system; (b) measurement of interface contact pressure distribution ..... - 22 -

Figure 2.7 Matric suction effect on axial sand-pipe interaction behaviour (Al-Khazaali & Vanapalli, 2019): (a) experimental system; (b) relationships between skin friction (axial resistance per unit area) and soil retention capability and matric suction (u_a-u_w)..... - 23 -

Figure 2.8 2D FDM on calculating soil-pipe interface contact pressure (Wijewickreme *et al.*, 2009): (a) schematic diagram of methodology; (b) simulation results ..... - 28 -

Figure 2.9 3D FEM on axial soil-pipe (Murugathasan *et al.*, 2021): (a) typical FE mesh; (b) numerical results of interface contact pressure distribution..... - 29 -

Figure 2.10 DEM simulation on axial soil-steel pipe interaction (Meidani *et al.*, 2017): (a) simulated pipeline using facet elements; (b) non-uniform contact force network during pipe pullout..... - 31 -

Figure 2.11 Coupled DEM-FEM simulation on MDPE pipe-soil interaction (Meidani *et al.*, 2020a): (a) schematic diagram of DE-FE coupling principle; (b) axial strain distribution along the pipe ..... - 32 -

Figure 2.12 Relationship between interface friction angle (δ_{center}) and normalised roughness (Paikowsky *et al.*, 1995)..... - 34 -

Figure 2.13 Relationship between peak interface friction coefficient (μ_p) and surface hardness (HV) (Abuel-Naga *et al.*, 2018) ..... - 35 -

Figure 2.14 Matric suction effect on interface shear strength (Borana *et al.*, 2016)..... - 38 -

Figure 2.15 Matric suction effect on interface dilatancy (Hossain & Yin, 2015) ..... - 38 -

Figure 2.16 Typical simulation loop of DEM in YADE (Šmilauer & Chareyre, 2021)..... - 41 -

Figure 2.17 Periodic boundary (O'Sullivan, 2011)..... - 42 -

Figure 2.18 Empirical adhesive force method (Shen *et al.*, 2016): (a) components of the contact model with capillary force; (b) normal force (F_n) versus inter-particle displacement (u_n) - 43 -

Figure 2.19 Modified capillary method (Liu *et al.*, 2020): (a) Liquid–solid interfaces on particle; (b) calculation of capillary force via discretising particle surface with Fibonacci-Lattice points ..... - 44 -

Figure 2.20 Three-structure method (Melnikov *et al.*, 2015; Melnikov *et al.*, 2016)..... - 46 -

Figure 2.21 Comparison of soil bed profile around unburied pipe during cyclic lateral displacement in DEM simulation and physical modelling (Macaro *et al.*, 2021)..... - 48 -

Figure 2.22 Rotation field of unsaturated soil around pipe during lateral displacement (Peng *et al.*, 2024) ..... - 49 -

Figure 3.1 Experiment system for ASPI physical modelling tests: (a) schematic diagram; (b) photograph ..... - 53 -
Figure 3.2 Pipe sleeves: (a) schematic diagram; (b) photograph ..... - 54 -
Figure 3.3 Pipe-actuator connection between free vertical displacement: (a) schematic diagram of top view; (b) photograph ..... - 55 -
Figure 3.4 Photographs of vertical loading subsystem for controlling nominal pressure: (a) top cap with reinforcing beams and pneumatic regulator; (b) pneumatic bag ..... - 56 -
Figure 3.5 Measuring axial strain distribution with different axial displacements (*u*) using OFDR (optical frequency domain reflectometry) ..... - 58 -
Figure 3.6 Tools and materials for preparing interface contact pressure transducers and earth pressure cells based on TPS ..... - 61 -
Figure 3.7 Design of TPS-based EPC sensors: (a) schematic side view; (b) photograph.. - 61 -
Figure 3.8 Design of TPS-based ICPT sensors: (a) schematic side view; (b) photograph - 62 -
Figure 3.9 Measurement wiring and method: (a) method I: resistance-voltage conversion by electrical interface; (b) method II: 4-wire electrical resistance measurement by dataTaker DT85 ..... - 62 -
Figure 3.10 Proposed calibration method of TPS-based ICPT: (a) photograph; (b) schematic diagram of internal details ..... - 64 -
Figure 3.11 Typical calibration result (Loading path: 0~200 kPa; Unloading path: 200~0 kPa; 17 stages in total; 4 kPa/min) ..... - 65 -
Figure 3.12 Non-linearity error of TPS-based sensor (number of TPS-ICPT=15, number of TPS-EPC=3, 4 kPa/min, error bar of Y-axis = ± standard error of the mean): (a) typical air pressure - electrical conductance relationship in loop path; (b) non-linearity error vs. maximum pressure ..... - 67 -

Figure 3.13 Hysteresis errors of TPS-based sensor (number of TPS-ICPT=15, number of TPS-EPC=3, 4 kPa/min, error bar of Y-axis = ± standard error of the mean): (a) typical air pressure - electrical conductance relationship in loading and unloading paths; (b) hysteresis error vs. maximum pressure ..... - 69 -

Figure 3.14 Influence of loading rate on pressure-electrical conductance relationship (number of TPS-ICPT=15, number of TPS-EPC=3) ..... - 70 -

Figure 3.15 Comparison between TPS-based EPC and traditional EPC in the oedometer - 72 -

Figure 3.16 Vertical displacement with applied pressure increasing from 0 to 100 kPa in DEM simulation: (a) Condition I; (b) Condition II; (c) Condition III ..... - 74 -

Figure 3.17 Force chain network with applied pressure of 100 kPa in DEM simulation: (a) Condition I (the maximum contact normal force = 2.12 N); (b) Condition II (the maximum contact normal force = 3.08 N); (c) Condition III (the maximum contact normal force = 2.16 N) ..... - 75 -

Figure 3.18 Pipe with different surface treatments ..... - 81 -

Figure 3.19 Particle size distribution of FJM sand and CDG ..... - 83 -

Figure 3.20 Typical interface shear behaviour between steel interface with different roughness and dry FJM sand ..... - 83 -

Figure 3.21 Soil-water retention curve of CDG ..... - 84 -

Figure 3.22 Typical interface shear behaviour between the steel interface and CDG with varying matric suction ..... - 84 -

Figure 3.23 Soil pluviation method: (a) pluviation system; (b) box for calibration; (c) relative density at different drop distances ..... - 86 -

Figure 3.24 Model preparation of dry FJM sand ..... - 88 -

Figure 3.25 Model preparation of CDG: (a) sieve; (b) soil before compaction; (c) electric earth rammer ..... - 89 -

Figure 4.1 Surface roughness effect on axial force-displacement relationship during monotonic loading ..... - 92 -
Figure 4.2 Nominal vertical pressure at the centre against the pullout resistance ..... - 93 -
Figure 4.3 Normalised roughness effect on μ_{phy} and interface friction coefficient ..... - 93 -
Figure 4.4 Interface contact pressure development and distribution of Rough-34 ..... - 96 -
Figure 4.5 Interface contact pressure development and distribution of Smooth-34 ..... - 97 -
Figure 4.6 Schematic diagram of negative soil arching effect on pipes during monotonic loading ..... - 100 -
Figure 4.7 Vertical earth pressure development: (a) Smooth-34; (b) Rough-34 ..... - 101 -
Figure 4.8 Stress path based on average interface contact pressure measured by TPS: (a) smooth pipe; (b) intermediate and rough pipes ..... - 102 -
Figure 4.9 Hardness effect on axial force-displacement relationship during monotonic loading ..... - 103 -
Figure 4.10 Surface hardness effect on μ_{phy} and interface friction coefficient ..... - 104 -
Figure 4.11 Axial pullout resistance at dry conditions predicted by: (a) ALA (2001); (b) new equation ..... - 109 -
Figure 5.1 Schematic diagram of cyclic and post-cyclic paths ..... - 114 -
Figure 5.2 Effects of nominal pressure at pipe centre and surface roughness on cyclic axial force (Series I, u_A = 20 mm): (a) rough pipe and (b) smooth pipe ..... - 117 -
Figure 5.3 Cyclic degradation of axial resistance: (a) axial resistance vs. cycle number; (b) ultimate degradation factor vs. surface roughness ..... - 119 -
Figure 5.4 Typical evolution of interface contact pressure (σ_c' = 34 kPa, u_A = 20 mm): (a) rough pipe and (b) smooth pipe ..... - 122 -
Figure 5.5 Typical pipe settlement behaviour (σ_c' = 34 kPa, u_A = 20 mm, first five cycles) - 124 -

Figure 5.6 Irreversible settlement vs. cyclic number (u_A = 20 mm)..... - 126 -

Figure 5.7 Schematic diagram of soil arching evolution during cycling loading ..... - 127 -

Figure 5.8 Typical evolution of earth pressure (σ_c' = 34 kPa, u_A = 20 mm, first five cycles).....

..... - 128 -

Figure 5.9 Typical cyclic and post-cyclic behaviour in Series II (σ_c' = 34 kPa, u_A = 5 mm): (a) rough pipe and (b) smooth pipe..... - 131 -

Figure 5.10 Comparison between stress paths during cycling for different displacement amplitudes, σ_c' = 34 kPa: (a) rough pipe and (b) smooth pipe ..... - 133 -

Figure 5.11 Cyclic degradation of maximum axial force per unit length at a given cyclic displacement amplitude (σ_c' = 34 kPa): (a) rough pipe and (b) smooth pipe ..... - 136 -

Figure 5.12 Effects of cyclic displacement amplitude on post-cyclic pullout behaviour (σ_c' = 34 kPa): (a) rough pipe and (b) smooth pipe..... - 138 -

Figure 5.13 Effects of pipe roughness and cyclic amplitude on the change factors of maximum axial resistance (i.e., the ratio of post-cyclic and monotonic pullout resistances) (σ_c' =34 kPa)

..... - 139 -

Figure 6.1 Axial behaviour of pipe: (a) axial force against axial displacement; (b) vertical displacement against axial displacement..... - 146 -

Figure 6.2 Axial resistance against average matric suction ..... - 147 -

Figure 6.3 Axial resistance against nominal vertical pressure at the pipe centre..... - 148 -

Figure 6.4 Interface contact pressure (σ_c'= 17 kPa, s = 0 kPa): (a) development; (b) distribution

..... - 149 -

Figure 6.5 Interface contact pressure ($\sigma_{c\text{-}net}$, s = 17.8 kPa): (a) development; (b) distribution ...

..... - 150 -

Figure 6.6 Interface contact pressure ($\sigma_{c\text{-}net}$ = 17 kPa, s = 50.0 kPa): (a) development; (b) distribution ..... - 151 -

Figure 6.7 Stress path based on average interface contact pressure measured by TPS ... - 154 -
Figure 6.8 Axial pullout resistance at the unsaturated conditions predicted by (a) ALA (2001); (b) new equation ... - 157 -
Figure 7.1 Schematic diagram of the numerical model for investigating the axial pipe-soil interaction ... - 163 -
Figure 7.2 Validation of the contact model parameters using interface direct shear tests with rigid boundary (scaling factor for particle size, $f_s = 4$): (a) rough interface (normalised roughness, $R_n = 1.01$); (b) smooth interface ($R_n = 0.04$) ... - 168 -
Figure 7.3 Schematic diagram of pipe ... - 169 -
Figure 7.4 Comparison of interface shear stress in DEM interface shear simulations with different horizontal boundaries ($\sigma_n' = 34$ kPa, $f_s = 4$, $R_n = 1.01$) ... - 171 -
Figure 7.5 Soil particle displacement fields in DEM interface shear simulations with different horizontal boundaries ($\sigma_n' = 34$ kPa, $f_s = 4$, $R_n = 1.01$, horizontal displacement of interface = 6.0 mm): (a) rigid boundary; (b) periodic boundary ... - 171 -
Figure 7.6 Force chain in DEM interface shear simulations with different horizontal boundaries ($\sigma_n' = 34$ kPa, $f_s = 4$, $R_n = 1.01$, horizontal displacement of interface = 1.2 mm): (a) rigid boundary (maximum normal contact force = 5.78 N); (b) periodic boundary (maximum normal contact force = 1.84 N) ... - 172 -
Figure 7.7 Effects of DEM periodic domain thickness ($n_p \times d_{50}$) on the soil-interface shear behaviour ($\sigma_n' = 34$ kPa, $f_s = 4$, $R_n = 1.01$) ... - 172 -
Figure 7.8 Comparisons between the measured and computed pipe pullout behaviour at various roughness (nominal vertical pressure at the pipe centre, $\sigma_c' = 34$ kPa): (a) axial force; (b) pipe settlement ... - 176 -
Figure 7.9 Comparisons between the measured and computed pipe pullout with different nominal pressures (σ_c') ($R_n = 1.01$) ... - 178 -

Figure 7.10 Validation of interface contact pressure development and distribution (σ_c' = 34 kPa): (a) rough pipe (R_n = 1.01); (b) smooth pipe (R_n = 0.04) ..... - 181 -
Figure 7.11 Stress path of rough pipe (R_n = 1.01): (a) measured and computed average stress paths; (b) computed stress paths of local positions at the pipe surface (axial displacement, u, 0~10 mm); (c) computed local stress ratio ..... - 184 -
Figure 7.12 Soil particles in y direction: (a) development of average soil particle displacement against distance from soil particle centre to pipe surface; (b) displacement field within Zone A (σ_c' = 34 kPa, u = 20 mm) ..... - 186 -
Figure 7.13 Soil particle displacement in the x-z plane within Zone A (five times in vector length) ..... - 188 -
Figure 7.14 Soil particle displacement in z direction within Zone C (positive: upward) - 189 -
Figure 7.15 Force chain evolution within Zone A ..... - 191 -
Figure 7.16 Stress field within Zone C: (a) vertical earth pressure; (b) lateral earth pressure ... . - 192 -
Figure 7.17 Computed axial pullout behaviour of pipes with normalised roughness levels of 0.01~1.40 (σ_c' = 34 kPa): (a) axial force-displacement relationship; (b) normalised roughness against axial pullout resistance ..... - 195 -
Figure 7.18 Computed axial pullout behaviour of pipes with different outer diameters (σ_c' = 34 kPa, R_n = 1.01): (a) axial force; (b) vertical displacement ..... - 196 -
Figure 8.1 Schematic diagram of capillary model: (a) liquid bridge between particles; (b) the relationship between capillary force, F_{cap}, and inter-particle normal distance,d, or particle-centre wall normal distance, d_c; (c)liquid bridge through the symmetric centre wall..... - 202 -
Figure 8.2 Validation of scaling law for the stress induced by capillary forces of liquid menisci using triaxial compaction simulation (confining pressure = 34 kPa, axial strain rate = 0.01/s, particle size of the prototype = 0.0025~0.005 mm): (a) deviatoric stress; (b) volumetric strain;

(c) axial stress induced by capillary forces of liquid menisci; and (d) degree of saturation .....
..... - 207 -
Figure 8.3 DEM parameter validation using interface direct shearing: (a) matric suction, s = 0 kPa; (b) s = 70 kPa ..... - 210 -
Figure 8.4 Comparisons between the measured and computed axial behaviour (net nominal vertical pressure at the pipe centre, σc-net = 17 kPa): (a) axial force; (b) vertical displacement
..... - 213 -
Figure 8.5 The computed axial behaviour at dry and unsaturated conditions ($\sigma_{c\text{-net}}$ or $\sigma_c{}'$ = 17 kPa): (a) axial force; (b) vertical displacement; (c) soil-water retention curve based on data before the pipe pullout; (d) matric suction effect on axial resistance ..... - 216 -
Figure 8.6 Buried pressure effect on the computed pipe pullout behaviour: (a) axial force (s = 70 kPa); (b) axial resistance against nominal pressure at the pipe centre ..... - 217 -
Figure 8.7 Interface contact pressure ($\sigma_{c\text{-net}}$ or $\sigma_c{}'$ = 17 kPa;): (a) net interface contact pressure (s = 70 kPa); (b) Bishop's interface contact pressure (s = 70 kPa); (c) the interface contact pressure induced by capillary forces of liquid menisci (s = 70 kPa) and (d) effective interface contact pressure (s = 0 kPa)..... - 219 -
Figure 8.8 The computed soil-pipe interface stress path ($\sigma_{c\text{-net}}$ or $\sigma_c{}'$ = 17 kPa): (a) net stress; (b) Bishop's stress ..... - 222 -
Figure 8.9 Soil particle displacement in y direction: (a) development of average soil particle displacement against distance from soil particle centre to pipe surface; (b) displacement field within Zone A ($\sigma_{c\text{-net}}$ or $\sigma_c{}'$ = 17 kPa, u = 20 mm)..... - 224 -
Figure 8.10 Soil particle displacement in x-z plane within Zone A ($\sigma_{c\text{-net}}$ or $\sigma_c{}'$ = 17 kPa, five times in vector length)..... - 225 -
Figure 8.11 Inter-particle contact normal force chain evolution within Zone A ($\sigma_{c\text{-net}}$ or $\sigma_c{}'$ = 17 kPa)..... - 226 -

Figure 8.12 Vertical earth pressure field within Zone C ($\sigma_{c\text{-}net}$ or $\sigma_c' = 17$ kPa)..... - 229 -

Figure 8.13 Lateral earth pressure field within Zone C ($\sigma_{c\text{-}net}$ or $\sigma_c' = 17$ kPa)..... - 230 -

List of Abbreviations

ASPI	Axial soil-pipe interaction
CDG	Completely decomposed granite
CNL	Constant normal loading
CNS	Constant normal stiffness
DE, DEM	Dicrete element, Dicrete element method
DN	Nominal diameter
EA	Epoxy asphalt
EPC	Earth pressure cell
FDM	Finite difference method
FE, FEM	Finite element, Finite element method
FBE	Fusion-bonded epoxy
FJM sand	Fujian medium sand
FSR	Force sensing resistor
LVDT	Linear variable differential transformer
HRA	Rockwell hardness
OFDR	Optical frequency domain reflectometry
PGD	Permanent ground deformation
RMSE	Root mean square error
TPS	Tactile pressure sensor
ICPT	Interface contact pressure transducer
WEPP	West-East gas pipeline project
YADE	Yet another discrete element

List of Notations

$A(\gamma)$, $m(\gamma)$	Strain-dependent parameters related to G
a_ψ, A_ψ, Q, R	Empirical parameters related to ψ_{max}
a_{vG}, n_{vG}, m_{vG}	Fitting parameters in van Genuchten model
C	Curvature of the liquid bridge surface
c_{int}'	Effective interface shear strength intercept if assuming a linear envelope
D	Pipe nominal outer diameter
d_P	Distance from one end of the pipe test section
d, d_c, $d_{creation}$, $d_{rupture}$	Inter-particle distance, distance between a particle and the centre wall, inter-particle distance to create the liquid meniscus, and inter-particle distance where the liquid meniscus ruptures
d_{50}, $d_{50\text{-}A}$, d_{max}, d_{min}	Average soil particle size, average soil particle size of Zone A in DEM simulation, maximum and minimum particle size
d_{pipe}	Size of pipe particles in DEM simulation
$d\varepsilon_v$	Volumetric strain increment
e, e_{max}, e_{min}	Void ratio, maximum void ratio and minimum void ratio
e_{sum}	Sum static error
F, $F_{contact}$, F_{cap}	Inter-particle resultant force, contact force and capillary force
f, f_R	Soil-pipe interface friction factor and roughness-dependent soil-pipe interface friction factor
f_s	Scaling factor for soil particle size in DEM simulation
f_γ	Scaling factor for the surface tension coefficient

G, G_u	Shear modulus for saturated or dry soils and unsaturated soils
g, g_0, g_{TPS}	Electrical conductance, zero offset of electrical conductance, electrical conductance of TPS
H_c, H_{c0}	Buried depth of the pipe centre and its real value in the experiment
I_D	Relative density
K_0	Coefficient of lateral earth pressure at rest
k	Sensitivity of TPS
k_n, k_s	Normal and shear stiffness of materials in DEM simulation
m_{real}	Pipe mass per meter
N, u_A	Cycle number, axial cyclic displacement amplitude
N_{pipe}	Number of pipe particles per meter
n_p	Ratio of the distance between two periodic boundary walls to $d_{50\text{-}A}$
$\boldsymbol{n}$	Unit vector
P	Air pressure inside the flexible pneumatic bag
p_a	Reference pressure of 100 kPa
R, R_{TPS}, $R_{Trimmer}$, R_{out}, R_0	Electrical resistance, electrical resistance of TPS, electrical resistance of trimmer, output electrical resistance value and electrical resistance of a parallel resistor
R_{max}, R_a	Maximum height and average height deviations on the surface profile over a travel length of d_{50}
R_n	Normalised surface roughness based on R_{max}
r	Particle radius

S	Thickness of the shear band
s	Matric suction
S_r	Degree of saturation
T	Axial resistance (maximum value of axial force per unit length during axial loading to failure)
T_1	Mobilised axial resistance during the first loading at a cyclic amplitude of 20 mm, which is also equal to axial resistance during monotonic loading without cyclic loading
T_u	Ultimate value of axial resistance with a large number of cycles
T_u/T_1	Degradation factor of axial resistance over cycle
T_p	Axial resistance during post-cyclic pullout
T_p/T_1	Change factor of axial resistance
t_{min}	Minimum horizontal thickness of Zone A to E
t_{pipe}	Pipe wall thickness
u, u_c	Axial displacement and critical axial displacement
u_r	Radial expanding displacement of the shear band due to interface dilation
u_a, u_w	Air pressure and pore pressure
V_{out}, V_{ref}	Output electrical voltage and input reference electrical voltage
V_{pipe}	Volume per pipe particle
V_{cap}, $V_{cap\text{-}c}$	Water volume of the liquid meniscus, water volume of the liquid meniscus between a particle and the centre wall

X_{mod}, X_{proto}	Parameter X in the model sample and prototype sample
$y(z)$	Liquid bridge profile curve
z	Position on the symmetry axis of the liquid meniscus
α_R, β_R	Empirical parameters related to f_R
γ, $d\gamma$	Shear strain and shear strain increment
γ', γ_b, $\overline{\gamma}_{pipe}$, $\Delta\gamma$, γ_{dry}	Soil effective unit weight, soil bulk unit weight, apparent unit weight of the pipe, unit weight difference between the pipe and soil and dry unit weight
γ_t	Surface tension coefficient
$\Delta\sigma_D'$	Average increase in interface contact pressure caused by constrained dilation
Δh	Buried depth of the tensiometer related to that of the pipe springline
Δl	the distance between two adjacent and touching pipe particles
$\boldsymbol{l}$	Distance vector between the centres of two particles
ΔW	Normal force increase per unit length caused by the pipe weight
ρ_{steel}	Steel density
δ', $\tan\delta'$, δ_{peak}, δ_{cr}	Effective soil-interface friction angle, soil-interface friction coefficient, peak and critical state soil-interface friction angles
δ_i	Filling angle on the particle i (i is 1 or 2)
θ	Solid-liquid contact angle
κ, κ_{int}	Empirical exponent parameter of Bishop's stress for pure soils and soil-interface

μ_{ALA}, μ_{dir}	Soil-pipe interface friction coefficient from the guidelines' prediction and interface direct shear tests
μ_{phy}	Ratio of the axial resistance to the assumed interface contact force per unit length
σ_c', $\sigma_{c\text{-}net}$	Nominal vertical pressure at the pipe centre and net nominal vertical pressure at the pipe centre
σ_f'	Effective stress at failure
σ_n', $\sigma_{n\text{-}net}$	Effective normal stress and net normal stress
σ_i',$\sigma_{i\text{-}net}$	Initial effective stress and initial net stress
σ_{int}, σ_{int}'	Total interface contact pressure and effective interface contact pressure
$\sigma_{int\text{-}net}$, $\overline{\sigma}_{int\text{-}net}$	Net interface contact pressure and its average value
$\sigma_{int\text{-}bishop}$	Bishop's interface contact pressure
$\sigma_{int\text{-}cap}$	Interface contact pressure induced by capillary forces of liquid menisci between the pipe and soil particles
σ_{cap}	stress induced by capillary forces of liquid menisci
τ_f	Interface shear strength
φ'	Soil internal friction angle
φ_{micro}	inter-particle friction angle
χ, χ_{int}	Bishop's stress parameter for pure soils and soil-interface
ψ, ψ_{max}, $\psi_{max\text{-}u}$	Dilation angle, maximum dilation angle and maximum dilation angle of unsaturated soils

CHAPTER 1
INTRODUCTION

1.1 Background of the research

Buried pipelines, economical, efficient, and effective transporters of natural resources, such as natural gas, oil, and water, are termed lifelines (Nair *et al.*, 2018). Relative ground movement (e.g., induced by landslides) is one of the leading causes of pipeline accidents, severely threatening the safety of lives and properties (Karamanos *et al.*, 2021). EGIG (2020) reports that, in 2010~2019, around 16% of pipeline accidents resulted from ground movements, 96% of which were due to landslides. Figure 1.1 (a) shows the landslide situation in Shenzhen, China, in December 2015. The main gas pipeline of the West-East Gas Pipeline Project (WEPP) was ruptured by this accident, interrupting Hong Kong's natural gas supply for 13 days. Figure 1.1 (b) shows another typical landslide-caused gas pipeline explosion in West Virginia, U.S.A., in December 2012. This accident was considered to affect the gas supply of around 5,000,000 households. Figure 1.1 (c) gives the schematic model of this accident, where the pipe is buried longitudinally to the slope. Once landslides, permanent ground deformation (PGD) causes axial tension and compression on the pipe and even breaks it once the load exceeds its strength.

The loads on buried pipelines are generally divided into three components (i.e., loads in axial, vertical, and horizontal directions) (ASCE, 1984; ALA, 2001; PRCI, 2009). This study focuses on the axial soil-pipeline interaction (ASPI). A good understanding of ASPI is essential because both underestimation and overestimation can cause unsafe pipeline design in certain cases. Underestimation of the soil load results in a lower pipeline design strength, increasing the possibility of pipeline damage during its service life. In the event of overestimation, the actual constraint from the soil to the pipeline is smaller than the design value, leading to greater pipeline deformation and consequently increasing susceptibility to buckling failures (e.g., upheaval buckling and sharp bend ruptures) (PRCI, 2009; Ni *et al.*, 2020; Vazouras *et al.*, 2021).

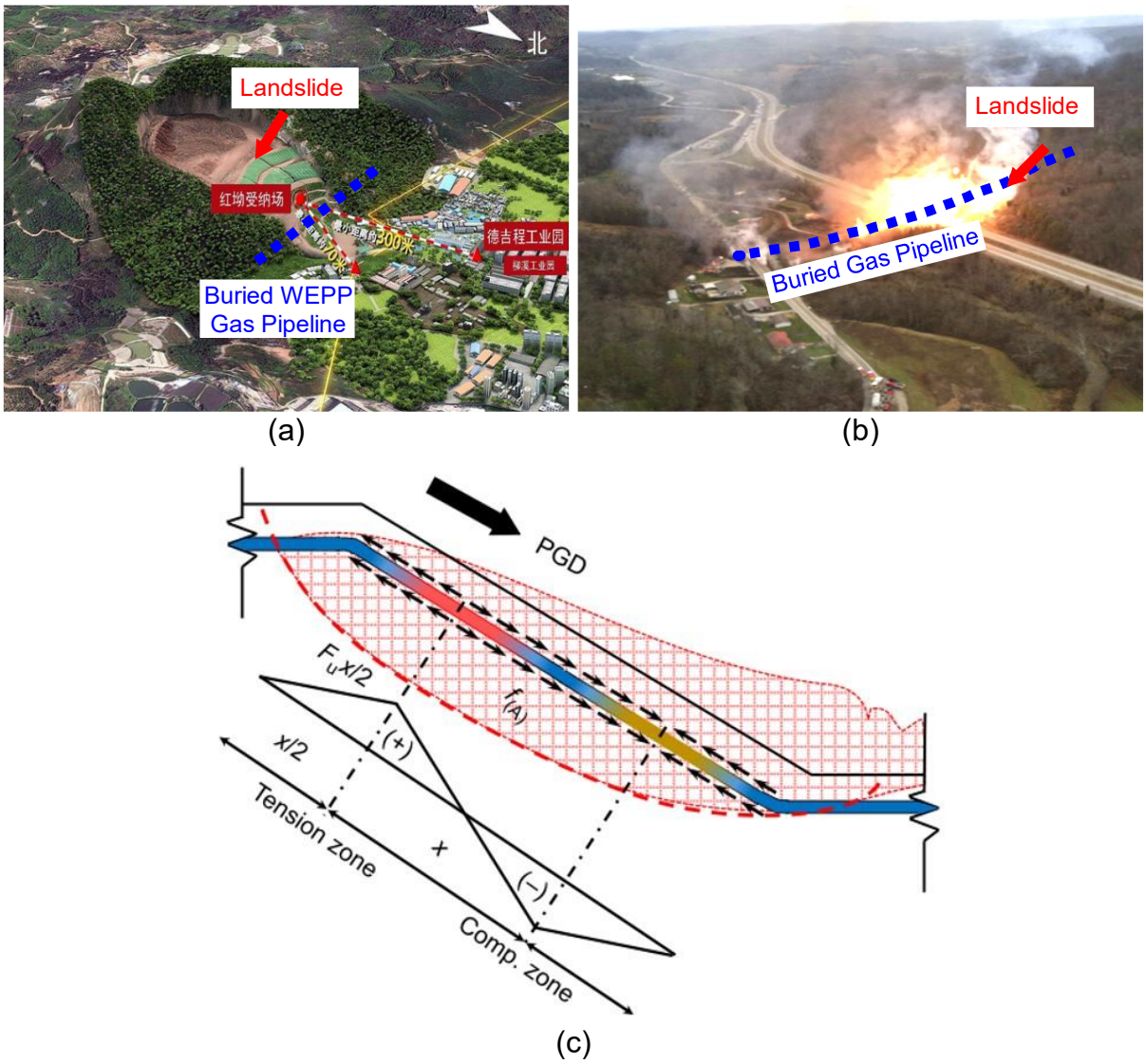

Figure 1.1 Landslide-caused pipeline rupture: (a) Shenzhen, December 2015; (b) West Virginia, USA, December 2012; (c) schematic diagram of soil-pipe axial displacement (Al-Khazaali & Vanapalli, 2019)

However, current design guidelines and previous experimental research have not fully addressed three key factors of ASPI as follows:

a) Surface treatment techniques such as coating, wrapping, and sand-blasting are commonly employed on underground pipelines to prevent corrosion and provide thermal insulation (ISO 8501-1, 2007; CEDD, 2020). These treatments can greatly impact the pipe surface roughness and hardness, which significantly affect interface shear strength and dilatancy and thus are crucial determinants of axial resistance (Dove

& Frost, 1999; Han *et al.*, 2018; Ghanadizadeh *et al.*, 2022). However, the guidelines only recommended the soil-pipe interface friction angle of pipes with different surface conditions, where the classification of surface conditions is qualitative but not quantitative. More importantly, previous studies ignore roughness and hardness impacts on the interface contact pressure between soil and pipe during ASPI (Tejchman & Wu, 1995; Lings & Dietz, 2005; Abuel-Naga *et al.*, 2018). The evolution of interface contact pressure could be complex due to various factors, especially the constrained dilatancy and soil arching (Wijewickreme *et al.*, 2009; Meidani *et al.*, 2017; Sheil *et al.*, 2018; Al-Khazaali & Vanapalli, 2019; Muntakim & Dhar, 2021; Murugathasan *et al.*, 2021; Saberi *et al.*, 2022). More experimental results are needed to understand and quantify the effects of roughness and hardness on the ASPI mechanism and axial resistance.

b) Buried pipelines carrying hot fluids are routinely exposed to cyclic displacement relative to the surrounding soils during thermal expansion/contraction (Saadawi, 2001). Additionally, a post-cyclic large axial relative displacement might happen due to the PGD caused by geohazards and other activities (Rizkalla & Read, 2019). Cyclic loading significantly affects axial soil resistance on pipes during and after it (Mortara *et al.*, 2007; Weidlich & Achmus, 2008; Rui *et al.*, 2020b). The understanding of cyclic ASPI seems limited for several reasons. Firstly, surface roughness is also a critical factor in cyclic and post-cyclic interface shear strength (Fakharian & Evgin, 1997; Frost & Han, 1999; Mortara *et al.*, 2007; Di Donna *et al.*, 2016; Faizal *et al.*, 2018; Han *et al.*, 2018; Rui *et al.*, 2020b; Tian *et al.*, 2022), but no study has explored its effects on cyclic ASPI. Secondly, the unique data of Sheil *et al.* (2018) highlights the importance of cyclic amplitude on ASPI, but the use of alternating amplitudes cannot fully reveal its effects because soil-pipe interface behaviour is path-dependent (Mortara *et al.*, 2007; Zhou *et al.*, 2020). Finally, no studies have examined post-cyclic pullout behaviour.

c) Typically, onshore pipelines are shallowly buried above the underground water table, where the soil is unsaturated and exhibits negative water pressure (i.e., matric suction, *s*) (BSI, 2003; WSD, 2012). The suction effect, which significantly impacts interface shear strength and dilatancy, is a critical factor affecting axial load (Hamid & Miller, 2009; Hossain & Yin, 2015; Li *et al*., 2021; Liu *et al*., 2021b). Commonly used design guidelines and previous studies typically analyse ASPI based on the traditional soil mechanics framework, suitable for dry and saturated soils. However, when pipes are buried on steep slopes, soils containing a certain amount of fine particles, such as completely decomposed granite (CDG) in Hong Kong (Zhu *et al*., 2018), are typically used instead of clean sand (USBR, 1996). Compared to clean sand, the suction effects on ASPI using soils with fine particles are expected to be more pronounced with three factors as follows. First, under constant normal loading (CNL) conditions, the suction effect on the interface shear strength of soils with fine particles, mainly due to the additional interface contact pressure due to capillary forces of liquid menisci between the interface and soil particles, is more notable. Second, unsaturated soils with fine particles exhibit higher dilation and stiffness than saturated soils and unsaturated sand, leading to more significant constrained dilatancy and, consequently, increased axial resistance (Salgado et al., 2000; Alonso et al., 2010; Hossain & Yin, 2010; Han & Vanapalli, 2016). Third, the lateral earth pressure coefficient at rest, K_0, typically decreases with increasing suction (Fredlund & Rahardjo, 1993; Lu & Likos, 2004), which might influence the average interface contact pressure on the pipe surface. Neglecting the three suction effect factors on axial load can compromise the resilience of pipeline system design. Therefore, a new physical modelling study is expected to quantify the axial resistance of pipes buried in soils with fine particles and investigate the suction effects on the above three factors.

Moreover, investigating ASPI behaviour based on physical modelling and continuum-based simulation lacks micro-level evidence. The distinct-element method (DEM) simulation, which models soil as discrete particles, offers unique advantages for analysing microscopic behaviour and is well-suited for large plastic deformation problems (Cundall & Strack, 1979). The understanding of ASPI is expected to be improved by utilising DEM simulation. Although some attempts have been made in ASPI DEM simulation (Meidani *et al.*, 2017, 2020), three key challenges limit the further development of ASPI DEM simulations. Firstly, in engineering practice, pipes are typically so long that they can be considered semi-infinite in the axial direction. The unwanted boundary effect of rigid walls in previous DEM simulations would induce the results of soil response to be inaccurate. Secondly, excessive numerical particle size scaling factors may weaken the reliability of the particle-scale analysis results (O'Sullivan, 2011). An optimised balance between the computational efficiency and the particle size scaling factor is long-awaited to improve the industrial practicability of DEM simulation on large-scale problems. Thirdly, increasing particle size in DEM simulation would decrease the suction effect on soils if the input parameters related to the capillary force calculation are constant. The elimination of the particle size scaling effect is expected in the DEM simulation on unsaturated soil-pipe interaction.

1.2 Research objectives and strategies

To enhance the understanding of ASPI, the main objectives of this study are as follows:

(i) To develop a large-scale physical modelling system and methodology to conduct ASPI tests in dry, unsaturated and saturated soils, during which the variation of interface contact pressure on the pipe surface is expected to be monitored;

(ii) To investigate the extent to which surface roughness and hardness affect the pullout resistance during monotonic loading and to examine the mechanisms of surface condition effects through physical modelling;

(iii) To investigate how displacement amplitude influences axial resistance degradation over cycles and the post-cyclic pullout behaviour through physical modelling;

(iv) To reveal the extent to which matric suction affects pullout resistance and to examine the mechanisms of suction effects through physical modelling;

(v) To develop new code using the Discrete Element Method (DEM) to back-analyse the physical modelling tests in both dry and wet soils and to uncover the micro-level mechanisms of ASPI;

(vi) To develop a new equation for predicting the axial resistance of buried pipes that considers the interface contact pressure variation and partial saturation.

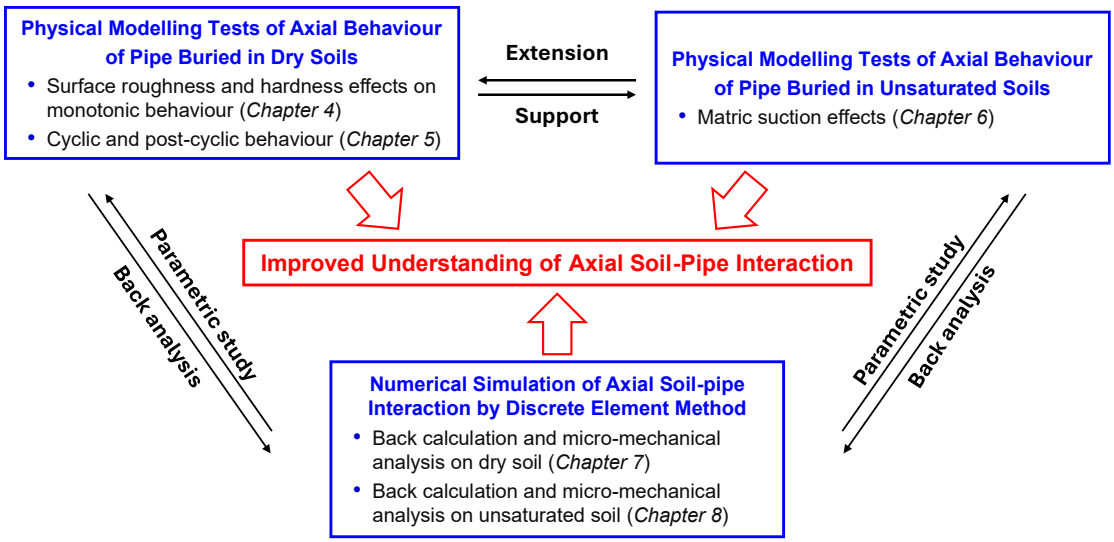

Figure 1.2 Technical route of this thesis

The technical route of this thesis is illustrated in Figure 1.2. To achieve the above objectives, a new large-scale physical modelling system was developed, featuring a steel box to contain soil and pipe, a linear actuator for axial displacement, and a flexible pneumatic bag for adjusting buried pressure. Two sleeves with rubber membranes were introduced to minimise the boundary effects of the front and rear walls of the box. A new interface contact pressure transducer conforming to curved interfaces and a new earth pressure cell (EPC) with limited arching effect were developed using a tactile pressure sensor to measure interface contact pressures at the soil-pipe interface and earth pressures in the surrounding soils. A total of 27 physical modelling tests

were conducted in dry, saturated and unsaturated soils. Key variables in the physical modelling included surface roughness, coating hardness, buried pressure, cyclic number, cyclic displacement amplitude and average matric suction around the pipe. Based on experimental observations, a new and simple equation was proposed to predict axial resistance. The elastic expanding cylinder theory was extended in this new equation to calculate the interface contact pressure increase caused by constrained dilatancy. The relationship between roughness and interface friction angle and the effects of pipe self-weight were also considered. Furthermore, this equation was extended to calculate the axial resistance of pipes in unsaturated soils using Bishop's stress. The suction effects on interface contact pressure, soil stiffness and dilatancy were considered. Finally, an advanced code was developed to simulate ASPI using an open-source 3D DEM software, YADE. The pipe was modelled with overlapping particle clumps to adjust surface roughness. Boundary effects were eliminated by employing parallel periodic boundaries as the front and rear walls. Particle refinement methods were used to reduce the number of particles and thus enhance computational efficiency. Subsequently, the code was extended to calculate ASPI in unsaturated soil by adding capillary force in inter-particle contacts. The source code of YADE was modified to address the problem of particle size scaling effects for the stress induced by capillary forces of liquid menisci using the principle of scaling law. The physical modelling tests were back-analysed at a micro-level using the new code.

1.3 Structure of the thesis

The experimental and numerical results are analysed and reported in this thesis, which is structured as follows:

CHAPTER 1 briefly overviews the background, scientific challenges, objectives, research content and layout of this thesis.

CHAPTER 2 reviews the basic knowledge of buried pipeline systems, experimental and theoretical studies on ASPI, soil-interface shear behaviour and DEM simulation.

CHAPTER 3 introduces an experimental system for physical modelling, including the development of new apparatus, material parameters of soils and pipes, instrumentation, test program, and the procedure for sampling and testing. Furthermore, it details the methodology for using tactile pressure sensors to measure soil-pipe interface contact pressure and earth pressure, including sensor design, signal processing, and calibration.

CHAPTER 4 presents nine physical modelling tests on pipes subjected to monotonic axial displacement buried in dry soil to study the effects of surface roughness and coating hardness on ASPI. A new and simple method is proposed for calculating axial resistance, considering the effects of roughness and dilatancy.

CHAPTER 5 reports twelve physical modelling tests on pipes subjected to cyclic axial displacement buried in dry soil to study ASPI's cyclic and post-cyclic behaviour.

CHAPTER 6 details six physical modelling tests on pipes buried in unsaturated soil to study the suction effect on ASPI. The method in CHAPTER 4 is extended for calculating the axial resistance of unsaturated soil, considering the effects of suction on interface shear strength, lateral earth pressure, stiffness, and dilatancy.

CHAPTER 7 develops a DEM code to simulate axial interaction between dry soil and pipe. After validating the tests in CHAPTER 4, a micro-level analysis of ASPI is conducted.

CHAPTER 8 extends the DEM code from CHAPTER 7 to simulate axial interaction between unsaturated soil and pipe. The experimental observations from CHAPTER 6 are back-calculated and analysed at a micro-level.

CHAPTER 9 summarises the major conclusions of this study and suggests directions for future research in this area.

CHAPTER 2
LITERATURE REVIEW

2.1 Engineering practices for buried pipeline systems

2.1.1 Applications and construction for buried pipeline engineering

Since the dawn of urbanisation, buried pipeline systems have been integral to human society, primarily serving water supply and drainage needs for daily life and agriculture (Needham, 1971; Hodge, 1992; Whidden, 2009). Today, modern buried pipeline systems have been employed across various applications, reflecting their versatility and essential role in infrastructure. These systems encompass sewer and drainage lines, water mains, gas and oil pipelines, conduits for telephone, electrical and military services, subway tunnels, and heat distribution lines (Moser & Folkman, 2008).

Onshore pipelines are typically buried underground rather than exposed to the air for several reasons, including protection from weather-related damage or human interference, land use, and environmental protection (Mohitpour *et al.*, 2007).

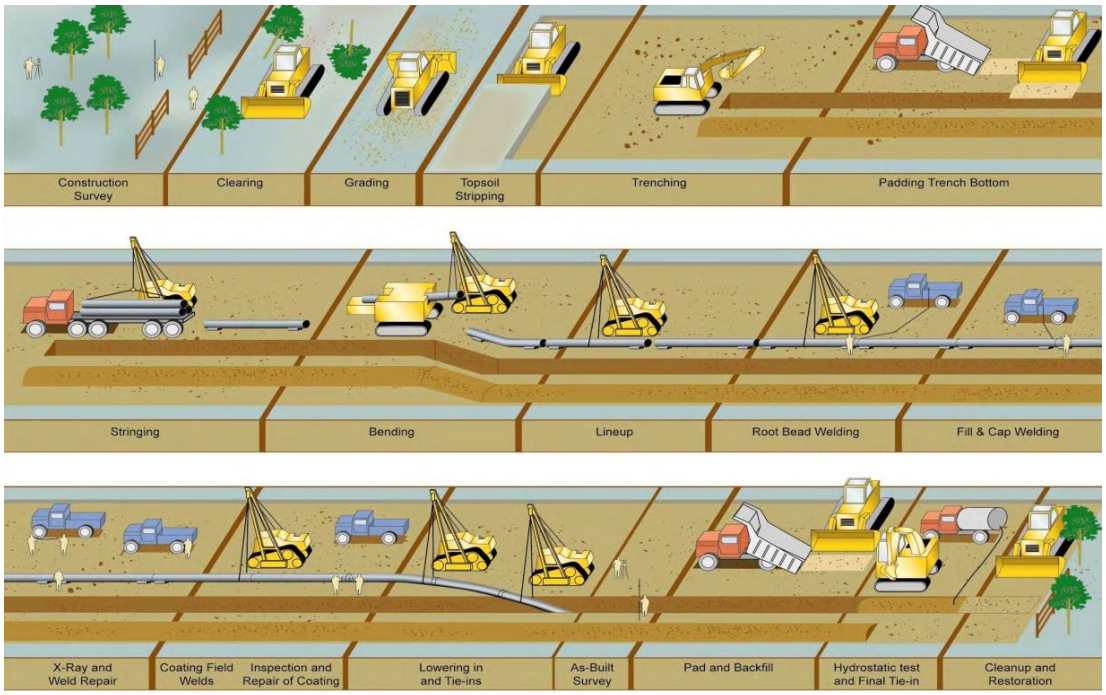

Figure 2.1 Typical pipeline construction sequence (Rizkalla & Read, 2019)

The typical pipeline construction process, illustrated in Figure 2.1, can be succinctly divided into eight steps (Mohitpour *et al.*, 2007), including survey and pre-construction, clearing, trenching, pipe stringing and bending, welding and coating, lowering pipe and backfilling, testing, and restoration.

During the trenching stage, the trench sides must be strong enough to prevent collapse, so the walls are usually shored or sloped for safety, especially when the excavation depth exceeds 1.5 meters (USBR, 1996; WSD, 2012). The trench width must provide sufficient workspace for inspecting pipe joints, compacting soils and conducting field density tests. Therefore, a minimum trench width is usually required. For instance, the minimum trench width, which depends on pipe diameter, trench slope, support, and trench depth, is specified in standards like BSI (2015), as shown in Table 2.1 and Table 2.2. The minimum depth of cover (i.e., the buried depth of the pipe centre) is typically specified to protect the pipe from surface activities such as agriculture and traffic loading. For example, in Europe, the minimum depths for pipelines in rights-of-way, under railroad crossings, and highway crossings are 0.8, 2.0, and 1.4 meters, respectively (Mohitpour *et al.*, 2007). In Hong Kong, the minimum depth ranges from 0.45 to 1.5 meters, depending on the application and location (WSD, 2012).

Trench backfilling is crucial for protecting the pipe and preventing uneven settlement. Some guidelines divide the backfilling zone into three components: (a) bedding for laying the pipe, (b) embedment to support the load on the pipe, and (c) backfill to refill the trench above the pipe and embedment (USBR, 1996). Cohesionless and free-draining soils are typically recommended as backfilling materials, and it is suggested that the soil be compacted to no less than 70% relative density to prevent uneven settlement and soil liquefaction (USBR, 1996; Moser & Folkman, 2008; WSD, 2012; CEDD, 2020). However, when pipes are buried on steep slopes (where the pipeline grade exceeds 0.3), silty or clayey soils may be used instead of cohesionless soils to avoid the challenges of compacting cohesionless soils on steep slopes

(USBR, 1996). Silty or clayey soils must be compacted to a density of at least 95% relative compaction within the embedment (USBR, 1996; WSD, 2012). Common compaction methods include dumping, sluicing, ponding or flooding, jetting, puddling, saturation and internal vibration, surface vibration, tamping, and rolling (USBR, 1996).

Table 2.1 Minimum trench width with varying nominal diameters (DN) (BSI BS EN 1610, 2015)

DN: m	Minimum trench width: m		
	Supported trench	Unsupported trench	
		$b > 60°$	$b \leq 60°$
≤0.225	$OD_h + 0.40$	$OD_h + 0.40$	
0.225~0.35	$OD_h + 0.50$	$OD_h + 0.50$	$OD_h + 0.40$
0.35~0.7	$OD_h + 0.70$	$OD_h + 0.70$	$OD_h + 0.40$
0.7~1.2	$OD_h + 0.85$	$OD_h + 0.85$	$OD_h + 0.40$
>1.2	$OD_h + 1.00$	$OD_h + 1.00$	$OD_h + 0.40$

OD_h is the horizontal outside diameter

b is the angle of the unsupported trench side measured to the horizontal

Table 2.2 Minimum trench width with varying trench depths (BSI BS EN 1610, 2015)

Trench depth: m	Minimum trench width: m
< 1.00	No requirement
1.00~1.75	0.80
1.75~4.00	0.90
> 4.00	100

2.1.2 Pipe material, size and surface treatment

Determining the pipe material, size, and surface treatment method is a crucial aspect of pipeline system design, aiming to achieve an optimal balance between performance, safety, and cost-effectiveness.

Common materials used in buried pipeline engineering include steel, iron, aluminium alloy, polyethene (PE), polyvinyl chloride (PVC), fibre-reinforced polymer (FRP), cement, concrete,

and clay. Key factors in selecting pipe materials include the type and properties of the fluid being transported (e.g., PE pipes can be affected by hydrocarbons), safety requirements (e.g., for potable water), environmental conditions (e.g., mechanical performance in soil-pipe interactions), cost, and installation or maintenance needs (Bahadori, 2017).

Table 2.3 Common materials and sizes of water mains in Hong Kong (WSD, 2020)

Pipe Material	Nominal Diameter, DN: mm
Steel	≥100
Ductile iron	80~600
Asbestos cement	100~450
UPVC	≤100
Unlined galvanised iron	≤150
Lined galvanised iron	≤150
Polyethene	≤250
Stainless steel	≤50
Cast iron	≤450

Pipe sizing involves determining the nominal diameter and wall thickness. The primary consideration for the nominal diameter is ensuring it is sufficient to meet the required flow velocity and pressure drop. For instance, the design manual for water mains in Hong Kong specifies that the maximum flow velocity for both pumping and distribution mains should be less than 3 m/s (WSD, 2020). Specific values for pipe diameter and wall thickness are typically selected based on manufacturing standards (e.g., ASME (2018) for steel pipes and ISO (2019) for PE pipes). In practice, the choice of pipe diameter is influenced by material strength, cost, and application. For example, steel pipes, known for their impact and tensile stress resistance, are commonly used for large-diameter water mains in Hong Kong, as shown in Table 2.3.

Surface treatment techniques such as coating, wrapping, and sand-blasting are frequently applied to the external surfaces of steel pipes to protect against corrosion and damage, clean the surface, adjust resistance, or provide thermal insulation (ISO 8501-1, 2007; CEDD, 2020).

Typical coating and wrapping materials include fusion-bonded epoxy (FBE), epoxy asphalt (EA), PE, polypropylene (PP) and coal tar (CT) (Mohitpour *et al.*, 2007).

2.1.3 Loads on buried pipelines

Estimating the loads applied to buried pipelines is a crucial aspect of pipeline design. These loads can be broadly categorised into three main types:

1) **Loads caused by relative soil-pipe displacement**: This is the primary focus of this thesis. Relative displacement can result from ground movements due to landslides, liquefaction, surface fault rupture, frost heave, thaw settlement, and pipe movement induced by upheaval buckling, thermal expansion, and systematic deformation due to variations in soil resistance (Ni & Mangalathu, 2018; Oswell, 2021). Current design guidelines typically divide soil loads due to relative displacement into three components: axial, vertical, and lateral (ASCE, 1984; ALA, 2001; PRCI, 2009; Ye *et al.*, 2023). These soil loads are modelled as linear elastic-perfect plastic Winkler springs, as illustrated in Figure 2.2. They are often input into finite element method (FEM) software to analyse performance under relative displacement. The resistance calculations in different directions are usually based on semi-empirical equations derived from theories related to piles, retaining walls, soil anchors, and strip footings.
2) **Static and dynamic loads from surrounding soils**: These include vertical and lateral earth pressures, surface live loads from railway cars, locomotives, and aircraft, surface impact loads from heavy weights, buoyancy forces, seismic waves, and the effects of blasting due to nearby construction and mining activities (Ni *et al.*, 2018b).
3) **Loads from internal fluids**: These encompass the internal pressure of the fluid, fluid transients, and expansion loads and stresses resulting from temperature variations in the liquid.

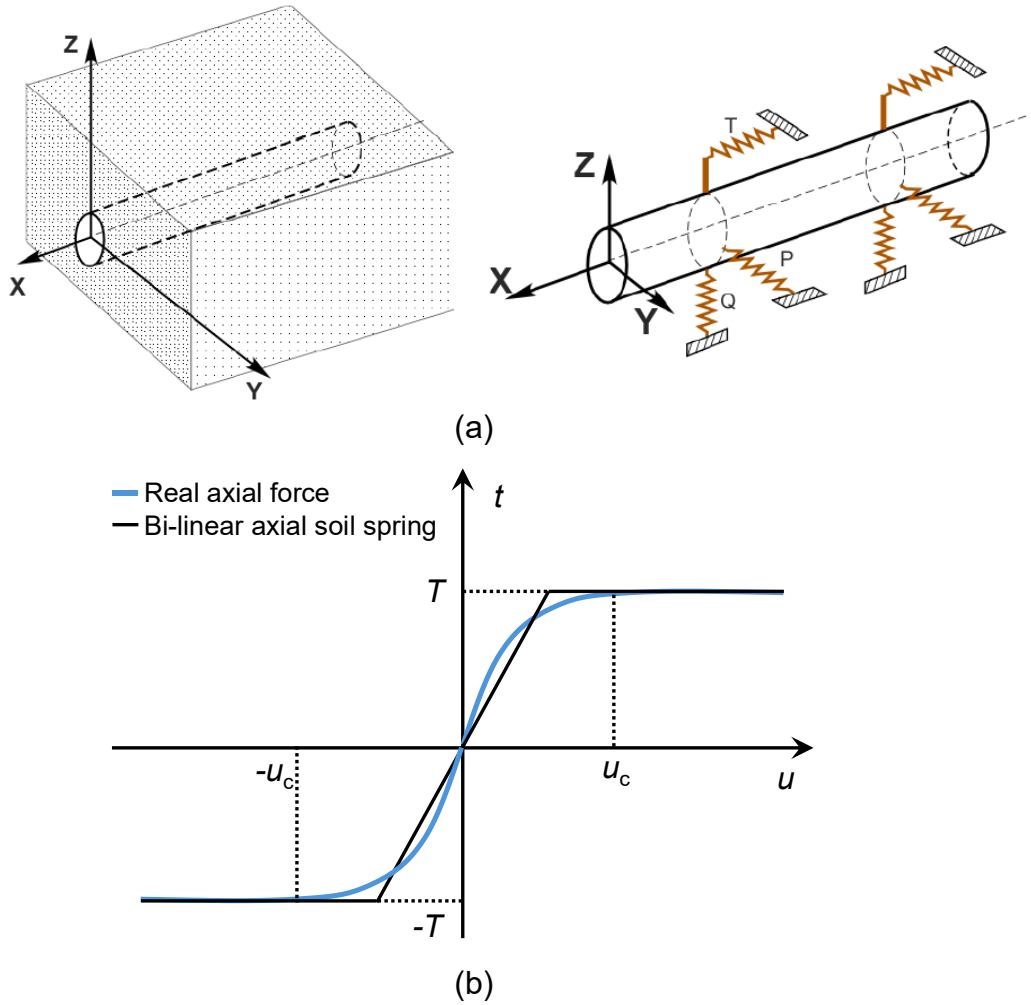

Figure 2.2 Idealisation of soil forces on buried pipe (ASCE, 1984): (a) idealised 3D soil loads with discrete springs in three dimensions; (b) bi-linear spring representing the relationship between axial force (*t*) and relative displacement (*u*)

2.1.4 Calculation of axial resistance in guidelines

In the current design method (ASCE, 1984), the soil surrounding the pipe is modelled as idealised bilinear discrete springs in three directions. This thesis focuses on the axial spring (see Figure 2.2 (b)), where the axial force per unit length, t, is expressed as:

$$t = \begin{cases} \dfrac{u}{0.5u_c} T & ,0 \le u < 0.5u_c \\ T & ,u \ge 0.5u_c \end{cases} \tag{2-1}$$

where T is the axial resistance (i.e., the maximum axial force per unit length), u is the soil-pipe relative displacement in the axial direction, and u_c is the critical axial displacement.

ASCE (1984) calculates the axial resistance, T, of pipes buried in sands using the Mohr-Coulomb theory and the extended β-method for pile design (Burland, 1973). It is assumed that the average interface contact pressure (the average normal stress) on pipes equals the mean of nominal vertical pressure at the pipe centre, σ_c' (= $\gamma' H_c$), and its lateral earth pressure at rest, K_0 σ_c'. Hence, T can be calculated as follows:

$$T = \pi D \frac{1+K_0}{2} \sigma_c' \tan\delta \tag{2-2}$$

where D is the pipe outer diameter; γ' is the effective unit weight of the soils; H_c is the buried depth of the pipe centre; tan δ is the soil-interface friction coefficient; δ is the interface friction angle. Based on early studies of piles and pipelines, the value of u_c is 3 mm for dense sand and 5 mm for loose sand.

ASCE (1984) suggests that δ equals 0.5~1.0 φ, where φ is the internal friction angle of pure soil for smooth and rough steel, Formica, and plastic pipe based on previous interface shearing testing results. For soft wrapping pipe and oxidised pipe, δ is recommended as 1.0 φ', and for pipes with smooth, relatively hard, and weathered coatings, it ranges from 0.5 to 0.7 φ'.

For pipelines buried in clays, T is calculated using the α-method

$$T = \pi D \alpha c_u \tag{2-3}$$

where c_u is the undrained soil shear strength and α is the empirical coefficient that varies with c_u. Unlike the lower value used in pile design, ASCE (1984) recommends a relatively high estimation of α, considering the imposed displacement for the pipeline. The critical displacement u_c equals 5 to 10 mm for stiff to soft clay.

Subsequently, ALA (2001) modified Eqs (2-2) and (2-3) by incorporating components of friction and cohesion:

$$T = \pi D \alpha c_u + \pi D \frac{1+K_0}{2} \sigma_c' \tan f\varphi \tag{2-4}$$

Table 2.4 Interface friction angle factor with different pipe coating (ALA, 2001)

Pipe Coating	f
Concrete	1.0
Coal tar	0.9
Rough steel	0.8
Smooth steel	0.7
Fusion-bonded epoxy	0.6
Polyethylene	0.6

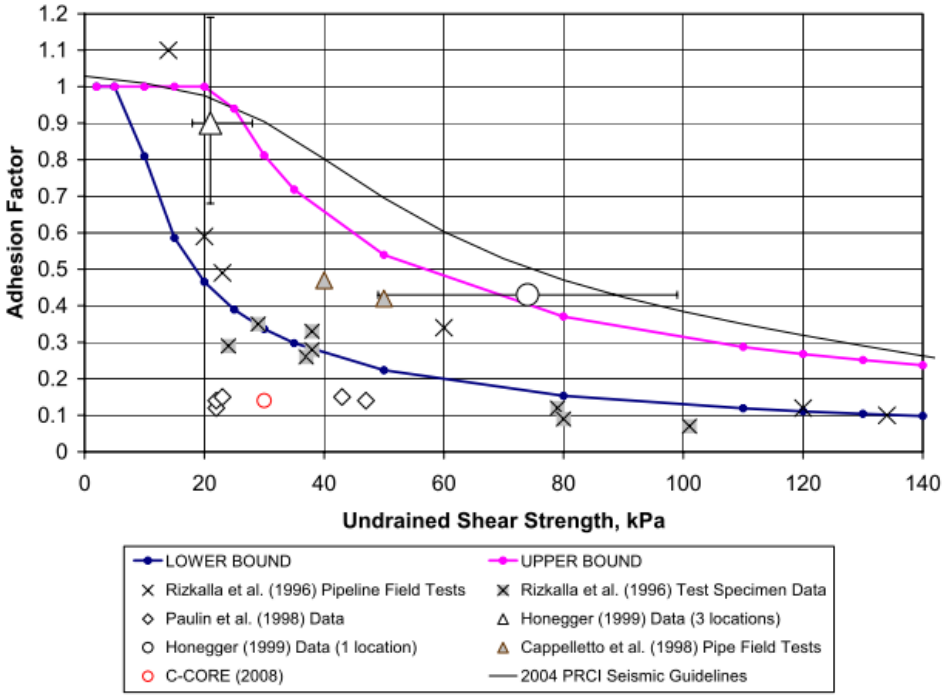

Figure 2.3 Recommended bounds for adhesion factor (PRCI, 2009)

where f is the soil-pipe interface friction factor. The value of f accounts for the effect of interface material and roughness, with recommended values provided in Table 2.4. α is calculated as $0.608 - 0.123c_u - 0.274/(c_u^2+1) + 0.695/(c_u^3+1)$.

Ultimately, PRCI (2009) further refined Eq. (2-4) as

$$T = \pi D\alpha c + \pi D\frac{1+K}{2}\sigma_c' \tan f\varphi_m \tag{2-5}$$

Table 2.5 Summary of physical modelling and field tests on ASPI

Reference	Soil	Moisture condition	Pipe material	Coating or wrapping	Roughness: μm	Cyclic displacement	Thermal loading	Discussion on roughness or hardness effects	Discussion on moisture content effects	Pressure measurement
Paulin *et al.* (1998)	Sand, clay	No given	No given	No given	No given	No	No	No	No	No
Scarpelli *et al.* (2003)	Granulate, sand, cohesive soil	Dry, w = 25%, saturated	Steel	PE, PP, CT	R_a=380	No	No	Yes	No	No
Weidlich & Achmus (2008)	Sand	Dry	No given	HDPE	No given	Yes	No	No	No	Interface contact pressure by array-type TPSs
Weerasekara & Wijewickreme (2008)	Sand	Dry	PE	None	No given	No	No	No	No	No
Wijewickreme *et al.* (2009)	Sand	Dry	Steel	None	R_{max}≈400	No	No	No	No	Interface contact pressure by EPCs
Bilgin & Stewart (2009a)	Sand	$w \approx 5\%$	HDPE	None	No given	Yes	2~21°C	Hardness effect	No	No
Bilgin & Stewart (2009b)	Sand	w = 12.4%	Cast iron	None	Not given	No	No	No	No	No
Daiyan *et al.* (2011)	Sand	Dry	Steel	None	Not given	No	No	No	No	No
Huber & Wijewickreme (2014)	Sand	$w \approx 4.02\%$	Steel	HDPE	Not given	No	ΔT = 50°C	No	No	No
Wijewickreme & Weerasekara (2015)	Sand	Moist	HDPE	None	Not given	No	No	No	No	No
Sarvanisa *et al.* (2018)	Sand	w = 5.7~8.0%	Steel	No given	Not given	No	No	Coating effect	No	No
Sheil *et al.* (2018)	Sand	Dry, w = 6.2~13.5%	Steel	FBE	R_{max}=39.2	Yes	No	No	No	Interface contact pressure and local shear stress by Stroud load cells
Al-Khazaali & Vanapalli (2019)	Sand	Saturated, s = 2.75~9.75 kPa	Steel	None	R_{max}=250	No	No	No	Yes	No
Murugathasan *et al.* (2021)	Sand	Dry	Ductile iron	None	Not given	No	No	No	No	Earth pressure by single-point-type TPS
Reza & Dhar (2021)	Sand	w = 0.8~ 1.5%	HDPE	None	Not given	No	No	No	No	No

Note: w is water content; s is matric suction; ΔT is temperature difference; R_a is the average height deviations over a travel length of mean particle size, d_{50}; R_{max} is the maximum height on the surface profile over a travel length of d_{50}.; EPC is the traditional earth pressure cell, and TPS is the tactile pressure sensor

where parameters are updated based on new testing results and engineering practices. First, K (i.e., lateral earth pressure) ranges from K_0 to 2 for loose soil to dilative soil based on the results of Weerasekara & Wijewickreme (2008). Second, φ is specific to the pure soil's maximum internal friction angle. Third, the lower and upper bounds of α are $0.7(120/c_u)^{0.8} \leq 1$ and $0.5(550/c_u)^{0.8} \leq 1$, based on previous experimental results as shown in Figure 2.3. Adding the lower bound for α is the most essential modification by PRCI (2009). Previous guidelines only considered the upper bound based on the maximum testing results for pipe safety. However, an overestimated (low, in actuality) axial soil resistance can cause stress to concentrate in more vulnerable locations, such as valve stations, sharp bends, or cracks, rather than at the soil-pipe interface. Therefore, a more accurate assessment is recommended.

2.2 Physical modelling and field tests on axial soil-pipe interaction

Physical modelling and field tests on axial soil-pipe interaction (ASPI) have been conducted using pipes with various materials and surface conditions. These studies aim to provide data for engineering practice and elucidate pipe behaviour mechanisms under axial displacement. A summary of these studies is presented in Table 2.5.

2.2.1 Axial behaviour of pipes subjected to monotonic loading

The pioneering work of Paulin *et al.* (1998) and Scarpelli *et al.* (2003) on axial resistance during monotonic loading is particularly practical. For instance, Paulin *et al.* (1998) highlighted that the equation proposed by ASCE (1984) significantly overestimates the axial resistance of pipes buried in clay. They noted that α can vary depending on the coating, burial depth, soil sampling technique, and soil conditions. Scarpelli *et al.* (2003) recommended using smooth and hard coating materials to achieve lower axial resistance.

Subsequent experiments have primarily focused on the axial interaction between sand and metal pipes subjected to monotonic loading. Wijewickreme *et al.* (2009) conducted four tests using a testing apparatus developed by Anderson *et al.* (2004). This apparatus mainly consisted

of a chamber and a hydraulic actuator to apply axial displacement. The pipe surface was sand-blasted before testing. The pipeline length is longer than the size of the experimental box to maintain a constant length of soil-pipe interaction during the tests. This method is widely accepted in subsequent studies. Soft foam gaskets were mounted at the soil-pipe interface of the front and rear walls to minimise uniform axial force along the pipe. Wijewickreme *et al.* (2009) embedded five EPCs on the pipe surface to measure interface contact stress distribution. The experimental results showed that constrained dilation increased interface contact pressure on the pipe surface, enhancing pullout resistance (see Figure 2.4, where dimensionless normal stress is the ratio of interface contact pressure to nominal pressure at the pipe centre). The lateral earth pressure coefficient could reach 2.2 by back-calculation, higher than the K_0 suggested in Eq (2-2).

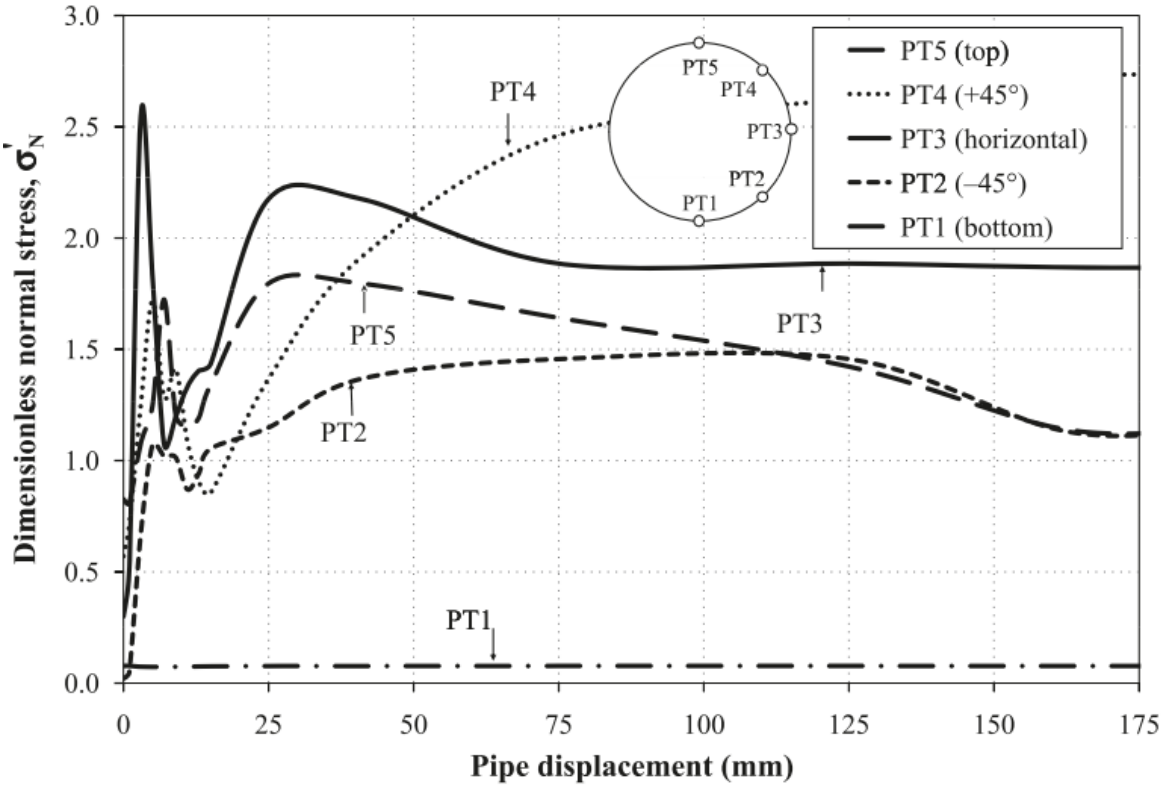

Figure 2.4 Interface contact pressure evolution during pipe pullout (Wijewickreme *et al.*, 2009)

Huber & Wijewickreme (2014) studied the effect of net temperature change cycling on monotonic axial resistance using HDPE-coated and polyurethane-insulated steel pipes in moist sand. Microprocessor-controlled electric heaters and a hydraulic pump achieved a 50°C net temperature change control. Pulling the pipe at high temperatures significantly increased axial resistance, while a decrease was observed after three heating-cooling cycles.

2.2.2 Axial behaviour of pipes subjected to cyclic loading

Several researchers have studied the cyclic effect on ASPI behaviour. Weidlich & Achmus (2006) investigated the cycling effect on HDPE-coated pipes, considering pipe diameter, relative cover height (H/D), and relative density of sand embedment in approximately 80 tests. Each test involved ten cycles, and the axial resistance stabilised after five to eight cycles. As the diameter increased, axial resistance also increased, but the ratio of initial loading friction to residual friction decreased. Relative density significantly affected results: loose samples with a relative density of 10% showed a slight increase during cycling. In contrast, denser samples exhibited a notable decline in the initial to residual resistance ratio, as shown in Figure 2.5. This ratio marginally increased with greater overburden height. An array-type flexible tactile sensor detected the interface contact pressure distribution on the pipe surface. During initial loading, pressure concentrated on the pipe's crown and invert, but stress distribution became constant and uniform after ten cycles.

Bilgin & Stewart (2009a) examined the axial sand-HDPE pipe interaction under varying operating temperatures. Pipes with a diameter/thickness ratio of 11 were buried in a wooden box at 21°C. They were then subjected to ten cycles of pulling and pushing at 21, 10, 7, 6, and 2°C in a controlled temperature chamber after 7~10 days of cooling. An instrumentation cage inside the pipe detected diameter changes. During the first pull, pullout resistance at 2°C was 60% lower than at 21°C due to thermal contraction and decreased hardness. After ten cycles, axial resistance was reduced by 75% at 21°C compared to the first cycle.

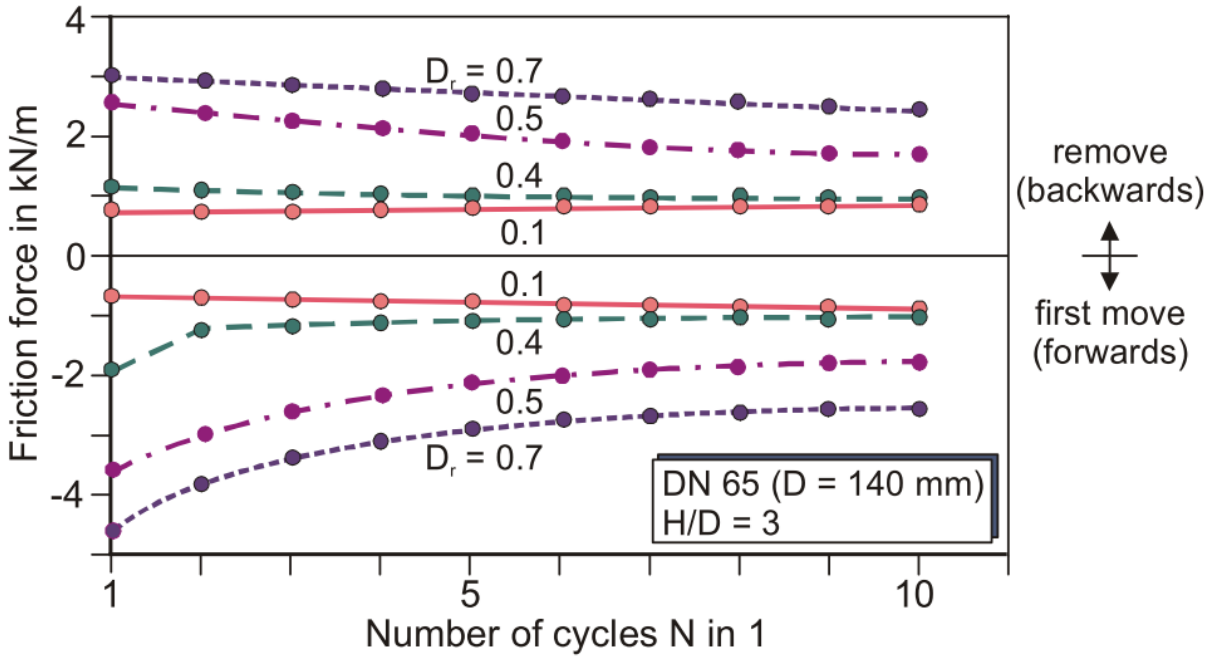

Figure 2.5 Cyclic degradation of axial resistance dependent on relative density (D_r)

(Weidlich & Achmus, 2006)

Sheil *et al.* (2018) developed a testing system to study soil resistance on heavy FBE-coated pipes subjected to cyclic axial displacement (see Figure 2.6). Wooden side walls of the experimental box were utilised to simulate trench roughness in practice. The pipe was divided into three sections, where the central one was connected to two end sections through internal spindle structures with two axial load cells to measure the axial force on the central section to minimise the boundary effect of the front and rear walls. Small gaps, with a width of 3 mm, were found among the three sections filled with soft silicone rubber. The pipe weight was added to 4 kN/m to simulate a heavy pipe in engineering practice. Compressible foam seals were used around the pipe on the front and rear walls to allow unrestrained settlement and prevent soil leakage. Two knuckle joints were used to fit load cells between the pipe and the jack, allowing vertical freedom. Two LVDTs were mounted on the front and rear walls to measure vertical displacement at each pipe end. Six 'Stroud' type transducers, capable of measuring normal, shear force, and moment of soil-pipe interface, were mounted into the pipe's central section. A pressure bag provided sufficient overburden pressure, originally limited by laboratory

conditions. Alternating larger (20 mm) and smaller amplitude (5 mm) cycles were applied. Cyclic degradation of axial resistance and pipe settlement with cycling were observed. The distribution and evolution of interface contact pressure on the pipe surface demonstrated the soil arching effect on pipe pullout behaviour.

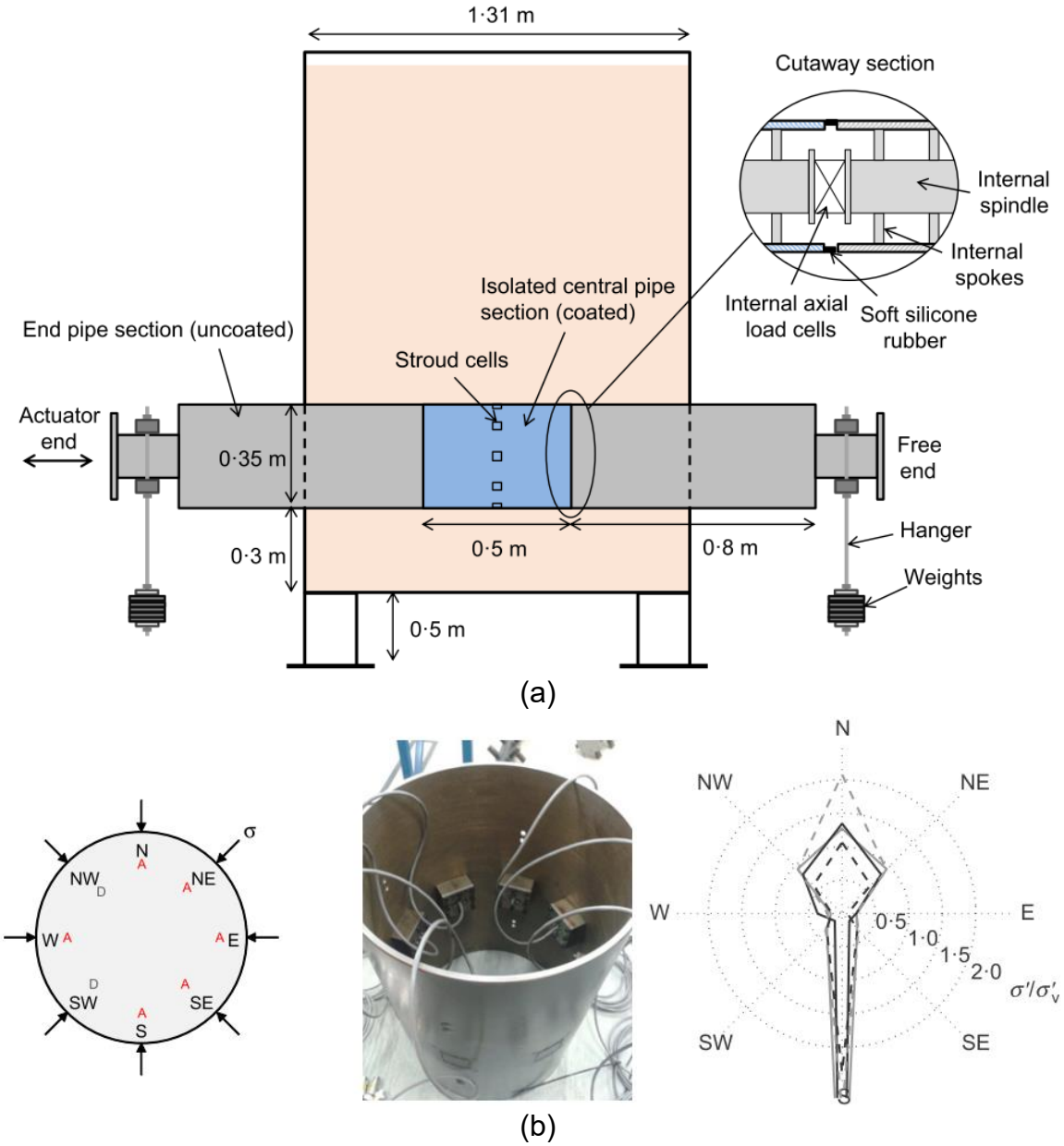

Figure 2.6 Experiment details of Sheil *et al.* (2018): (a) schematic diagram of the experimental system; (b) measurement of interface contact pressure distribution

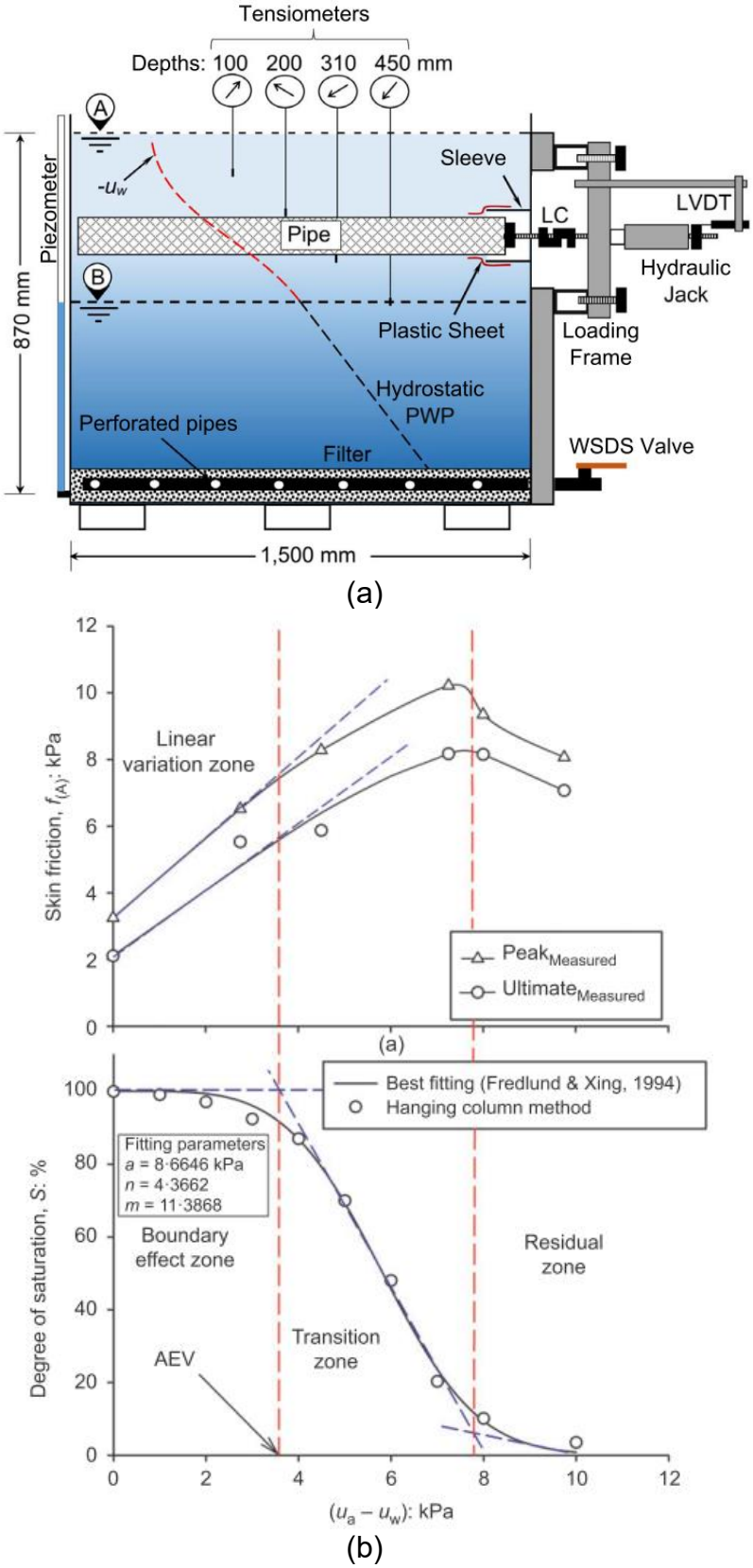

Figure 2.7 Matric suction effect on axial sand-pipe interaction behaviour (Al-Khazaali & Vanapalli, 2019): (a) experimental system; (b) relationships between skin friction (axial resistance per unit area) and soil retention capability and matric suction (u_a-u_w)

2.2.3 Unsaturated effect on axial soil-pipe interaction

Only Al-Khazaali & Vanapalli (2019) have conducted large-scale physical modelling to study the ASPI in unsaturated conditions. To minimise the boundary effect of the experimental box's front wall, a sleeve with a 200 mm diameter larger than 114.4 mm of the test pipe was mounted on the inner side of the box's front wall. A thin plastic sheet was wrapped around the overlapping part of the sleeve and pipe to avoid sand leakage. A desaturation method was used to control suction in the box. A transparent acrylic window was installed in a section of the box wall to observe water level changes during saturation and desaturation. Several tensiometers were buried around the pipe to measure real suction. A rough steel pipe was buried in sand at a constant depth of 0.2 m. The matric suction was controlled by adjusting the water table. They observed an increasing trend in axial resistance per unit area as the average measured matric suction increased from 0 (submerged condition) to 7.25 kPa, followed by a decrease as suction further increased to 9.75 kPa, as shown in Figure 2.7. A new equation considering the suction effect on normal effective pressure was developed to predict the axial resistance of pipes in unsaturated sand. However, the suction effect on axial resistance in sand is limited (increasing by less than 7 kPa per unit area in Al-Khazaali & Vanapalli (2019)) due to the limited suction effect on sand.

2.2.4 Measuring earth pressure and soil-structure interface contact pressure using tactile pressure sensors

Earth pressure plays a vital role in analysing the deformation and stability of foundations and buried structures. Accurate and long-term assessment of earth pressure is essential in geotechnical engineering practice and laboratory testing. Earth pressure cells (EPCs), also known as total pressure cells, have been widely used to measure earth pressure and soil-structure interface contact pressure. Three types of EPCs—based on strain gauge, vibrating wire, and piezoelectric ceramics—are commercially available (Peattie & Sparrow, 1954; Thomas &

Ward, 1969; Vennapusa *et al.*, 2012). Recently, a fibre-optic-based EPC has been developed, offering improved accuracy and a broader measurement range (Qin *et al.*, 2022).

However, researchers have often questioned the reliability of EPC results. Each type of EPC requires sufficient space to accommodate its internal structure, resulting in a certain thickness (usually at least 5 mm). This thickness can be affected by the negative soil-arching effect, leading to uneven deformation around the sensor. The soil prism above the sensor experiences relative displacement with the surrounding soil, resulting in additional downward friction and overestimating the measured earth pressure (Tory & Sparrow, 1967; Suits *et al.*, 2005).

Paikowsky & Hajduk (1997) introduced a tactile pressure sensor (TPS) for measuring pressure in granular materials. The TPS is flexible, thin, and can conform to curved surfaces. Its electrical resistance decreases with increasing applied force or pressure. There are two main types of TPS: array-type and single-point-type, based on the number of measuring points.

The array-type TPS typically consists of a grid matrix with small sensing points. Its high resolution of 0.1 mm allows for detailed pressure distribution measurement, detecting hundreds of thousands of measuring points. This feature makes it well-suited for applications in pressure distribution measurement. Gillis *et al.* (2015), Muszynski *et al.* (2016), and Madabhushi & Haigh (2019) used this sensor to measure earth pressure distribution on walls and container bottoms in geotechnical centrifuges. In soil-pipe interaction studies, scholars have also utilised the array-type TPS. Weidlich & Achmus (2008) applied this technique in cyclic ASPI physical model tests by directly attaching the TPS foil to the pipe surface. The experimental findings indicated an initial distribution of interface contact pressures at the pipe crown and invert, which gradually became more homogeneous during cycling. Palmer *et al.* (2009) employed the array-type TPS in physical modelling studies on lateral soil-pipe interaction, using a Teflon cover to protect the sensor and eliminate shear stress impact. Meguid & Ahmed (2020) used this sensor

to measure pipe interface contact pressure distribution and its evolution under cyclic overlying pressure, investigating the effect on buried pipes installed with the Geofoam inclusion technique. A thin layer of stiff rubber sheet was used to protect the sensor. However, while the array-type sensor allows for reliable qualitative analysis, quantitative analysis may not be as accurate. This is because the full-surface coverage of the sensor may influence the surface conditions of pipes, such as roughness and hardness, which can impact the reproducibility of engineering practices, particularly in cases involving significant interface friction. Moreover, this technique is quite expensive, as it requires a specialised data logging system.

In contrast, the single-point-type TPS is much more affordable. It can be measured using commonly available dataloggers equipped with a transmitter that users can easily purchase or make (Interlink, 2023). The active area diameter of this type of sensor can range from 5 mm to 40 mm. However, the utilisation and evaluation of single-point-type TPS are somewhat limited. Using an oedometer, Gao *et al.* (2017) used this sensor to measure lateral earth pressure in 1D consolidation testing. They developed a specialised needle probe to measure excess pore water pressure. Kootahi & Leung (2022) studied the effect of particle size on the single-point-type TPS. Their test results demonstrated that increasing the ratio between the sensor's active area diameter and the diameter of the particles can enhance measurement accuracy. When this ratio exceeded 10.5, the measurement error was below 5%. Furthermore, research by Liu *et al.* (2021a) indicated that the zero offset resistance of the TPS decreased as deflection increased.

It is worth noting that TPS (whether array-type or single-point-type) is not an ideal sensor compared to traditional commercial sensors. It can exhibit significant repeatability errors of up to 25% between different units and hysteresis errors of around 15% (Kootahi & Leung, 2023). Loading rate, loading history, and shear stress can also impact its output (Paikowsky & Hajduk, 1997; Muszynski *et al.*, 2016; Kootahi & Leung, 2023). Therefore, calibration is crucial when using this sensor.

2.3 Analytical and numerical simulation on axial soil-pipe interaction

2.3.1 Analytical solution on axial force during pipe pullout

In the aforementioned experimental studies, it is commonly observed that the average interface contact pressure on the pipe surface exceeds the value suggested by ASCE (1984) due to soil dilatancy. Also, tests involving metal and plastic pipes noted strain-softening behaviour. Two analytical models are proposed below to address these two issues.

Sarvanisa *et al.* (2018) improved the bi-linear spring in Eq (2-1), expressed as

$$t=\begin{cases}\pi D\dfrac{u}{u_{\mathrm{c}}}\left[\dfrac{1+K_0}{2}\sigma_{\mathrm{c}}{}'+\Delta\sigma_{\mathrm{D}}{}'\right]\tan f\varphi_{\mathrm{m}} & ,0\le u<u_{\mathrm{c}}\\ \pi D\left[\dfrac{1+K_0}{2}\sigma_{\mathrm{c}}{}'+\Delta\sigma(u')\right]\mu(u') & ,u\ge u_{\mathrm{c}}\end{cases} \tag{2-6}$$

Before axial displacement reaches u_{c} (taken as 2.5~5 mm, as suggested by ASCE (1984)), the interface friction coefficient is assumed constant. The axial force increases linearly with displacement. An average increase in interface contact pressure caused by constrained dilation $\Delta\sigma_{\mathrm{D}}'$ is introduced and calculated by the one-element numerical model with restraining motion in the vertical direction by ABAQUS. After u_{c}, the interface friction coefficient and $\Delta\sigma_{\mathrm{D}}'$ are replaced as $\Delta\sigma(u')$ and $\mu(u')$, functions of the post-critical axial displacement u' (= u - u_{c}), expressed as

$$\Delta\sigma(u')=\Delta\sigma_{\mathrm{res}}+\left(\Delta\sigma_{\mathrm{peak}}-\Delta\sigma_{\mathrm{res}}\right)e^{-\alpha_{\mathrm{s}}u'} \tag{2-7}$$

$$\mu(u')=\tan f\varphi_{\mathrm{res}}+\left(\tan f\varphi_{\mathrm{m}}-\tan f\varphi_{\mathrm{res}}\right)e^{-\alpha_{\mathrm{s}}u'} \tag{2-8}$$

where $\Delta\sigma_{\mathrm{res}}$ is the residual value of the average increase in interface contact pressure caused by constrained dilation, also obtained from one-element numerical analysis; φ_{res} is the residual internal friction angle of sand; α_{s} is the resistance decay factor, related to interface friction and dilatancy, taken as 9 mm^{-1} as suggested.

Wijewickreme & Weerasekara (2015) also introduced $\Delta\sigma_D'$ to describe dilation-caused interface contact pressure increase. But his method comes from the elastic cavity expansion theory (Boulon and Foray, 1986) and sawtooth-type model (Luo *et al.*, 2000), which is a function of the soil's shear modulus and maximum dilation angle.

The axial strain of a plastic pipe is solved by considering the equilibrium of a pipe element by

$$\frac{d}{dx}\left[EA_p\left(\frac{du}{dx}\right)\right]=T \tag{2-9}$$

where E is Young's modulus of the viscoelastic plastic material, which is a function of the stress and strain rate of the pipe; A_p is the pipe's cross-sectional area. The axial displacement of any pipe cross-section can then be calculated, allowing the soil-pipe interaction problem to be solved by dividing the pipe into small element lengths.

2.3.2 Numerical modelling on axial soil-pipe interaction

Numerical simulation presents a promising alternative for studying soil-pipe interaction, with various continuum-based methods employed to investigate ASPI.

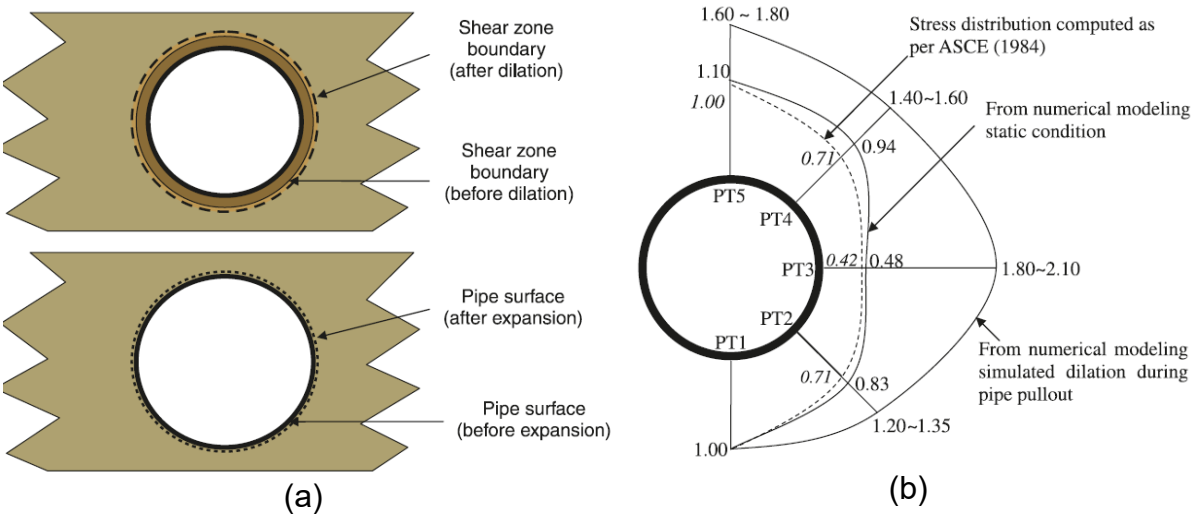

Figure 2.8 2D FDM on calculating soil-pipe interface contact pressure (Wijewickreme *et al.*, 2009): (a) schematic diagram of methodology; (b) simulation results

Wijewickreme *et al.* (2009) utilised a 2D FDM simulation to extend their physical modelling results (see Figure 2.8). For simplification, the simulation used a 2D vertical plane perpendicular to the buried pipe axis, omitting the pullout process, which is inherently three-dimensional. They assumed that volume changes due to dilation around the pipe surface could be numerically simulated by radially expanding the pipe. The expansion distance was considered constant around the pipe, estimated at 0.7~1 mm based on previous interface shear studies. The Duncan-Chang model, incorporating the empirical flow rule of Bolton (1986), was used to model the soil, while the classical Mohr-Coulomb theory was applied to model interface behaviour. The simulation results aligned with physical modelling, indicating that dilation-induced volume changes increase interface contact pressure around the pipe. Consequently, the lateral earth pressure coefficient in Eq (2-2) should be considered within the range of K_0 to 2.5 due to the pressure increase from dilation. This conclusion was subsequently adopted in the PRCI (2009) guidelines, as shown in Eq (2-5).

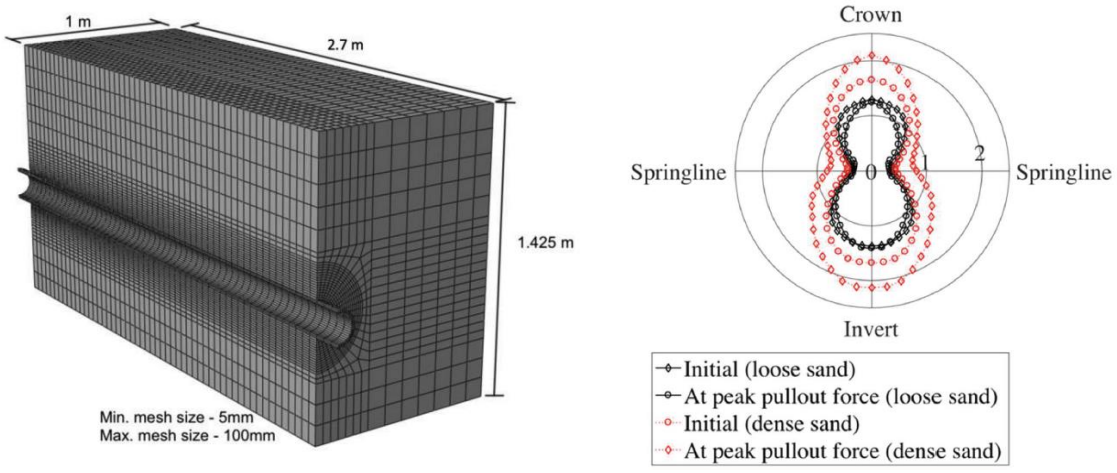

Figure 2.9 3D FEM on axial soil-pipe (Murugathasan *et al.*, 2021): (a) typical FE mesh; (b) numerical results of interface contact pressure distribution

Compared to FDM, FEM is more commonly used in ASPI simulations (Al-Khazaali & Vanapalli, 2018; Sarvanisa *et al.*, 2018; Muntakim & Dhar, 2021). For instance, Murugathasan *et al.* (2021) and Reza & Dhar (2021) employed 3D FEM to back-calculate physical modelling

results for ductile iron and MDPE pipes, respectively. The soil and pipe were simulated as deformable bodies using eight-node linear brick elements. The linear elastic-perfect plastic model was used to model the stress-strain behaviour of the soil. Young's modulus for the soil was determined using a stress-dependent equation by Hardin & Black (1966), while the elasticity modulus of plastic material was modelled using a strain rate-dependent model by Suleiman & Coree (2004). Plane symmetrical boundary conditions were applied to enhance calculation efficiency. Although the post-peak response could not be simulated, the development and redistribution of interface contact pressure during pipe pullout were modelled, demonstrating soil arching and constrained dilatancy (see Figure 2.9).

Furthermore, Saberi *et al.* (2022) utilised a hybrid-Winkler-interface method to simulate ASPI. Beam elements, Winkler springs, and thin-layer elements represent the pipe, surrounding soil, and soil-pipe interface. Winkler springs include vertical-upward, vertical-downward, and lateral soil springs, with equations from ALA (2001) applied at the pipe crown, invert, and springlines using initial normal pressures calculated by σ_c' and $K_0\,\sigma_c'$. The axial soil interaction is simplified as coupled constant stiffness loading interface shearing behaviour of three 2D soil-pipe interface elements. The interface shear behaviour was solved using FEM software, ABAQUS, with 4-node quadrilateral elements. The bounding surface model was used in FEM to capture comprehensive interface behaviour related to dilatancy and cyclic behaviour. The interface thickness was 7 mm, within the common range of 5~22 d_{50} observed in interface shear tests (DeJong & Westgate, 2009; Pra-ai & Boulon, 2016; Rui *et al.*, 2020a). This method proved efficient in back-calculating cyclic ASPI experimental results by Weidlich & Achmus (2008); Bilgin & Stewart (2009b); Sheil *et al.* (2018), even with simplified soil responses.

Scholars from McGill University conducted a series of DEM simulations on ASPI. The axial behaviour of rigid steel pipes in dense sand was evaluated first, where the pipe was created with facet discrete elements (Meidani *et al.*, 2017; Meidani *et al.*, 2018), as shown in Figure

2.10. The experimental results from Wijewickreme *et al.* (2009) were back-analysed at the micro-level, such as contact force networks and soil particle displacement. A parametric study on key influential parameters, including buried depth, soil stiffness, internal friction angle and pipe diameter, was conducted, leading to a new empirical equation for calculating the axial resistance (Meidani *et al.*, 2020b).

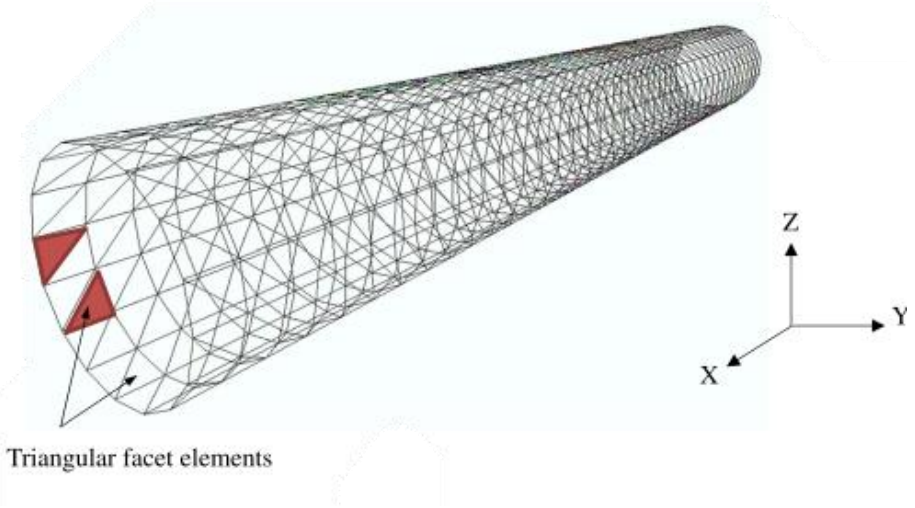

(a)

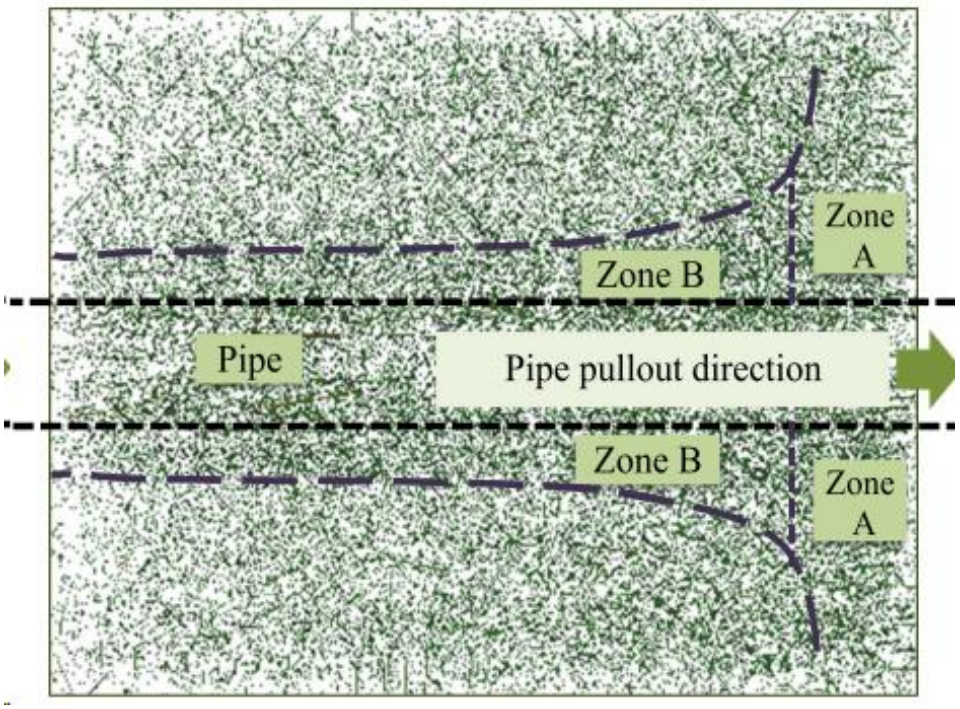

(b)

Figure 2.10 DEM simulation on axial soil-steel pipe interaction (Meidani *et al.*, 2017): (a) simulated pipeline using facet elements; (b) non-uniform contact force network during pipe pullout

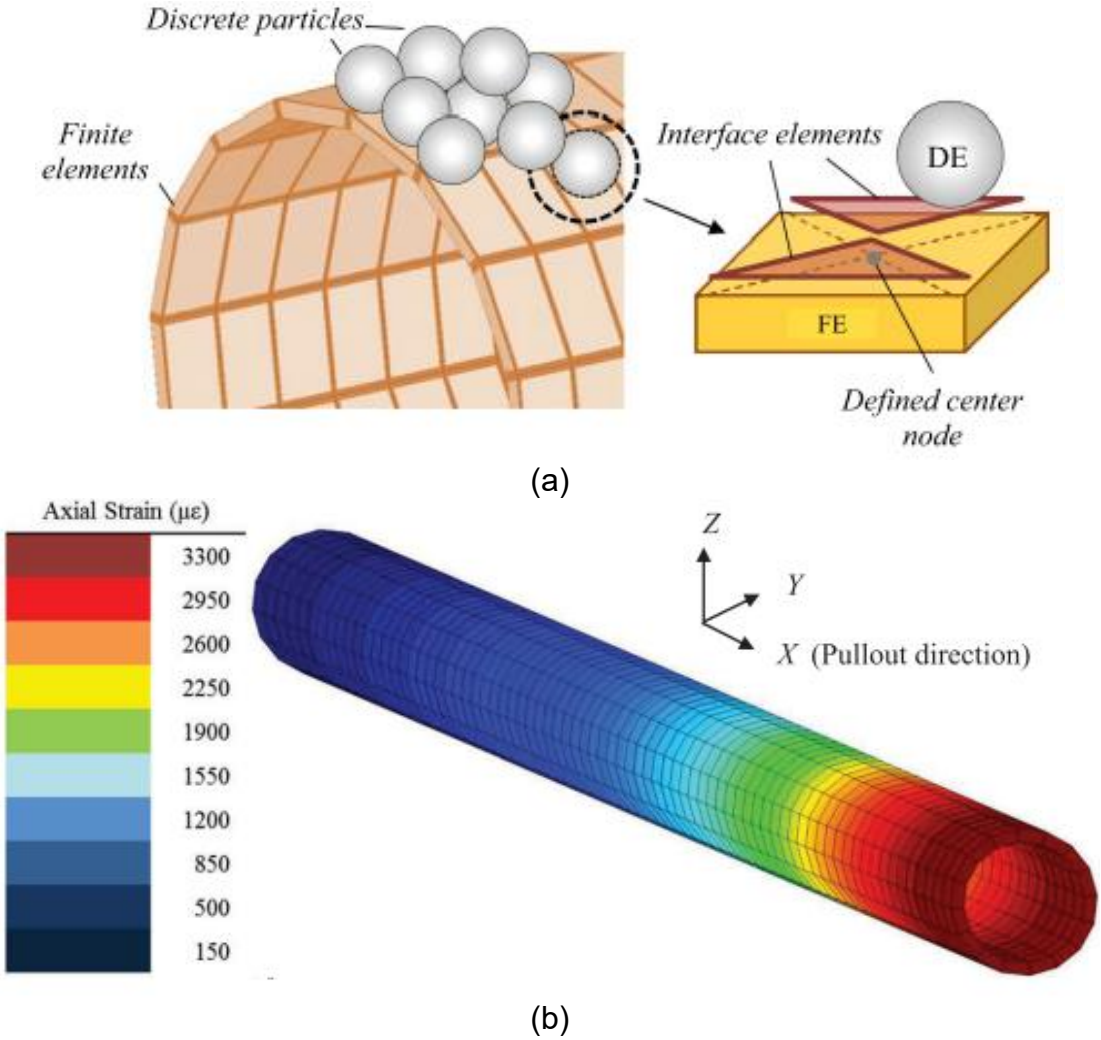

Figure 2.11 Coupled DEM-FEM simulation on MDPE pipe-soil interaction (Meidani *et al.*, 2020a): (a) schematic diagram of DE-FE coupling principle; (b) axial strain distribution along the pipe

Meidani *et al.* (2020a) extended their work using a coupled FE - DE framework to simulate the ASPI of a flexible MDPE pipe. The pipe was constructed with hexahedral FEs and covered by interface elements, which are triangular facet DEs, to calculate soil-pipe contact forces based on the DEM contact model and transfer them to FEs (see Figure 2.11). This simulation validated experimental data by Weerasekara (2007), capturing deformations and stresses of the pipe during the axial displacement related to the soils. Soil particle displacements and inter-particle contact force chains were also analysed. The results revealed that the pipe deformation would

induce a non-uniform distribution along the pipe surface, neglecting which would overestimate the axial resistance on the pipe.

2.4 Soil-interface shear behaviour

ASPI primarily involves soil-interface shear, a prevalent topic in soil-structure interaction, such as the skin friction of piles (Wu *et al.*, 2019). Consequently, a literature review on soil-interface shear behaviour is presented below, focusing on the key issues pertinent to this thesis.

2.4.1 Effects of surface roughness and hardness on soil-interface shear behaviour

Surface roughness and hardness are critical factors influencing interface shear behaviour and have been central to early studies. For instance, Potyondy (1961) examined the interface friction angles of smooth and rough steel and concrete. Uesugi & Kishida (1986) compared shear behaviours across steel interfaces with varying roughness and sands of different sizes, finding that the interface friction angle is positively related to the ratio of surface roughness to mean particle size, d_{50}. They introduced normalised roughness $R_n = R_{max}/d_{50}$ to quantify interface roughness, where R_{max} is the maximum height on the surface profile over a travel length of d_{50}. Lings & Dietz (2005) suggested using R_a instead of R_{max} for calculating normalised roughness, where R_a is the average height deviation over a travel length of d_{50}, providing more detailed information on surface roughness. There is no consensus on whether to use R_{max} (Farhadi & Lashkari, 2017; Martinez & Frost, 2018; Jitsangiam *et al.*, 2021; Li *et al.*, 2021; Tolun *et al.*, 2022; Wang *et al.*, 2022) or R_a (Martinez & Frost, 2017; Han *et al.*, 2018; Rui *et al.*, 2020b).

The interface shear strength, dilatancy and interface shear band thickness increase with surface roughness (Lings & Dietz, 2005; Zhang *et al.*, 2006; DeJong & Westgate, 2009; Han *et al.*, 2018). Considering strength and dilatancy, the roughness can be divided into three zones (smooth, intermediate and rough). It should be noted that different classification methods for rough, intermediate and smooth pipes are available in the literature. One method is based on

the variation of interface friction angles with the normalised roughness, as in Figure 2.12. The interface friction angles increase with the normalised roughness for intermediate interfaces and are normally kept constant for smooth and rough interfaces. The critical values of normalised roughness that differentiate smooth-intermediate and intermediate-rough interfaces are 0.02 and 0.5, respectively, as Paikowsky *et al.* (1995) suggested. Alternatively, some researchers use dilation/contraction during shearing (Lings & Dietz, 2005; Farhadi & Lashkari, 2017): the critical value of normalised roughness transiting the intermediate to rough ranges is normally 0.1~0.2 in this framework.

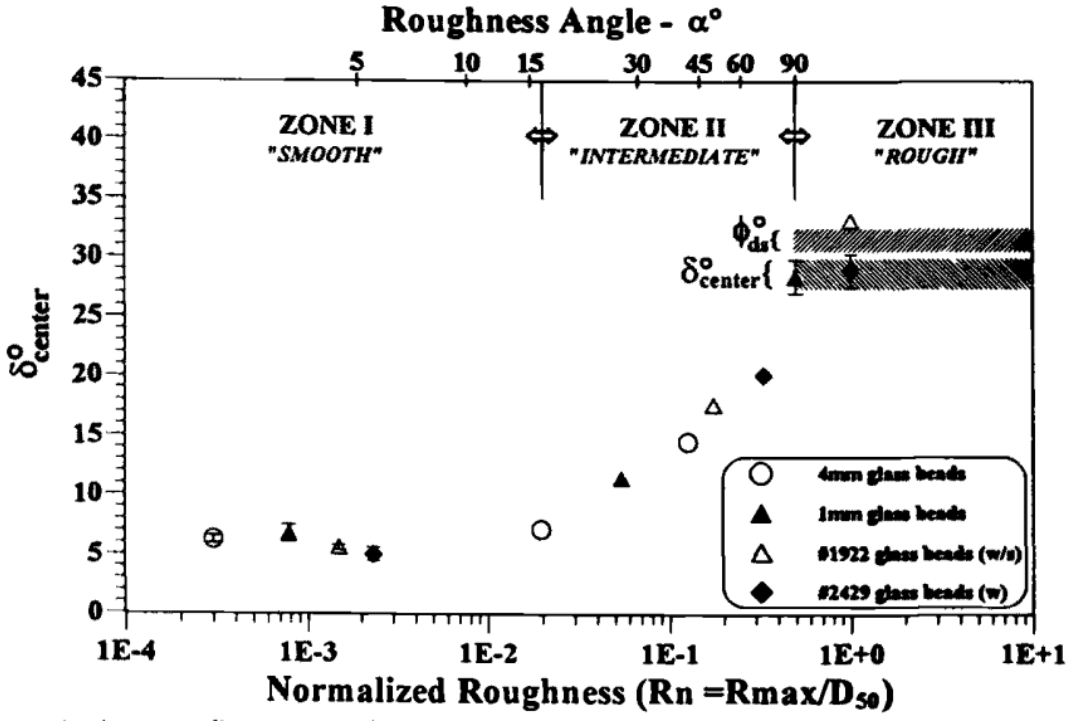

Figure 2.12 Relationship between interface friction angle (δ_{center}) and normalised roughness (Paikowsky *et al.*, 1995)

Interface shear strength, dilatancy, and shear band thickness increase with surface roughness (Lings & Dietz, 2005; Zhang *et al.*, 2006; DeJong & Westgate, 2009; Han *et al.*, 2018). Roughness can be categorised into smooth, intermediate, and rough zones. Different classification methods exist in the literature. One method is based on the variation of interface friction angles with normalised roughness, as shown in Figure 2.12. For intermediate interfaces,

friction angles increase with normalised roughness, while they remain constant for smooth and rough interfaces. Critical values of normalised roughness distinguishing smooth-intermediate and intermediate-rough interfaces are 0.02 and 0.5, respectively, as Paikowsky *et al.* (1995) suggested. Alternatively, some researchers use dilation/contraction during shearing (Lings & Dietz, 2005; Farhadi & Lashkari, 2017), with critical values for transitioning from intermediate to rough, typically between 0.1 and 0.2.

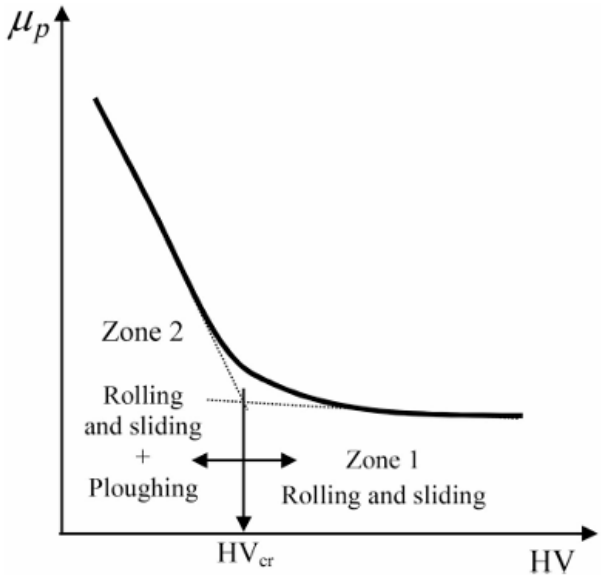

Figure 2.13 Relationship between peak interface friction coefficient (μ_p) and surface hardness (HV) (Abuel-Naga *et al.*, 2018)

Hardness becomes dominant in interface shear as hardness decreases and normal pressure increases, particularly for plastic, plastic-coated or plastic-wrapped interfaces. O'Rourke *et al.* (1990) observed a decrease in interface friction angle with increasing hardness in experiments using HDPE, PVC, Epoxy, and Plexiglas. This is because soft interfaces allow soil particles to penetrate, making the surface appear rougher and causing soil particles to plough rather than roll or slide. Abuel-Naga *et al.* (2018) introduced the concept of critical hardness (see Figure 2.13). Interfaces with hardness below this critical value are sensitive to surface hardness, while those above show minimal hardness effects on shear behaviour. Other factors, such as normal pressure, particle angularity, size, and grain size distribution, also influence soft interface shear

behaviour, as shown in studies on soil-geomembranes by Frost & Han (1999) and Dove & Frost (1999).

2.4.2 Cyclic effects on soil-interface shear behaviour

Cyclic loading on soil-structure interfaces is common in practice, as are wave and wind loads on offshore structures and thermal expansion/contraction on energy piles and heated pipes.

Early studies focused on constant normal loading (CNL) conditions. Desai *et al.* (1985) studied the effects of relative density, cyclic number, normal stress, and displacement amplitude on soil-concrete interfaces. They observed a significant increase in maximum shear stress in loose sand during cycling. Uesugi *et al.* (1989) conducted interface shear tests using dense sand and steel interfaces with varying roughness at one-way and two-way cyclic conditions. At the one-way cyclic loading condition, unloading and reloading remained in the elastic zone. The cyclic loading envelope was consistent with the monotonic loading curve for two-way conditions. The development of the coefficient of friction was related to roughness, with the friction angle decreasing for rough interfaces and increasing for smooth ones, all approaching the residual shear stress ratio of the sand. Zhang *et al.* (2011) studied sand dilatancy through CNL cyclic tests, finding a monotonic increase in irreversible dilatancy during cycling. The rate of increase during initial cycles was positively related to normal pressure, with similar values under different pressures. Roughness significantly affected cyclic behaviours, including transition shear stress and reversible dilatancy development. Rui *et al.* (2020b) used an interface ring shear device to study cyclic behaviours between carbonate sand and steel, finding cyclic interface shear stress more significant than under monotonic conditions. This is because particle breakage and redistribution make particle displacement gradually concentrate on the range of 2~3 d_{50}, thus strengthening the soil-interface interaction.

In practice, normal stress on soil-structure interfaces is not constant. Constant normal stiffness (CNS) or constant normal volume (CNV) conditions are more realistic. Fakharian &

Evgin (1997) conducted displacement-controlled CNS cyclic sand-steel shear tests, finding maximum shear stress degradation in each test due to soil compression during shearing, which reduces normal pressure and shear stress. This degradation is more pronounced in early cycles and positively related to normal stiffness and amplitude. The stress path initially lies within and gradually approaches the peak interface friction envelope, eventually returning to the residual envelope. Introducing the Particle Image Velocimetry (PIV) technique has enhanced the understanding of cyclic interface shear behaviours at a microscale (DeJong *et al.*, 2003; Zhang & Zhang, 2006; Zhang & Zhang, 2009). With increased cycling, the shear band widens from 5 d_{50} to 8 d_{50}, while shear strain in the shear zone decreases. The shear zone secant shear modulus for uncemented sand decreases and stabilises during cycling. Compression and dilation occur in each cycle, especially for rough interfaces, with compression slightly exceeding dilation, leading to gradual global compression. Mortara *et al.* (2007) examined post-cyclic interface shear behaviours, finding significant roughness effects. Despite degradation during cycling, post-cyclic shear strength for rough interfaces shows notable recovery, unlike smooth interfaces. Amplitude and normal stiffness negatively correlate with post-cyclic recovery. Di Donna *et al.* (2016) and Jitsangiam *et al.* (2021) conducted load-controlled cyclic CNL and CNS tests, observing normal stress degradation and contraction related to normal stiffness, amplitude, and stress. The stress path approaches the critical friction envelope during cycling, quickly for loose sand and slowly for dense sand. Post-cyclic peak friction exceeds monotonic conditions due to compression during cycling, while post-cyclic critical friction remains constant with monotonic conditions.

2.4.3 Interface shear behaviour of unsaturated soils

Several experimental studies have explored the interface shear behaviour of unsaturated soils, using two primary methods to control moisture content.

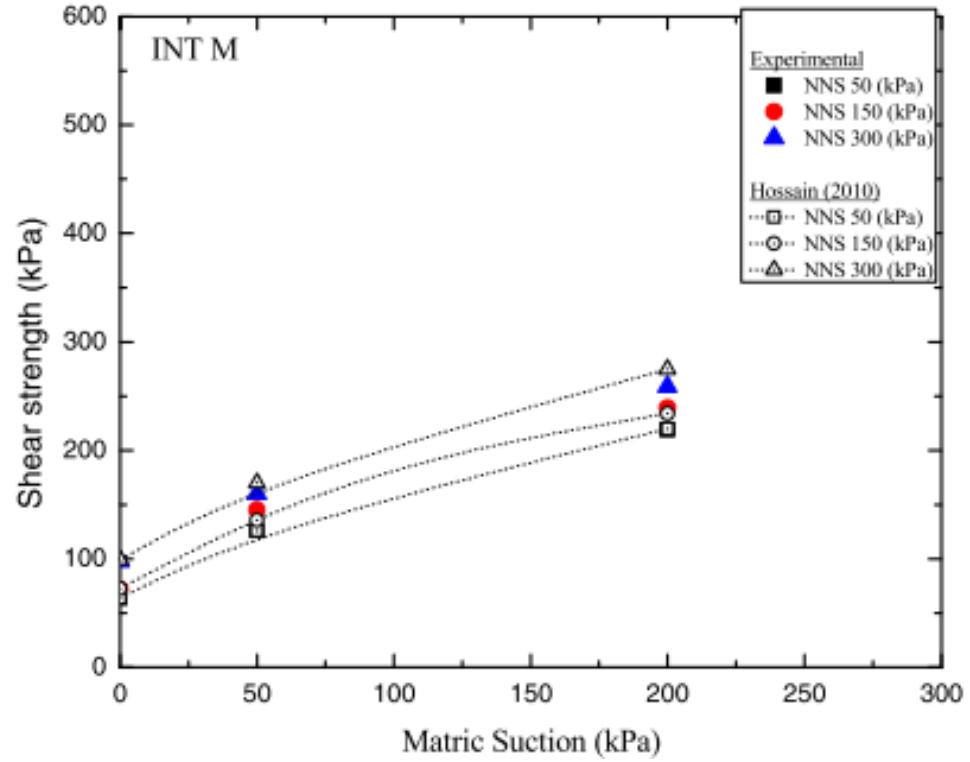

Figure 2.14 Matric suction effect on interface shear strength (Borana *et al.*, 2016)

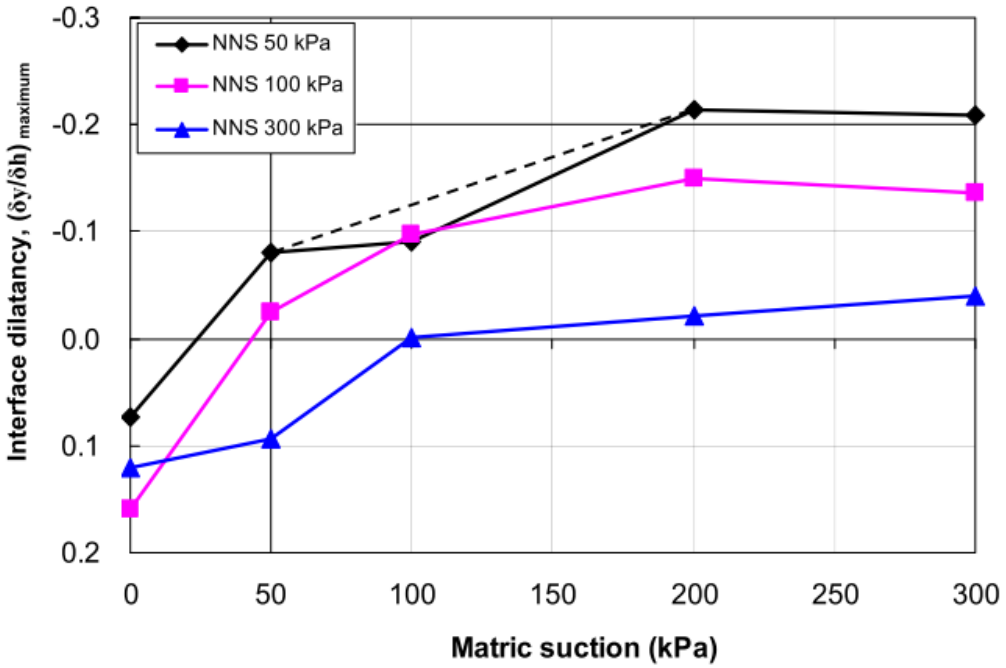

Figure 2.15 Matric suction effect on interface dilatancy (Hossain & Yin, 2015)

The first method involves directly controlling the initial water content. For example, Li *et al.* (2021) conducted interface tests between silt and cement mortar. Silt specimens at interfaces with roughness (R_{max}) from 0 to 8 mm were tested. Increased water content led to decreased

interface shear strength and a transition from strain-softening to strain-hardening in shear stress-displacement curves. Cohesion, friction angle, and vertical displacement increased with greater roughness and lower soil water content.

The second method uses the axis translation technique to control matric suction (Miller & Hamid, 2007). Hossain & Yin (2015) and Borana *et al.* (2016) conducted interface shear tests of CDG on rough steel and cement interfaces with matric suction from 0 to 300 kPa. Matric suction and net normal stress (NNS) significantly affect hardening-softening and dilation behaviours in soil-interface shearing (see Figure 2.14). More pronounced strain-softening and dilation behaviours were observed at lower NNS and higher suction (see Figure 2.15). Interface shear strength increased with rising suction and NNS. The relationship between shear strength and NNS is generally linear, while the apparent interface friction angle and adhesion intercept increase with matric suction. The angle indicating the rate of increase in interface shear strength relative to matric suction, δ_b, decreased as matric suction increased. Hamid & Miller (2009) compared the interface shear behaviours of unsaturated lean silt on rough and smooth steel interfaces, observing a smaller δ_b. Khoury & Miller (2012) studied the effect of hydraulic hysteresis on interface shear behaviour, finding greater interface shear strength after a drying-wetting cycle compared to only drying at the same NNS and matric suction. Cui *et al.* (2024) further developed the framework of Borana *et al.* (2016) to investigate the effects of temperature and suction on the interface shear behaviour of CDG, noting a slight decrease in the interface shear angle of about 2.2° as temperature increased from 8 to 42°C.

2.5 Discrete element method

2.5.1 Basic knowledge

The Discrete Element Method (DEM) was first introduced by Cundall & Strack (1979) as an alternative to continuum-based models like FEM. DEM models materials as discrete particles that interact with their neighbours. In DEM, inter-particle force increments are

calculated at all contact points based on the relative velocities of the contacting particles, and particle motion is governed by Newton's second law. This approach allows DEM to assess micromechanics and their impact on macroscopic behaviour directly.

DEM offers several advantages, such as simulating scenarios involving large plastic deformations in soils and providing insights into the statics and kinematics at the grain level. However, it also has limitations, including restrictions on the maximum number of particles and the duration of simulations due to computational constraints. Additionally, parameters like Young's modulus and damping coefficient can be ambiguous. Despite these challenges, numerous commercial and open-source DEM software packages are available, including PFC, YADE, LIGGGHTS, and ESyS-Particle (Itasca, 2005; Weatherley, 2009; Kloss & Goniva, 2011; Šmilauer & Chareyre, 2021).

Figure 2.16 illustrates a typical DEM simulation loop described by Šmilauer & Chareyre (2021) in the open-source software YADE. While loops in other software may vary, they share similar structures. The loop begins with "Bodies," representing discrete particles. Each body has four types of properties: shape (e.g., sphere, facet, cylinder), material (e.g., density, Young's modulus), state (e.g., position, linear velocity), and bound, which is used for approximate contact detection. A common bound in YADE is defined by the maximum and minimum values of each body in three dimensions, indicating position and approximate size without specifying shape. This bound helps detect potential particle collisions. The second part of the loop involves "Interactions." Extra collisions are calculated based on potential collisions and specific shapes, providing geometric information like relative displacement. Interaction properties, such as stiffness and friction angle, are derived from the material properties of the bodies. Interaction forces are then determined using contact laws. For instance, a typical elastic contact model in DEM assumes linear elastic springs in normal and tangential directions. The normal force is zero if the relative displacement is positive, while the shear force is capped by the Mohr-

Coulomb criterion. The final part is "Motion Integration," where Newton's second law and kinematic equations calculate accelerations, velocities, and positions based on the obtained forces. The critical time increment is normally determined by the maximum angular frequency of the particles' harmonic oscillation to ensure simulation stability for the explicit integration scheme.

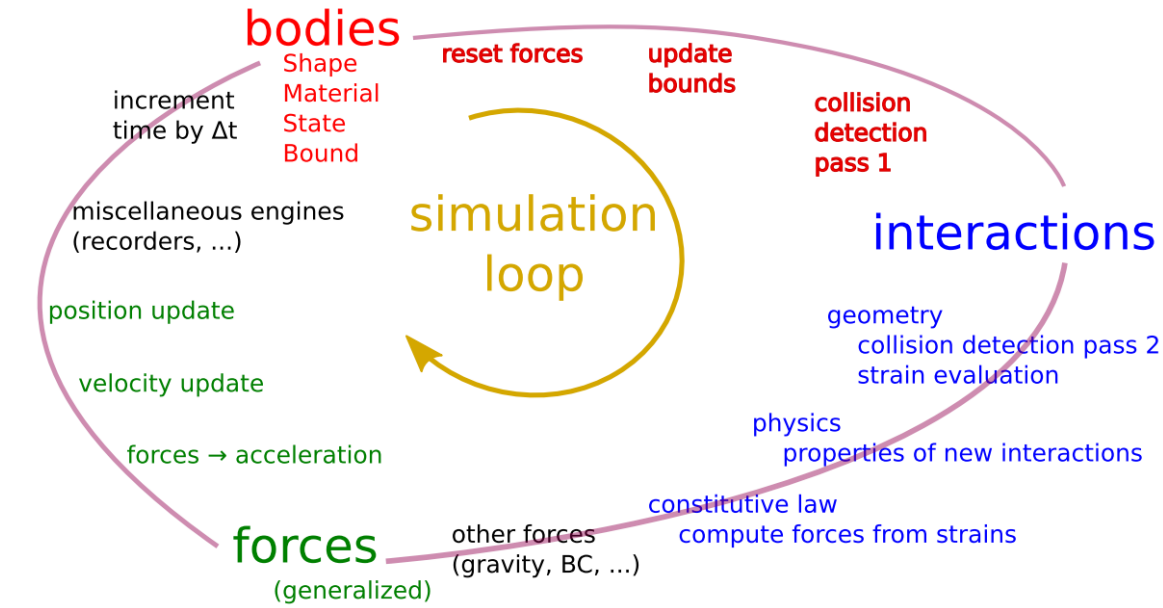

Figure 2.16 Typical simulation loop of DEM in YADE (Šmilauer & Chareyre, 2021)

DEM employs two typical boundary conditions: rigid and periodic boundaries. The rigid boundary, the most common in DEM, is akin to the displacement boundary in FEM, lacking inertia and solely determining particle kinematics (Cundall & Strack, 1979; Wu *et al.*, 2023). A point coordinate easily describes a rigid planar wall boundary, with the opposite side typically inactive unless specified otherwise. If the wall is too soft or the particle velocity near the boundary is too high, particles may escape (O'Sullivan, 2011). The displacement and velocity of the rigid boundary can be set directly or controlled by algorithms, with servo-controlled boundaries being widely used. The stress tensor within the sample or a representative region is calculated and compared with the target stress, adjusting the wall velocity or displacement based on the stress difference. Complex rigid boundaries can be created by combining finite-sized triangular rigid walls (Weatherley, 2009). For example, Meidani *et al.* (2017) used 1216

triangular facets in a hendecagonal shape to model a pipe. Pöschel & Schwager (2005) proposed an alternative method for forming rigid boundaries using overlapped particles, which can simulate complex geo-material surface roughness (Feng *et al.*, 2018; Liu *et al.*, 2021b).

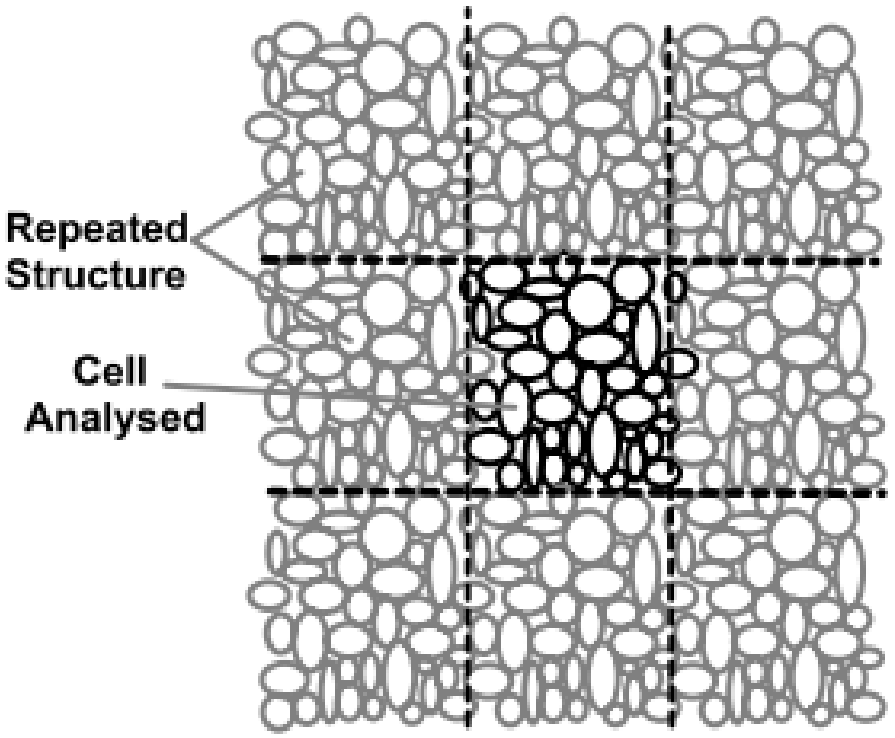

Figure 2.17 Periodic boundary (O'Sullivan, 2011)

Cundall (1988) also introduced the periodic boundary, which effectively mitigates boundary effects and, under certain conditions, reduces computational demands. This concept simplifies large particle assemblies using a representative volume element (RVE), a periodic cell surrounded by periodic remapping in an infinite solution space. In a periodic cell (typically an orthogon in 2D or a hexagon in 3D), particles touching any periodic boundary re-enter from the corresponding position on the opposite boundary, as depicted in Figure 2.17. This setup creates the effect of the original zone being adjacent to identical copies of itself. Numerically, the periodic boundary is achieved by taking the remainder of the position or length vector after division by the dimensions of the periodic boundary. For example, if a particle with centroid at x_i is outside the periodic boundary with dimension vector C_i, x_i is adjusted to $x_i = x_i - C_i$.

2.5.2 DEM simulation of unsaturated soil

Various methods have been attempted to simulate unsaturated soil using DEM. These can be summarised into five typical approaches, as outlined in Table 2.6 and briefly described below:

1) **Empirical adhesive force method**: Jiang *et al.* (2004) introduced this method to quantify the suction effect in PFC. Based on Bishop's stress, the suction effect is treated as part of cohesion, with suction-induced cohesion calculated as an adhesive force between particles at the grain level. An attractor is added to the inter-particle relationship (see Figure 2.18 (a)) (Shen *et al.*, 2016; Li *et al.*, 2018). The relationship between cohesion and adhesion is derived from empirical testing results. This adhesion forms when two particles contact and remains constant until the contact breaks at a critical inter-particle distance (see Figure 2.18 (b)).

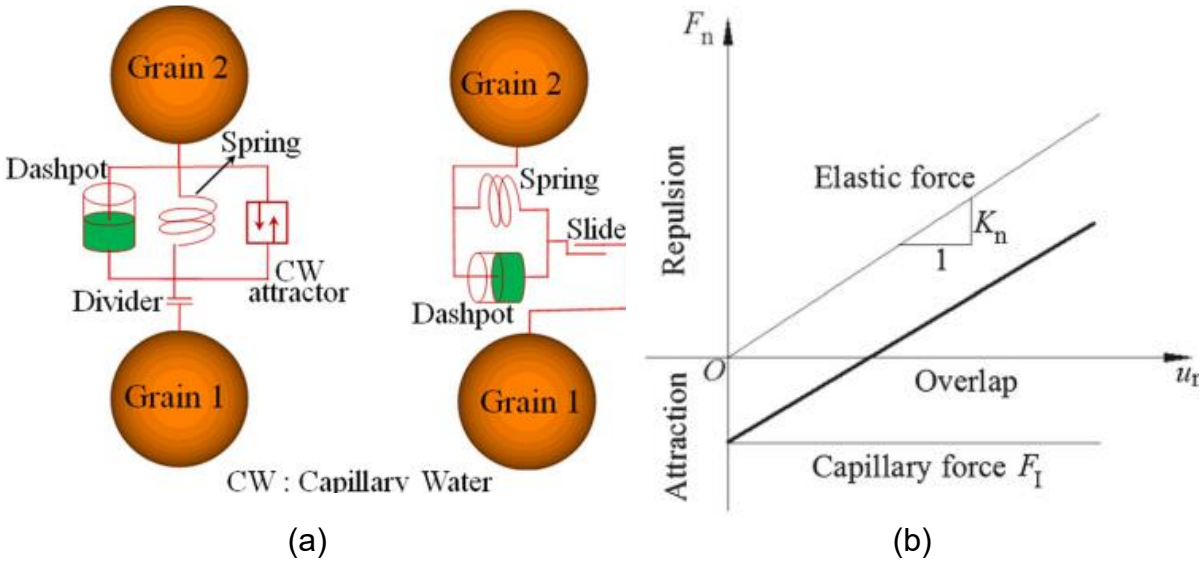

Figure 2.18 Empirical adhesive force method (Shen *et al.*, 2016): (a) components of the contact model with capillary force; (b) normal force (F_n) versus inter-particle displacement (u_n)

2) **Capillary method**: Scholtès *et al.* (2009) developed this method using YADE. It uses the Laplace equation and geometric formulas to determine the geometry of bridges, water volume, and capillary force based on suction and relative distance. Duriez & Wan (2017b) refined this method by incorporating contact angle and hysteresis (Wan *et al.*,

2015; Duriez & Wan, 2017a). This method is mature and stable, but is limited to soils in the pendular regime due to its focus on isolated water bridges.

3) **Modified capillary method**: Liu *et al.* (2020) proposed an approach considering both pendular and funicular bridges. The first step involves detecting bridges between particles using the Laplace equation, similar to Scholtès *et al.* (2009), resulting in water caps on particle surfaces. The second step detects funicular bridges when water caps overlap at the particle surface (see $\boldsymbol{n}_1$ and $\boldsymbol{n}_2$ in Figure 2.19 (a)), recalculating them based on a hemisphere assumption. The Fibonacci-Lattice method calculates capillary forces by discretising the particle surface, using each point to represent a surface area. Points inside caps experience water pressure forces ($\boldsymbol{f}_s$), and edge points experience tension forces($\boldsymbol{f}_\gamma$) (see Figure 2.19 (b)). This method is computationally intensive and does not provide water volume.

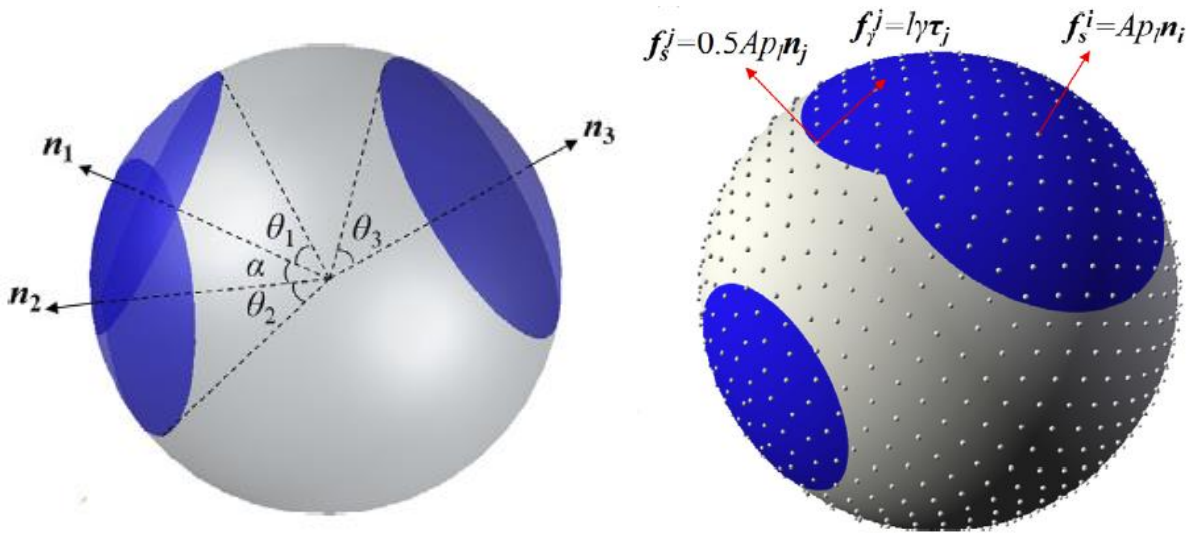

(a) (b)

Figure 2.19 Modified capillary method (Liu *et al.*, 2020): (a) Liquid–solid interfaces on particle; (b) calculation of capillary force via discretising particle surface with Fibonacci-Lattice points

Table 2.6 Summary of typical DEM unsaturation simulation methods

Method	Representative literature	DEM software	Pendular regime	Funicular regime	Water volume	Different particle sizes	Computational cost
Empirical Adhesive Force	Jiang *et al.* (2004)	PFC-3D	√	√	×	√	Lower
Capillary Method	Scholtès *et al.* (2009)	YADE	√	×	√	√	Lower
2PFV-DEM	Yuan & Chareyre (2017)	YADE	×	√	√	√	Higher
Modified Capillary Method	Liu *et al.* (2020)	ESyS	√	√	×	√	Higher
Three Structures	Melnikov *et al.* (2016)	DPM	√	√	√	×	Higher

4) **2PFV-DEM method**: Yuan & Chareyre (2017) introduced this method to address more complex soil-liquid structures, considering the funicular regime and fully saturated conditions (Yuan *et al.*, 2015; Yuan *et al.*, 2016). The regular Triangulation method divides the pore space into tetrahedral elements, forming a binary pore element network. Each pore element is saturated or dry, with air and water reservoirs at the top and bottom. Initially, all elements are saturated, and suction increases from zero. Air invades a pore when adjacent to an air-invaded pore, and suction exceeds a critical value calculated by a complex algorithm (Chareyre *et al.*, 2012). Capillary forces are integrated based on constant pressure in each element. This method is limited to dense packing media and cannot model low saturation regimes.

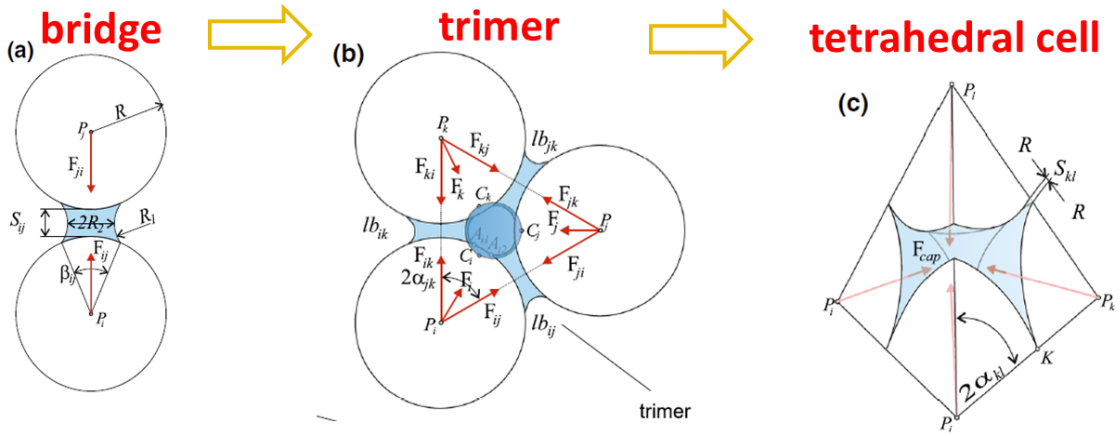

Figure 2.20 Three-structure method (Melnikov *et al.*, 2015; Melnikov *et al.*, 2016)

5) **Three-structure method**: Melnikov *et al.* (2015) introduced this approach, dividing unsaturated soil's liquid structures into bridges, trimers, and tetrahedral cells (see Figure 2.20). Bridges are isolated pendular bridges between two particles. Tetrahedral cells are similar to those in Yuan & Chareyre (2017). Trimers are locally saturated spaces enclosed by three particles, resembling a fidget spinner. The radius of caps is calculated using the Laplace equation, with criteria for transforming between structures. Capillary forces for bridges and tetrahedral cells follow the original capillary approach and the method of Yuan & Chareyre (2017). Trimer forces add the product of suction and the

contact area between the particle and the cylinder enclosed by particles to the bridge forces. This method requires uniform particle sizes, complicating calculations for tetrahedral cells and trimers otherwise.

In the above methods, simpler methods are mature but limited to the pendular regime or lack rationality, while advanced methods are computationally complex. Most studies on unsaturated soil DEM modelling focus on element testing, with limited attention to interface shear and soil-structure interaction due to computational constraints and particle size scaling.

2.5.3 DEM simulation of soil-pipe interaction subjected to lateral and vertical loading

DEM simulation has been extensively used to model soil-pipe interactions, one of the earliest topics in soil-structure interaction simulation via DEM. Apart from the simulation on ASPI, as viewed in 2.3.2, several studies have focused on lateral and vertical soil-pipe interactions.

Calvetti *et al.* (2004) pioneered using DEM to simulate soil-pipe interaction, generating around 7,000 particles with a scaling factor for particle size of 50 in a numerical box using PFC-3D. A tube with a 50 mm diameter represented the pipe. The numerical box dimensions matched the experimental setup, except for a 2.5-fold reduction in out-of-plane thickness to enhance computational efficiency. The pipe was laterally loaded to back-calculate experimental results, showing good agreement with experimental observations regarding lateral bearing capacity factor, displacement trends, and contact force networks. The study was later extended to simulate soil reactions to loads in different vertical plane directions, revealing strong coupling between vertical and lateral soil-pipe interaction components. Different interaction mechanisms were observed for pipes at varying burial depths and displacement directions.

Yimsiri & Soga (2006) expanded on the work of Calvetti *et al.* (2004) to explore lateral and vertical-upward soil-pipe interactions. They adjusted soil particle size scaling factors based on distance from the pipe to balance deep burial depth with computational cost. Their

simulation results were compared with the physical modelling of Trautmann & O'Rourke (1985) and the FEM simulation of (Yimsiri *et al.*, 2004). The DEM simulations demonstrated a smoother transition of failure mechanisms from shallow to deep burial depths, highlighting DEM's unique advantage in addressing large deformation problems.

Jiang *et al.* (2015) investigated the vertical-upward behaviour of pipes buried in cemented sand using 2D DEM simulations, incorporating bond inter-particle effects through a bond contact model. They analysed microscopic information, including displacement fields, bond breakage distributions, and uplift resistance, identifying a global slide failure mode.

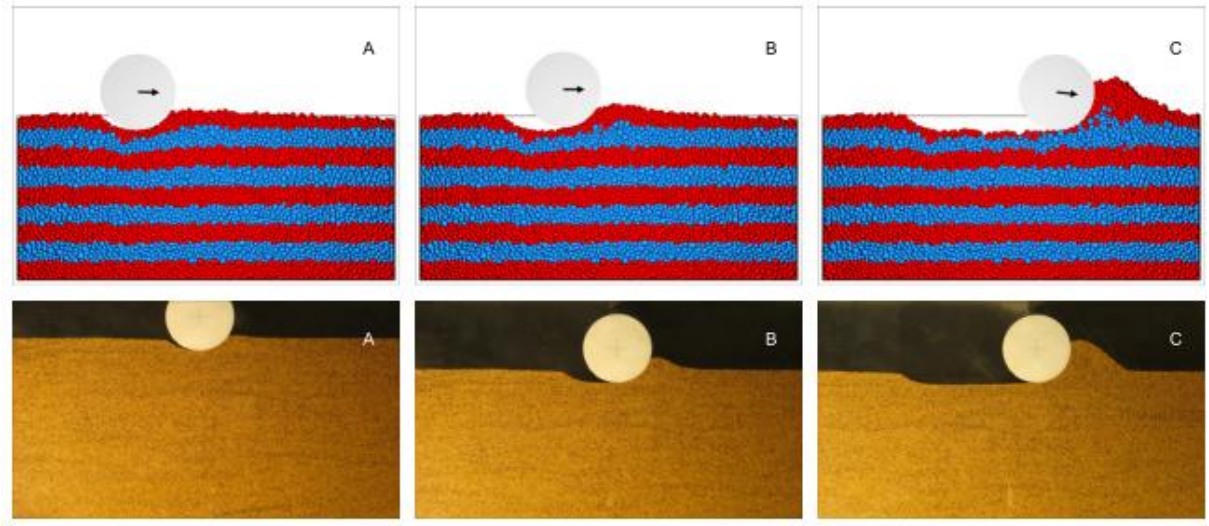

Figure 2.21 Comparison of soil bed profile around unburied pipe during cyclic lateral displacement in DEM simulation and physical modelling (Macaro *et al.*, 2021)

Macaro *et al.* (2021) conducted 3D DEM simulations on the lateral behaviour of unburied offshore pipelines using YADE. Samples were prepared using a deposition method, with out-of-plane thickness set to five times the average particle size after parameter studies. Although periodic boundaries were attempted to minimise thickness, compatibility issues arose with the pipe object size in YADE at that time. Simulations of a monotonic sideswipe, cyclic sideswipe, and cyclic lateral displacement under constant vertical load were compared with experiments, showing good agreement in loading paths, particle positions, and velocities (see Figure 2.21).

The study analysed soil berm evolution and the effects of the initial vertical overloading ratio and pipe weight.

Peng *et al.* (2024) focused on the lateral behaviour of pipes buried in unsaturated soil using PFC-3D. They back-calculated and microscopically analysed experimental results from Robert *et al.* (2016), combining DEM and FEM by simulating pipe sections with finite elements covering triangular objects to transfer contact forces. The Johnson-Kendall-Roberts (JKR) model calculates capillary forces among particles. The adhesive surface energy (U_{ASE}) in the JKR model was calibrated against experimental results. Despite lacking theoretical support for JKR model parameters, the simulation successfully replicated complex soil behaviors observed in experiments, such as cracks, cave-ins, and soil collapse in unsaturated soil model tests (see Figure 2.22).

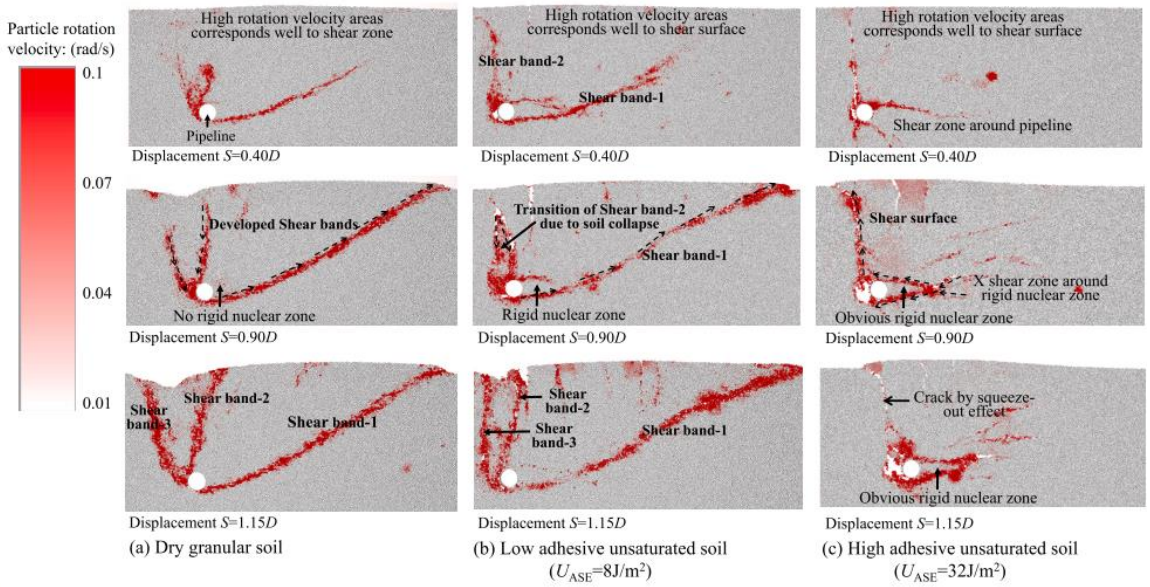

Figure 2.22 Rotation field of unsaturated soil around pipe during lateral displacement (Peng *et al.*, 2024)

2.6 Summary

Above all, numerous experimental and numerical studies have been carried out to explore the axial behaviour of buried pipelines. While these studies have yielded valuable data and

insights, five critical limitations remain that need to be addressed to enhance the resilience of buried pipeline systems in practical applications. These limitations are as follows:

First, no physical model test has been reported in the literature to investigate the effects of surface roughness and hardness on ASPI subjected to monotonic loading. The role of soil arching and constrained dilatancy was not explored. More experimental results are needed to understand and quantify the effects of roughness and hardness on the ASPI mechanism and monotonic pullout resistance.

Second, the understanding of cyclic ASPI seems limited. Firstly, surface roughness is a critical factor in cyclic and post-cyclic interface shear strength, but no study has explored its effects on cyclic ASPI. Secondly, the unique data of Sheil *et al.* (2018) highlights the importance of cyclic amplitude on ASPI, but the use of alternating amplitudes cannot fully reveal its effects because soil-pipe interface behaviour is path-dependent (Mortara *et al.*, 2007; Zhou *et al.*, 2020). Additionally, the mechanism of cyclic ASPI is still unclear due to limited data from the previous three studies. Finally, no studies have examined post-cyclic pullout behaviour.

Third, compared to clean sand, the suction effects on ASPI of soils with fine particles are expected to be significantly more pronounced. Primarily, the suction effect on the interface shear strength of soils with fine particles is notable, leading to a more substantial increase in axial resistance. Furthermore, unsaturated soils with fine particles exhibit higher dilation and stiffness than saturated soils and unsaturated sand, leading to more significant constrained dilatancy and, consequently, increased axial resistance (Salgado *et al.*, 2000; Alonso *et al.*, 2010; Hossain & Yin, 2010; Han & Vanapalli, 2016). Eventually, the lateral earth pressure coefficient at rest, K_0, typically decreases with increasing suction (Lu & Likos, 2004), which is expected to influence the average interface contact pressure on the pipe surface. A quantitative analysis of these effects on the axial resistance of pipes buried in soils with fine particles, compared to clean sand used by Al-Khazaali & Vanapalli (2019), is necessary.

Fourth, the single-point-type TPS has the potential to measure the interface contact pressure on the pipe surface during ASPI. It is because it has only one sensing area with a diameter or size length ranging from 3 to 80 mm, and can be used with a common datalogger that is more affordable. However, the current utilisation of single-point-type TPS mainly focuses on measuring contact pressure at flat interfaces in laboratory tests. The feasibility of measuring the earth and contact pressures at curved interfaces has not been confirmed. Furthermore, the input-output behaviour of TPS exhibits significant non-linearity and hysteresis and is influenced by specific installation conditions. Establishing a reliable methodology for using the single-point-type TPS to measure pressures with greater accuracy is necessary.

Fifth, some challenges in the methodology limit the further development of ASPI DEM simulations. Initially, rigid walls at the front and rear lead to a nonuniform longitudinal distribution of shear stress on the pipe, resulting in unrealistic particle displacement compared to actual field conditions (Meidani *et al.*, 2017). Furthermore, using smooth facet discrete elements with high interface friction to simulate the pipe may overlook important aspects of complex soil-interface interaction responses. An optimised balance between computational efficiency and particle scaling factors is needed to enhance industrial practicability. Finally, increasing particle size in DEM would decrease the suction effect on soils if the input parameters related to the capillary force are constant. An improved method to solve the scaling effect on capillary force is needed.

CHAPTER 3
EXPERIMENTAL SYSTEM, INSTRUMENTATION, MATERIALS AND PROCEDURES OF PHYSICAL MODELLING TESTS

3.1 A new large-scale system for axial soil-pipe interaction physical modelling tests

An experimental apparatus for testing ASPI was modified from the soil nail testing system of Yin & Su (2006), as shown in Figure 3.1. It consists of a steel box, pipes, an axial actuation subsystem, and a vertical loading subsystem. The key components are described below.

3.1.1 Steel box for simulating pipeline trench

As shown in Figure 3.1 (a), the steel box with strengthening beams was used to simulate the trench condition. It has internal dimensions of 1.0 m in length, 0.8 m in height, and 0.6 m in width, meeting the minimum requirements as specified in the guidelines of USBR (1996) and BSI (2015). Two holes are provided on the front and rear walls at 0.35 m. The pipe can pass through these holes to ensure a constant soil-pipe interaction length during the pullout process.

In engineering practice, pipelines are typically so long that they can be seen as quasi-infinite in the axial direction. However, due to the limitations of the laboratory testing, the pipe displacement during the pullout process would often make soil concentrated in the zone close to the front wall and thus cause non-uniform shear stress distribution along the pipe. This problem was observed in physical model tests by Al-Khazaali & Vanapalli (2019) and in DEM simulation by Meidani *et al.* (2017). Therefore, this study introduced two pipe sleeves with an inner diameter of 132 mm, as shown in Figure 3.2, to avoid the soil-pipe interaction in the zone close to the front and rear walls. They are flange-mounted to these holes with a rubber layer for waterproofing. These sleeves inside the box are 0.15 m long, resulting in an interaction length of 0.7 m.

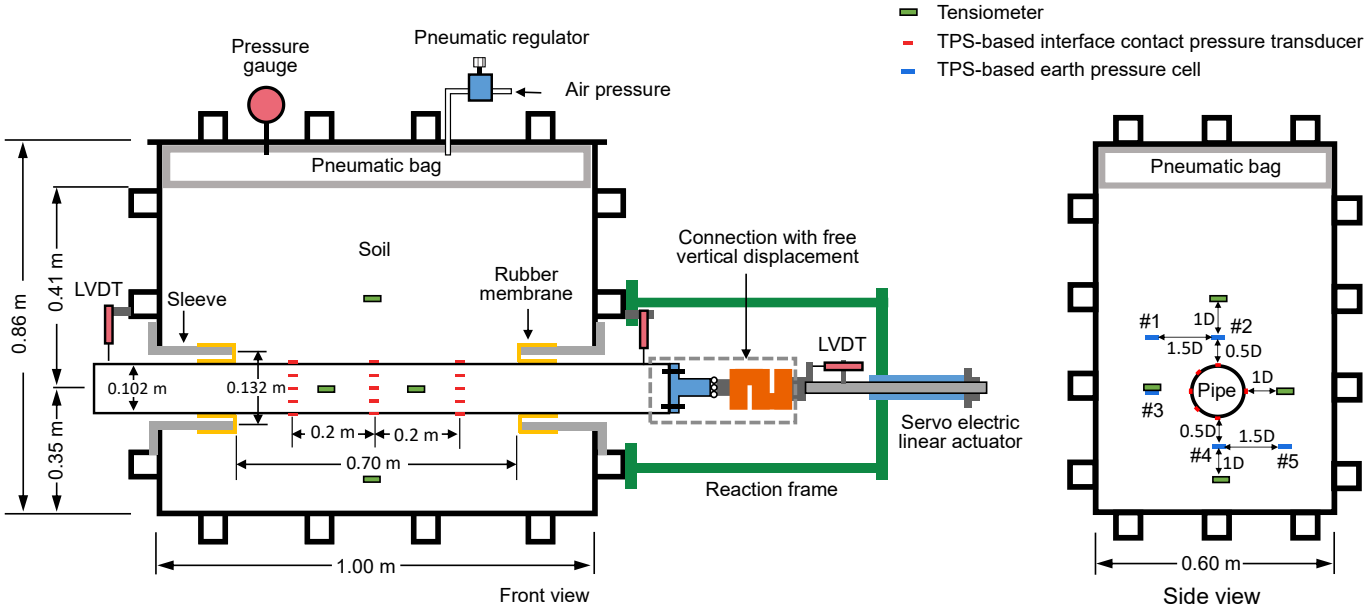

(a)

(b)

Figure 3.1 Experiment system for ASPI physical modelling tests: (a) schematic diagram; (b) photograph

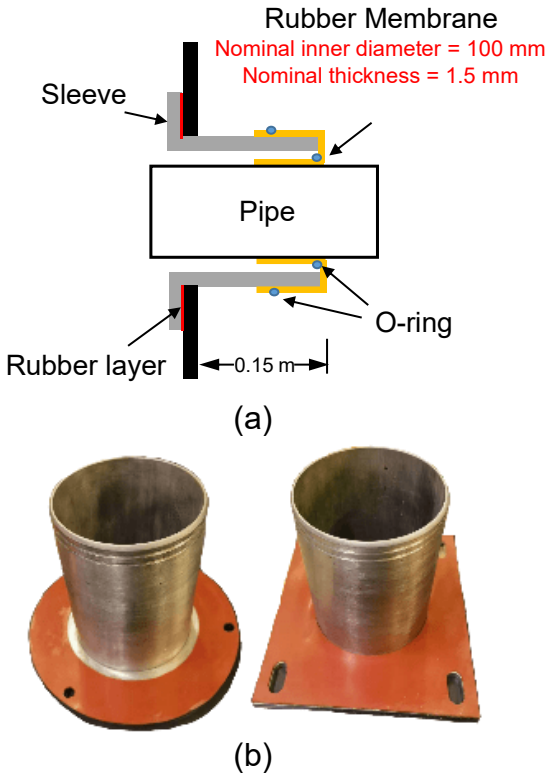

Figure 3.2 Pipe sleeves: (a) schematic diagram; (b) photograph

3.1.2 Axial actuation subsystem for pipeline pullout

The axial actuation subsystem, including an electric cylinder jack, a servo control panel, and a reaction frame, was used to achieve controllable axial displacement. In previous studies, the connections between the pipe and the jack were usually rigid (Wijewickreme & Weerasekara, 2015; Al-Khazaali & Vanapalli, 2019; Reza & Dhar, 2021) or hinged connections (Wijewickreme *et al.*, 2009; Sheil *et al.*, 2018; Murugathasan *et al.*, 2021). It may cause additional normal force or misalignment if there is any vertical displacement trend during sampling and axial loading. Therefore, a connector (see Figure 3.3) was introduced to allow a free relative vertical movement between the pipe and the jack. One end of this connector is connected to the pipe through a flange for ease of installation. The other end is similar to the connection between the shear box and the actuator in the commonly used direct shear apparatus: a T-shaped head pole was placed at the end of the jack, and the connector end was designed to match it. Rubber sleeve membranes with an inner diameter of 100 mm were inserted between the pipe and sleeves to prevent soil leakage. The thickness of the rubber membranes is 1.5 mm,

providing ample lateral support for the surrounding soils. O-rings were used to secure the membranes between the pipe and sleeves, preventing friction between the two components. The pipe was installed through these two sleeves along the sleeve's axis, creating a gap of approximately 8.5 mm between the pipe and sleeves. This gap is equivalent to 22 d_{50} of the Fujian medium (FJM) sand and 109 d_{50} of completely decomposed granite (CDG) used in this study, providing sufficient space for pipe settlement. As a result, the pipe is allowed to move vertically during the axial pullout.

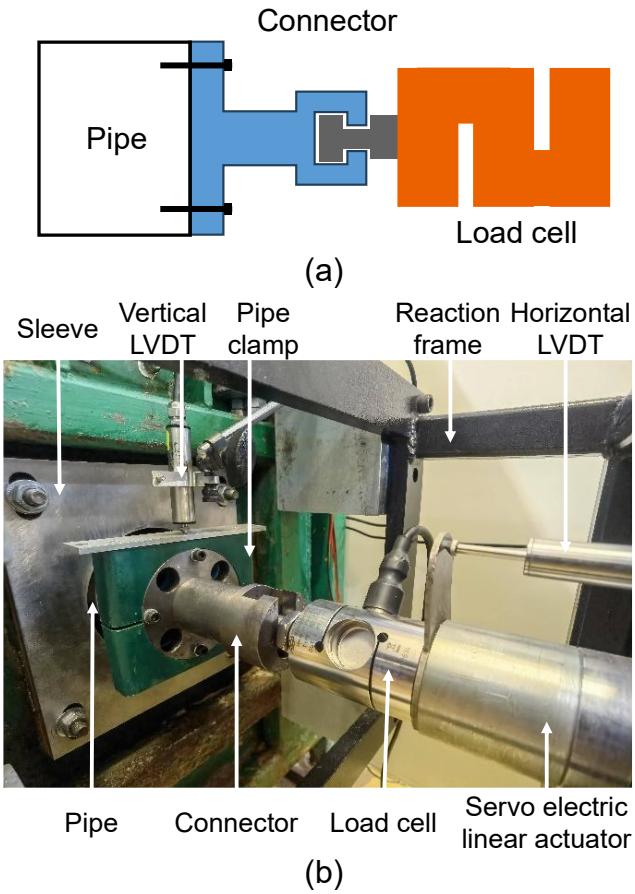

Figure 3.3 Pipe-actuator connection between free vertical displacement: (a) schematic diagram of top view; (b) photograph

3.1.3 Vertical loading subsystem for controlling nominal pressure

A flexible pneumatic bag (see Figure 3.4 (b)) was installed between the upper surface of the soil and the top cap. The height of this pneumatic bag is 0.12 m, slightly larger than the gap (0.1 m). The length and width of the pneumatic bag match the dimensions of the box's interior.

There are two holes on the top surface of the pressure bag, one for connecting with a pneumatic regulator and the other for an air pressure gauge (see Figure 3.4 (a)). A top cap with reinforcing beams was installed above the pneumatic bag and the box to provide a reaction force. By adjusting the air pressure P inside the bag, the effective nominal pressure, σ_c', at the centre can be controlled by $\sigma_c' = \gamma' H_{c0} + P$ in dry and submerged conditions, and the net nominal pressure, $\sigma_{c\text{-net}}$, at the centre can be controlled by $\sigma_{c\text{-net}} = \gamma H_{c0} + P$ in unsaturated conditions, where H_{c0} = real buried depth from the ground surface to the centre of the pipe.

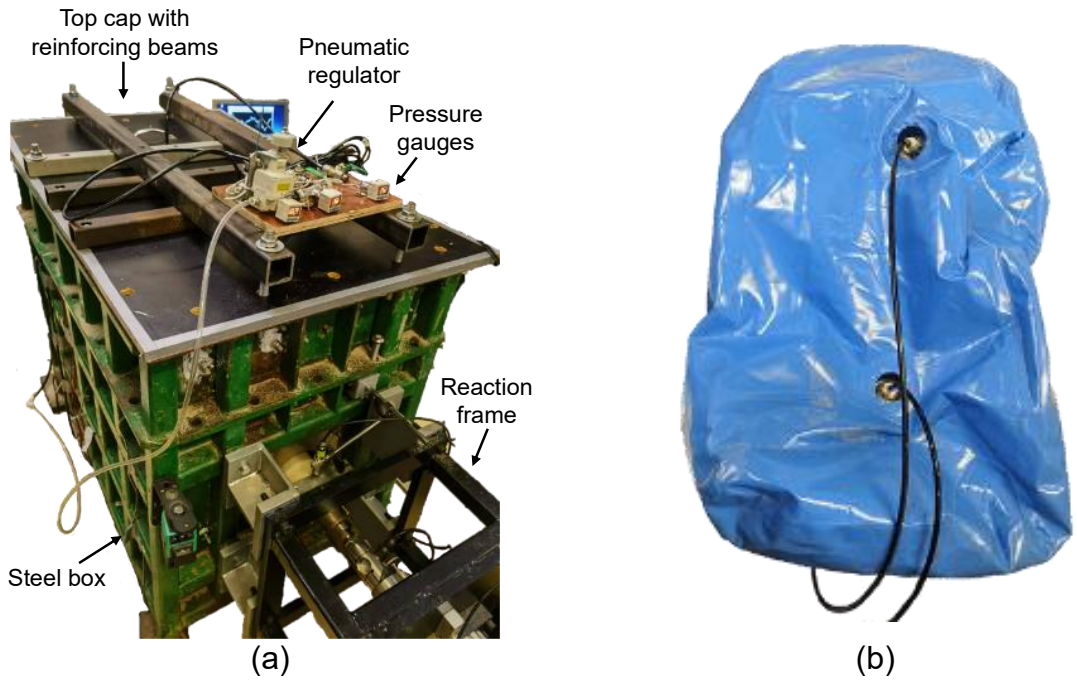

Figure 3.4 Photographs of vertical loading subsystem for controlling nominal pressure: (a) top cap with reinforcing beams and pneumatic regulator; (b) pneumatic bag

3.1.4 Instrumentation

Two pipe clamps were installed at each pipe end to create horizontal planes. Two LVDTs were utilised to measure the vertical displacement of these planes and the pipe's vertical displacement (see Figure 3.3). Additionally, a load cell with a measurement range of ± 10,000 N or ± 50,000 N and an accuracy of 0.03% and an LVDT with a measurement range of 50 mm and an accuracy of 1%were positioned between the pipe and the loading system to monitor the

axial force and axial displacement, respectively. The schematic diagram of these sensors can be seen in Figure 3.1 (a).

Six remote tensiometers (2100F), manufactured by Soilmoisture Equipment Corp., with a vacuum dial gauge range of 0 to 100 kPa and an accuracy of 0.1 kPa, were used to measure the matric suction around the pipe buried in unsaturated soils. The distribution of the tensiometers' porous ceramic cups at their buried positions is illustrated in Figure 3.1 (a). The porous ceramic cups were fully saturated before installation to ensure maximum sensitivity. After filling the tensiometer bottle and removing air from the vent tube, the service cap was connected to a vacuum pump set at -20 kPa through a waste bottle, and the porous ceramic cup was immersed in a water tank to create seepage over the ceramic. This process lasted for at least 12 hours. The ceramic cups were installed through holes in the box walls. Once the soil layer above the target buried position was compacted, a copper tube with an outer diameter slightly smaller than the ceramic cup was inserted through the hole to loosen the soil. Subsequently, the ceramic cup was covered with a layer of saturated clay slurry to ensure good soil-cap contact and minimise air entry. Finally, the ceramic cups were inserted into their target positions and secured using cable glands mounted on the box walls for waterproofing.

3.1.5 Evaluation of boundary effects

Two boundary effects were addressed in this study. The first one is the non-uniform distribution of shear stress caused by the presence of front and rear walls. As mentioned above, two sleeves with rubber membranes were introduced to address this problem. An optical fibre was utilised for the optical frequency domain reflectometry (OFDR) method to measure the pipe strain distribution (as Ni *et al.* (2018a)) in the longitudinal direction and evaluate the boundary effects. The strain accuracy and resolution of the fibre are 10^{-6} and 1 mm, respectively. This fibre was attached to the pipe's inner surface at two shoulders and two haunches to obtain precise axial strain measurements. Before installation, the inner surface of the pipe was

thoroughly cleaned using detergent and a metallic brush. While the fibre was in a straightened state, it was initially secured with quick-drying glue and then firmly bonded with epoxy resin. A long rod was used to assist in applying the epoxy resin. Figure 3.5 illustrates the axial strain distribution measured by optic fibre with various axial displacements during the pullout of the rough pipe under a surcharge of 50 kPa. The square points represent the axial strain at the side of the actuator (d_P = 700 mm) calculated by the axial force measured by the load cell, Young's modulus of steel and pipe cross-sectional area. These measurements align with the micro-strains obtained through the fibre at the pipe end, confirming the accuracy of the strain measurement. Throughout the pullout process, the distance d_P and the axial strain show a good linear relationship ($R^2 > 0.99$). It indicates that the non-uniformity of the shear stress distribution was minimised successfully by sleeves and membranes, and that the size of the gap between the pipe and sleeves is applicable to guarantee sufficient lateral support for the surrounding soils by rubber membranes.

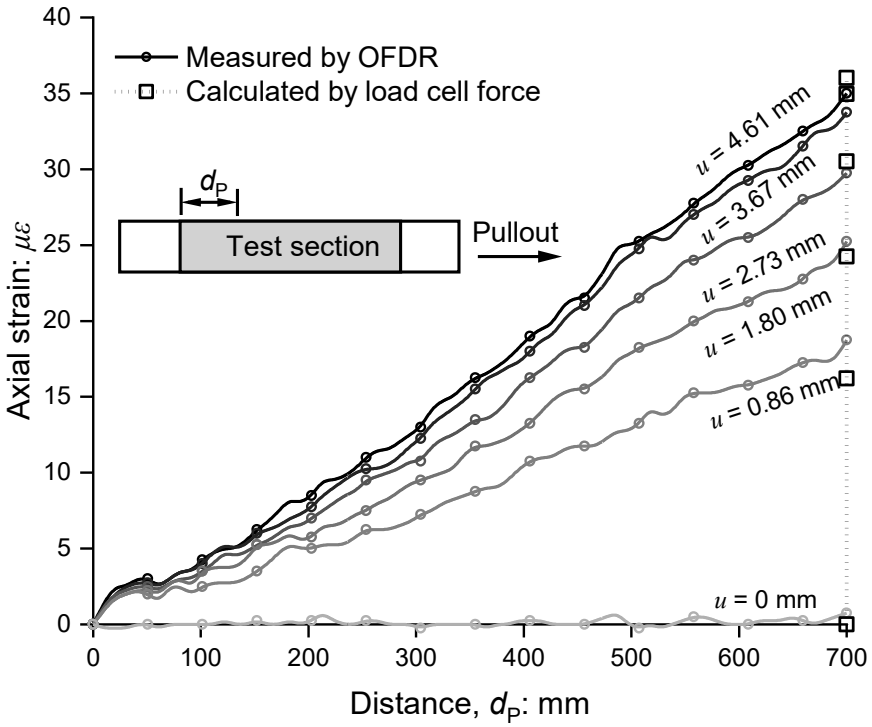

Figure 3.5 Measuring axial strain distribution with different axial displacements (u) using OFDR (optical frequency domain reflectometry)

The second boundary effect pertains to the roughness of the side walls. Two tests were conducted using the smooth pipe under a surcharge of 34 kPa. The side walls of the first test consisted of smooth steel plates (R_n = 0.01 for FJM sand), while for the second test, two pieces of sandpaper with a grit size of P40 ($R_n \approx 1.13$ for FJM sand) were attached to the steel plates to simulate rough trench conditions. The measured axial force-displacement relationships for the two tests exhibit remarkable consistency, suggesting that the roughness of the side walls has negligible effects.

3.2 Measurement of soil-pipe interface contact pressure and earth pressure around the pipe using tactile pressure sensors (TPS)

This study introduces a new earth pressure cell (TPS-EPC) and a new soil-structure interface contact pressure transducer (TPS-ICPT), based on the single-point-type tactile pressure sensor (TPS), and a corresponding methodology for measuring earth pressure around pipe and contact pressures at soil-pipe interfaces, respectively. Subsequently, the performance of the TPS-EPC, using the proposed methodology, is compared with that of the traditional EPC in an oedometer.

3.2.1 Design of thin TPS-EPS and curved surface-fitted TPS-ICPT

A typical single-point-type TPS manufactured by Interlink Electronics - Force Sensing Resistor (FSR) 402 was used. The active area has a diameter of 12.7 mm, larger than 30 d_{50} of FJM sand and CDG used in this study, sufficiently avoiding the particle size effects on the measurement accuracy based on the results of Kootahi & Leung (2022). More details can be found in Interlink (2023).

Two new transducers (i.e., TPS-EPC and TPS-ICPT) were developed using tools and materials in Figure 3.6. Figure 3.7 shows a schematic diagram and photograph of the TPS-EPC. TPS could not be buried in the soil directly because the soil deformation may stretch or bend the flexible sensors, resulting in unpredictable effects on the TPS's sensitivity and zero offset

(Interlink, 2023). Therefore, TPS is stuck on a 0.5-mm-thickness insulating-paint-coated steel slice whose shape adapts to TPS via water-cutting. Meanwhile, a coating layer made of epoxy adhesive DP100 manufactured by 3M protects the TPS. After 48 hours of curing, the epoxy adhesive would form a stiff coating layer with a thickness of around 0.5 mm. The coating may affect the sensitivity of TPS, and eighteen coated TPS-based sensors were calibrated with a loading path of 0~60 kPa and a pressure loading rate of 4 kPa/min. Their average sensitivity is 7.75 $(GPa \cdot \Omega)^{-1}$, sufficiently sensitive for measuring earth and soil-structure interface pressures. More details of calibration are discussed later. The short tail version of FSR 402 (FSR 402 Short) is used in TPS-EPC for a smaller volume. A heat shrink tube is set at the tail of TPS, and a steel slice is used to protect the wiring position further. The outsides of the slice's tail have a couple of grooves for better fixing the heat shrink tube. The thickness of the new sensor is around 1.5 mm, equaling 4 d_{50} of the FJM sand used in this study, significantly smaller than the thickness of the commonly used earth pressure cell. The overall Young's modulus of the TPS-EPC is approximately 4.5 GPa, as estimated based on the modulus of its constituent materials. This is significantly lower than the 240 GPa typical of steel, which is commonly used in traditional EPCs. The effects of negative soil arching on TPS-EPC are verified and later compared with traditional EPC.

The schematic diagram and photograph of the TPS-ICPT on a pipe surface are illustrated in Figure 3.8. The long-tail version of FSR 402 is used in TPS-ICPT for better wiring. Holes with a diameter of 8 mm are opened on the pipe. After wiring through the holes, the FSR 402 is stuck on the pipe surface by using its flexibility and coated using the same method as TPS-EPC. The total thickness of FSR 402 and the epoxy coating is around 0.5 mm, close to the d_{50} of the FJM sand used in this study. Hence, the effects of thickness are negligible.

Based on the results of some trial tests, the threshold pressure that induces a noticeable change in the electrical conductance (>1 MPa^{-1}) of bare FSR 402 varies from 0~10 kPa.

Increasing the surface roughness of the pipe or steel slice was found to reduce the threshold pressure to almost zero in all cases. The working principle of this method is probably due to the more significant prestressing during the sticking process for a rougher surface. The surface roughness can be controlled using mechanical surface treatment technology directly or by mixing some silty soil evenly into the epoxy adhesive used between TPS and the surface of the pipe or slice.

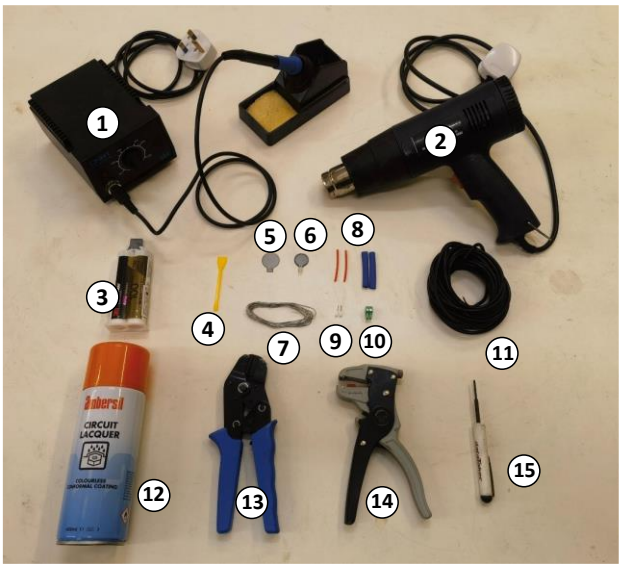

1.Soldering iron 2.Heat gun 3.Epoxy Adhesive DP100
4.Stir stick 5.Steel slice 6.FSR 402 short
7.Solder wire 8.Heat shrink tubing 9.Crimp connectors
10.Block connector 11.Twin-core cable 12.Conformal coating
13.Crimping plier 14.Cable stripper 15.Screwdriver

Figure 3.6 Tools and materials for preparing interface contact pressure transducers and earth pressure cells based on TPS

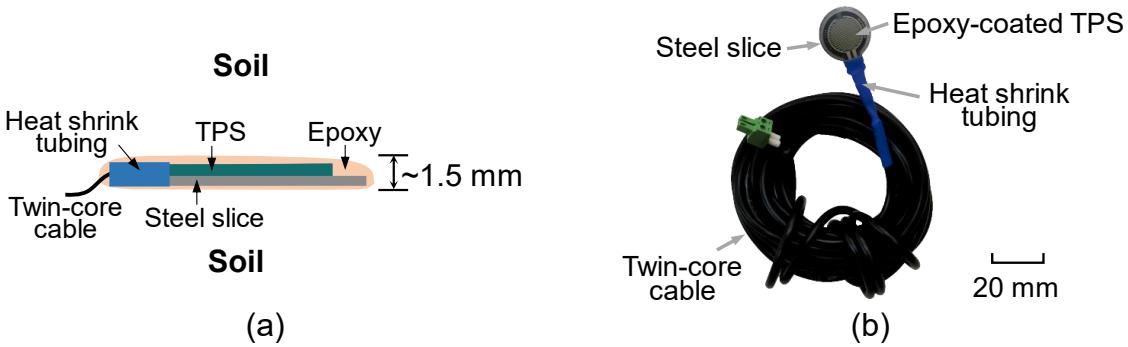

Figure 3.7 Design of TPS-based EPC sensors: (a) schematic side view; (b) photograph

Figure 3.8 Design of TPS-based ICPT sensors: (a) schematic side view; (b) photograph

3.2.2 Multi-channel measurement

The output signal of single-point-type TPS is its electrical conductance (g) (the reciprocal of electrical resistance (R)). It cannot be directly measured by common data loggers used in geotechnical testing.

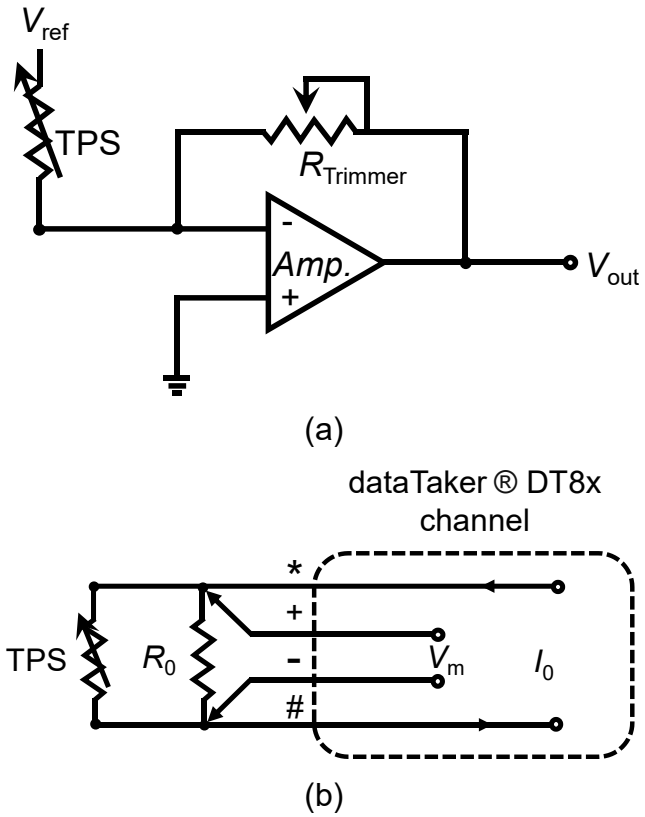

Figure 3.9 Measurement wiring and method: (a) method I: resistance-voltage conversion by electrical interface; (b) method II: 4-wire electrical resistance measurement by dataTaker DT85

Figure 3.9 (a) shows a method suggested by Interlink (2023) and used in some other studies (Gao *et al.*, 2017). This method adds an amplifier (denoted as *Amp.* in the figure) and a trimmer resistor with a constant and known resistance $R_{\text{Trimmer.}}$ The resultant electrical interface could convert the electrical conductance signal to voltage. The electrical conductance of TPS can be calculated as follows:

$$g_{\text{TPS}} = -\frac{V_{\text{out}}}{R_{\text{Trimmer}} V_{\text{ref}}} \tag{3-1}$$

where V_{out} is the output electrical voltage, and V_{ref} is the input reference electrical voltage. The wiring and debugging processes using this method are troublesome and complicated. Hence, this method is suitable for cases where the number of measurement targets is limited.

Figure 3.9 (b) is a newly proposed method that is more convenient and available for many measurement targets. This method is based on a specific data logger - dataTaker DT85, manufactured by Thermo Fisher. Compared to other common data loggers in geotechnical testing, dataTaker DT85 can measure the electrical resistance (the reciprocal of electrical conductance) directly using the 4-wire Kelvin method via the corresponding module embedded in the dataTaker DT85. Users can easily connect the TPSs to the dataTaker DT85, as illustrated in Figure 3.9 (b). One problem found by the authors is that the measurement is easily affected by electromagnetic interference from electromechanical apparatuses in the experimental environment. It is because the default 4-wire Kelvin method excitation current in dataTaker DT85 for the electrical resistance range of TPS (normally 0.1~100 kΩ) is as weak as 2 or 200 μA. To minimise the effects of electromagnetic interference, a stronger excitation current of 2.5 mA (I_0 in Figure 3.9 (b), optional in dataTaker DT85) is recommended. However, it would limit the maximum resistance measurement range to 700 Ω. Thus, a resistor with a resistance, R_0, of 700 Ω is suggested to be parallel with TPS. Then, the electrical conductance of the TPS could be calculated as

$$g_{\mathrm{TPS}} = \frac{1}{R_{\mathrm{TPS}}} = \frac{1}{R_{\mathrm{out}}} - \frac{1}{R_0} \tag{3-2}$$

where R_{out} is the output electrical resistance value. Meanwhile, common methods, such as using a grounding system and shielded twisted pair cables, should also be employed to eliminate electromagnetic interference.

DT85 also has an advantage in multi-channel measurement. One set of DT85 Series 4 is available simultaneously to measure sixteen electrical resistance signals. Coupled with the channel expansion module, CEM20, the maximum number of electrical resistance signal measurements is expandable to 320. In the physical modelling of this study, there are twenty-two TPS-based sensors, including four TPS-EPCs and eighteen TPS-ICPTs, and thus, one set of DT85 Series 4 and one set of CEM20 are used.

3.2.3 Post-installation calibration of TPS-EPC and TPS-ICPT

The performance of TPS highly depends on specific installation conditions. Hence, calibration after installation is necessary. A sealed tank is used for the calibration of TPS-EPCs. TPS-EPCs are put inside the tank, and the wire exits through sealed joints. During calibration, the air pressure can be controlled using a pneumatic regulator with a preset pressure path.

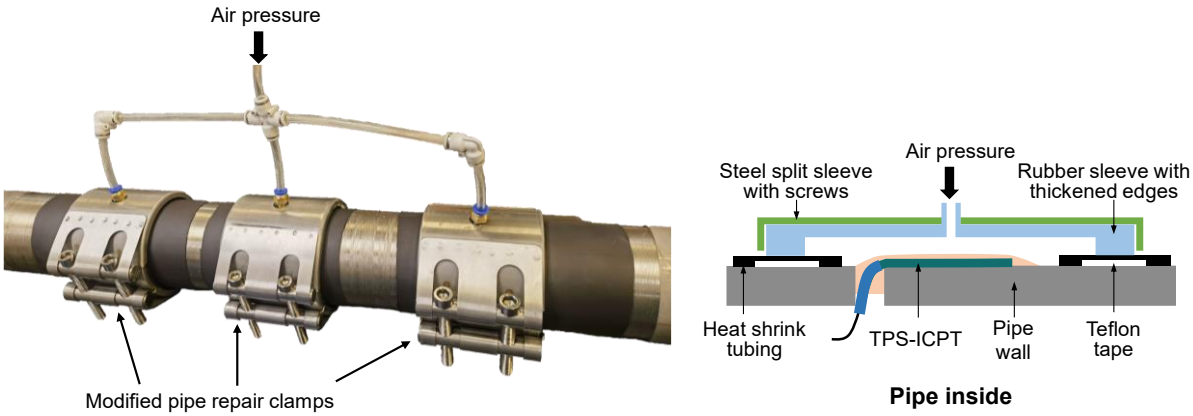

Figure 3.10 Proposed calibration method of TPS-based ICPT: (a) photograph; (b) schematic diagram of internal details

As for TPS-ICPTs, modified pipe repair clamps are utilised, as shown in Figure 3.10. The pipe repair clamp, consisting of a rubber sleeve with thickened edges and a steel split sleeve with screws, was initially used for repairing leaking pipes. A through hole is punched in the middle of the repair clamp and hermetically connected with a pneumatic connector. Hence, a sealed space that can control the air pressure is formed on the pipe surface with TPS-ICPTs (see Figure 3.10 (b)). Teflon tape and heat shrink tubing can be used to prevent gas leakage between the pipe and the edges of the repair clamp's rubber sleeve. The relationship between applied pressure and output can be determined using a method similar to that of TPS-EPC in controlling pressure.

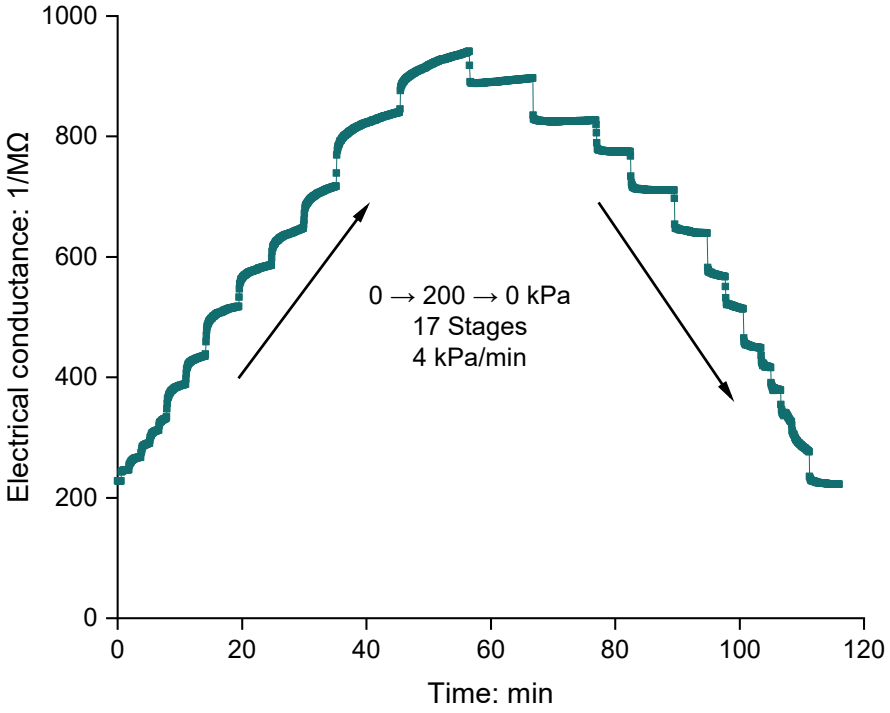

Figure 3.11 Typical calibration result (Loading path: 0~200 kPa; Unloading path: 200~0 kPa; 17 stages in total; 4 kPa/min)

Figure 3.11 shows the typical results of the electrical conductance evolution over elapsed time for TPS-EPC and TPS-ICPT. The air pressure was increased stepwise from 0 to 200 kPa (loading path), a typical range in geotechnical engineering, and then reverted to 0 kPa (unloading path) in 17 stages. At each stage, the pressure was swiftly adjusted and sustained for

a duration of $\Delta P/v$, where ΔP represents the variation in air pressure and v signifies the loading rate, equaling 4 kPa/min. Figure 3.12 (a) and Figure 3.13 (a) show a detailed analysis of the results from Figure 3.11, showing the relationship between electrical conductance and pressure during the loop, loading, and unloading paths, respectively. The data points for the loading and unloading paths in Figure 3.13 (a) represent the outputs at the end of each stage in Figure 3.11. The data for the loop path in Figure 3.12 (a) are the mean values of calibration results under the same pressure during loading and unloading paths.

Three key characteristics can be observed in Figure 3.11, Figure 3.12 (a), and Figure 3.13 (a) (Talesnick *et al.*, 2008; Talesnick *et al.*, 2011; Talesnick, 2013). Firstly, the electrical conductance of the TPS rises and falls with pressure. However, the curves representing the relationship between electrical conductance and pressure are non-linear, diminishing their slopes as pressure increases. Secondly, noticeable hysteresis is present in the loop of the electrical conductance-pressure curves. Although the outputs revert to nearly initial values when the pressure is regulated to zero, the electrical conductance during the unloading path is typically higher than that during the loading path. The behaviour observed during the unloading path is linked to the maximum calibration pressure. Thirdly, a short-term drift is evident in each stage, especially during the loading path. This is because the epoxy and materials of TPS are thermoplastic materials, whose response is often rate-dependent. Despite the TPS's rapid response to pressure changes (less than 3 microseconds, as stated in Interlink (2023)), the output value of electrical conductance continues to rise over time. Post-installation calibration of eighteen TPS-based sensors (comprising fifteen TPS-ICPTs and three TPS-EPCs) regarding these features is provided below.

The non-linearity of a sensor can be gauged by its non-linearity error. As depicted in Figure 3.12 (a), calibration data can be fitted using the best-fit straight line (BSL): $g=kp+g_0$, where p

represents the output value of pressure, g is the measured electrical conductance, k is sensitivity, and g_0 is the zero offset of the sensor. The non-linearity error is defined as the percentage of the

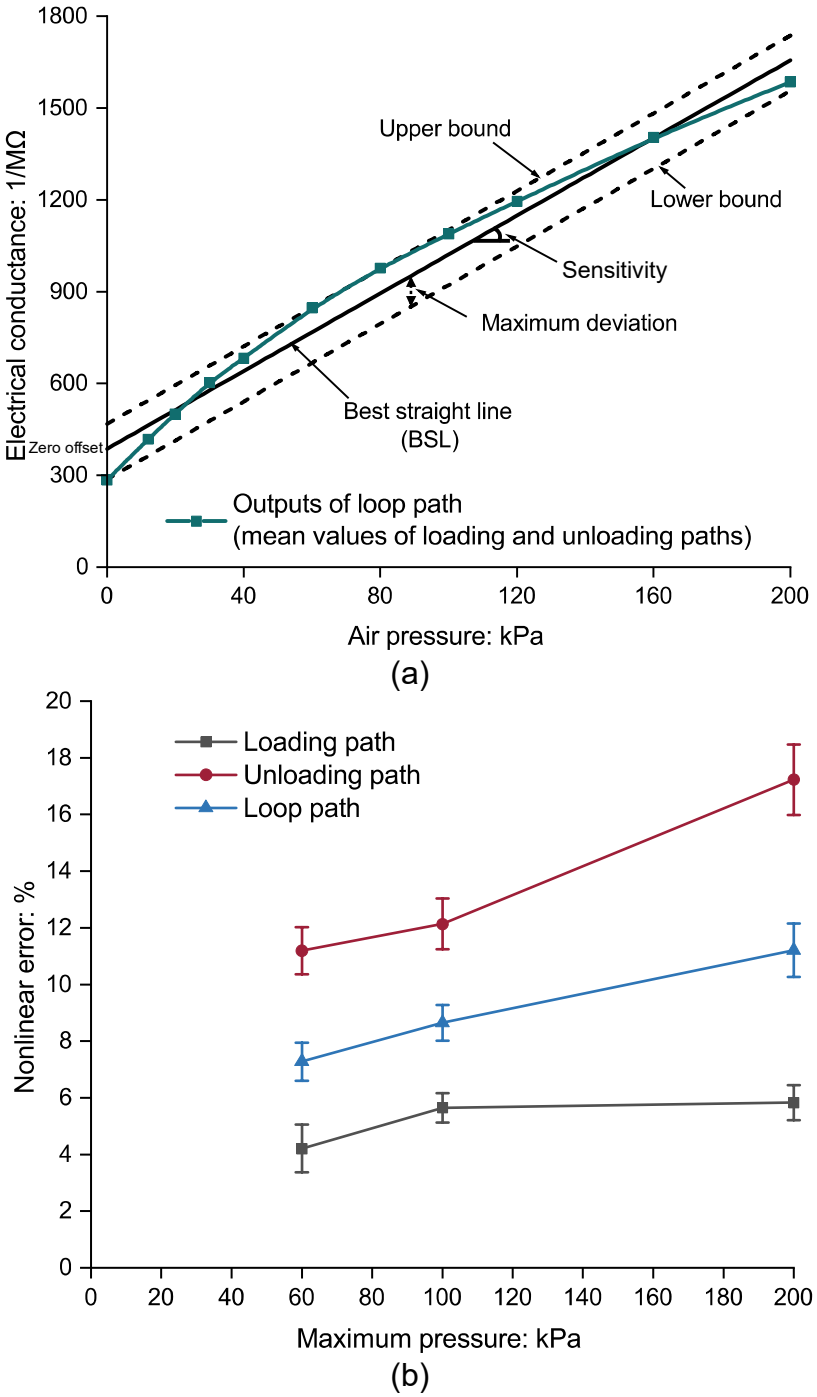

Figure 3.12 Non-linearity error of TPS-based sensor (number of TPS-ICPT=15, number of TPS-EPC=3, 4 kPa/min, error bar of Y-axis = ± standard error of the mean): (a) typical air pressure - electrical conductance relationship in loop path; (b) non-linearity error vs. maximum pressure

maximum output deviation between the calibration curve and its BSL to the maximum output range, as outlined by Nyce (2004). Figure 3.12 (b) presents the average non-linearity error of the loading path based on the calibration results of eighteen TPS-based sensors with a pressure loading rate of 4 kPa/min. The non-linearity errors of the unloading and loop path (calculated using values of the mean of calibration results under the same pressure during loading and unloading paths) are also depicted. The non-linearity error escalates with the maximum calibration pressure, irrespective of the path. The values of the three paths increase from 4.2 to 5.8%, 11.2~17.2%, and 7.3~11.2%, respectively. The calibration results under the loading path exhibit the best linearity. The standard errors of the average non-linearity errors are no more than ± 8.4‰.

Figure 3.13 depicts the hysteresis errors with varying calibration pressures based on the calibration results of eighteen TPS-based sensors. The hysteresis error is defined as the ratio of the maximum output deviation between the loading and unloading paths to the output range, as shown in Figure 3.13 (a). Although the effect of maximum pressure is not significant, the values of hysteresis errors are as high as at least 10% (see Figure 3.13 (b)).

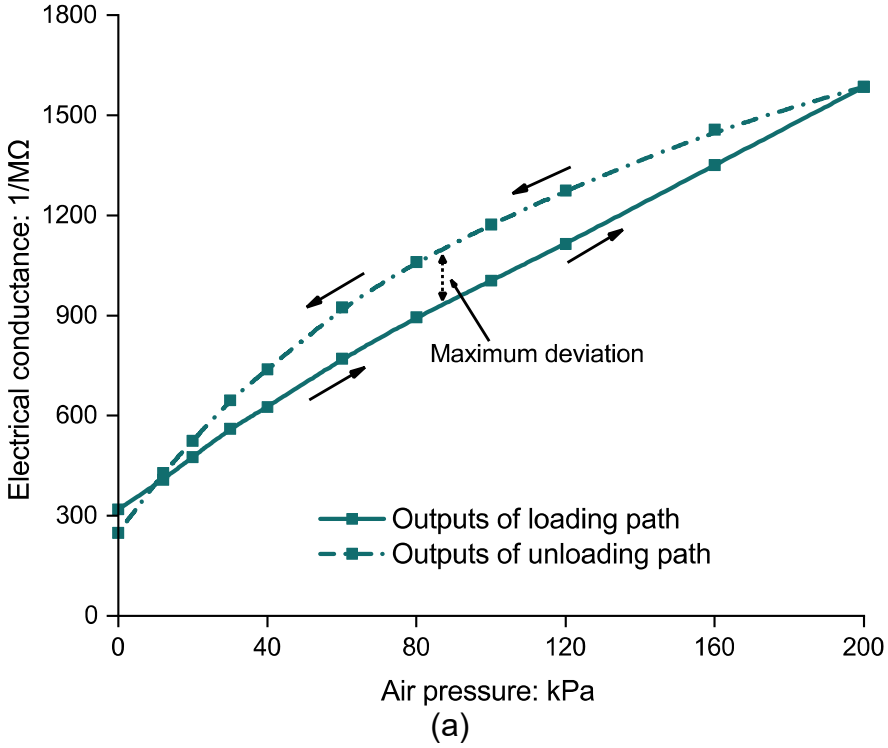

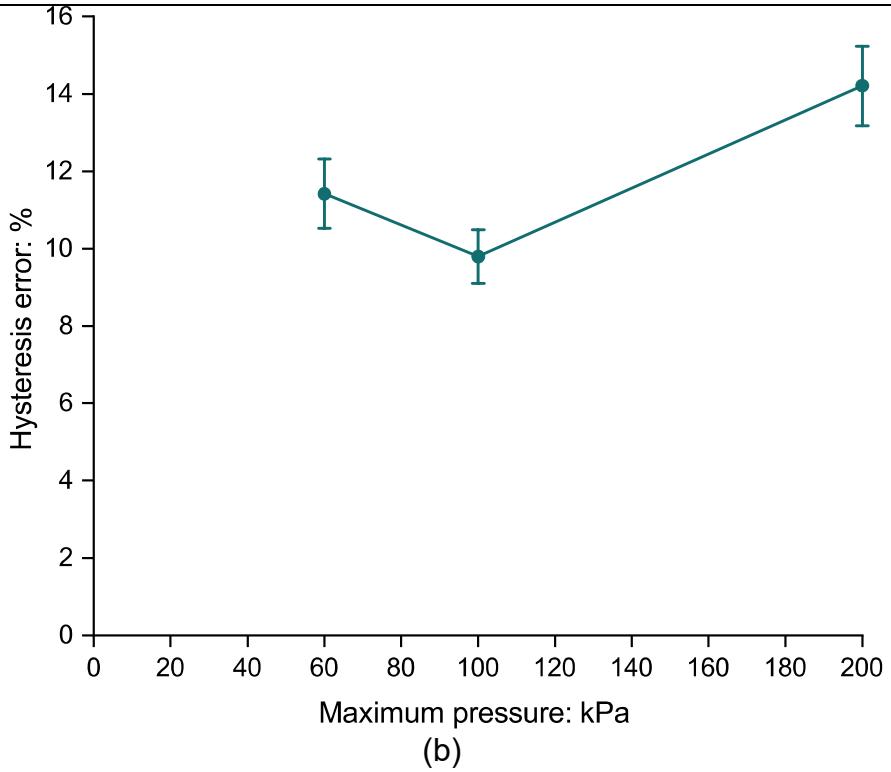

Figure 3.13 Hysteresis errors of TPS-based sensor (number of TPS-ICPT=15, number of TPS-EPC=3, 4 kPa/min, error bar of Y-axis = ± standard error of the mean): (a) typical air pressure - electrical conductance relationship in loading and unloading paths; (b) hysteresis error vs. maximum pressure

The non-linearity and hysteresis errors contribute to the sum static error, which is a crucial measure of a sensor's performance. The sum static error, e_{sum}, of a sensor is normally estimated using the root-sum-of-squares (RSS) method with $e_{sum} = \sqrt{\sum_{j=1}^{n} e_j^2}$, where e_j is an individual error (i.e., non-linearity, hysteresis or repeatability error in this case) and n is the number of errors. Therefore, based on the above results, the TPS's sum static error could reach up to 22%. However, utilising the non-linear signal conversion method recommended in the following section could be helpful to improve measurement accuracy.

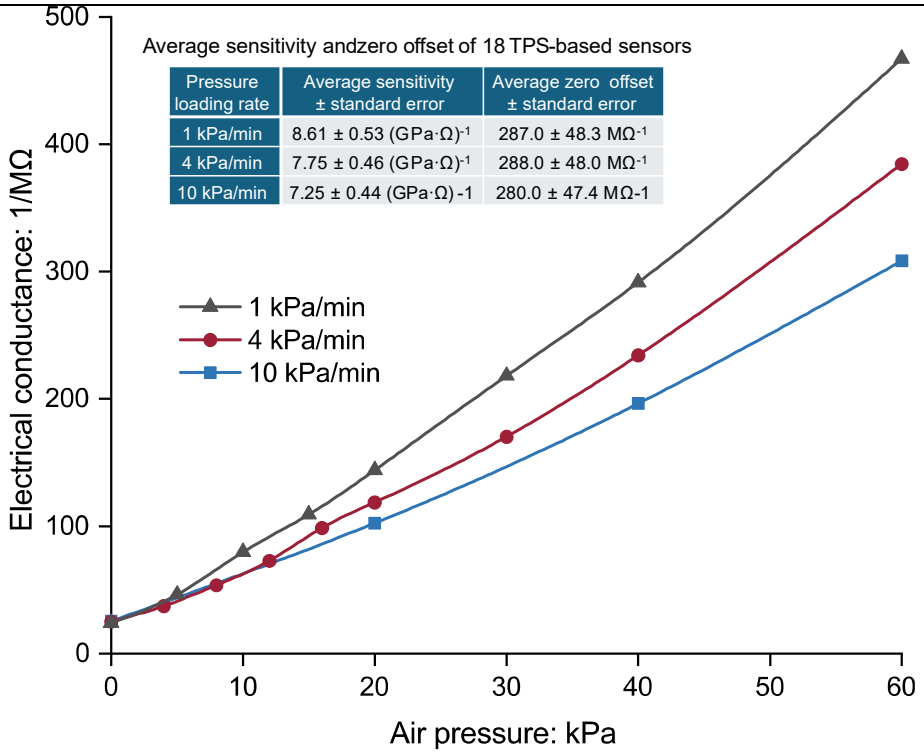

Figure 3.14 Influence of loading rate on pressure-electrical conductance relationship (number of TPS-ICPT=15, number of TPS-EPC=3)

Figure 3.14 illustrates the typical calibration results of a TPS-ICPT with different loading rates. Three loading rates, 1, 4, and 10 kPa/min, estimated as the values in the following physical modelling, were selected. The maximum calibration pressure is 60 kPa. The electrical conductance of each stage increases with the loading rate, which is consistent with the results in Figure 3.11. The calibration results of eighteen TPS-based sensors indicate that as the loading rate increases from 1 to 10 kPa/min, the average sensitivity experiences a decrease from 8.61 to 7.25 $(GPa \cdot \Omega)^{-1}$, while the average zero offset decreases to around 7 $M\Omega^{-1}$.

3.2.4 Non-linear signal conversion

The relationship between the physical quantity being measured and the output signal of common geotechnical sensors, such as pore pressure transducers and linear variable displacement transducers, is usually highly linear within their measurement range. Thus, the output signal results are typically converted into a physical quantity based on the fitted BSL. However, the performance of the TPS-based sensor is not ideal, according to the calibration

results above. A non-linear signal conversion method is suggested to be used to improve its accuracy. After calibrating the sensor, its electrical conductance-pressure relationship is fitted using the smoothing spline algorithm in MATLAB's Curve Fitting app. Then, the results of electrical conductance measured during experiments can be input into this relationship to return the results of pressure on the sensor. Utilising the non-linear signal conversion method and selecting a conductance-pressure curve calibrated under a condition close to the measurement could eliminate the effect of non-linearity error and minimise the effect of the hysteresis error. Consequently, the deviation caused by the sum static error might be less than 7.1%.

The loading range and rate in the calibration should be as close as possible to the experimental condition. If the measured pressure increases, the calibration results under the loading path should be used as the reference for signal conversion. For the unloading path, aside from the non-linearity, the curve of the unloading path is highly dependent on the maximum calibration pressure and is only reliable when the maximum calibration pressure is close to the maximum pressure in the experiment. Conversely, if the measured pressure continually fluctuates, the calibration results of the loop path may serve as a better reference.

3.2.5 Comparison between traditional EPC and TPS-based EPC

As previously mentioned, the large thickness and stiffness of traditional EPC can lead to stress concentration due to arching when buried inside the soil. Hence, the earth pressure they measured is higher than the actual value. The TPS-based EPC, with a limited thickness, can significantly minimise this problem. Three calibration tests were conducted using a modified oedometer to quantify this effect, as illustrated on the right side of Figure 3.15. A piezoelectric-ceramics-based EPC with a thickness (height) of 10 mm and a diameter of 20 mm represents the traditional EPC. Its nominal maximum pressure is 100 kPa with a static error of no more than 0.4%. In Condition I, the traditional EPC was embedded in the baseplate of the oedometer to create an ideal condition with no EPC thickness and compared to Conditions II and III, where

the traditional EPC and TPS-EPC were placed on the baseplate of the oedometer to simulate the buried conditions in the experiment and practice.

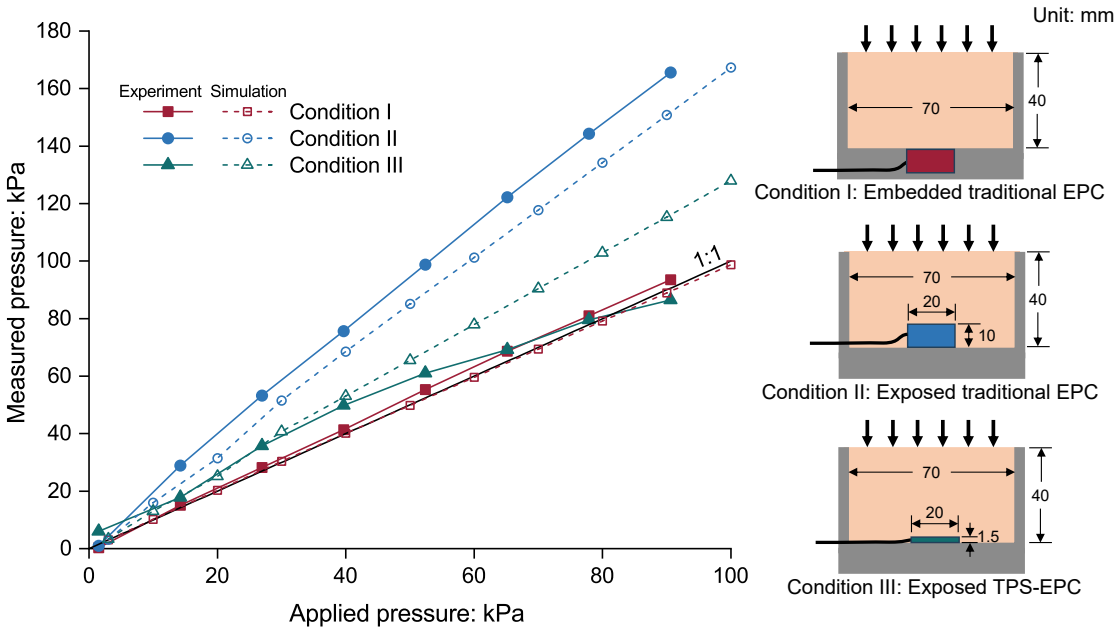

Figure 3.15 Comparison between TPS-based EPC and traditional EPC in the oedometer

Table 3.1 Parameters in DEM simulation of earth pressure cell thickness effect

Simulation parameter	Value
Particle density: kg/m^3	2 680
Normal stiffness to particle radius, k_n/r: MPa	150
Shear to normal stiffness ratio, k_s/k_n	0.2
Inter-particle friction angle, φ_{micro}: °	34
Sensor and boundary walls' normal stiffness to particle radius: MPa	19 000
Shear to normal stiffness ratio of the sensor wall	0.7
Sensor walls contact friction angle: °	10
Boundary walls contact friction angle: °	0
Relative density, I_D: %	85
Damping ratio	0.7

The testing soil used in this study is FJM sand, which is introduced in detail later. The dimensions of the soil specimen inside the oedometer are 40 mm in height and 70 mm in diameter. The specimens were compacted in layers of 10 mm with a relative density of 85%. After that, the specimen was loaded in stages. Each stage lasted at least two minutes until the readings of settlement and pressure were stable.

Figure 3.15 illustrates the experimental results. In Condition I, the measured pressures are consistent with pressures applied on the top of the specimen. It confirms the good performance of the traditional EPC when there is no thickness effect. Also, it confirms that piezoelectric ceramics utilised by the traditional EPC are a mature technique in pressure measurement. The measured pressures in Condition II exhibit a linear relationship with applied pressures, but the former is approximately 80% larger. This difference demonstrates the significant influence of the traditional EPC's thickness. As for Condition III, the measured pressure is slightly higher than the applied value at early loading stages and then approaches the applied value at later stages. Its error is no more than 10%, demonstrating the good performance of TPS-based sensors compared to traditional EPCs.

3D DEM simulation was carried out to interpret the experimental results and understand the results of the oedometer tests. The simulation was conducted using YADE. A six-wall box was established as the boundary to model the oedometer cell. Another six-wall box set in the middle of the boundary bottom wall represented the sensor. The dimensions of the boundary and sensor model were the same as those of the experiments. The shapes of the boundary and the sensors were cuboid rather than cylindrical for easier modelling. The linear elastic-friction model (Šmilauer & Chareyre, 2021) is used to simulate the particle-particle and particle-wall contacts. The model parameters used in this study are summarised in Table 3.1. Approximately 30,000 particles with uniform diameters were randomly generated and were compacted to the target relative density (85%) using the radius expansion method (Scholtès *et al.*, 2009). The

final particle diameter was around 1.88 mm, consistent with 5 times the mean particle size in the experiment. Finally, the normal pressure on the specimens was controlled using the top wall of the boundary cuboid. The specimens were also loaded in stages. Each stage continued until the top pressure reached the target and the unbalanced force was less than 0.1%.

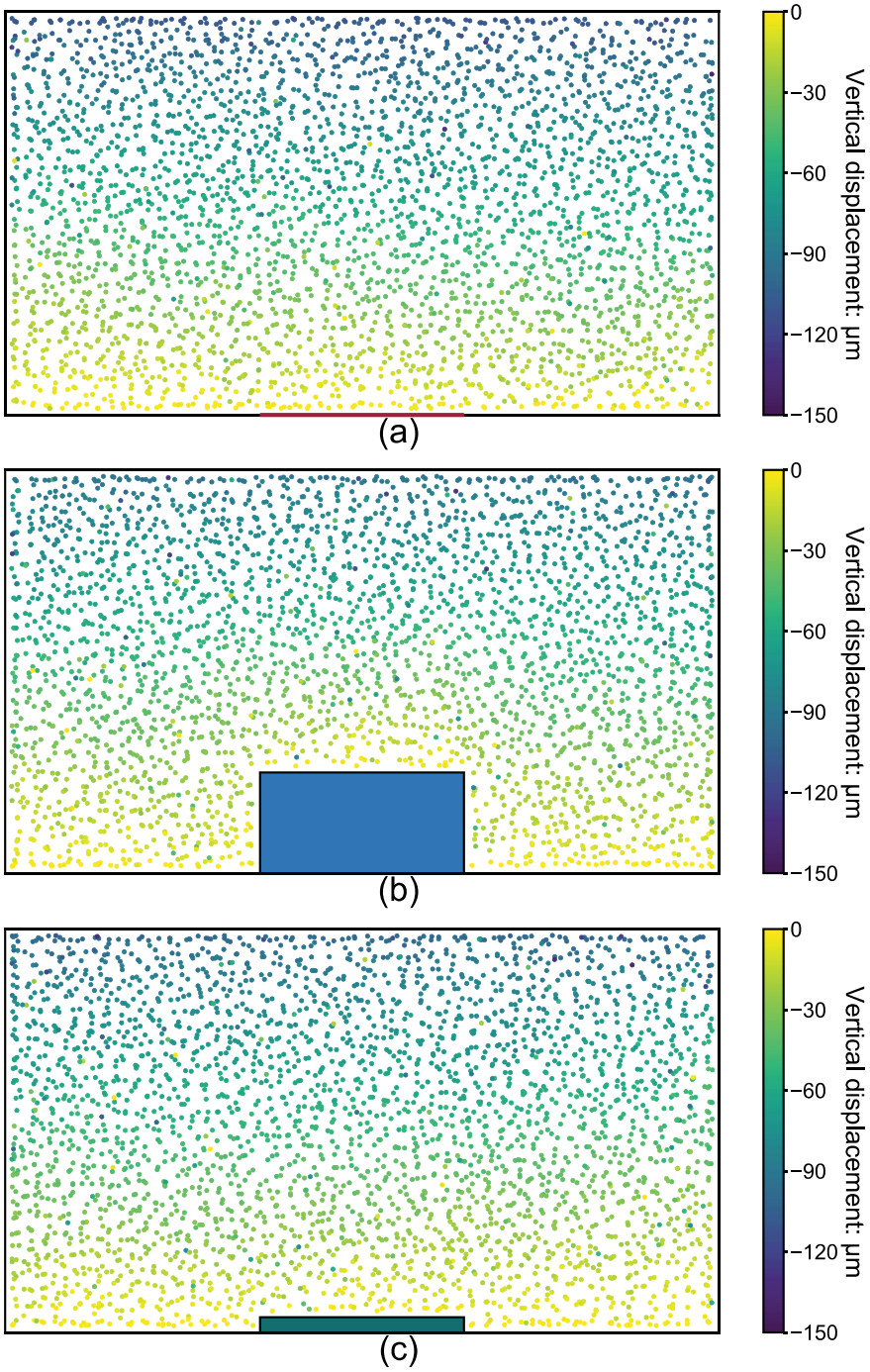

Figure 3.16 Vertical displacement with applied pressure increasing from 0 to 100 kPa in DEM simulation: (a) Condition I; (b) Condition II; (c) Condition III

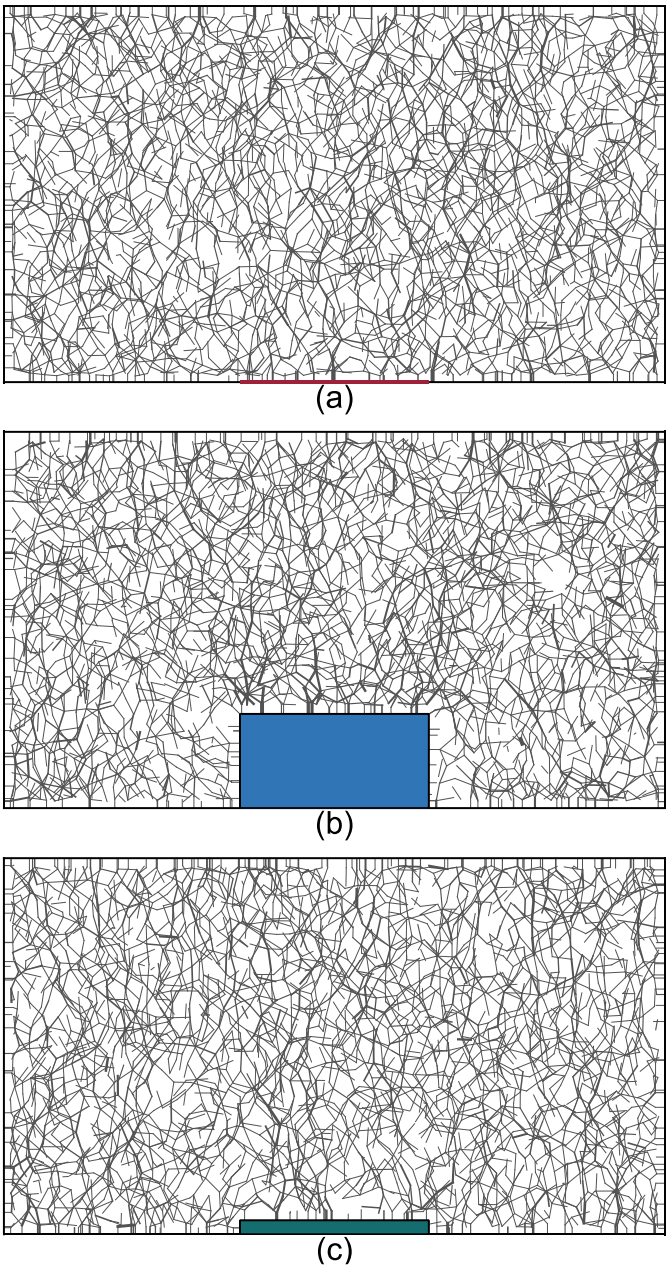

Figure 3.17 Force chain network with applied pressure of 100 kPa in DEM simulation: (a) Condition I (the maximum contact normal force = 2.12 N); (b) Condition II (the maximum contact normal force = 3.08 N); (c) Condition III (the maximum contact normal force = 2.16 N)

Computed pressures are also shown in Figure 3.15 for comparison. The trends observed in experiments are all confirmed by the numerical results, although the computed and measured results are slightly different. The arching effects mechanism can be analysed using the DEM simulation results. Figure 3.16 illustrates the vertical displacement of soil particles as the

applied top pressure increases from 0 to 100 kPa. All the values are negative due to soil compaction as pressure increases. Figure 3.17 shows the strong force chain network projection in the DEM simulation of Conditions I to III. The strong force chain is a network of contact normal forces larger than their median values (Peters *et al.*, 2005). The thickness of each chain is proportional to the magnitude of the force. For a clear distinction, only the data from particles between the sensor's front and rear walls are shown in Figure 3.16 and Figure 3.17. In Condition I, shown in Figure 3.16 (a), particles' vertical settlements (negative values of vertical displacement) decrease from around 150 μm to 0 μm with increasing depth, and all settlements are uniform at the same depth. Correspondingly, the force chains in Condition I (see Figure 3.17 (a)) distribute uniformly in space, with the maximum contact normal force of 2.12 N, proving that the soil particles support the loading from the top wall evenly. As for Condition II, the particle settlements above the sensor's top wall are smaller than those on the left and right sides due to varying soil thickness (see Figure 3.16 (b)). This non-uniform settlement indicates a relative displacement, applying an additional downward force above the sensor's top wall with stronger force chains (maximum contact normal force = 3.08 N, see Figure 3.17 (b)). This corresponds to the higher measured pressures shown in Figure 3.15. By comparison, non-uniform particle displacement and the concentration of the force chain (2.16 N in maximum) on the sensor top wall in Condition III (see Figure 3.16 (c) and Figure 3.17 (c)) is not as evident as that of Condition II, causing a limited difference between the measured and applied pressures in Figure 3.15.

Based on the above tests and DEM simulations, the limited thickness and stiffness of the TPS-EPC can reduce the error caused by the arching effects on the sensors from around 80% to no more than 10% when the sensor is buried inside the soil, demonstrating a more accurate measurement of earth pressure. Furthermore, in field or physical modelling, the soil around the buried sensors can be disturbed during sensor installation. Compared to the traditional

commercial EPC, the TPS-EPC, with its smaller volume and mass, would cause fewer disturbances.

3.2.6 Specific application in physical modelling of this study

Eighteen TPS-ICPTs were placed across three cross-sections of the pipe, with a spacing of 0.2 m between each section. On each cross-section, six TPS-ICPTs were installed at the crown, one shoulder, two springlines, one haunch, and the invert, as indicated by red points in Figure 3.1 (a). Four TPS-EPCs were employed to measure overburden pressures at various positions (see side view of Figure 3.1 (a)). Four traditional EPCs, based on piezoelectric ceramics, were buried in the same distribution as the TPS-EPCs for comparison. All TPS-based sensors were calibrated under a 0~200 kPa loop path. The loading path curves were used as a reference during the first loading (the loading process of the first cycle), as the pressures were primarily increasing. After the first loading, the loop path curves were used for conductance-pressure conversion due to repeated increases and decreases.

3.3 Pipes with different surface roughness and hardness

Hot-rolled seamless steel pipes, commonly used in Hong Kong, with a nominal outer diameter of 102 mm and a nominal thickness of 4 mm, were used (BSI EN 10220:2002, 2002; HKIUS, 2011). The results provided in this study could be a reference for pipes with other diameters or materials. Further details can be found in Table 3.2. Five pipes were prepared, including three non-coated raw steel pipes with different roughness and two coated steel pipes with different coating materials (see Table 3.3 and Figure 3.18). The normalised surface roughness (R_n) can be determined using the equation proposed by Kishida & Uesugi (1987): $R_n = R_{max}/d_{50}$, where R_{max} is the maximum height on the surface profile over a travel length of d_{50}, and d_{50} is the average particle size. These five pipes were tested with FJM sand to investigate the effects of surface roughness and coating hardness on the ASPI behaviour in CHAPTER 4 and CHAPTER 5. Therefore, pipes with varying surface roughness values were designed and

named according to R_n of FJM sand, as in Table 3.3. According to the classification framework proposed by Paikowsky *et al.* (1995), the critical values of normalised roughness that differentiate smooth-intermediate and intermediate-rough interfaces are 0.02 and 0.5, respectively. Without any treatment, the raw seamless steel pipe has a roughness value of 0.015 in R_{max} and thus 0.04 in R_n for FJM sand, as measured by a surface roughness tester (SJ-210, Mitutoyo). Although slightly larger, this value is very close to the critical value of 0.02, so the raw pipe is referred to as a smooth pipe in this study. The surfaces of the rough and intermediate pipes were treated using the turning method. Turning depths of 0.38 mm with an interval of 0.9 and 0.08 mm with an interval of 0.4 mm were applied to achieve normalised roughness values of 1.01 and 0.21 for FJM sand, respectively. The R_n for CDG of the so-called intermediate pipe is 1.02, which was tested with CDG to study the matric suction effect on ASPI in CHAPTER 6.

Two commonly used coatings, epoxy asphalt (EA) and fusion bonded epoxy (FBE), were applied to two raw steel pipes to evaluate the hardness effects. Surface hardness tests were conducted using the Rockwell hardness scale of HRA by a hardness tester (OMAG 206) to measure the surface hardness of the coated pipes and raw steel pipe (ASTM E18, 2022; ASTM D785, 2023). The measured surface hardness values for EA, FBE, and raw steel are 32.6, 44.2, and 59.0, respectively. The measured values of R_n for the FJM sand of the two coated pipes are both 0.01.

3.4 Soil materials

3.4.1 Fujian medium sand (FJM sand)

The soil used in CHAPTER 4 and CHAPTER 5 is standard medium sand sourced from Fujian Province (FJM sand), China, with a particle size ranging from 0.25 to 0.5 mm (see particle size distribution in Figure 3.19). The parameters of this sand are provided in Table 3.4. The target relative density is 85%, meeting the compaction requirement in practice (USBR,

1996). A series of direct shear tests were conducted to measure the internal friction angles of pure sand and the interfaces (treated using the same methods on pipes in Table 3.3). The shear box and test method are similar to the study of Cui (2023). The typical interface shear behaviours of steel interfaces with different roughness values are illustrated in Figure 3.20. Values of interface shear angles are given in Table 3.5.

3.4.2 Completely decomposed granite (CDG)

The soil used in CHAPTER 6 is completely decomposed granite (CDG), typical in-situ soil in Hong Kong. The particle size distribution curve and key properties of CDG used in this study are shown in Figure 3.19 and Table 3.6. The plastic and liquid limits of the fines of CDG are 22.7 and 32.8%, as measured by Hossain & Yin (2010). Based on the Unified Soil Classification System (ASTM, 2017), this soil is classified as clayey sand (SC). The maximum dry density and optimum water content are 1780 kg/m^3 and 15.1% using standard Proctor tests (ASTM, 2021). The target relative compaction is 95%, corresponding to the target dry density of 1691 kg/m^3, meeting the compaction requirement in practice (USBR, 1996).

Figure 3.21 illustrates the soil-water retention curve of CDG measured in the drying path by Hossain & Yin (2010) using a suction-controllable direct shear apparatus via the axis-translation method under a net normal pressure of 0 kPa. It can be fitted by the van Genuchten model (van Genuchten, 1980) as

$$S_{\mathrm{r}} = \left[1+\left(a_{\mathrm{vG}}s\right)^{n_{\mathrm{vG}}}\right]^{-m_{\mathrm{vG}}} \tag{3-3}$$

where a_{vG}, n_{vG} and m_{vG} are fitting parameters, equaling 0.07 kPa^{-1}, 0.11 and 0.7, respectively, for CDG used in this study.

A series of interface direct shear tests were conducted to evaluate the interface shear strength between CDG and the steel interface with an R_{n} of 1.02, similar to those on pipes. The shear rate was set at 0.02 mm/s, matching the pipe pullout speed used in subsequent physical modelling. CDG samples were collected after tests from areas at the same elevation as the pipe

Table 3.2 Pipe properties

Properties	Values
Diameter, D: mm	102
Thickness: mm	4
Total length: m	1.25
Testing length: m	0.7
Steel density: kg/m^3	7930
Linear temperature expansion coefficient at 25°C: 10^{-6}/°C	17.3
Young's modulus: MPa	204
Poisson's ratio	0.3

Table 3.3 Pipe surface conditions

Pipe type	Surface treatment	R_{max}: mm	R_n* for FJM sand	R_n* for CDG	R_a: mm	Surface material hardness: HRA†
Smooth#	Raw seamless steel	0.015	0.04	N/A‡	0.0024	59.0
Intermediate#	Turning surface	0.08	0.21	1.02	0.0313	59.0
Rough#	Turning surface	0.38	1.01	N/A‡	0.0944	59.0
FBE	Fusion bonded epoxy coated	0.004	0.01	N/A‡	0.0006	44.3
EA	Epoxy asphalt coated	0.003	0.01	N/A‡	0.0004	32.6

*R_n: Normalised surface roughness using R_{max}/d_{50}.

#Classification according to R_n for FJM sand

†HRA: Rockwell hardness based on ASTM (2022) and ASTM (2023).

‡Not used in tests of CDG

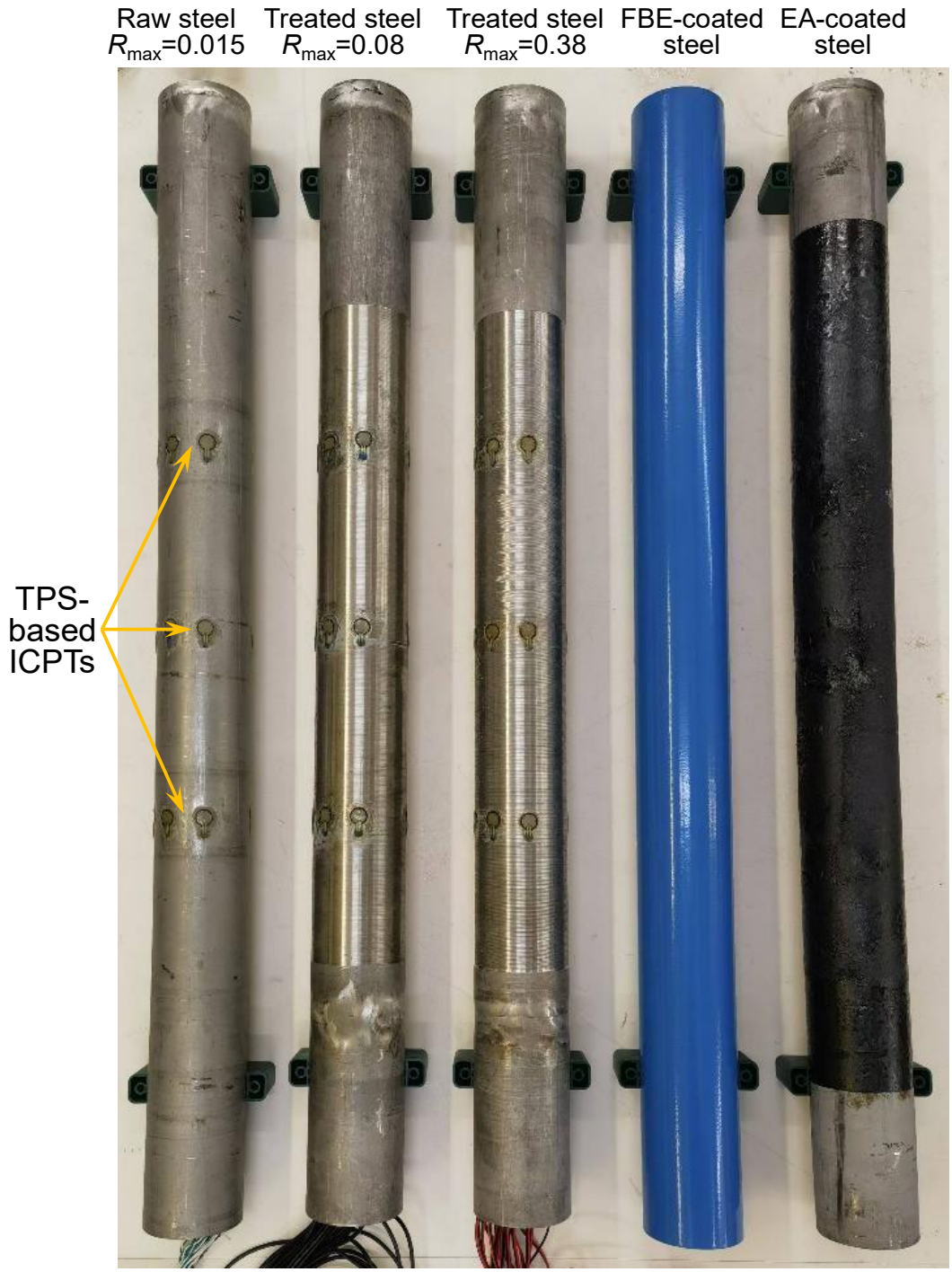

Figure 3.18 Pipe with different surface treatments

Table 3.4 Properties of Fujian medium (FJM) sand

Properties	Values
Specific gravity	2.68
Particle size: mm	0.25-0.5
Median particle size, d_{50}: mm	0.375
Maximum void ratio, e_{max}	0.797
Minimum void ratio, e_{min}	0.526
Target relative density, I_D: %	85
Dry unit weight at target relative density, γ': kN/m^3	17.0
Peak friction angle*: °	39.6
Critical state friction angle*: °	32.8
Particle sphericity†	0.92
Particle roundness†	0.728
Particle roughness†	1.021

*Measured by direct shear tests with applied effective normal stresses of 17, 34, 50, and 100 kPa.

†Data from Liang *et al.* (2021).

Table 3.5 Friction angle between FJM sand and steel pipe interface

Pipe type	Peak friction angle*: °	Critical state friction angle*: °
Smooth	18.4	17.3
Intermediate	34.7	29.4
Rough	37.9	33.5
FBE	19.2	19.0
EA	36.8	33.8

*Measured by interface direct shear tests with applied effective normal stresses of 17, 34, 50, and 100 kPa.

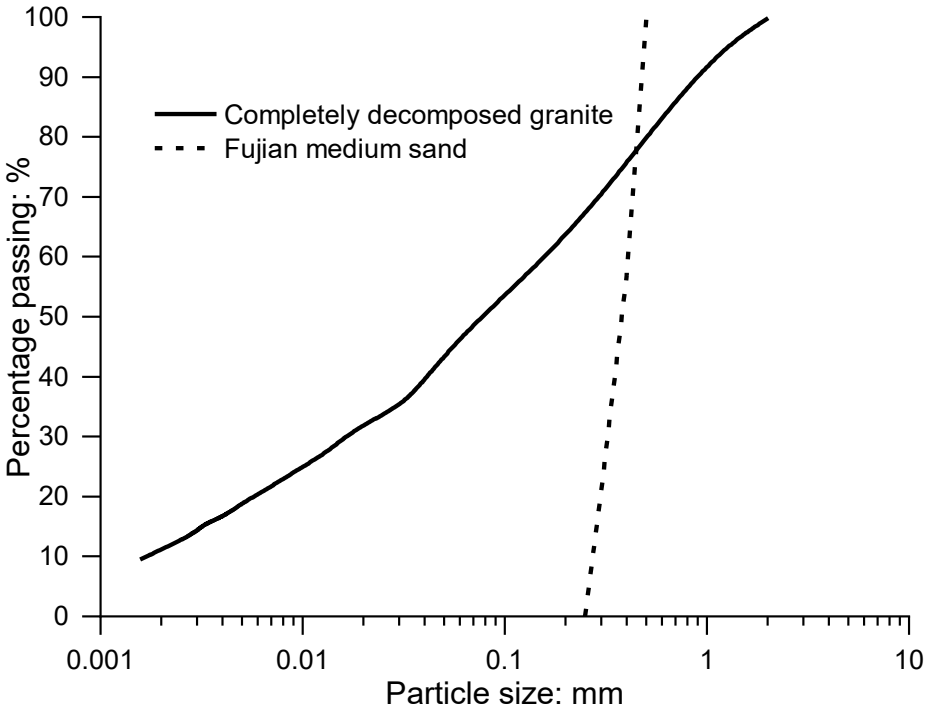

Figure 3.19 Particle size distribution of FJM sand and CDG

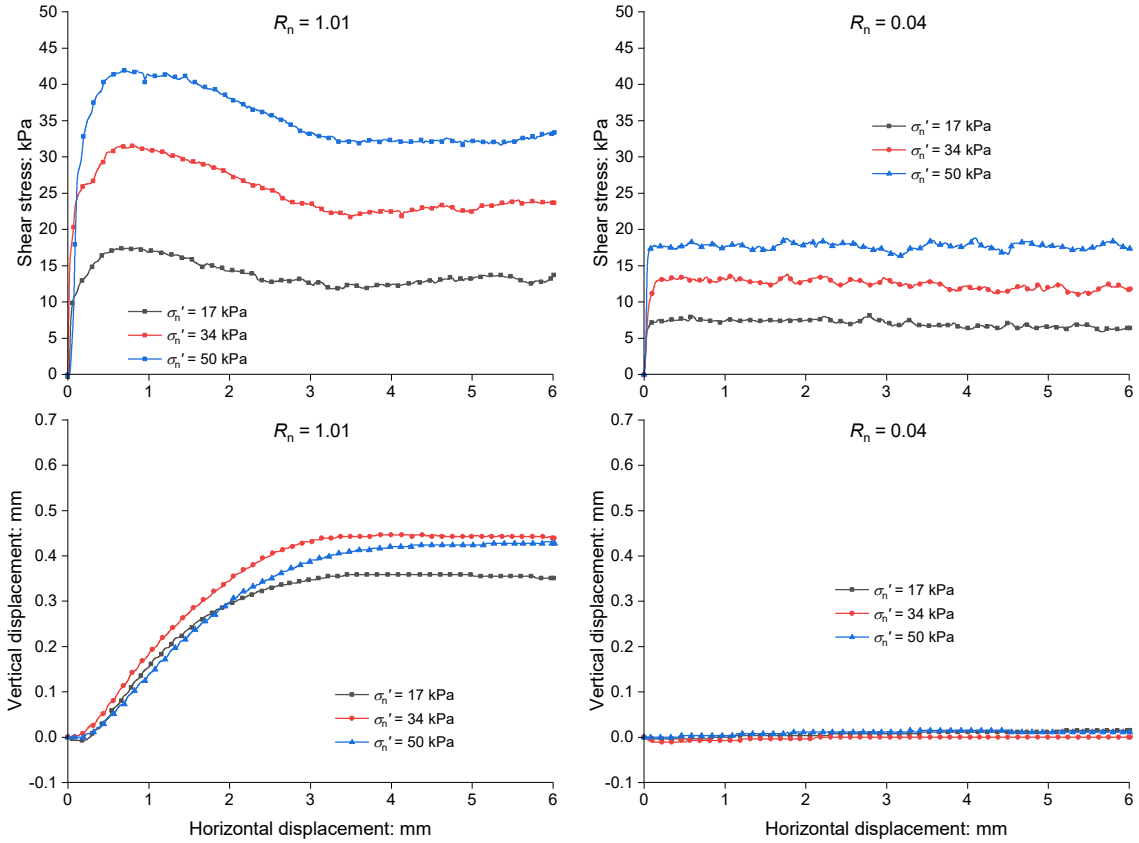

Figure 3.20 Typical interface shear behaviour between steel interface with different roughness and dry FJM sand

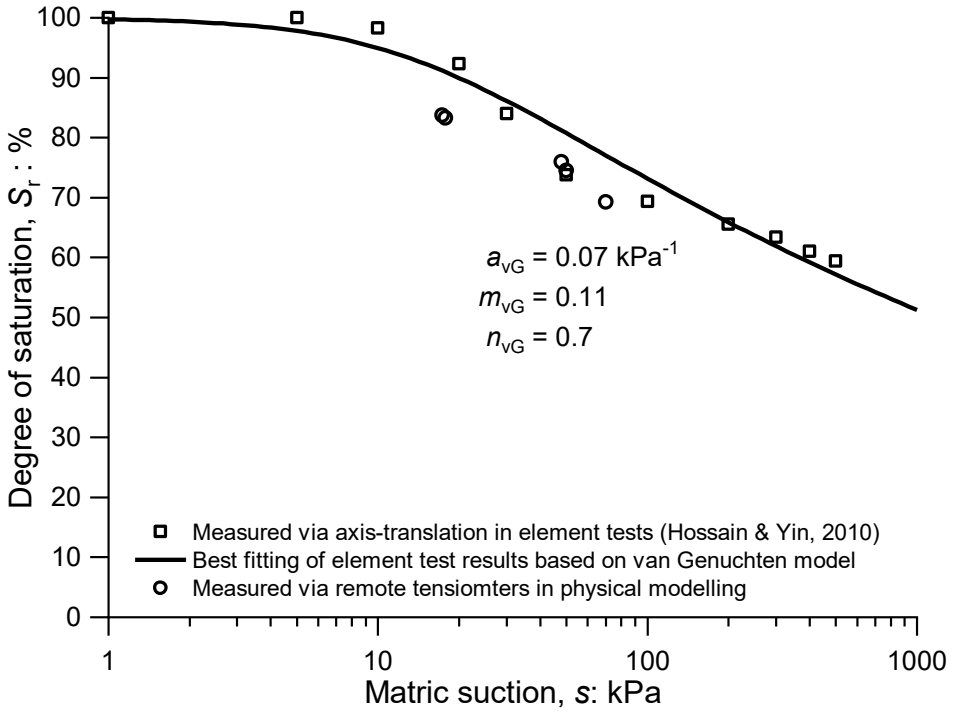

Figure 3.21 Soil-water retention curve of CDG

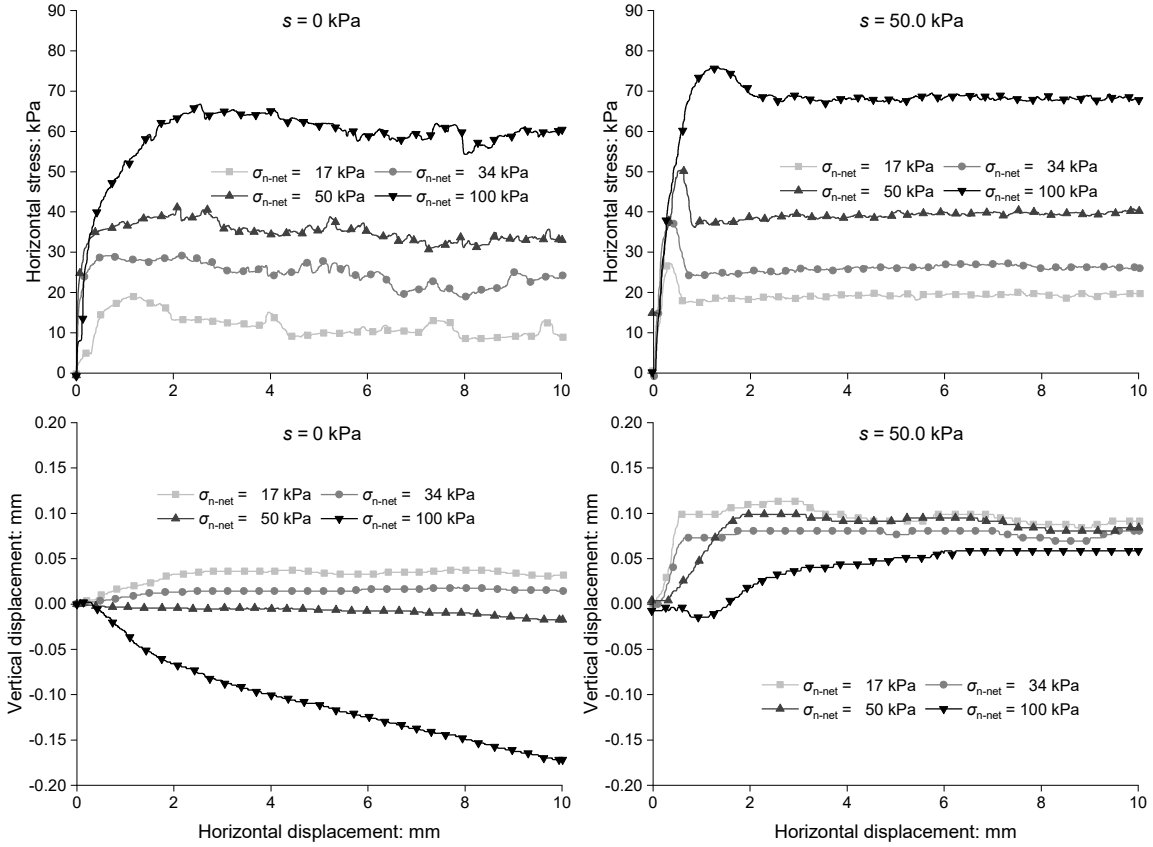

Figure 3.22 Typical interface shear behaviour between the steel interface and CDG with varying matric suction

Table 3.6 Properties of CDG

Properties	Values
Unified Soil Classification System (ASTM, 2017)	SC
Specific gravity*	2.60
Median particle size, d_{50}: mm	0.078
Plastic limit*: %	22.7
Liquid limit*: %	32.8
Maximum dry density: kg/m^3	1780
Optimum moisture content: %	15.1
Target relative compaction: %	95
Peak friction angle#, φ': °	38

*Data from Hossain & Yin (2010).

#Data from Geoguide 1 (2020).

Table 3.7 Shear strength between unsaturated CDG and steel pipe interface with R_{max} = 0.08 and R_n = 1.02

Peak interface shear strength at the CNL condition: kPa		Net normal stress, $\sigma_{n\text{-}net}$: kPa			
Degree of saturation, S_r: %	Matric suction, s: kPa	17	34	50	100
100	0	17.12	26.24	37.08	55.98
83.3	17.3	25.95	32.62	46.60	70.46
74.5	50.0	27.35	37.52	50.33	75.97
69.2	70.2	28.07	40.14	53.72	79.73

springline, but at least 100 mm away from the pipe and tensiometer caps. The collected soil was sieved through a 2 mm mesh and remoulded into 60 × 60 × 20 mm^3 specimens, maintaining the initial density. This process was conducted swiftly and carefully to ensure that the water content and suction remained consistent with the values in physical modelling. The net normal stresses applied were 17, 34, 50, and 100 kPa, corresponding to the target nominal pressure at the pipe

centre in the physical modelling. Figure 3.22 illustrates typical interface shear behaviours for both saturated and unsaturated soils. Saturated soils under 17 and 34 kPa exhibited dilation behaviour with strain-softening in the stress curves and positive vertical displacements of 0.036 and 0.018 mm, respectively. As the normal stress increased, soils displayed compaction behaviour, with vertical displacement reaching -0.15 mm at a surcharge of 100 kPa. For unsaturated CDG with a matric suction of 50.0 kPa, significant dilation behaviours were observed under all normal pressures, indicated by pronounced softening in the stress curves and positive vertical displacements reaching 0.1 mm. The shear strength results are presented in Table 3.7.

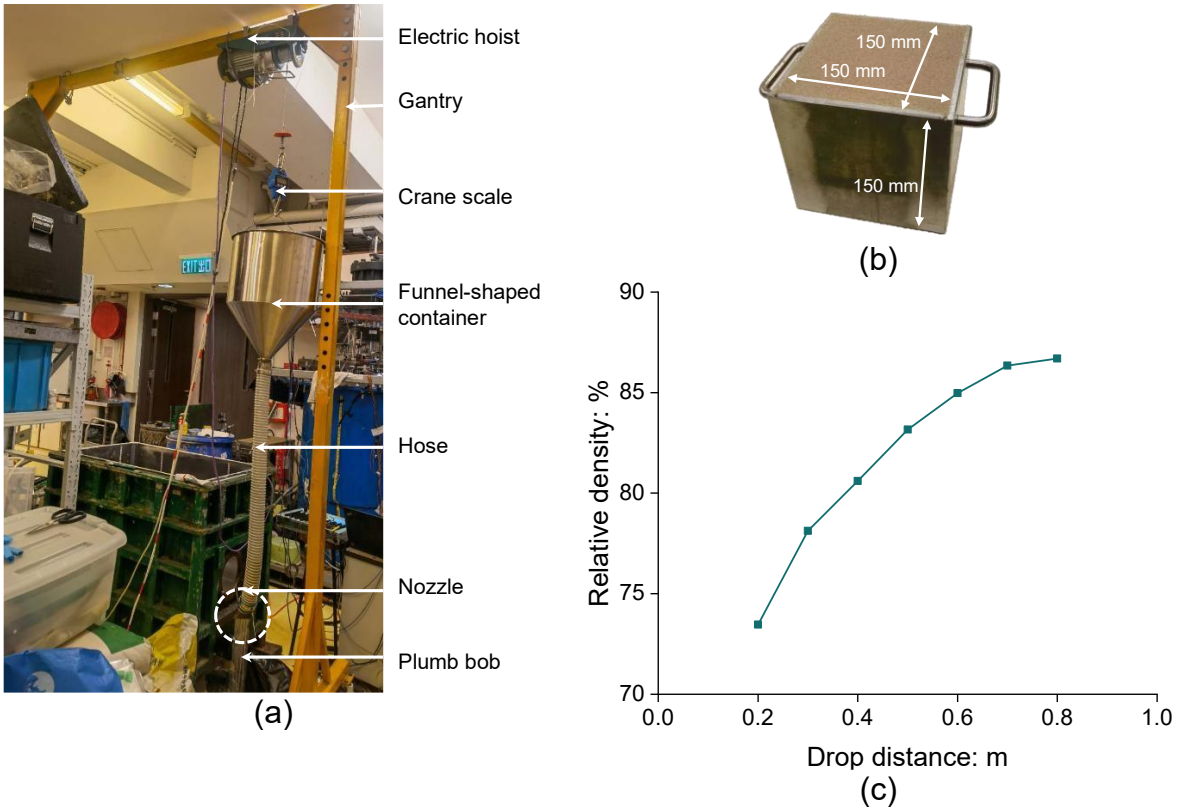

Figure 3.23 Soil pluviation method: (a) pluviation system; (b) box for calibration; (c) relative density at different drop distances

3.5 Model preparation and test procedures

The sand pluviation method (Fretti *et al.*, 1995) was introduced to prepare dense and uniform samples of dry FJM sand (see Figure 3.23 (a)). This method can be seen as the

simulation of the dumping technique in the engineering practice of compaction. The relative density under varying drop distances was calibrated using a steel box with a dimension of 150 × 150 × 150 mm^3, as shown in Figure 3.23 (b). Based on the calibration results in Figure 3.23 (c), the drop distance was set as 0.6 m for the target relative density of 85%. A laser level magnetically attached to the box's inner wall and six rulers affixed to the side walls were used to aid model preparation in layers (see Figure 3.24). Each layer had a thickness of approximately 25 mm.

As for the compaction of CDG, dry soil, adjusted to the target water content, was thoroughly mixed in a blender and crumbled to pass through a 600 × 400 mm^2 sieve with 10 × 10 mm^2 meshes (see Figure 3.25). The soil was then compacted using a 1900W electric earth rammer equipped with a 150 × 150 mm^2 tamping plate to achieve the target high relative compaction, similar to engineering practices in the field (USBR, 1996; WSD, 2012). The models were constructed in layers, each approximately 50 mm thick, to meet the practical requirement of 150 mm (USBR, 1996).

The saturated sample of CDG was initially compacted with a target water content of 17%. Water was injected from the bottom of the sample through four holes in the box walls, using a water cylinder with an elevation of 2.0~2.4 m relative to the box bottom. This process was maintained for seven days to allow maximum venting through seepage. A plate with a small air vent covered the box to minimise evaporation. The degree of saturation was estimated at 96.8% based on the added water volume.

During sampling, sleeves were installed once the depth reached an elevation of 0.28 m. At an elevation of 0.33 m, the pipe with rubber membranes was put into the box. The soil around the ends of the sleeves was temporarily moved, and after placing the rubber membranes and adjusting the pipe to the desired position, the removed soil was backfilled and compacted to its

original state. At this stage, the pipe was buried to a depth equalling 30% of its diameter. Subsequently, soil was continuously added until the elevation reached 0.76 m.

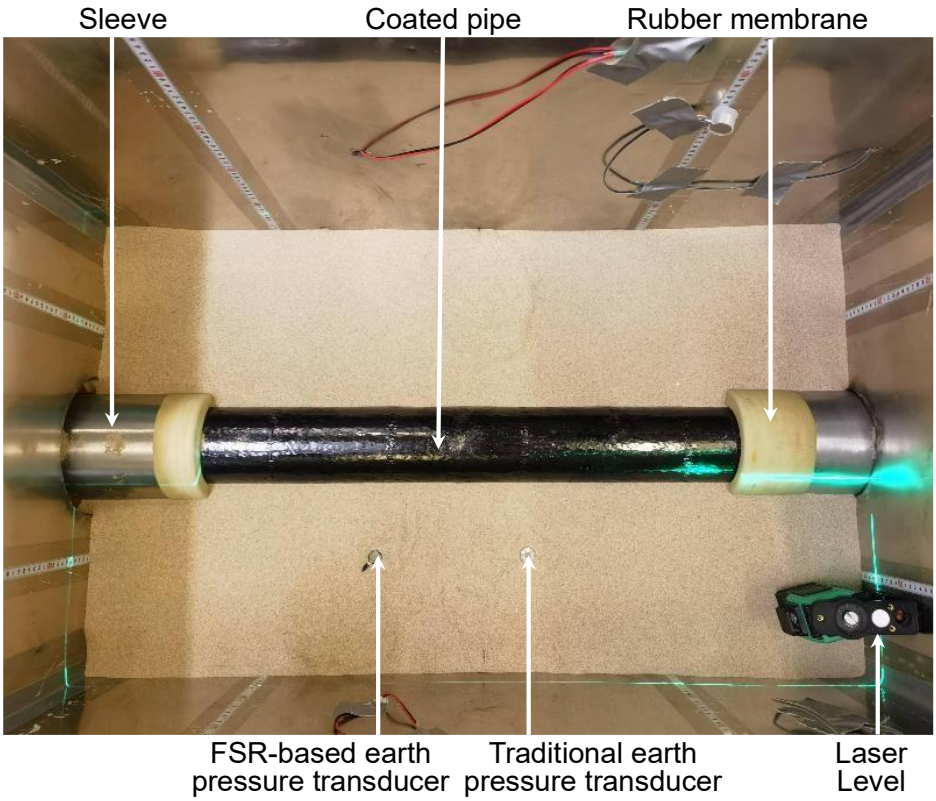

Figure 3.24 Model preparation of dry FJM sand

After sampling, the pneumatic bag and top cap were put on the soil. The air pressure was controlled. This condition was maintained for approximately 30 minutes in the dry condition tests and for seven days in the unsaturated and submerged CDG tests, until consolidation and matric suction equilibrium were achieved, as indicated by the stabilisation of sensor readings such as vertical displacement, earth pressure, and matric suction. Finally, the pipe's pullout speed was set at 0.02 mm/s, a common value in previous studies (Sheil *et al.*, 2018; Reza & Dhar, 2021).

(a)

(b)

(c)

Figure 3.25 Model preparation of CDG: (a) sieve; (b) soil before compaction; (c) electric earth rammer

CHAPTER 4
PHYSICAL MODELLING ON AXIAL BEHAVIOUR OF BURIED PIPES SUBJECTED TO MONOTONIC LOADING

4.1 Introduction

This chapter presents physical modelling tests of the axial behaviour of steel pipes buried in dry FJM sand and subjected to monotonic loading using the large-scale experimental system and novel earth pressure and interface contact pressure measurement technology developed in CHAPTER 3. Nine pullout tests were conducted using five pipes with different surface treatments. The main objectives are: (a) to investigate the extent to which surface roughness and hardness affect the pullout resistance, (b) to examine the mechanisms of surface condition effects, and (c) to propose a new method of calculating pipe pullout resistance.

4.2 Testing programme

Two series of pullout tests were conducted, as summarised in Table 4.1. Series I consisted of seven tests to study the effects of roughness and stress. Smooth and rough pipes were buried at different nominal pressures σ_c'. The target nominal pressures σ_c' include 17, 34, and 50 kPa, corresponding to 1, 2, and 3 m in burial depths. It should be noted that the axial resistance per unit area ($T/\pi D$) presented in this study can serve as a reference for pipes of different diameters or materials. Therefore, nominal pressure is considered a more important factor in axial soil-pipe interaction than the ratio of buried depth to pipe diameter. An intermediate pipe was also tested under a nominal pressure σ_c' of 34 kPa. Series II involved the pullout testing of FBE-coated and EA-coated pipes under a nominal pressure σ_c' of 34 kPa. These coated pipes were compared with the smooth pipe to analyse the effects of coating hardness.

4.3 Experimental results and discussion

4.3.1 Roughness effects on pullout force-displacement relationship and pullout resistance

Figure 4.1 illustrates the relationship between axial displacement and axial force in Series I. The axial pullout behaviour is significantly influenced by roughness. The results show that rough and intermediate pipes exhibit obvious strain-softening behaviour, while strain-softening is negligible for smooth pipes. This finding aligns with the results of soil-interface direct shear tests, where rough interfaces exhibit significant dilatant behaviour, while smooth interfaces show limited dilation. Under the same nominal pressure, the pullout resistance of rough pipes is 1.70~1.85 times higher than smooth pipes. This value is much larger than 0.17 (i.e., tan(0.8φ')/tan(0.7φ')-1) suggested by guidelines (see Table 2.4). Such a significant increment is due to different mechanisms. The increase in friction coefficient from soil-pipe smooth to rough

Table 4.1 Testing program of surface roughness and coating hardness effects on ASPI subjected to monotonic loading

	Reference	Roughness or coating	Nominal pressure at the centre: kPa
Series I Roughness and stress effects	Smooth-17	Smooth steel	17
	Smooth-34	Smooth steel	34
	Smooth-50	Smooth steel	50
	Rough-17	Rough steel	17
	Rough-34	Rough steel	34
	Rough-50	Rough steel	50
	Intermediate-34	Intermediate steel	34
Series II Coating hardness effects	Smooth-34	Smooth steel	34
	EA-34	EA-coated steel	34
	FBE-34	FBE-coated steel	34

soil-pipe interfaces (see Table 3.5) is 1.34 times (tan(37.9°)/tan(18.4°)-1). It means that 72-79% of the roughness-caused resistance increase is attributed to the increase in interface friction coefficient. The remaining 21-28% is mainly attributed to the increment of soil-pipe interface contact pressure that is closely related to the constrained dilation, as discussed later.

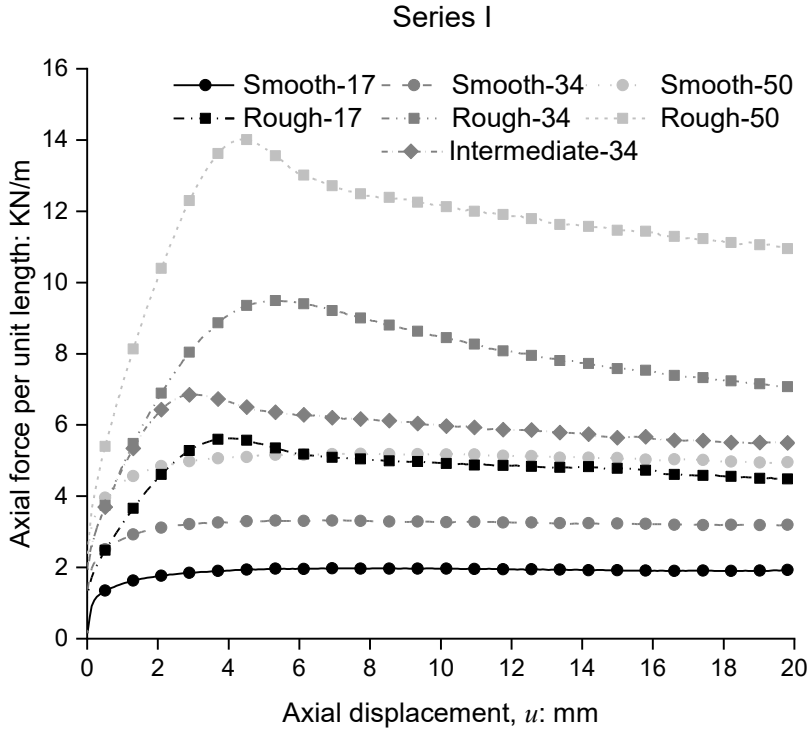

Figure 4.1 Surface roughness effect on axial force-displacement relationship during monotonic loading

Figure 4.2 demonstrates the relationship between the pullout resistance and the nominal vertical pressure at the centre for rough and smooth pipes. For both pipe types, the intercept of the trend line is higher than zero if assuming a linear envelope. This phenomenon is similar to the nonlinear failure envelope in interface shear. The soil's dilatancy becomes more pronounced at lower pressure, leading to this non-linearity.

Figure 4.3 compares the interface friction coefficients measured in the interface direct shear tests (μ_{dir}) (see Table 3.5) and predicted by the guidelines (μ_{ALA}) (see Table 2.4) to μ_{phy} (= $T/[\pi D(1/2)(1+K_0)\sigma_c']$). The value of μ_{dir} ranges from 0.49 to 0.78, aligning with the findings of previous shear studies on dense sand-structure interfaces (Lings & Dietz, 2005; Farhadi &

Lashkari, 2017; Han *et al.*, 2018). μ_{ALA} is calculated from tan$f\varphi'$. The guidelines (ALA, 2001; PRCI, 2009) do not define "rough" and "smooth"; thus, a range is depicted in Figure 4.3. According to Table 2.4, the values of μ_{ALA} for smooth and rough steel pipe are tan0.7φ' (= 0.53) and tan0.8φ' (= 0.62), respectively. Finally, μ_{phy} is the back-calculated value based on pullout

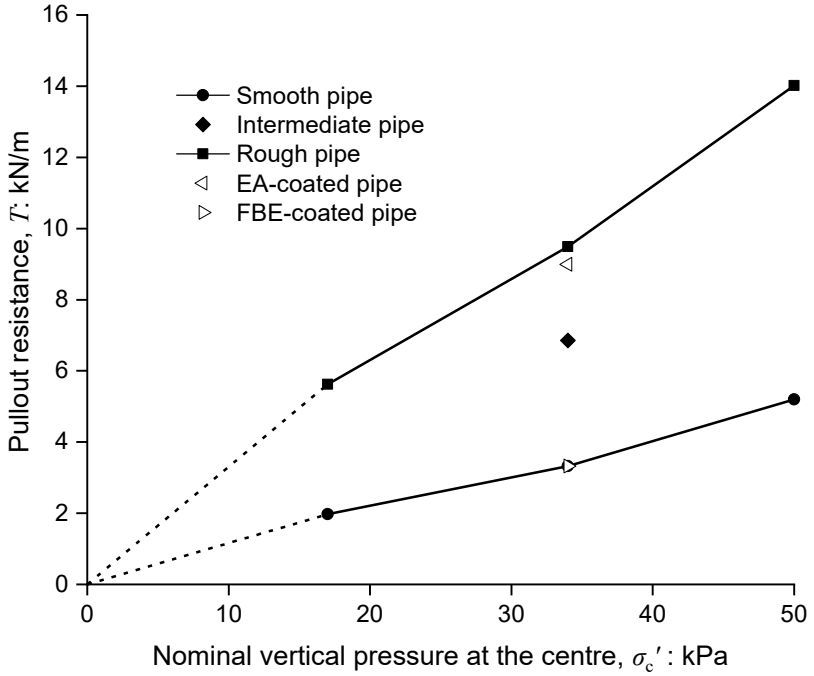

Figure 4.2 Nominal vertical pressure at the centre against the pullout resistance

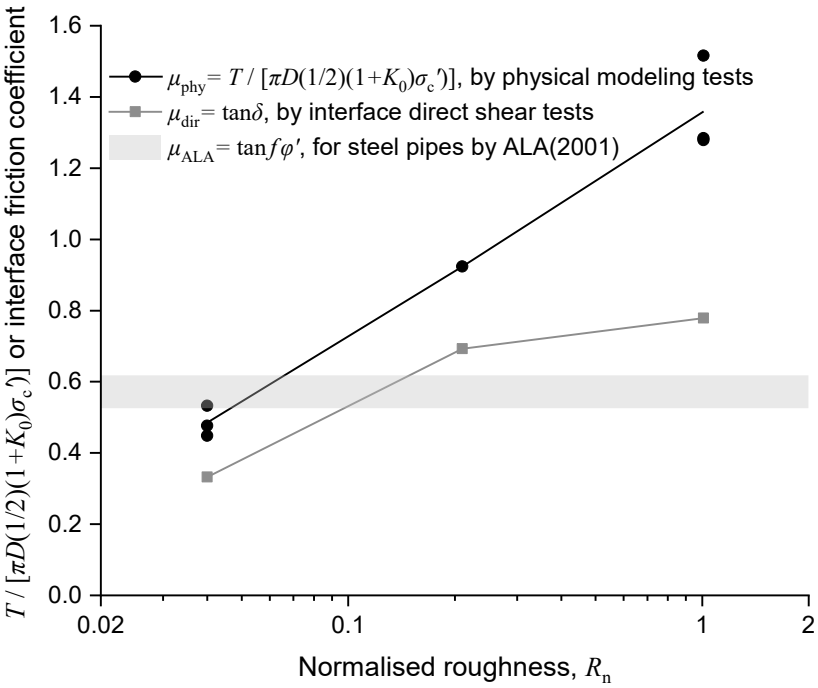

Figure 4.3 Normalised roughness effect on μ_{phy} and interface friction coefficient

resistances from physical modelling and Equation (2-2), representing the ratio of the pullout resistance to the assumed soil-pipe contact force per unit length. For the sake of simplicity in expression, it is denoted as μ_{phy}, although it differs from the concept of the interface friction coefficient, given changes in soil-pipe interface contact pressure during the pullout process. The value of μ_{phy} ranges from 0.45 to 1.52 and increases with the normalised roughness, showing an approximate linear relationship with the logarithmic value of roughness. If the average interface contact pressure is constant (CNL conditions) during pullout, μ_{phy} should be equal to μ_{dir}. However, μ_{dir} consistently remains lower than μ_{phy} in Figure 4.3. It implies that the average interface contact pressure on the pipe surface increased during the pullout process. The pipe pullout behaviour aligns more closely with the CNS condition rather than the CNL condition due to the constrained dilation behaviour (DeJong & Westgate, 2009; Pra-ai & Boulon, 2016; Ng *et al.*, 2020; Zhou *et al.*, 2020): the presence of sands far away from the interface constrains the dilation trend at the interface, leading to an increase in interface contact pressures during shearing. The dilatancy of the soil-pipe interface is positively correlated with the interface roughness (Lings & Dietz, 2005; Zhang *et al.*, 2011; Farhadi & Lashkari, 2017). Therefore, although μ_{dir} also increases as the roughness increases, its growth rate with roughness increase is not as steep as that of μ_{phy} and their difference, μ_{phy}-μ_{dir}, widens with increasing roughness.

The values of μ_{ALA} only encompass a small range of the measured values of μ_{phy}. The guidelines slightly overestimate smooth pipes' pullout resistance and significantly underestimate that of rough pipes. Both underestimation and overestimation can pose safety risks to the pipeline system. Underestimation implies a lower design pipeline strength. When there is any relative axial displacement between the pipe and the soil, the stress experienced by the pipe may exceed the pipeline strength, potentially causing damage to the pipe. On the other hand, overestimating the pullout resistance results in higher expectations for the soil's ability to limit deformation in the pipeline system. This can potentially lead to issues like upheaval

buckling due to thermal expansion, bending due to nearby tunnel construction (Marshall *et al.*, 2010; Wang *et al.*, 2011), or excessive loads concentrated on weak points, such as valve stations or cracks in the piping system, as discussed by PRCI (2009). Moreover, the wide range of μ_{phy} underscores the importance of quantifying roughness in pipeline design rather than relying on the qualitative definition provided by guidelines (ALA, 2001; PRCI, 2009).

4.3.2 Roughness effects on interface contact pressures distribution and evolution

Figure 4.4 and Figure 4.5 illustrate the distribution and evolution of interface contact pressures for smooth and rough pipes subjected to a nominal vertical pressure of 34 kPa at the centre. The difference in the interface contact pressures measured by TPS sensors is generally within ±10% of the average value at the corresponding positions on the three cross-sections. The interface contact pressure difference between the left and right springlines is kept under 2 kPa, indicating good symmetry. Therefore, the average values at the crown, shoulders, springlines, haunches, and invert are directly displayed. The interface contact pressure assumed by the guidelines is σ_c' (34 kPa) at the crown and invert, $K_0\sigma_c'$ (12.3 kPa, K_0 takes as 1- sin φ') at the springlines, $(1+K_0)\sigma_c'/2$ (23.2 kPa) at the shoulders and haunches, respectively.

Before the pullout, the roughness did not affect the initial interface contact pressure distribution. It is distributed with the shape of a “Norman Shield”, as shown in Figure 4.4 and Figure 4.5. This shape is consistent with the testing results of Wijewickreme *et al.* (2009) and Sheil *et al.* (2018). The interface contact pressures at the invert and shoulders are always larger than the assumed values, while those at the crown, springlines, and haunches are normally less than the expected value. However, the differences between measured values and expected values are typically not more than 25% of the expected values. The mean values of initial average interface contact pressure with σ_c' of 17, 34, and 50 kPa are 12.6, 22.5, and 37.5 kPa, respectively. These average values closely align with the assumed values by $(1+K_0)\sigma_c'/2$ (11.6, 23.2, and 34.1, respectively) because the increase and decrease in interface contact pressure at

different locations offset each other. Calculating the initial interface average contact pressure using $(1+K_0)\sigma_c'/2$ is acceptable.

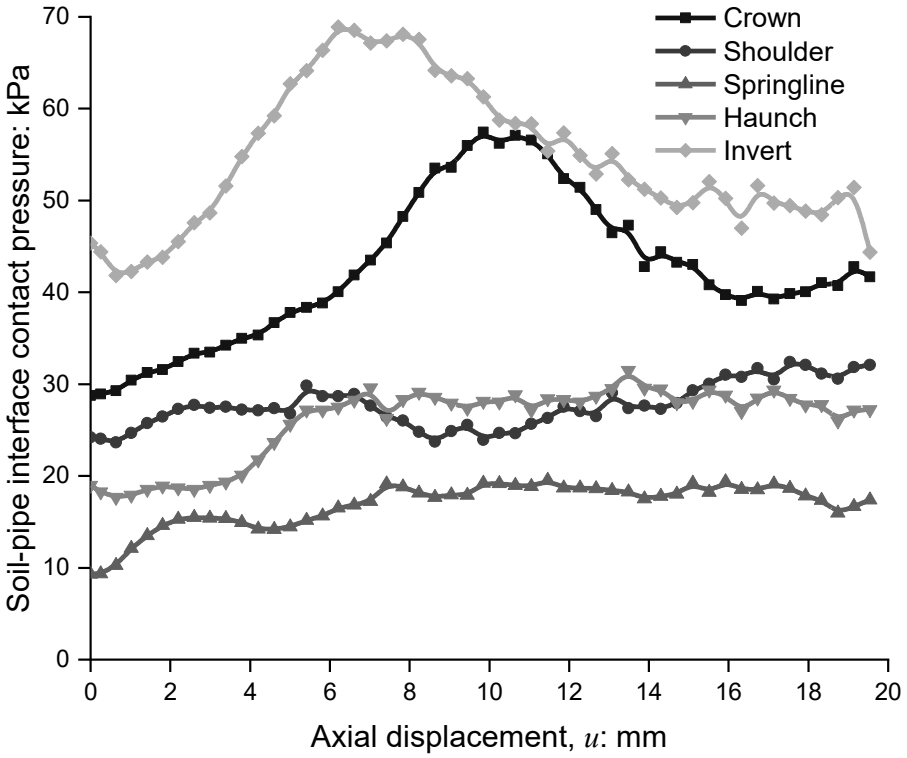

(a)

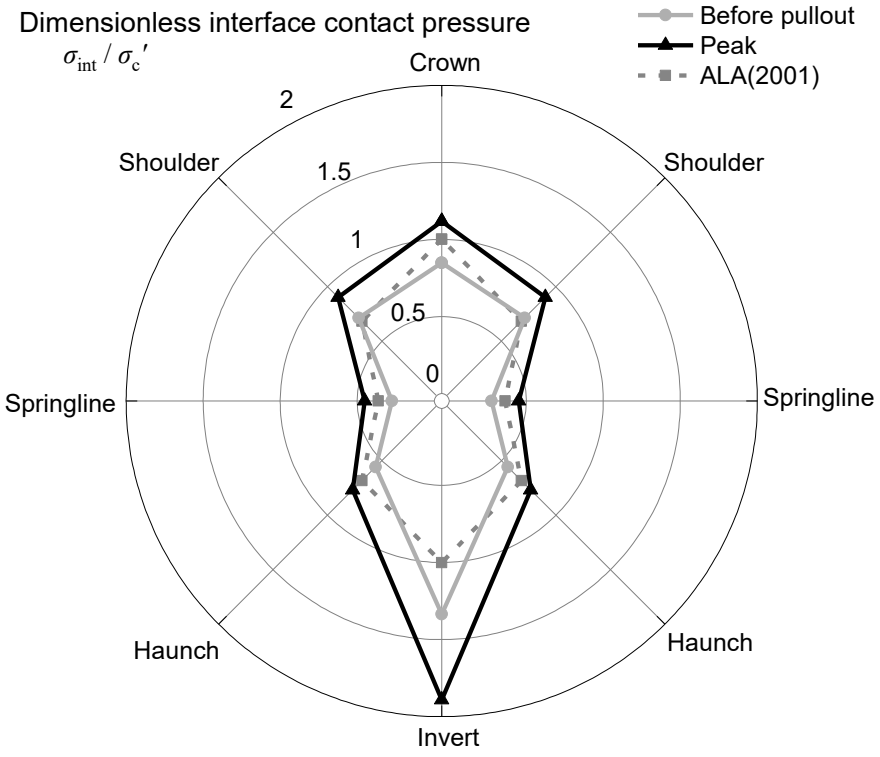

(b)

Figure 4.4 Interface contact pressure development and distribution of Rough-34

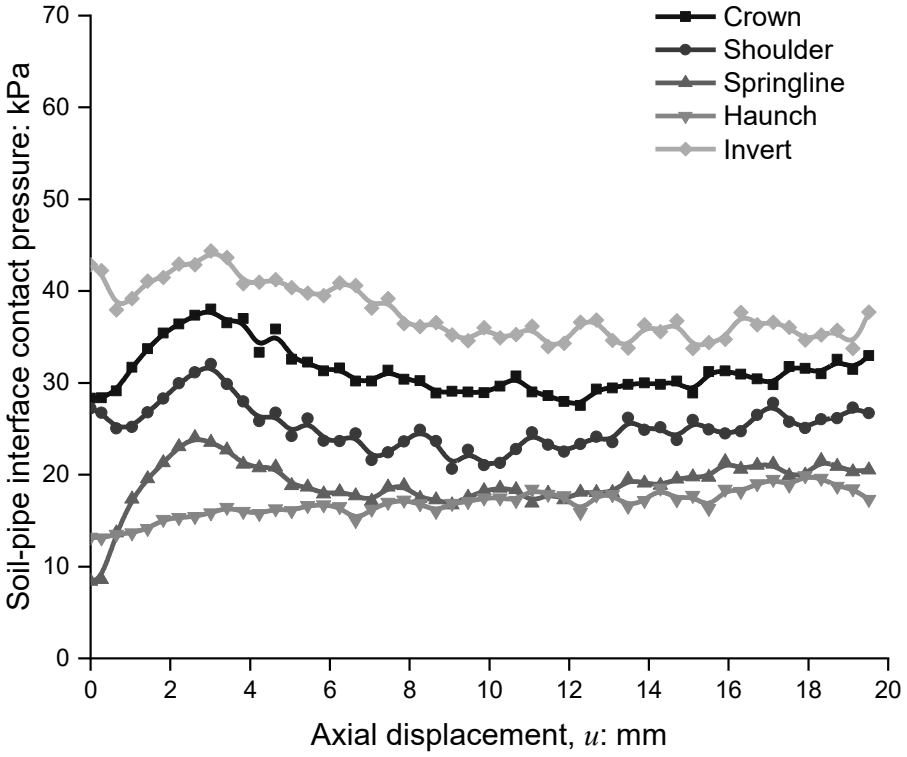

(a)

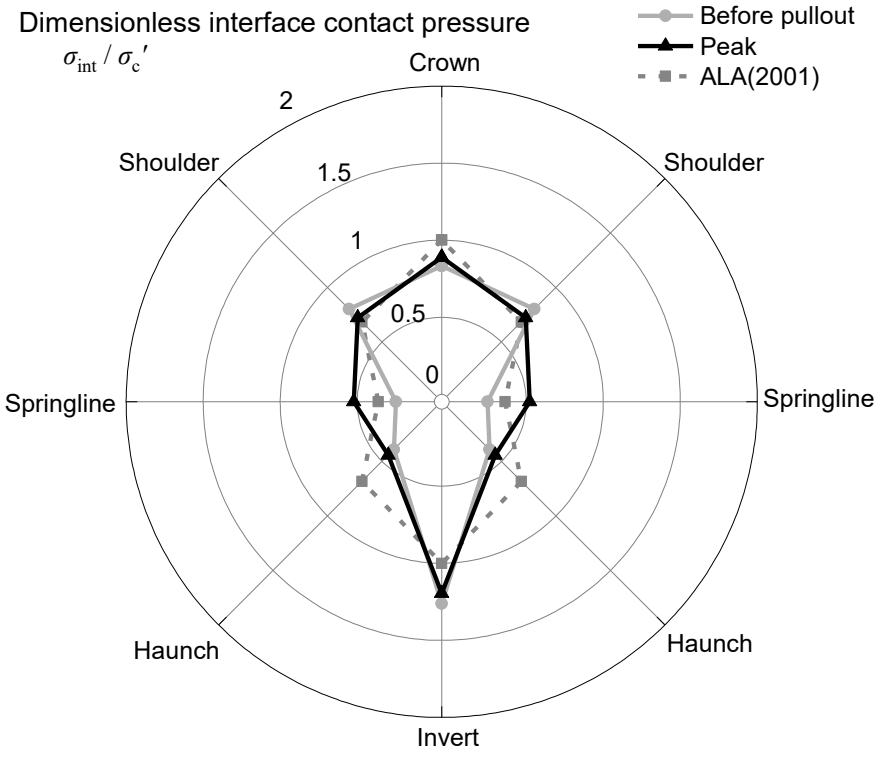

(b)

Figure 4.5 Interface contact pressure development and distribution of Smooth-34

During the pullout process, the interface contact pressures on different pipes exhibit an overall increasing trend, with the magnitude of the increase being positively correlated with the

roughness. This finding supports the explanation provided earlier regarding why μ_{phy} consistently exceeds μ_{dir} and why μ_{phy}-μ_{dir} is influenced by the surface roughness and hardness.

Different evolution processes of interface contact pressures reflect on pipes with different roughness. For the rough pipe (Figure 4.4), the interface contact pressure increase is persistent and notable. This increase predominantly occurs at the crown and the invert, where the pressures can reach around 55 and 70 kPa, respectively. The increase at the springlines (around 8 kPa) is insignificant. Moving to the smooth pipe (Figure 4.5), most of the interface contact pressures experience an initial increase before reaching a displacement of 3 mm, a subsequent decrease after the peak, and finally, a slight increase. This fluctuation trend is similar to the results of Wijewickreme *et al.* (2009).

4.3.3 Effects of soil arching and constrained dilatancy on pipe pullout mechanism

The distribution and evolution of soil-pipe interface contact pressure in Figure 4.4 and Figure 4.5 are closely related to the negative soil arching effects (Sheil *et al.*, 2018; Meguid, 2019; Ye *et al.*, 2023), and they are explained using the schematic diagram in Figure 4.6. During the backfilling process, the soil above the pipe is expected to experience a smaller settlement than the soil at the pipe sides, owing to the stiffening effects of pipe. The relative movement results in internal friction in the soil, concentrating more pressure on the pipe, especially at the crown, shoulders and the invert. This pressure concentration also causes the pipe to settle. In this study, the measured pipe settlements during this process are 0.1~0.5 mm, increasing pressure at the invert but reducing the pressure at the crown towards σ_c'. In addition, the concentration of overburden pressure on the pipe reduces the vertical pressure on the sides, thus lowering the interface contact pressure on the springlines (lateral earth pressure).

During the pullout process, the evolution of soil-pipe contract pressure is likely affected by two different mechanisms. Firstly, shearing at the soil-pipe interface disturbs the original stress equilibrium, weakening the negative soil arching effects developed during the backfilling

process and tending to reduce the interface contact pressure. Secondly, the constrained dilation at the soil-pipe interface tends to increase the interface contact pressure and could cause additional negative soil arching due to further relative vertical displacement between the soils at pipe sides and above the pipe, resulting in a more significant increase of interface contact pressures at the crown, shoulders, and invert. The overall change in interface contact pressure depends on the relative importance of these mechanisms. For the smooth pipe, the interface contact pressure at most points increases slightly due to the second mechanism, while interface contact pressure at the springlines increases more significantly due to the first mechanism, as shown in Figure 4.5. As for the rough pipe, the second mechanism likely plays a dominant role (Martinez & Frost, 2017). The average interface contact pressure increases sharply due to its significantly constrained interface dilation behaviour. The additional negative soil arching makes this increase concentrate on the crown and invert, and the vertical component of the interface contact pressures of shoulders and haunches. This additional negative soil arching also weakens the overburden vertical pressure on the soil of the pipe sides, reducing the corresponding lateral earth pressure (interface contact pressure at the springlines). It offsets part of the interface contact pressure increase caused by constrained dilation, resulting in limited pressure change at the springlines (as shown in Figure 4.4).

The evolution of earth pressure in Figure 4.7 further supports the above explanation. Before pullout, the earth pressures above and below the pipe are consistently greater than the earth pressure on the pipe sides at the same level due to the pressure concentration on the pipe. During the pullout process, the earth pressures around the smooth pipe remain unchanged or increase slightly, indicating that the impact of dilation behaviour is limited. In contrast, the earth pressures above and below the rough pipe experience significant growth, while the vertical pressure on the pipe sides slightly decreases. This is consistent with the evolution of interface contact pressures shown in Figure 4.4.

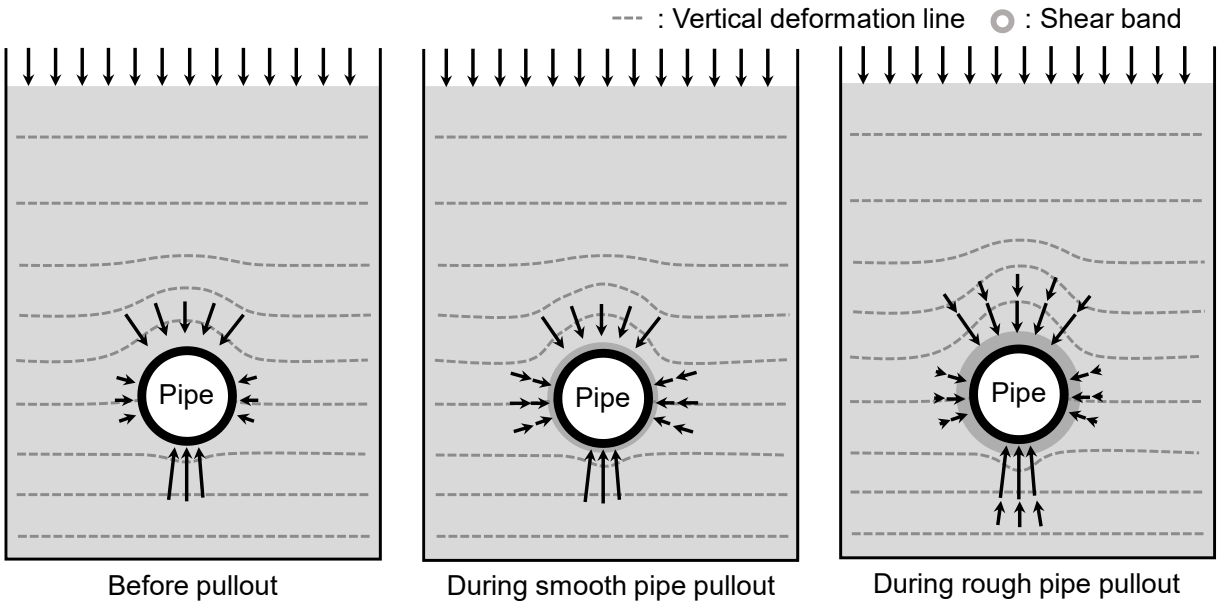

Figure 4.6 Schematic diagram of negative soil arching effect on pipes during monotonic loading

4.3.4 Roughness effects on stress path

Figure 4.8 illustrates the stress paths at the soil-pipe interfaces in physical modelling. The failure envelopes of three interfaces are determined through CNL interface direct shear tests and included as references. The shape of the stress path remains unaffected by the overburden pressure but is influenced by the roughness. For the smooth pipe, the stress path generally includes four stages. In the first stage, the stress path rises vertically, meaning the friction angle mobilisation is essentially elastic during this process. Then, the path turns to the second stage by moving towards the top right direction. It illustrates an increase in average interface contact pressure caused by constrained dilatancy, as explained above. Subsequently, the stress path turns to the upper left in the third stage due to the average interface contact pressure decrease caused by the disturbance of negative soil arching. During the ultimate stage, the path moves slightly to the bottom right after touching the peak failure envelope. It indicates a slow decrease in the mobilised friction angle and slight constrained dilation behaviour.

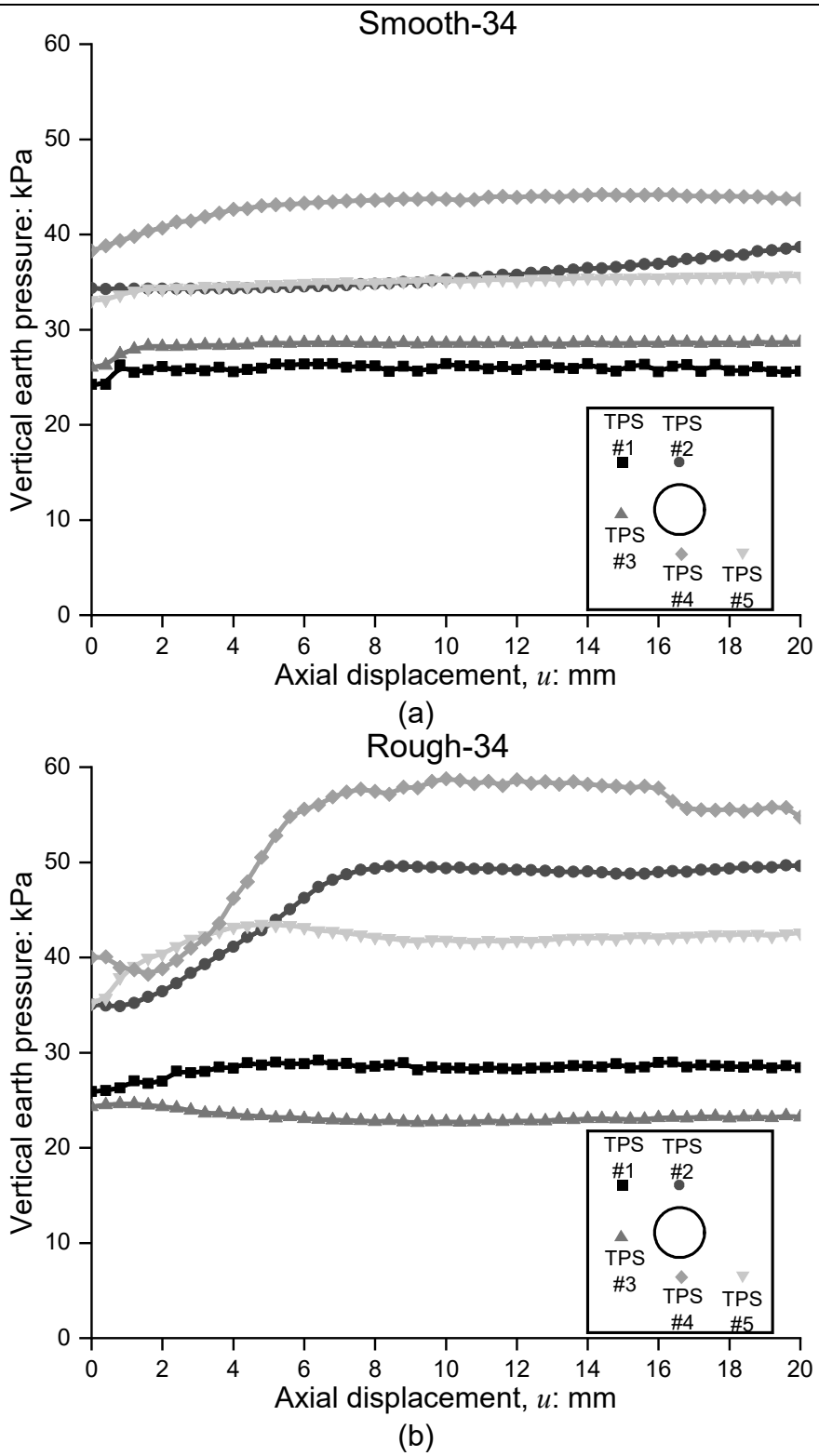

Figure 4.7 Vertical earth pressure development: (a) Smooth-34; (b) Rough-34

As for the stress paths of rough and intermediate pipes, they generally include three stages resembling the typical stress path observed in CNS tests on the rough interface (Ooi & Carter, 1987; Pra-ai & Boulon, 2016). The stress paths of rough and intermediate pipes during the first

and second stages are similar to those of smooth pipes, which rise vertically and then turn to the top right. The major difference is that, before touching the peak failure envelope, the stress

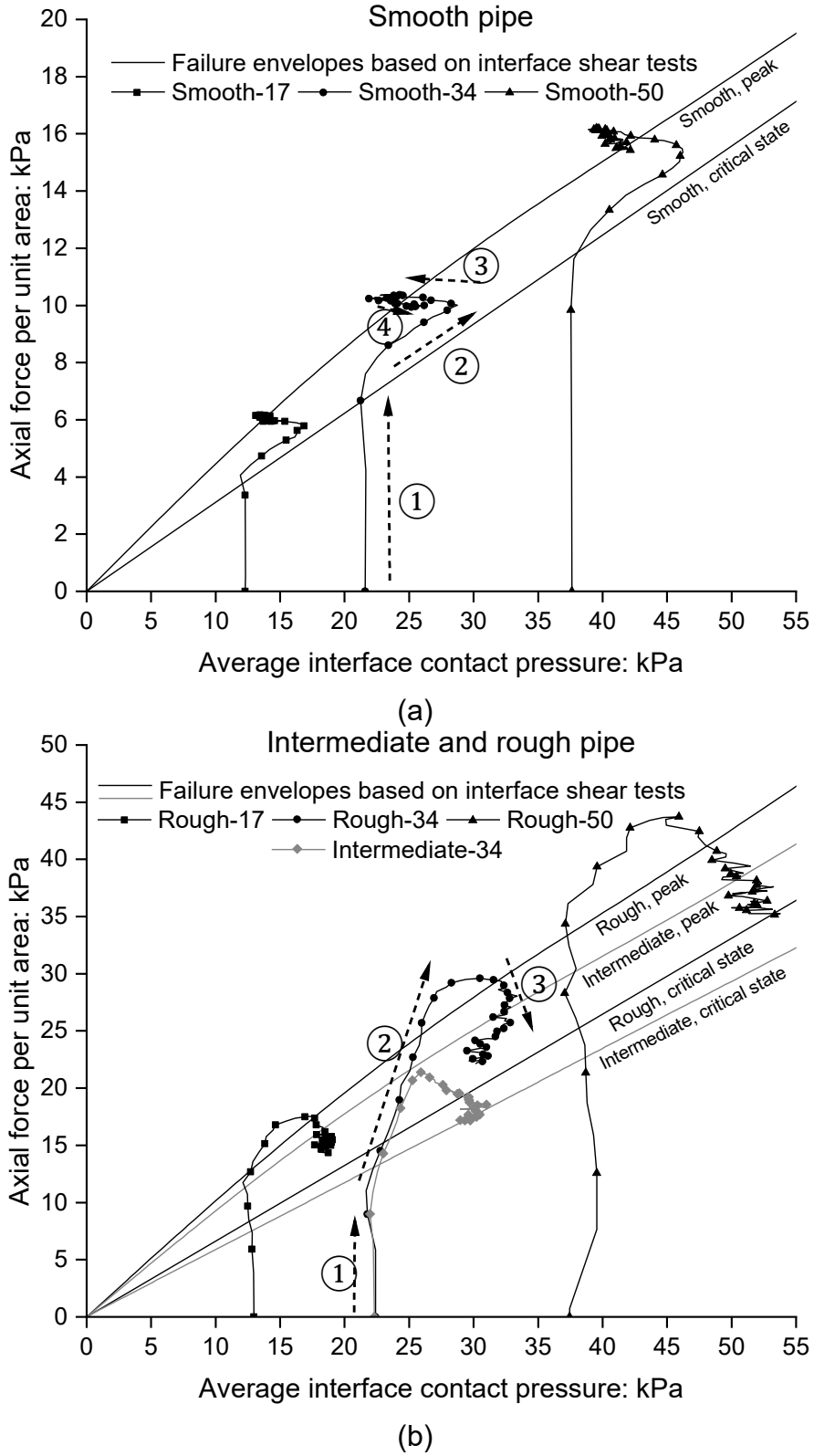

Figure 4.8 Stress path based on average interface contact pressure measured by TPS: (a) smooth pipe; (b) intermediate and rough pipes

path keeps the trend moving towards the top left rather than undergoing the smooth pipes' third stage due to its significant constrained dilation. Subsequently, the stress paths turn to the bottom right and tend to touch the critical state envelope in the third stage of rough and intermediate pipes. During this process, the degradation of the mobilised friction angle is much more evident than the further increase in interface contact pressure, corresponding to the obvious softening behaviour in Figure 4.1.

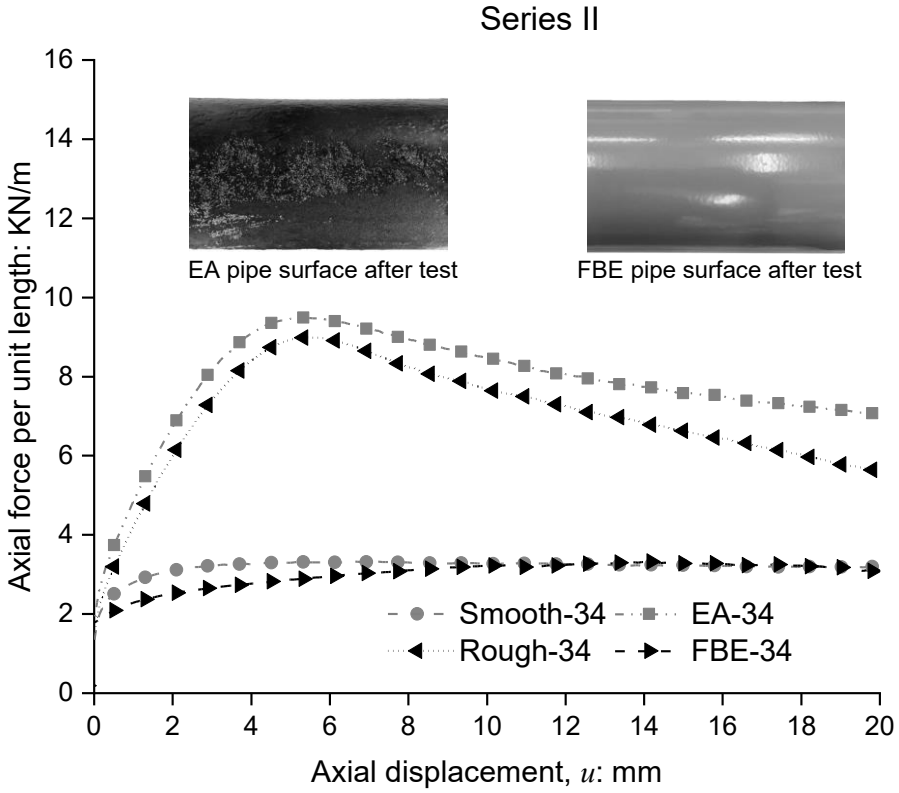

Figure 4.9 Hardness effect on axial force-displacement relationship during monotonic loading

4.3.5 Coating hardness effects on pullout behaviour

Moving on to the coating hardness effects in Series II, the pullout force-displacement curves of the EA-coated and FBE-coated pipes in Figure 4.9 resemble those of rough and smooth pipes, respectively, although the values of normalised roughness are both small for these two coated surfaces. Additionally, the pullout resistance of the EA-coated and FBE-coated pipes is close to that of rough and smooth pipes, respectively (see Figure 4.10). These observations

are mainly related to particle embedment. After tests, numerous particles were found embedded in the surface of the EA-coated pipe, while no embedment or scratches were observed on the FBE-coated pipe (see Figure 4.9). The pipes coated with softer materials may be considered a specialised form of rough pipe due to the increase in equivalent roughness caused by embedment. Conversely, the pipes coated with harder materials do not experience this increase in equivalent roughness.

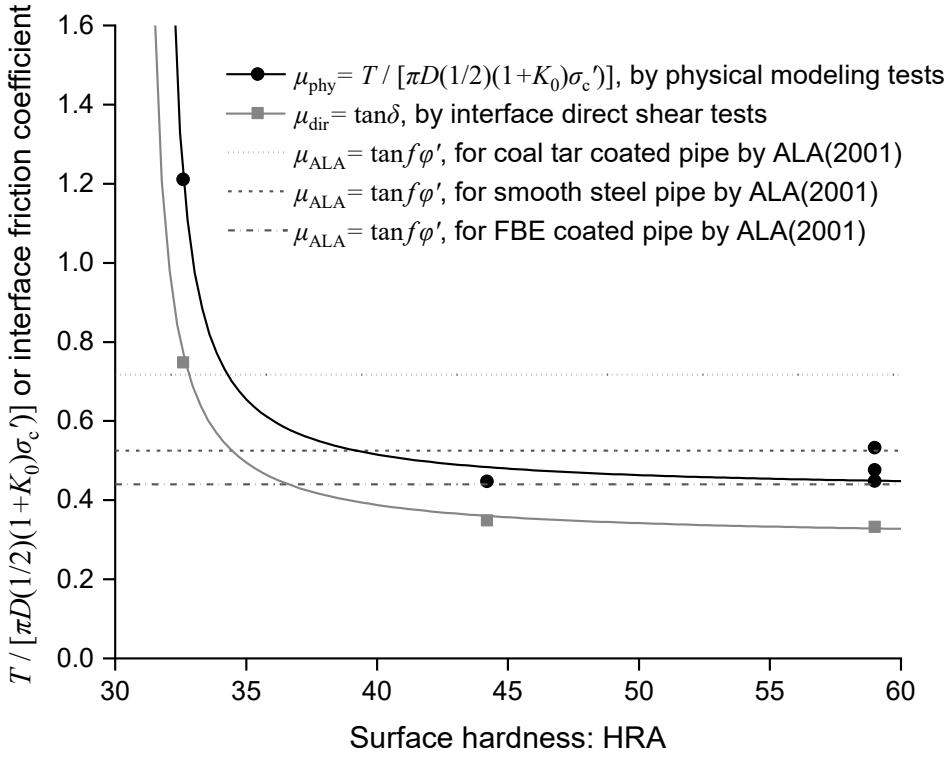

Figure 4.10 Surface hardness effect on μ_{phy} and interface friction coefficient

The above results are further supported by Figure 4.10. On the one hand, μ_{phy} for EA-coated, FBE-coated, and smooth steel pipes are 1.21, 0.45, and 0.45-0.54, respectively, larger than the corresponding μ_{dir} values of 0.75, 0.35, and 0.33. The μ_{phy}-μ_{dir} of EA-coated and FBE-coated pipes also closely resemble those of rough and smooth pipes, respectively. On the other hand, similar to rough pipes, the pullout resistance of pipes with soft material coatings (such as coal tar and EA) is notably underestimated by the guidelines, as shown in Figure 4.10. This underestimation can be attributed to the dilation behaviour. Additionally, μ_{phy} for the EA-coated pipe is slightly smaller than that of the rough steel pipe. The reason might be that the stiffness

of the coating layer is much smaller than steel. A volume change in the coating layer would happen, though not large, due to the limited coating thickness, reducing the interface contact pressure increase caused by constrained dilation. Hence, the pullout resistance of the EA-coated pipe is slightly lower. However, μ_{phy} of FBE-coated pipe aligns well with the guidelines' predictions because there is limited dilatancy at the hard and smooth interface, making its axial pullout behaviour resemble the assumption of the guidelines.

There appears to be a critical hardness of around 35 HRA. The pullout resistance of pipes with hardness less than this critical value is susceptible to surface hardness, whereas, for pipes with surface hardness greater than this value, the effect of hardness on ASPI is minimal. This concept of critical hardness has also been used by Abuel-Naga *et al.* (2018). It is highlighted that the above value of critical hardness cannot be generalised because it is also dependent on other important factors, such as normal pressure, particle angularity, size, and grain size distribution based on the experimental results on soil-geomembranes by Frost & Han (1999) and Dove & Frost (1999). The overall morphology of this sand, measured by Liang *et al.* (2021), is given in Table 3.4 for information.

4.4 Development of a new method for calculating pipe pullout resistance

Figure 4.11 (a) compares the measured values of pullout resistance with the ALA predictions(Equation (2-2)) using the experimental results in Wijewickreme *et al.* (2009), Sheil *et al.* (2018), and this study. The interface friction angle, δ, uses the value measured by direct shear testing. Equation (2-2) cannot predict the pullout resistance well, especially for rough pipes buried in dense sands. As discussed earlier, this equation neglects the interface contact pressure increase caused by constrained dilation. Additionally, it does not account for the effects of pipe self-weight, as Sheil *et al.* (2018) highlighted. A new equation is proposed to address these limitations as

$$T = \left[\pi D(\gamma' H_c \frac{1+K_0}{2} + \Delta\sigma_D') + \Delta W \right] \tan\left(f_R \varphi'\right) \tag{4-1}$$

where three new terms are introduced: $\Delta\sigma_D'$ is the average increase in interface contact pressure caused by constrained dilation; ΔW is the normal force increase per unit length caused by the pipe weight; and f_R is the roughness-dependent soil-pipe interface friction factor. These three terms are determined below:

Firstly, $\Delta\sigma_D'$ can be determined by the linear elastic expanding cylinder theory, as given by Houlsby & Italiana (1991):

$$\Delta\sigma_D' = 4G\frac{u_r}{D} \tag{4-2}$$

where u_r is the radial expanding displacement of the shear band due to interface dilation and G is the soil shear modulus. This model was further developed to predict the pullout resistance of soil nails and pipes in subsequent studies (Luo *et al.*, 2000; Yin *et al.*, 2012; Wijewickreme & Weerasekara, 2015). u_r can be determined as follows:

$$u_r = \int_0^{u_c} \frac{du_r}{du} du = \int_0^{u_c} \frac{du_r / S}{du / S} du = \int_0^{u_c} \frac{d\varepsilon_v}{d\gamma} du = \int_0^{u_c} \tan\psi du \tag{4-3}$$

where u_c is the critical axial displacement where the mobilised dilation angle reaches its peak value; S is the thickness of the shear band; $d\varepsilon_v$ is the volumetric strain increment, equaling du_r/S for the soil in the shear band; $d\gamma$ is the shear strain increment, equaling du/S; tan ψ (= $d\varepsilon_v/d\gamma$) is the dilatancy. Luo *et al.* (2000) and Yin *et al.* (2012) assumed that tanψ linearly increases with the axial displacement until reaching the maximum dilation angle (ψ_{max}). Under this assumption, u_r can be further calculated by

$$u_r = \int_0^{u_c} \tan\psi du = \int_0^{u_c} \frac{u}{u_c} \tan\psi_{max} du = \frac{1}{2} u_c \tan\psi_{max} \tag{4-4}$$

Assuming that the mobilised dilation angle and the axial force reach their peak values at the same critical axial displacement u_c, Equations (4-2) and (4-4) suggest that

$$\Delta\sigma_{\mathrm{D}}' = 2G\frac{u_{\mathrm{c}}}{D}\tan\psi_{\max} \tag{4-5}$$

where u_{c} is affected by surface roughness and coating hardness. The method of Audibert & Nyman (1977) is employed to determine u_{c} from the results in Figure 4.1 and Figure 4.9. This method consists of a horizontal line through the maximum axial force and a secant line passing through the origin and the point of 70% of the maximum axial force. The intersection of these two lines determines u_{c}. Table 4.2 summarises the values of u_{c} for different pipes in this study and Wijewickreme *et al.* (2009). u_{c} for non-coated steel pipes ranges from 0.77 to 2.85 mm, showing a positive correlation with the normalised roughness. u_{c} for FBE-coated and EA-coated pipes are 1.85 and 3.76 mm, relatively larger than those of the non-coated steel pipes. In contrast, $\psi_{\max}$ in Equation (4-5) can be determined using the method of Bolton (1986), simplified as

$$\psi_{\max} = A_{\psi} / a_{\psi}\left[I_{\mathrm{D}}(Q - \ln\sigma_{\mathrm{f}}') - R\right] \tag{4-6}$$

where I_{D} is relative density; σ_{f}' is the effective stress at failure; a_{ψ}, A_{ψ}, Q and R are empirical coefficients. For dense sand at low pressure ($I_{\mathrm{D}}(Q\text{-}\ln\sigma_{\mathrm{f}}')\text{-}R>4$, common in soil-pipe interaction), Chakraborty & Salgado (2010) obtained values of these four coefficients as 0.62, 3.8, 7.1 + 0.75ln σ_i', and 1, respectively. σ_i' is the initial effective stress, taken as $\gamma' H_{\mathrm{c}}(1+K_0)/2$ in this study. It should be noted that σ_{f}' is the effective normal stress at the failure, but it is hard to determine the effective stress at failure σ_{f}' in Equation (4-6) for engineers. Hence, σ_{f}' is also approximately taken as the average initial effective stress, $\gamma' H_{\mathrm{c}}(1+K_0)/2$, in this study. The potential error of this approximation on $\psi_{\max}$ is as small as not more than 4% based on the value of Q and R.

Moreover, G can be determined by the model of Oztoprak & Bolton (2013) as

$$G = \frac{A(\gamma)\cdot p_{\mathrm{a}}}{(1+e)^3}\cdot\left(\frac{\sigma_{\mathrm{i}}'}{p_{\mathrm{a}}}\right)^{m(\gamma)} \tag{4-7}$$

where e is the void ratio; p_{a} is a reference pressure of 100 kPa. $A(\gamma)$ and $m(\gamma)$ are empirical parameters dependent on the shear strain γ (= u/S). Based on the values of u_{c} in Table 4.2 and the empirical data in interface shear band thickness (DeJong & Westgate, 2009), the critical

interface shear strains at which the axial force reaches its peak values are determined to be no less than 10%. It is practical to adopt the empirical values of $A(\gamma) = 126$ and $m(\gamma) = 1$ for γ =10%, as suggested by Oztoprak & Bolton (2013).

Secondly, ΔW can be calculated by the product of the pipe's volume per unit length, V and the unit weight difference ($\Delta\gamma$) between the pipe and backfilled soil as

$$\Delta W = V\Delta\gamma = \frac{\pi D^2}{4}\left(\bar{\gamma}_{\text{pipe}} - \gamma_{\text{b}}\right) \tag{4-8}$$

In this equation, $\bar{\gamma}_{\text{pipe}}$ is the apparent unit weight of the pipe. It is the ratio between the actual pipe weight (the total weight of pipe and fluid contained in the pipe under operating conditions) and the volume occupied by the pipe in the soil. γ_{b} is the bulk unit weight of the soil. While ΔW has a minimal impact on lightweight pipes (e.g., pipes used in Wijewickreme *et al.* (2009) and this study), it can increase the normal force by up to 50% for heavy pipes by Sheil *et al.* (2018).

Thirdly, f_{R} can be evaluated by the normalised roughness. As mentioned above, the critical normalised roughness among smooth, intermediate, and rough interfaces is 0.02 and 0.5, respectively (the framework of Paikowsky *et al.* (1995)). Experimental results by Paikowsky *et al.* (1995) and Lings & Dietz (2005) indicate that the interface friction angles increase linearly with the natural logarithm of the normalised roughness for intermediate interfaces and remain constant for smooth and rough interfaces. Therefore, f_{R} can be calculated as follows:

$$f_{\text{R}} = \begin{cases} \alpha_{\text{R}} + \beta_{\text{R}} \ln 0.02 & R_{\text{n}} \le 0.02 \\ \alpha_{\text{R}} + \beta_{\text{R}} \ln R_{\text{n}} & 0.02 < R_{\text{n}} < 0.5 \\ \alpha_{\text{R}} + \beta_{\text{R}} \ln 0.5 & R_{\text{n}} \ge 0.5 \end{cases} \tag{4-9}$$

where α_{R} and β_{R} are the empirical coefficients, whose values are dependent on the specific soil and interface in this study and affected by many other factors, such as void ratio, particle angularity, and grain size distribution. For the testing material in this study, α_{R} and β_{R} are taken as 1.13 and 0.20, respectively.

Substituting Equations (4-5) and (4-8) into (4-1), the new equation can be expressed as

$$T = \pi D(\gamma' H \frac{1+K_0}{2} + 2G\frac{u_c}{D}\tan\psi_{max} + \frac{D}{4}\Delta\gamma)\tan\left(f_R\varphi'\right) \quad (4\text{-}10)$$

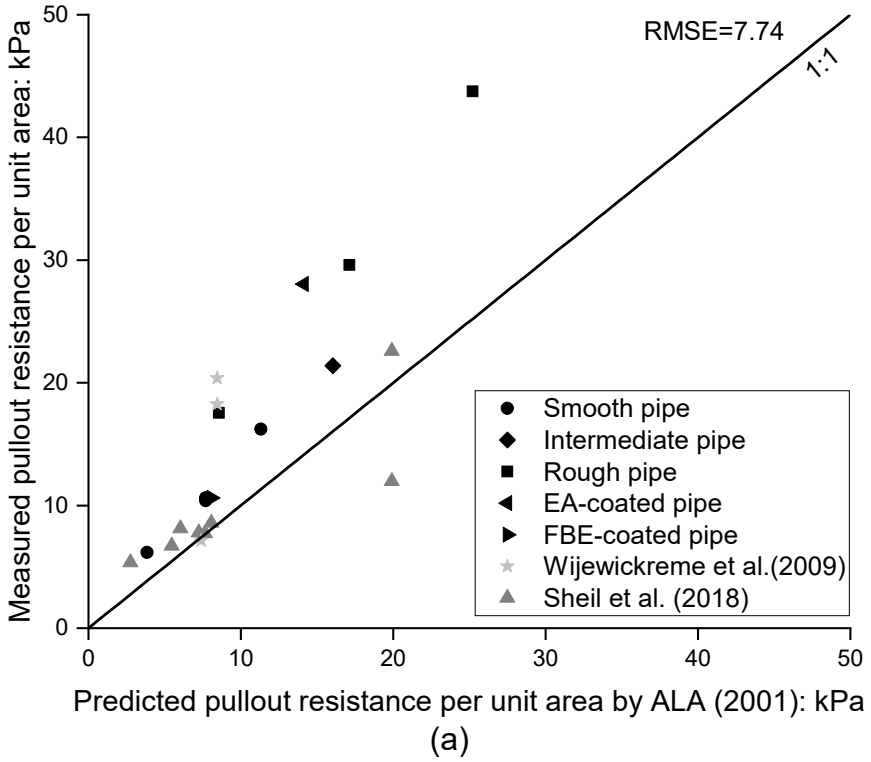

(a)

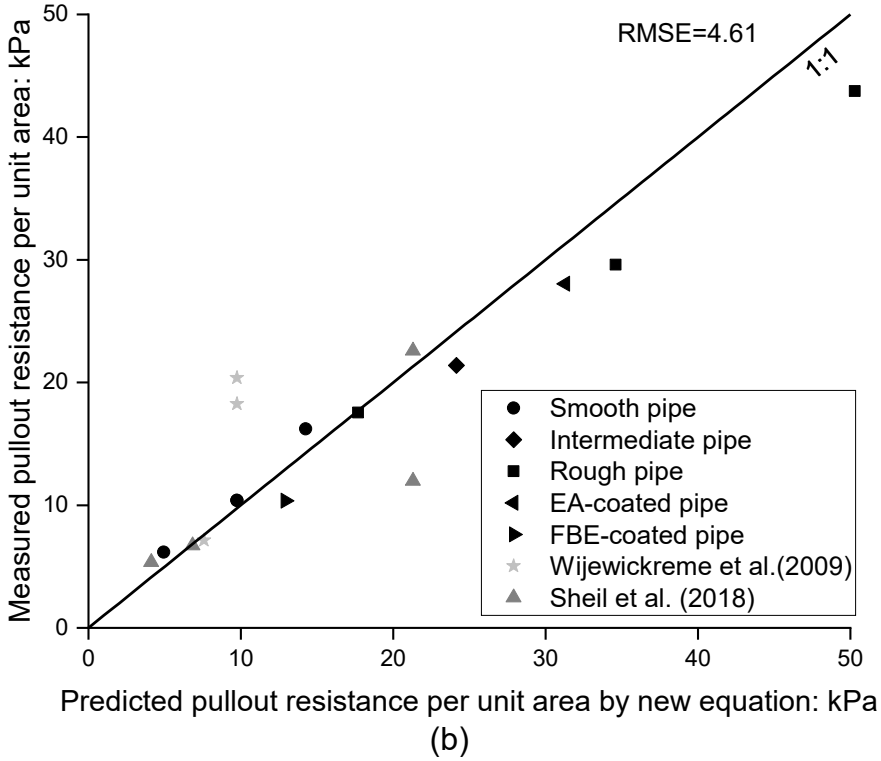

(b)

Figure 4.11 Axial pullout resistance at dry conditions predicted by: (a) ALA (2001); (b) new equation

Table 4.2 summarises the parameters for the new equation, incorporating data from Wijewickreme *et al.* (2009), Sheil *et al.* (2018) and the present study. Figure 4.11 (b) displays the newly predicted values based on these parameters. The Root Mean Square Error (RMSE) of the new model stands at 4.61, markedly lower than the 7.74 observed in the ALA predictions.

4.5 Summary

Nine physical modelling tests were conducted to investigate the effects of surface roughness and coating hardness on the ASPI behaviour subjected to monotonic loading. Based on the experiments, the following conclusions were drawn:

Surface roughness significantly affects the pipe pullout resistance. The pullout resistance of the rough pipe is 1.70-1.85 times higher than that of the smooth pipe under the same buried condition. This increment is much greater than the value specified in the current design guidelines (i.e., 0.17). Moreover, this increase stems from different mechanisms of roughness effects. The increase in interface friction coefficient accounts for 72-79%, while the remaining 21-28% is attributed to the interface contact pressure increase induced by the interrelated constrained dilation and negative soil arching. Soil arching greatly affects the interface contact pressure between soil and pipes during both backfilling and pullout processes. During the backfilling, the interface contact pressures are concentrated at the shoulders and invert of the pipe due to the initial negative soil arching. During the pullout process, an additional negative soil arching due to the soil-interface dilation and a disturbance due to the loading determine the interface contact pressure evolution behaviour. For the rough pipe, the former plays a dominant role. The thick shear band induces further relative displacement, leading to a noticeable increase in interface contact pressure at the pipe crown and invert (Wu, 2000). For the smooth pipe, the limited soil-interface dilation does not reinforce the negative soil arching. Instead, the pullout process disturbs the original equilibrium of the surrounding soil, releasing part of the internal

friction of the initial negative soil arching. Consequently, the increase in interface contact pressure is only observed at the springlines of the smooth pipe.

For the test materials in this study, a critical coating hardness of approximately 35 HRA was identified based on experimental results. When the hardness is below this critical value (e.g., EA-coated pipes in this study), the pipes behave similarly to rough pipes due to an equivalent roughness caused by particle embedment. When the coating hardness exceeds this critical value (e.g., FBE-coated and raw steel pipes in this study), the influence of hardness seems limited.

A new method for predicting monotonic pullout resistance was proposed. This method considers the increase in normal force due to constrained dilatant and pipe weight, and it provides a quantitative estimation of the interface friction angle based on surface roughness. The new equation demonstrated good model capabilities, as verified using test results from previous studies and this study.

Table 4.2 Parameters for the new equation of dry sands

Parameters	This study					Wijewickreme *et al.* (2009)		Sheil *et al.* (2018)
	Smooth	Intermediate	Rough	FBE	EA	AB-3, 4, 6	AB-5	H1-4
Pipe diameter, D: mm	102	102	102	102	102	457	457	350
Normalised roughness, R_n	0.04	0.21	1.01	0.01	0.01	0.84	0.84	0.11
Parameter, α_R	1.13	1.13	1.13	-	-	-	-	-
Parameter, β_R	0.2	0.2	0.2	-	-	-	-	-
Interface friction factor, f	Equation (4-9)	Equation (4-9)	Equation (4-9)	0.49	0.93	0.81	0.74	0.79
Unit weight difference, $\Delta\gamma$: kN/m^3	4.53	4.53	4.53	4.53	4.53	2.43	2.43	27.34
Nominal pressure at the pipe centre, σ_c': kPa	17-50	34	17-50	34	34	17.91	17.53	6.9-50
Internal friction angle, φ': °	39.6	39.6	39.6	39.6	39.6	44.5	44.5	37.9
Relative density, I_D: %	85	85	85	85	85	75	20	12
Void ratio, e	0.57	0.57	0.57	0.57	0.57	0.7	0.88	0.94
$A(\gamma)$	126	126	126	126	126	126	126	126
$m(\gamma)$	1	1	1	1	1	1	1	1
Critical displacement, u_c: mm	0.77	1.7	2.85	1.85	3.76	2.6	-	-

CHAPTER 5
PHYSICAL MODELLING ON AXIAL BEHAVIOUR OF BURIED PIPES SUBJECTED TO CYCLIC LOADING

5.1 Introduction

This chapter conducted twelve large-scale physical modelling tests to examine the cyclic and post-cyclic behaviours of ASPI using FJM sand. The primary objectives are (i) to investigate how surface roughness, burial pressure, and cyclic displacement amplitude influence axial resistance degradation over cycles, (ii) to examine the mechanisms underlying cyclic ASPI, and (iii) to explore the post-cyclic pullout behaviour.

5.2 Testing programme

Two series of pulling-pushing cyclic tests were performed, as detailed in Table 5.1 and Figure 5.1. Series I encompassed seven tests aimed at investigating the influence of surface roughness and overburden pressure on cyclic ASPI. Smooth and rough pipes were tested at σ_c' of 17, 34, and 50 kPa, equivalent to burial depths of around 1, 2, and 3 meters, respectively, meeting the minimum buried depth of 0.8 m in practice (Mohitpour *et al.*, 2007). The intermediate pipe underwent a test at a σ_c' of 34 kPa. Cyclic displacement amplitude (u_A) for this series was 20 mm, a common value where the axial force could basically reach its residual value in previous studies (Wijewickreme *et al.*, 2009; Sheil *et al.*, 2018). The number of cycles, N, for smooth, intermediate, and rough pipes was determined as 5, 10, and 10, respectively, where their maximum force per unit length during the N-th loading stabilised.

Series II examined the impact of cycle displacement amplitude on cyclic ASPI at a σ_c' of 34 kPa. A critical displacement of approximately 5 mm, where the axial force of rough pipes peaked during the first loading, was observed in tests of Series I. Consequently, u_A for Series II was set to 2.5, 5, and 10 mm to assess cyclic ASPI under conditions where u_A is less than, equal

to, and greater than the critical displacement, respectively. Post-cyclic behaviour was also explored in Series II. After 20 cycles, when the maximum force per unit length during the *N*-th loading at the given cyclic displacement stabilised, a post-cyclic pullout with an amplitude of 20 mm was applied (see Figure 5.1).

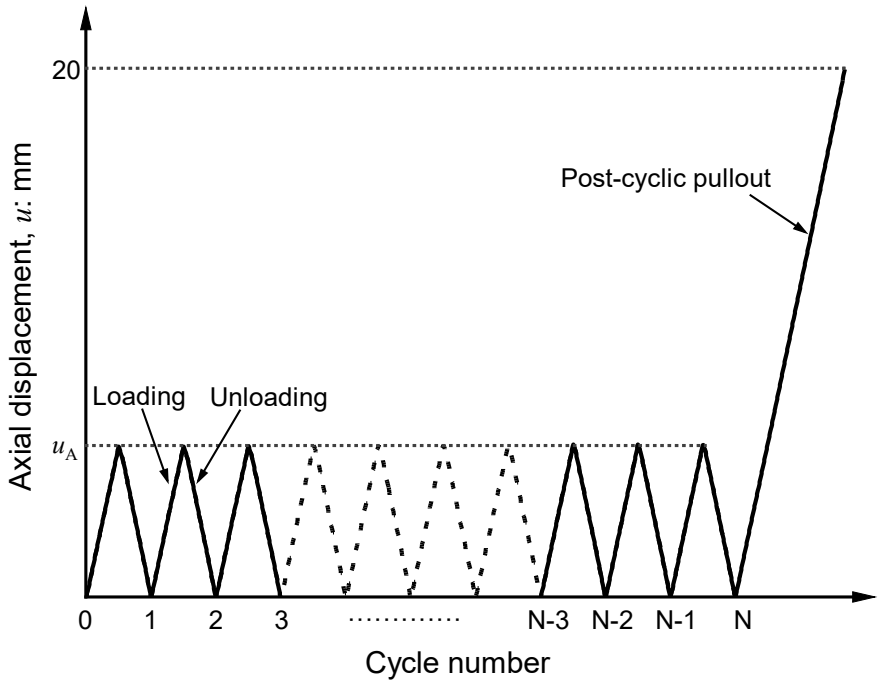

Figure 5.1 Schematic diagram of cyclic and post-cyclic paths

5.3 Experimental results and discussion

5.3.1 Effects of roughness and nominal overburden pressure on cyclic ASPI

Figure 5.2 shows the relationship between axial displacement and the axial force in Series I. The figure includes axial resistances predicted by Equation (2-2) using the measured interface peak friction angle (δ_{peak}) and the critical state friction angle (δ_{cr}) as δ for comparison. As CHAPTER 4 discussed, the first loading curve for the rough pipe exhibits pronounced displacement-softening behaviour, whereas the curve for the smooth pipe demonstrates minimal softening. The predictions using Equation (2-2) and δ_{peak} substantially underestimate axial resistance during the first loading (T_1) for both rough and smooth pipes, with discrepancies

ranging from 64 to 95% and 35 to 60%, respectively. This underestimation is primarily attributed to the ignorance of the constrained dilatancy at the soil-pipe interface.

Table 5.1 Testing program of cyclic and post-cyclic effects on ASPI

Test series	Reference	Pipe type	Nominal pressure on the centre, σ_c': kPa	Cyclic displacement amplitude, u_A: mm	Cycle number, N	Post-cyclic pullout
Series I Roughness and pressure effects on cyclic ASPI	S-17-A20	Smooth	17	20	5	No
	S-34-A20	Smooth	34	20	5	No
	S-50-A20	Smooth	50	20	5	No
	R-17-A20	Rough	17	20	10	No
	R-34-A20	Rough	34	20	10	No
	R-50-A20	Rough	50	20	10	No
	M-34-A20	Intermediate	34	20	10	No
Series II Amplitude effects on cyclic ASPI and post-cyclic pullout	S-34-A2.5	Smooth	34	2.5	20	Yes
	S-34-A5	Smooth	34	5	20	Yes
	R-34-A2.5	Rough	34	2.5	20	Yes
	R-34-A5	Rough	34	5	20	Yes
	R-34-A10	Rough	34	10	20	Yes

Upon the first unloading, both rough and smooth pipes exhibit displacement-hardening behaviour, with the curve's shape being influenced by the surface roughness. These curve shapes are consistent with typical cyclic interface shear behaviour (DeJong *et al.*, 2003; Mortara *et al.*, 2007). Both rough and smooth pipes experience a notable degradation in axial resistance compared to T_1, consistent with previous research on dense sand in soil-interface shearing tests and ASPI modelling (DeJong *et al.*, 2003; Mortara *et al.*, 2007; Pra-ai & Boulon, 2016; Rui *et al.*, 2020b). This degradation is mainly linked to the change of soil state (e.g., porosity and stress) around the pipe, as discussed later.

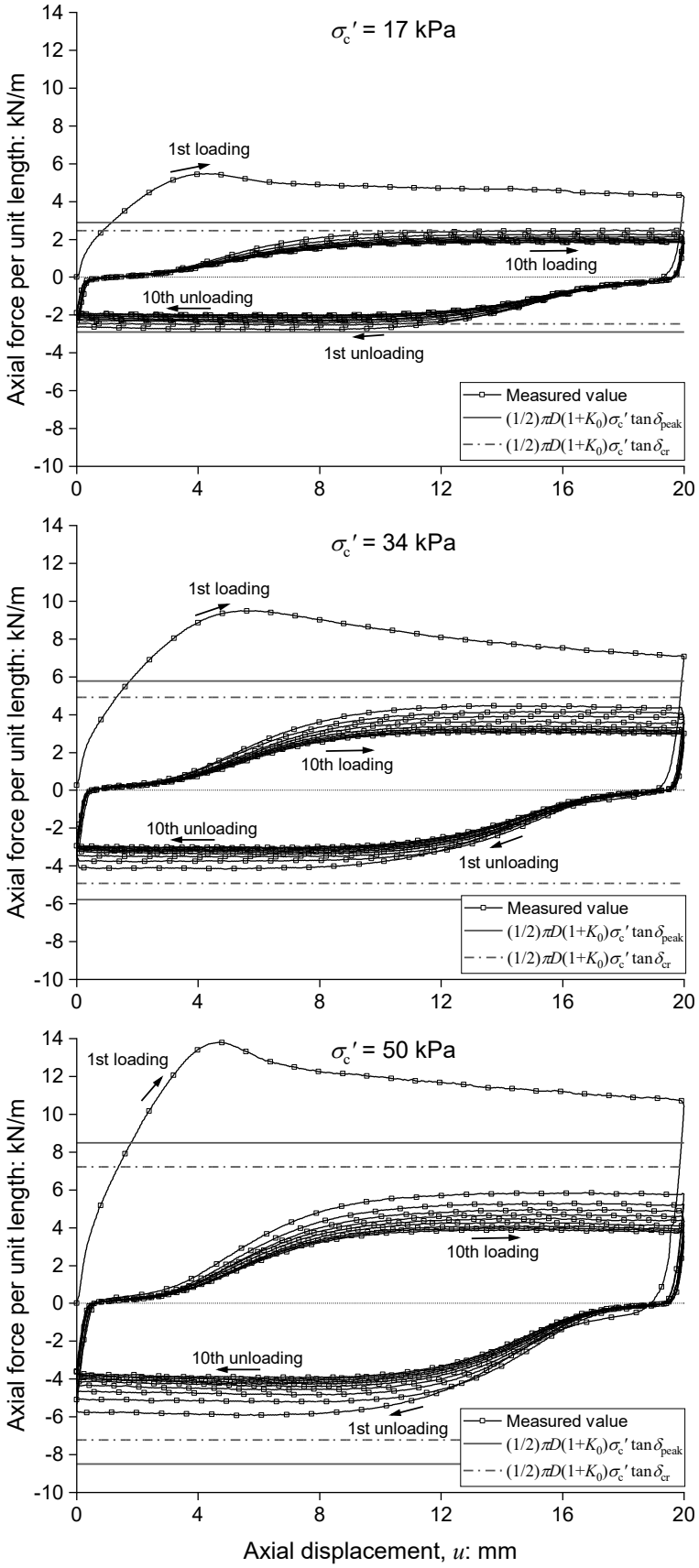
σc′ = 17 kPa
1st loading
10th loading
10th unloading
1st unloading
σc′ = 34 kPa
1st loading
10th loading
10th unloading
1st unloading
σc′ = 50 kPa
1st loading
10th loading
10th unloading
1st unloading
Measured value
(1/2)πD(1+K0)σc′ tanδpeak
(1/2)πD(1+K0)σc′ tanδcr
Axial force per unit length: kN/m
Axial displacement, u: mm

(a)

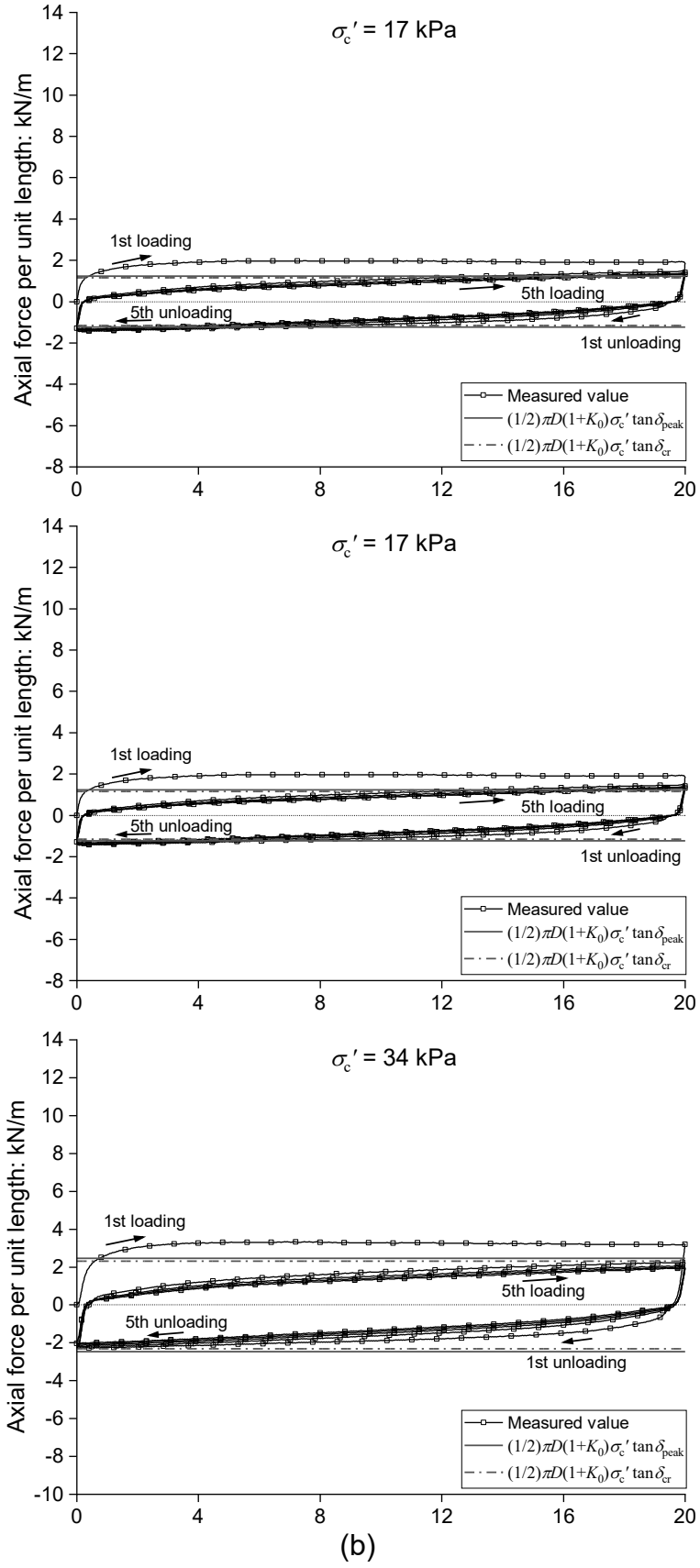

Figure 5.2 Effects of nominal pressure at pipe centre and surface roughness on cyclic axial force (Series I, u_A = 20 mm): (a) rough pipe and (b) smooth pipe

The second loading resembles the first unloading instead of the first loading. It indicates that the change of soil state has been largely finished in the first loading, which is supported by the stress path given later. The curve of the second unloading exhibits an approximate rotational symmetry with the second loading. Results of the following cycles remain qualitatively similar, but the axial resistance decreases slightly and stabilises over the cycles, consistent with the studies of Weidlich & Achmus (2008) and Bilgin & Stewart (2009a). Rough pipes require more cycles to reach stability compared to smooth pipes due to more soil disturbance. Consequently, the tests were stopped after five and ten cycles for smooth and rough pipes, respectively. The ultimate values of axial resistance measured in the last cycle (T_u) for two pipes are generally lower than the predictions using Equation (2-2) and δ_{cr}, with the maximum discrepancy reaching 48%. This difference indicates a potential risk for pipeline systems after being subjected to thermal expansion and contraction cycles. The significant drop in soil resistance would increase the load transferred to other vulnerable pipeline components (e.g., valve stations and sharp bends) rather than soils, increasing the risk of buckling failures (PRCI, 2009).

Figure 5.3 (a) illustrates the degradation of axial resistance over cycles for all tests in Series I. The axial resistance decreases with the cycles, especially during the first two cycles. The axial resistance during loading is generally slightly higher than that during the unloading of the preceding cycle, likely because soil anisotropy during loading may not be fully reversed during unloading. The influence of nominal pressure on the ultimate degradation factors, T_u/T_1, is small, with a reduction of less than 10% when σ_c' increases from 17 to 50 kPa. However, T_u/T_1 decreases sharply with increasing roughness, as shown in Figure 5.3 (b). The reduction results from more prominent constrained dilation and interface friction strength mobilisation on rough pipes, as discussed later. The average values of T_u/T_1 for rough, intermediate, and smooth pipes are about 0.62, 0.39, and 0.32, respectively. T_u can be calculated using the predicted equation of T_1 proposed in CHAPTER 4 and the above data on degradation factors. The obtained T_u can

be used by engineers as the lower bound of axial resistance (i.e., the resistance after many cycles) to calculate the potential maximum axial strain of pipe upon thermal expansion and contraction.

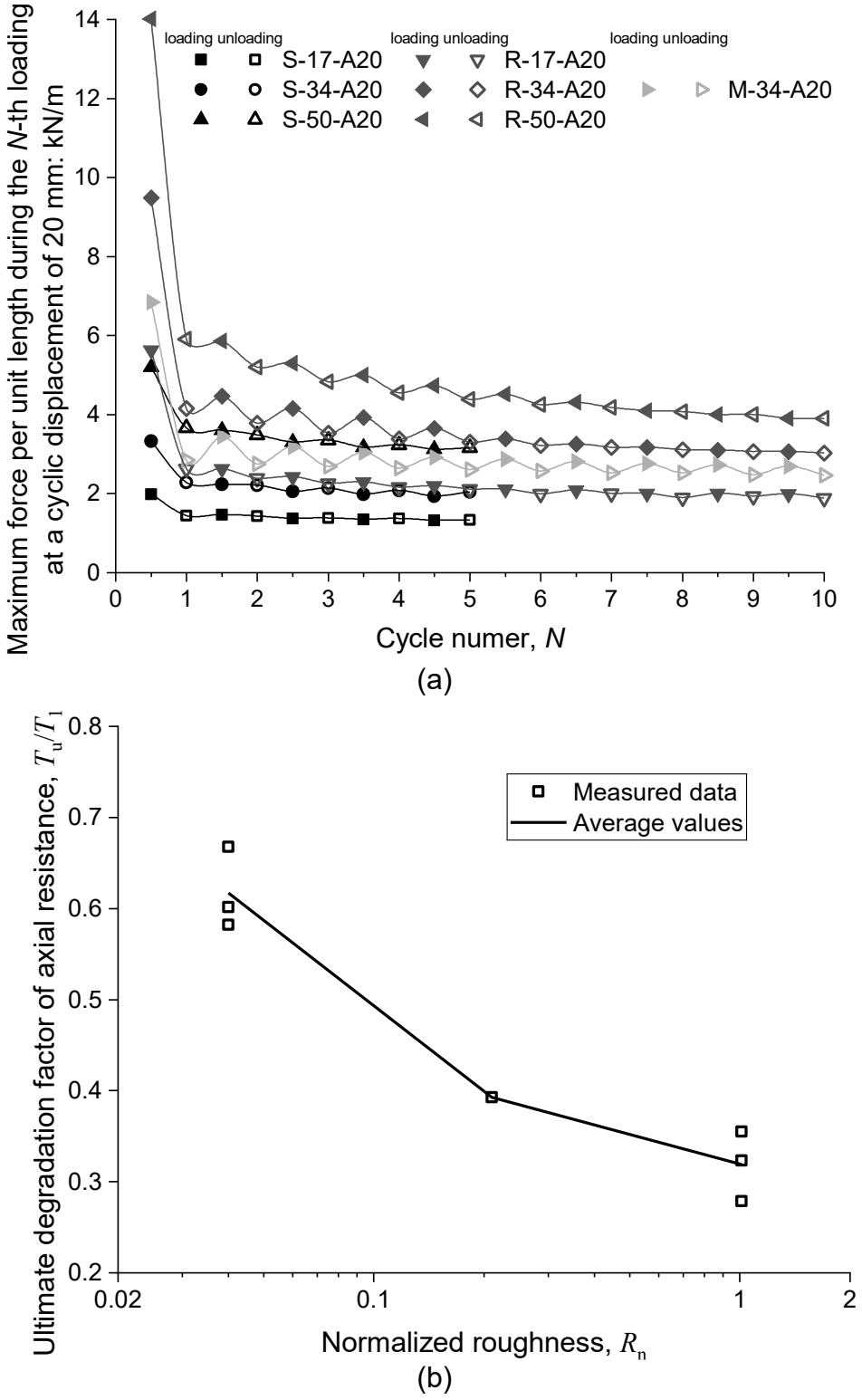

Figure 5.3 Cyclic degradation of axial resistance: (a) axial resistance vs. cycle number; (b) ultimate degradation factor vs. surface roughness

5.3.2 Evolution of interface contact pressures during cyclic loading

Figure 5.4 illustrates the typical evolution process of soil-pipe interface contact pressure using the results obtained from rough and smooth pipes under a surcharge of 34 kPa. Theoretical values of average interface contact pressure, $(1+K_0)\sigma_c'/2$ (23.2 kPa, where K_0 is taken as 1-sin φ'), according to ALA (2001), are also incorporated for comparison. As CHAPTER 4 mentioned, before testing, the average interface contact pressures for both pipes closely approximate their theoretical values. However, during the first loading, the average interface contact pressure of the rough pipe increases owing to constrained dilation (Zhou & Yin, 2008; Wijewickreme *et al.*, 2009; Hubler *et al.*, 2017; Wu *et al.*, 2017), where the soil surrounding the pipe restricts the dilation of the soil-pipe interface, resulting in increased interface contact pressures. Furthermore, the tendency of dilatancy increases with increasing interface roughness (see Figure 5.4).

During the first unloading, the average interface contact pressure decreases before increasing to a value slightly smaller than the theoretical value. The loading and unloading paths of the subsequent cycles exhibit consistent behaviour with the first unloading. The variation in interface contact pressure of the rough pipe (reaching a minimum of 6.6 kPa) is more significant than that of the smooth pipe (minimum of 13.9 kPa). This behaviour is related to the reconstruction of the interface shear band, which can be explained using the force chain evolution supported by DEM simulations (Faizal *et al.*, 2018; Grabowski *et al.*, 2020; Wang *et al.*, 2022). Before loading, the preferential orientation of contacts is typically perpendicular to pipes. Upon the first loading, the preferential orientation in the vicinity of the interface experiences a rotation towards alignment with the pipe's axial direction, forming a shear band with strong force chains due to the constrained dilation. During the subsequent loading reversal, the preferential orientation of contacts reverses with the loading direction, resulting in the vanishment and subsequent reconstruction of strong force chains, causing a decrease followed

by an increase in soil-pipe interface contact pressures. The thicker interface shear band of rough pipes leads to a larger periodic change of average interface contact pressure compared to that of smooth pipes.

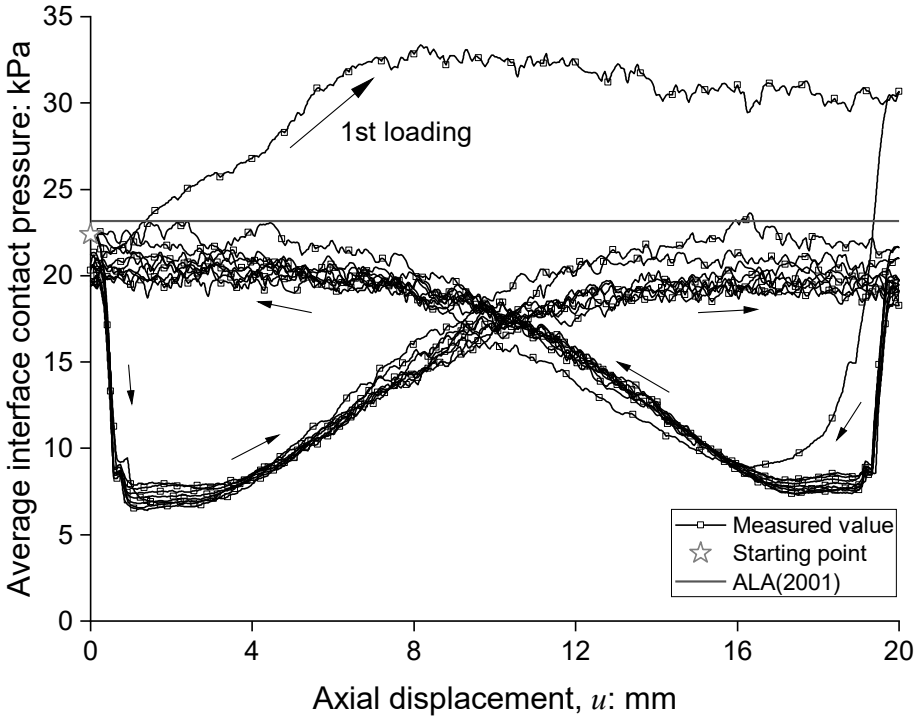

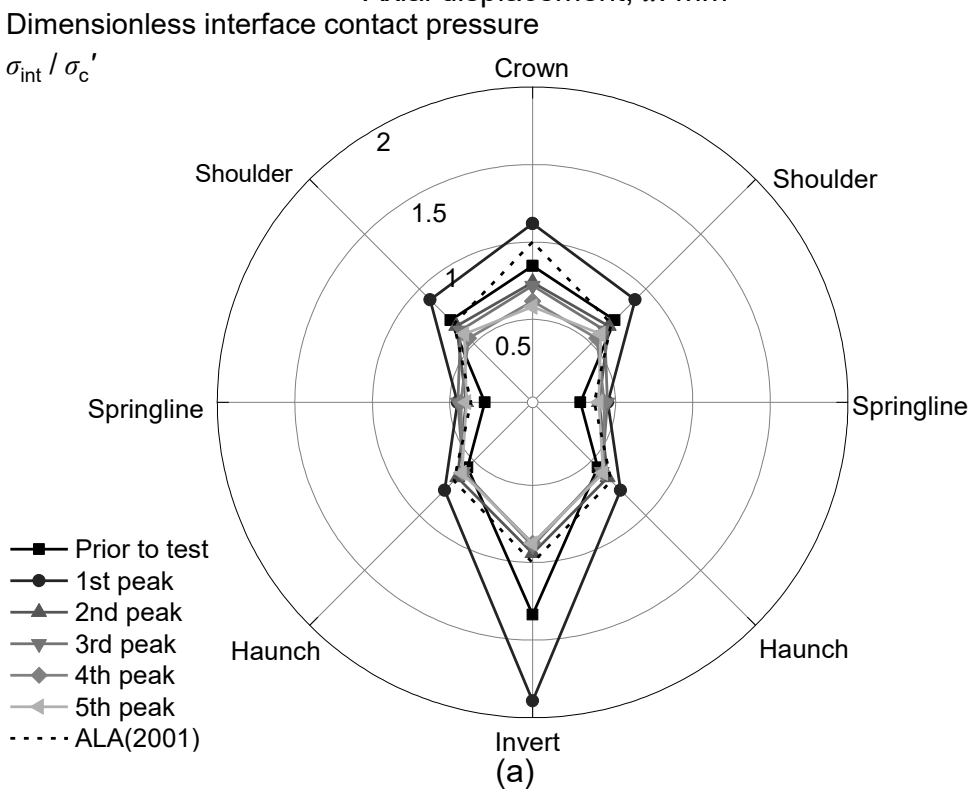

(a)

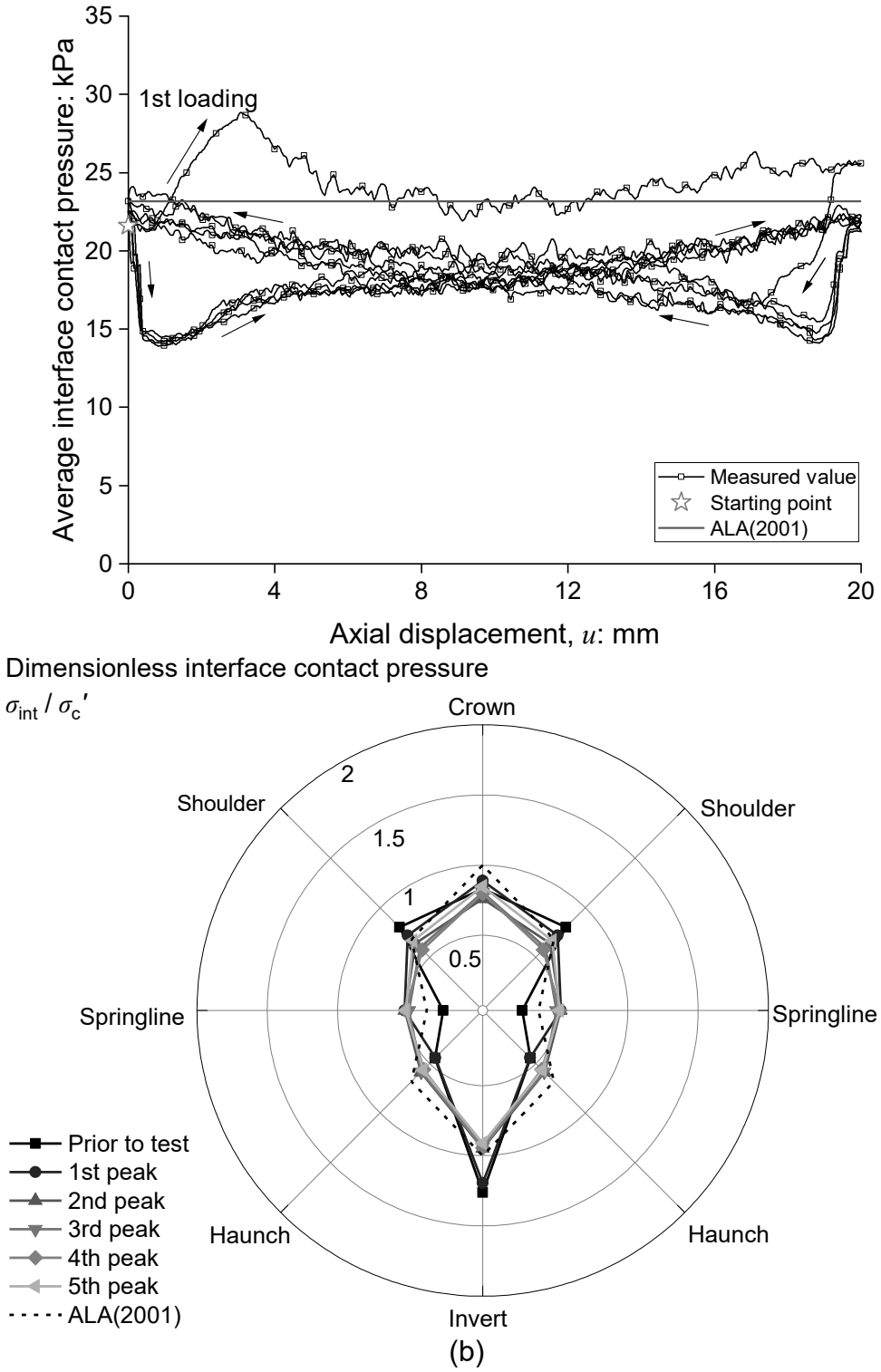

Figure 5.4 Typical evolution of interface contact pressure (σ_c' = 34 kPa, u_A = 20 mm): (a) rough pipe and (b) smooth pipe

Figure 5.4 also illustrates the typical interface contact pressure distribution. According to ALA (2001), the assumed interface contact pressure is σ_c' (34 kPa) at the crown and invert,

$K_0\sigma_c'$ (12.3 kPa) at the springlines, and $(1+K_0)\sigma_c'/2$ (23.2 kPa) at the shoulders and haunches, respectively. Before testing, the differences between measured and expected values typically do not exceed 25% of the expected values. During cyclic loading and unloading, interface contact pressures are redistributed with varying trends across different pipes. For the rough pipe, all interface contact pressures notably increase during the first loading, particularly at the crown and invert, reaching 38 and 64 kPa, respectively. Subsequent cycles bring all interface contact pressures, except that of the crown, closer to the predicted value with a deviation of less than 8.5%. The pressure at the pipe crown is 26% lower than expected, explaining the slightly smaller axial resistances of the rough pipe than the prediction during the second loading phase in Figure 5.2. In subsequent cycles, pressures at springlines, haunches, and the invert stabilise at theoretical values, while those at the crown and shoulders continue to decrease, reaching 19.9 and 19.8 kPa, respectively, by the fifth loading. This trend of interface contact pressure variation is consistent with the study of Weidlich & Achmus (2008) and corresponds to the decreasing axial resistance over cycles in Figure 5.2.

As for the smooth pipe, the increase in interface contact pressure during the first loading primarily focuses on the springlines, reaching around 17.7 kPa, corresponding to the limited increase in average interface contact pressure. In the second loading, interface contact pressures at shoulders, haunches, and the invert align closely with predicted values, with a deviation not exceeding 5.8%. In subsequent cycles, pressures at haunches and the invert also maintain proximity to theoretical values, while those at the crown and shoulders continue to decrease, although the magnitude of the decrease is not as large as that observed in the rough pipe, with interface contact pressures reaching 28.8 and 22.6 kPa, respectively, by the fifth loading.

5.3.3 Pipe settlement behaviour during cyclic loading

Figure 5.5 illustrates the typical results of the axial and vertical displacements of rough and smooth pipes under a surcharge of 34 kPa. Only the first five cycles of the rough pipe are shown

to facilitate comparison with those of the smooth pipe. Both pipes settle continuously over cycles, aligning with the results of Sheil *et al.* (2018). These settlement curves reflect the influence of soil-pipe interface behaviour on the soil beneath the pipe, encompassing two distinct mechanisms: the soil compression due to repeated average effective stress variation and the compaction/dilation behaviour of the soil-pipe interface shear band.

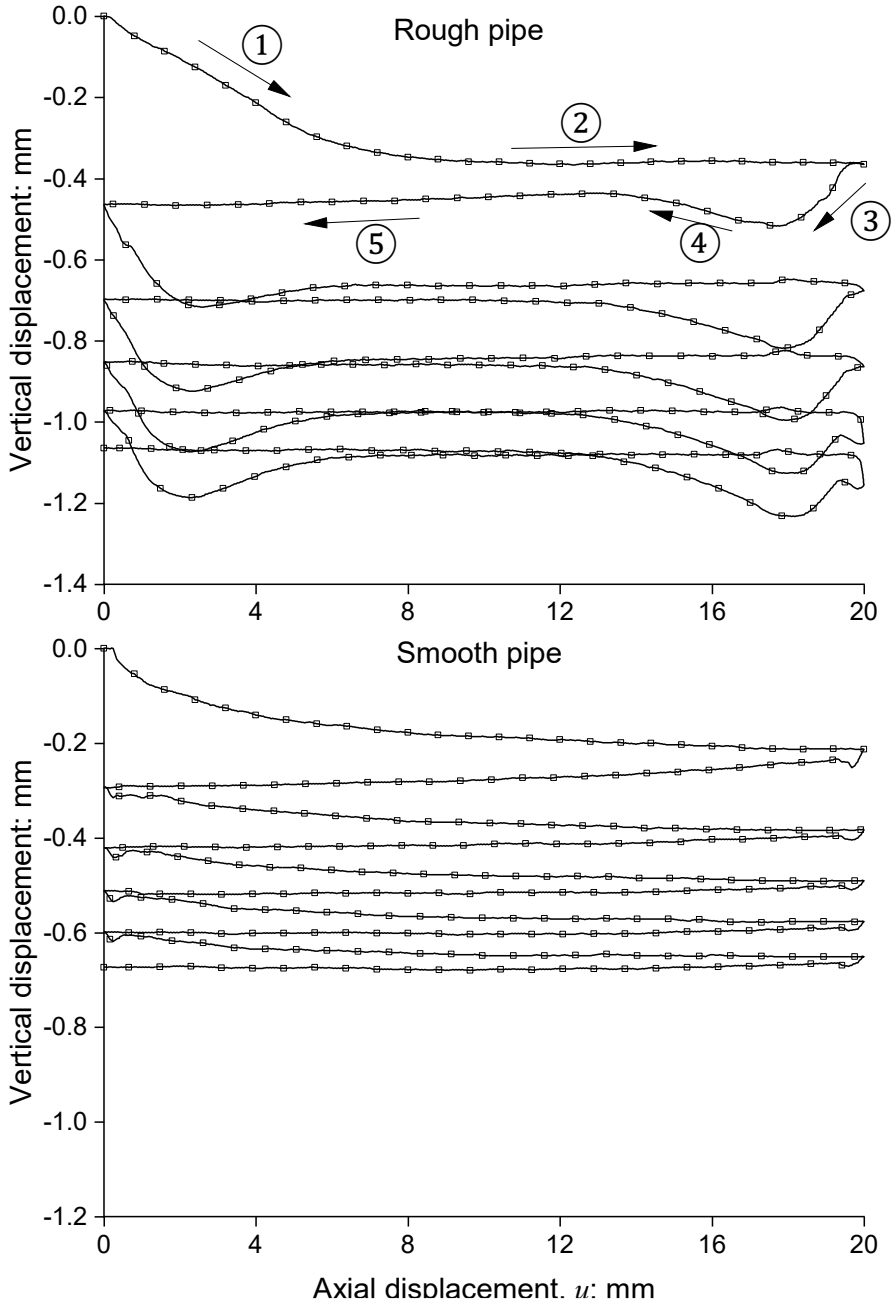

Figure 5.5 Typical pipe settlement behaviour (σ_c' = 34 kPa, u_A = 20 mm, first five cycles)

During the first loading (the first and second stages in Figure 5.5) of the rough pipe, the vertical displacement is dominated by the soil compression due to average effective stress variation. The rapid settlement in the first stage corresponds to the increasing average interface contact pressure depicted in Figure 5.4 (a) and increasing axial force in Figure 5.2 (a), while the unchanged vertical displacement in the second stage aligns with the stable interface contact pressure and axial force at the same displacement. The third and fourth stages of the rough pipe in Figure 5.5 display an opposing pattern to the first two stages. The vertical position experienced a descent followed by an ascent, even if the average effective stress decreased and then increased. This discrepancy arises from the compaction/dilation behaviour of the upper portion of the interface shear band. During the typical interface shearing, the soil typically undergoes compaction followed by dilation (Zhang & Zhang, 2006). Thus, the compaction/dilation behaviour of the interface shear band tends to induce the settling and then rising of pipes. This trend is dominant and opposed to the average effective stress effects on pipe vertical displacement during the third and fourth stages in Figure 5.5. At the fifth stage, the dilation might become minimal so that the average effective stress effects on pipe vertical displacement take back their dominance. The results of the smooth pipe and subsequent cycles of the rough pipe exhibit similar settlement patterns to those observed in the first cycle of the rough pipe.

Figure 5.6 depicts irreversible settlement, defined as the change in the pipe's initial vertical position of each cycle relative to its vertical position before testing. Irreversible settlement increases with the cycle number and surface roughness. This is consistent with the periodic variation of average effective stress and prior research on cyclic interface shear behaviour (Fakharian & Evgin, 1997; Mortara *et al.*, 2007; Di Donna *et al.*, 2016; Rui *et al.*, 2020b): the larger magnitude of average effective stress in tests of rough pipe leads to larger soil

compression than that of smooth pipes; higher roughness causes a larger permanent volumetric decrease on the soil-pipe interface.

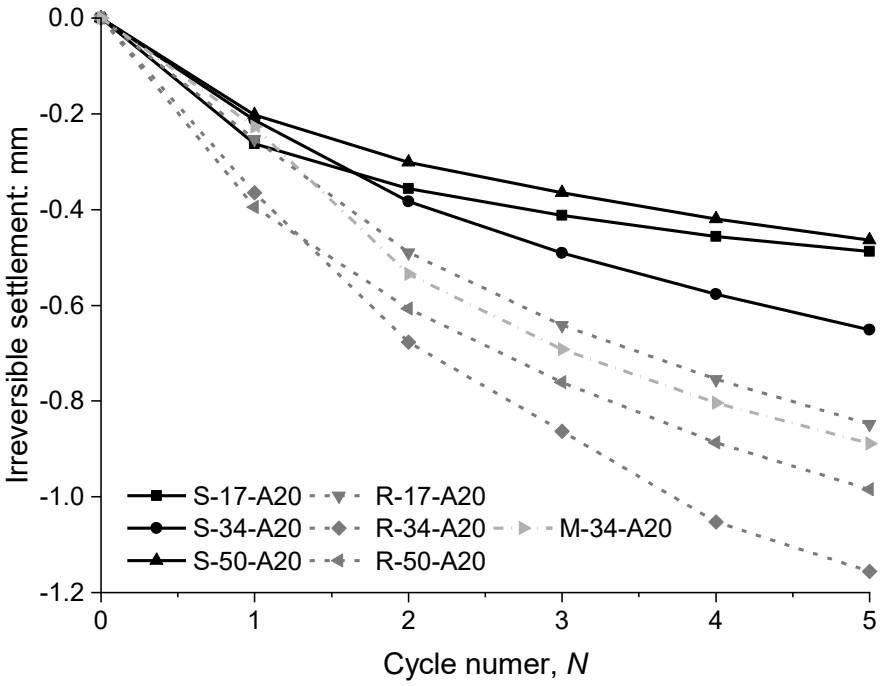

Figure 5.6 Irreversible settlement vs. cyclic number (u_A = 20 mm)

5.3.4 Soil arching effects on cyclic ASPI

The evolution and redistribution of interface contact pressures shown in Figure 5.4 can be linked to the development of soil arching on the pipe (Bartlett *et al.*, 2015; Sheil *et al.*, 2018; Meguid, 2019; Costa & Zornberg, 2020), which is simultaneously influenced by the combined effects of the soil-pipe interface dilation and pipe settlement behaviour. The process of soil arching is schematically represented in Figure 5.7. It is also supported by data on vertical earth pressure in Figure 5.8, where the theoretical vertical earth pressure, σ_e', calculated without considering stress redistribution ($\sigma_e' = \gamma' H_0 + P$, where H_0 represents the buried depth from the ground surface to the sensor), is included for comparison.

As discussed in CHAPTER 4, before the tests, the pipe might undergo a slight negative soil arching, where the soil at the sides of the pipe is subjected to a downward movement relative to the pipe due to soil compaction. This relative movement forces more overburden pressure on the shoulders and the invert of the pipe. Hence, in Figure 5.8, the measured vertical earth

pressures above and below the rough pipes (TPS # 1 and # 4) are slightly higher than their respective σ_e'. During the first loading, the pronounced interface dilatancy of rough pipes emphasises an additional negative soil arching due to further relative vertical displacement, significantly increasing the interface contact pressures at the crown and the invert (see Figure 5.4). Correspondingly, these vertical earth pressures above and below the rough pipes increase due to the additional negative arching effects and the pressure rise induced by the constrained dilation on the pipe, while pressures at the pipe sides (TPS # 2, # 3, and # 5) show a slight decrease during shearing. For smooth pipes, the more dominant mechanism is that the pipe movement disrupts the initial negative soil arching equilibrium, causing a notable increase in interface contact pressure at the springlines (see Figure 5.4). The vertical earth pressure variation for smooth pipes in Figure 5.8 is not as marked as that for rough pipes. Yet, their evolution pattern mirrors that of rough pipes.

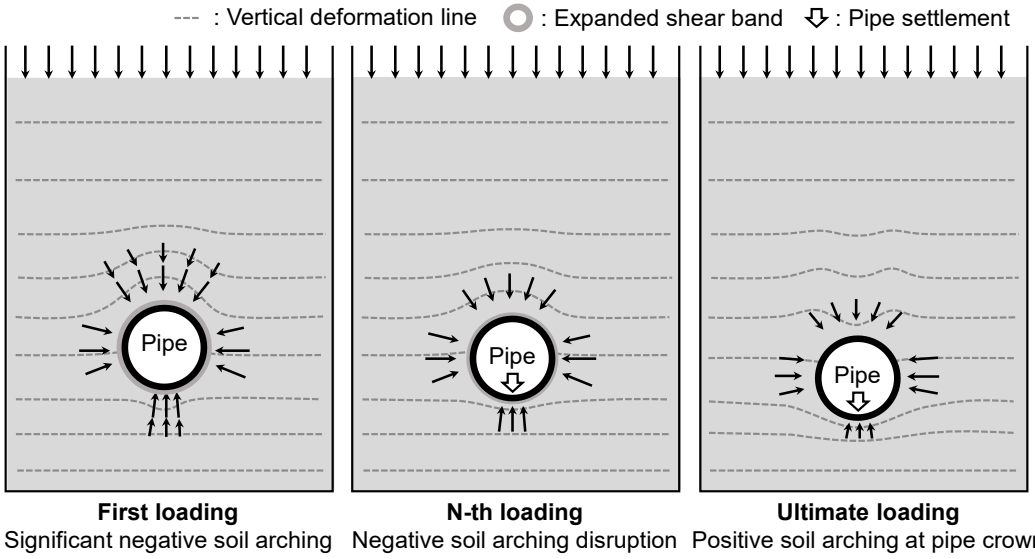

Figure 5.7 Schematic diagram of soil arching evolution during cycling loading

In the first unloading or the second loading, the negative soil arching may be largely disrupted due to the reconstruction of the shear band and pipe settlement. The soil around the pipe interface in Series I tests also transitions from a dense to a critical state, which is demonstrated later. Consequently, the stress distribution closely aligns with the predicted

condition for the second loading, with an axial resistance nearing the prediction based on δ_{cr} (see Figure 5.2).

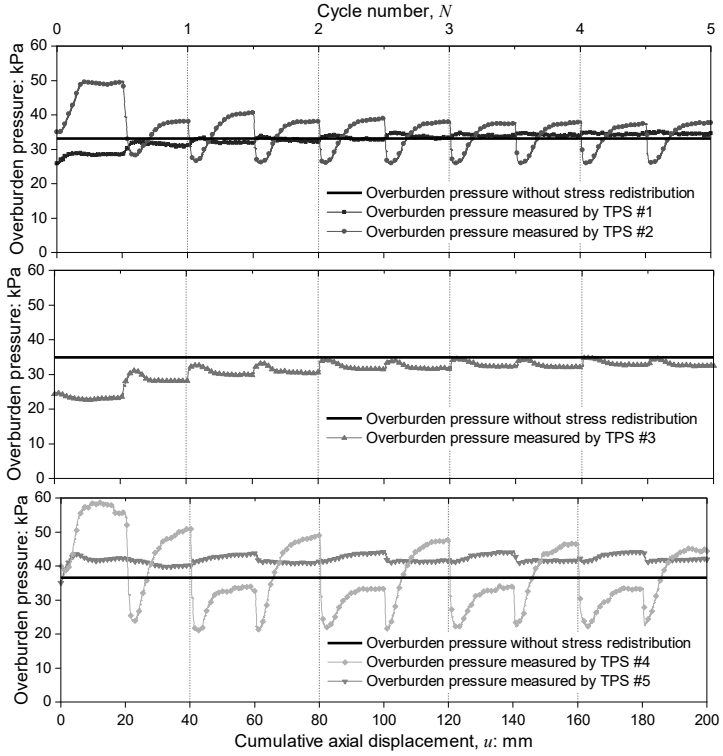

(a)

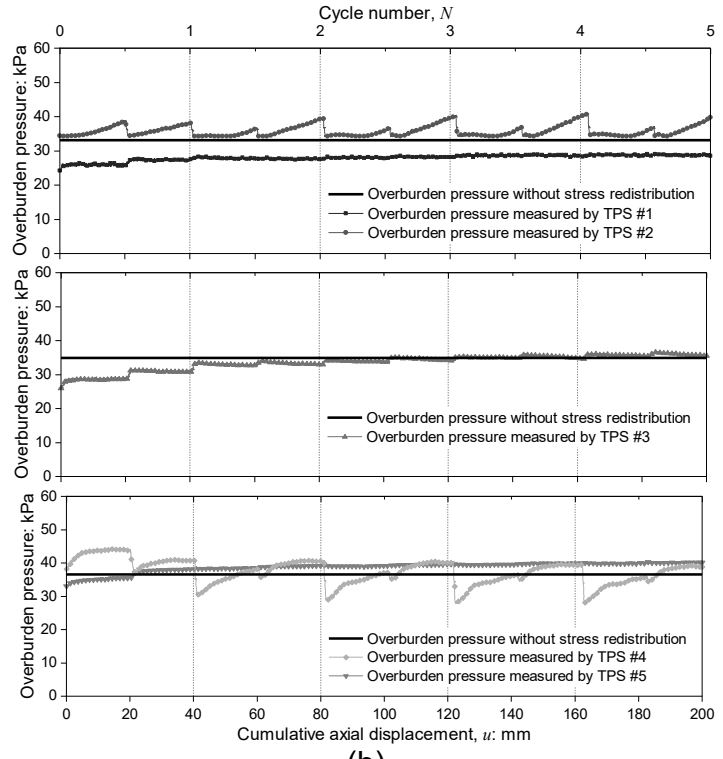

(b)

Figure 5.8 Typical evolution of earth pressure (σ_c' = 34 kPa, u_A = 20 mm, first five cycles)

In subsequent cycles, the ongoing settlement leads to the pipe being subjected to a downward movement relative to the soil at the sides of the pipe, reversing the negative soil arching to a positive soil arching on the upper part of the pipe. It results in a decrease in interface contact pressure at the crown and shoulders over cycles (see Figure 5.4). This decrease is more pronounced for rough pipes due to their higher settlement (see Figure 5.5). The earth pressures of TPS # 1 and # 4 in Figure 5.8 rise during each loading and unloading and fall during each reversal of the axial direction, with the measured values gradually decreasing and eventually aligning with or even falling below σ_e'. This trend illustrates the weakening of negative soil arching and the emergence of positive soil arching.

5.3.5 Effects of cyclic displacement amplitude on ASPI

Figure 5.9 (a) shows the typical cyclic behaviour of rough pipes in Series II with 5 mm amplitude. The axial force-displacement curve during the first loading aligns with the early portion of the curve with 20 mm amplitude (see Figure 5.2 (a)), but 5 mm displacement is insufficient to induce softening. In the subsequent loading and unloading cycles, consistent with Figure 5.2 (a), the maximum axial force degrades over cycles, but the degradation rate is not as pronounced as that observed with a 20 mm amplitude. Furthermore, the maximum axial force during unloading exhibits minimal variation over cycles and is typically lower than the corresponding maximum axial force in the loading path of the same cycle. The above behaviour of axial force is related to the interface contact pressure evolution. During the first loading of rough pipe with 5 mm amplitude, same as Figure 5.4 (a), the average interface contact pressure consistently increases due to the constrained dilation and stops at around 31 kPa. During the first unloading, the average interface contact pressure decreases to around 12.5 kPa, but there is no subsequent rise, being different from the trend in Figure 5.4 (a), likely because the reconstruction of the shear band is not fully finished within the 5 mm displacement. Moreover,

the reduction of interface contact pressure can well explain the lower maximum axial force during unloading than that during the previous loading from the same cycle. In the second and

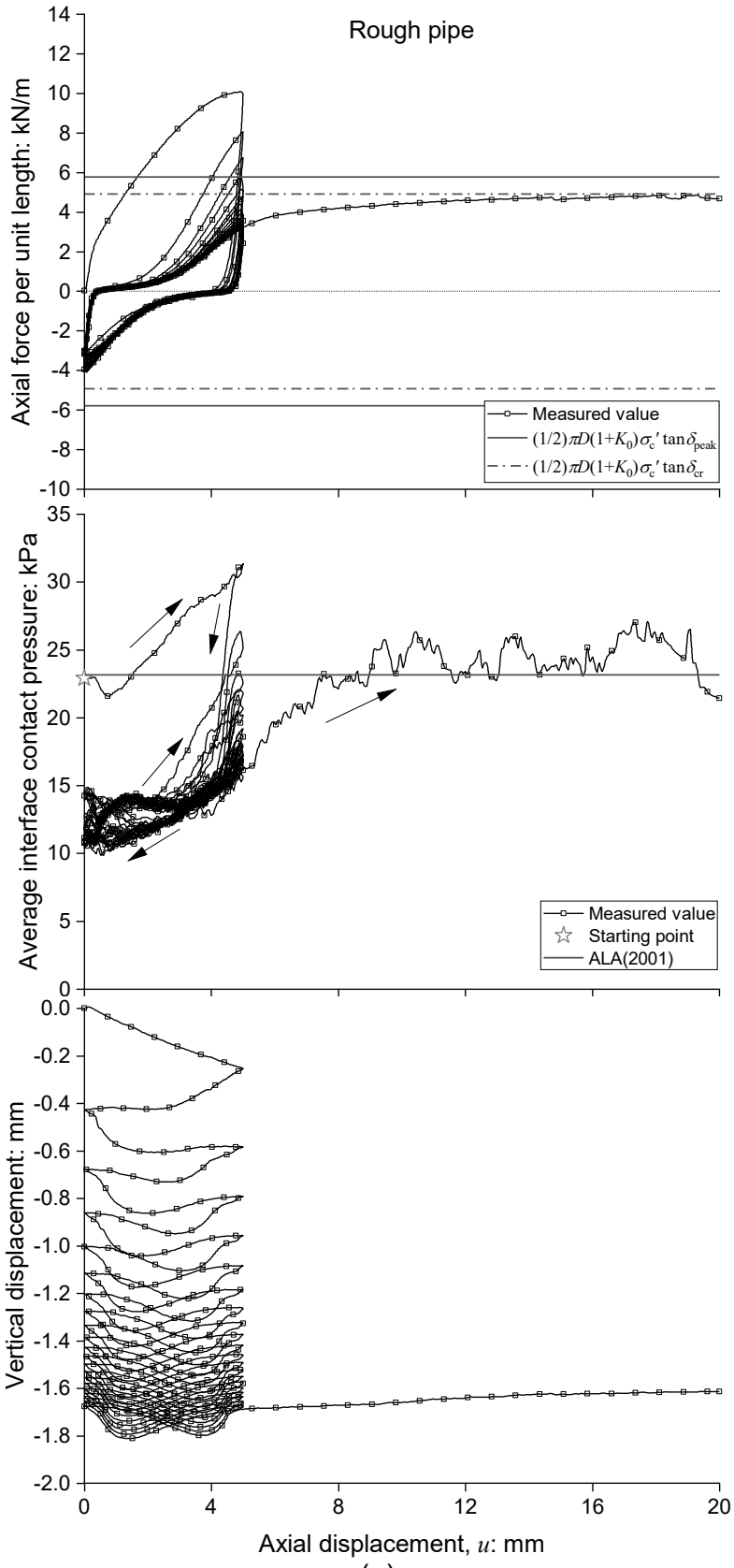

(a)

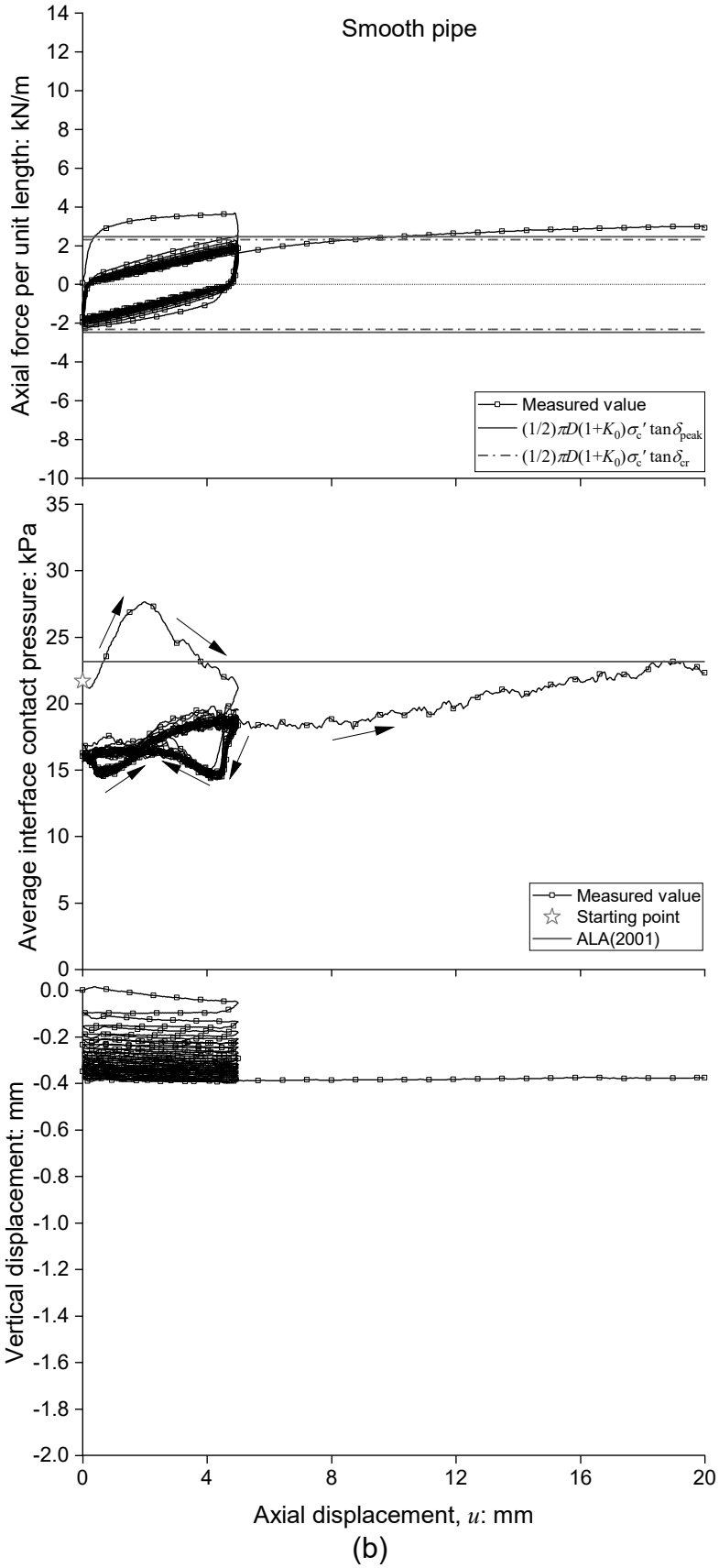

(b)

Figure 5.9 Typical cyclic and post-cyclic behaviour in Series II (σ_c' = 34 kPa, u_A = 5 mm): (a) rough pipe and (b) smooth pipe

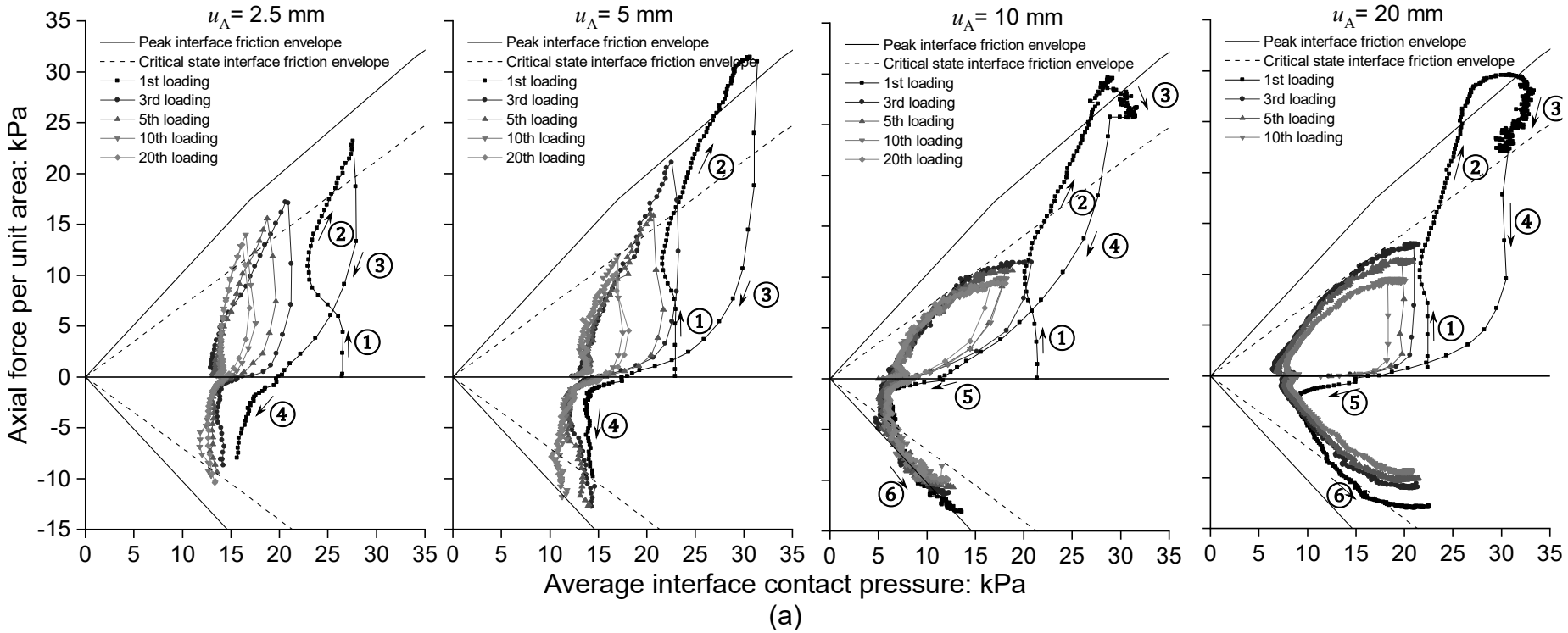
u_A= 2.5 mm
u_A= 5 mm
u_A= 10 mm
u_A= 20 mm
Peak interface friction envelope
Critical state interface friction envelope
1st loading
3rd loading
5th loading
10th loading
20th loading
Axial force per unit area: kPa
Average interface contact pressure: kPa
(a)

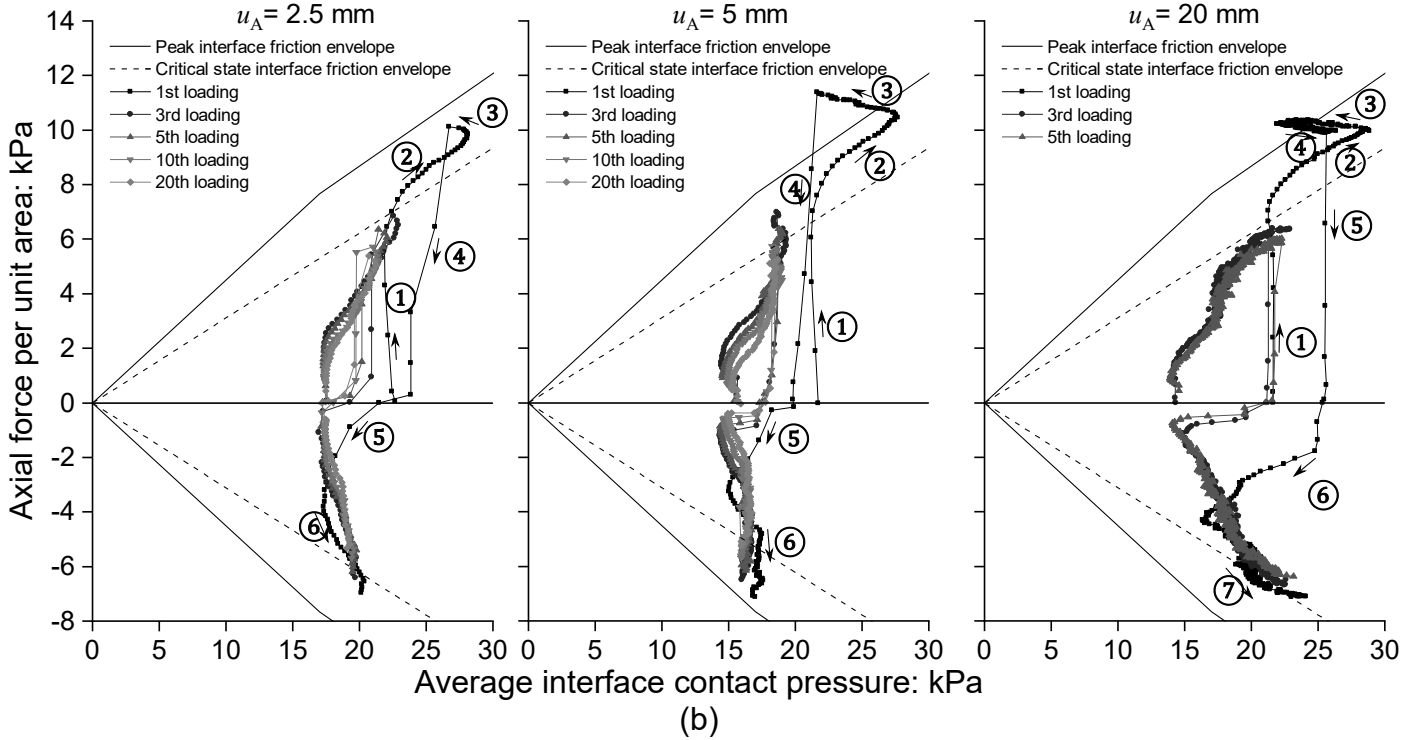

Figure 5.10 Comparison between stress paths during cycling for different displacement amplitudes, $\sigma_c' = 34$ kPa: (a) rough pipe and (b) smooth pipe

third loadings, the average interface contact pressure increases to around 26 and 23 kPa, higher than the theoretical values by ALA (2001), aligning with the corresponding higher maximum axial force than the predicted. In the subsequent cycles, the pressure increments during the loading path continuously decline.

Figure 5.9 (b) shows the results of smooth pipes subjected to cyclic loading with 5 mm amplitude. The axial force and interface contact pressure evolutions of smooth pipes are similar to those under 20 mm amplitude in Figure 5.2 (b), suggesting limited effects of amplitude on smooth pipes.

Figure 5.9 also illustrates the pipe settlement behaviour. The average effective stress variation caused by soil compression and compaction/dilation behaviour of the upper portion of the interface shear band is also reflected in the shapes of vertical displacement curves. The irreversible settlement over cycles under 5 mm amplitude is close to that under 20 mm in Figure 5.5. It might be due to the limited amplitude effects on the average effective stress variation during cyclic shearing.

Figure 5.10 presents the stress paths at the soil-pipe interfaces in physical modelling, offering insights into ASPI. The failure envelopes for three interfaces, determined through CNL interface direct shear tests, are included for reference. The first cycle's stress paths for rough pipes with 20 mm amplitude include six stages, resembling the typical stress path observed in CNS tests on rough interfaces (Ooi & Carter, 1987; Pra-ai & Boulon, 2016). Initially, the stress path ascends vertically, indicating primarily elastic friction angle mobilisation. It then shifts to the second stage by moving upwards to the right, reflecting an increase in average interface contact pressure due to constrained dilatancy. After reaching the peak failure envelope, the stress paths in the third stage go downwards to the right, approaching the critical state envelope. With the reversal of axial displacement direction, the fourth and fifth stages are marked by a significant reduction in axial force and average interface contact pressure, attributed to the

vanishment of strong force chains in the shear band. It follows an increase in the sixth stage as these chains are re-established. Subsequent cycles follow a path similar to the first unloading. They never surpass the critical state interface envelopes after the first unloading, indicating a mobilisation from peak to critical interface shear strength. For rough pipes with amplitudes of 2.5, 5, and 10 mm, the shear strength mobilisation to the critical state remains incomplete during the first loading, influencing subsequent axial pipe behaviour. The stress paths for a 10 mm amplitude do not fully transition from peak to critical state in the third stage of its first loading, resulting in subsequent paths reaching the zone between the peak and critical state envelopes. For a 5 mm amplitude, the stress paths only approach the peak envelope by the end of the second stage in the first loading. Hence, in later cycles, they mobilise from approaching the peak envelopes to approaching the critical state envelopes. In the case of a 2.5 mm amplitude, the first loading stress paths do not reach the peak envelope, leading to a slower shear strength mobilisation and, consequently, less degradation in the maximum axial force, as shown in Figure 5.9. The soil-pipe interface mobilisation mechanism for smooth pipes, as illustrated in Figure 5.10 (b), is similar. The only notable distinction is that the first cycle stress path includes an additional stage (the third stage in Figure 5.10 (b)), where the path turns to the upper left due to a decrease in average interface contact pressure caused by soil arching disturbance.

Figure 5.11 illustrates the degradation of the maximum axial force for rough and smooth pipes under various displacement amplitudes over cycles, with a surcharge of 34 kPa. Except for the rough pipe at a 2.5 mm amplitude, T_u converges to approximately 3.2 and 1.9 kN/m for rough and smooth pipes, respectively. The influence of amplitude is only obvious for the degradation rate.

Given the limited impacts of nominal pressure and cyclic amplitude on T_u, as Figure 5.3 and Figure 5.11, the ultimate degradation factor can be seen as a function of pipe surface

roughness and T_u can be estimated using data from Figure 5.3 (b) and the equation of T_l proposed by CHAPTER 4, as previously discussed.

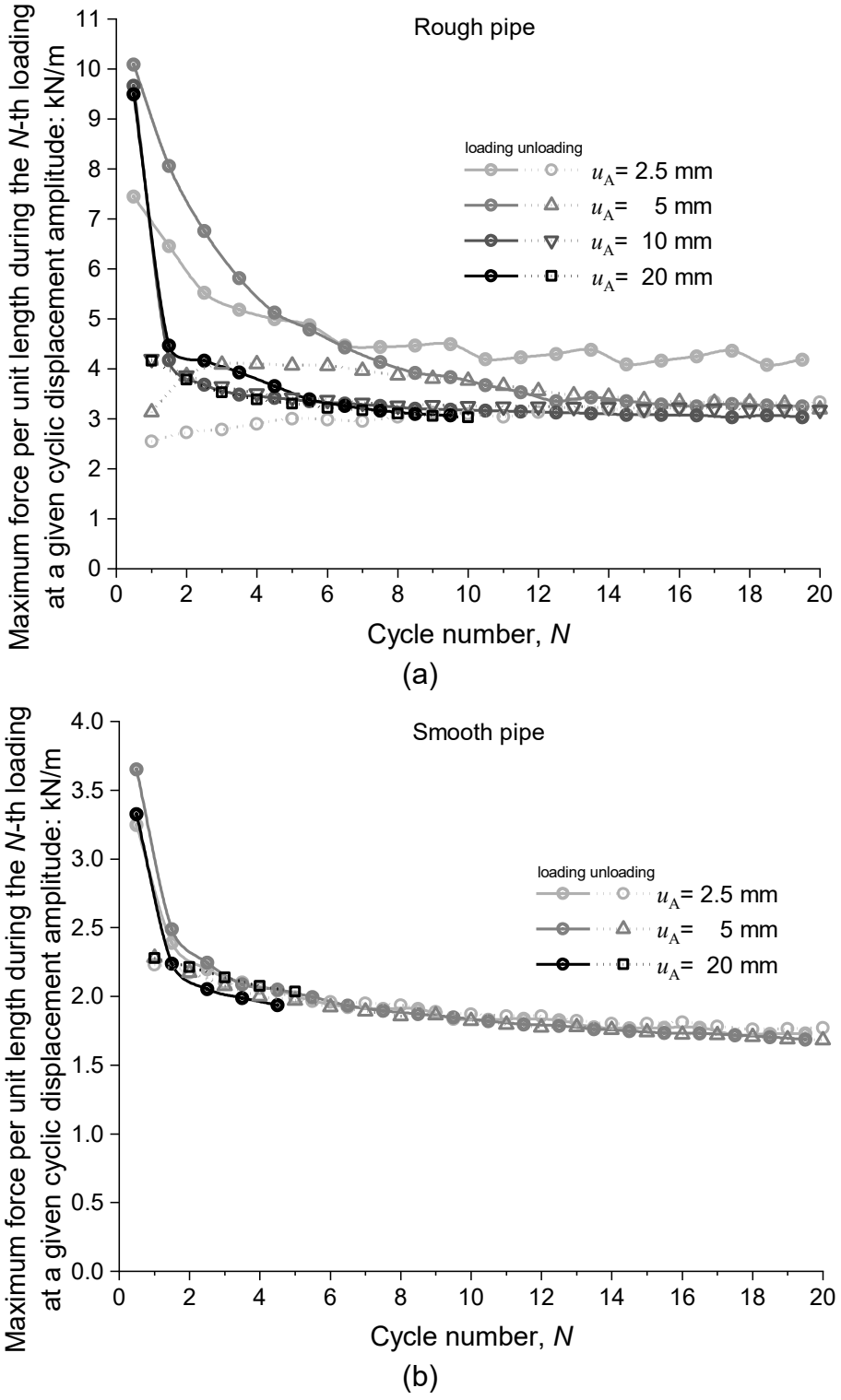

Figure 5.11 Cyclic degradation of maximum axial force per unit length at a given cyclic displacement amplitude ($\sigma_c' = 34$ kPa): (a) rough pipe and (b) smooth pipe

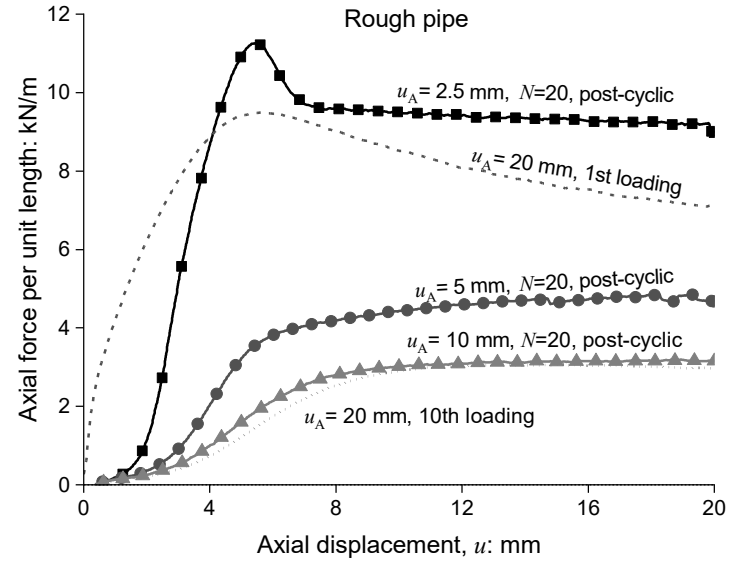
Rough pipe
u_A= 2.5 mm, N=20, post-cyclic
u_A= 20 mm, 1st loading
u_A= 5 mm, N=20, post-cyclic
u_A= 10 mm, N=20, post-cyclic
u_A= 20 mm, 10th loading
Axial force per unit length: kN/m
Axial displacement, u: mm

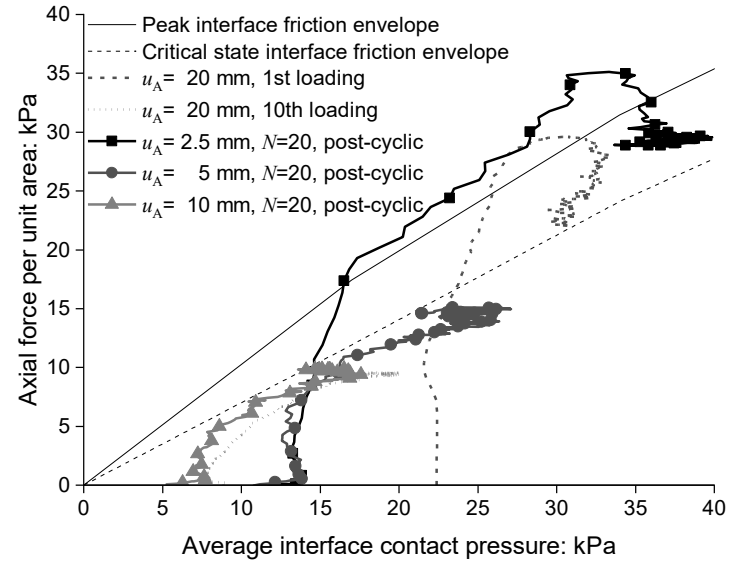
Peak interface friction envelope
Critical state interface friction envelope
u_A= 20 mm, 1st loading
u_A= 20 mm, 10th loading
u_A= 2.5 mm, N=20, post-cyclic
u_A= 5 mm, N=20, post-cyclic
u_A= 10 mm, N=20, post-cyclic
Axial force per unit area: kPa
Average interface contact pressure: kPa

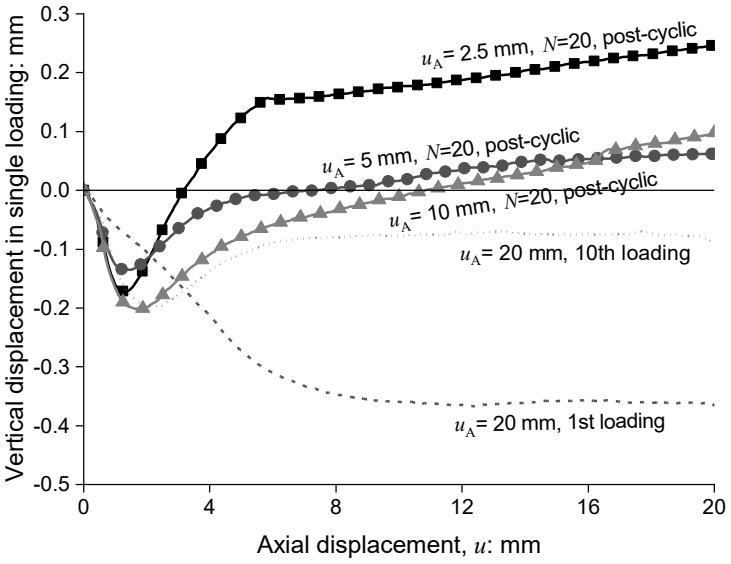
u_A= 2.5 mm, N=20, post-cyclic
u_A= 5 mm, N=20, post-cyclic
u_A= 10 mm, N=20, post-cyclic
u_A= 20 mm, 10th loading
u_A= 20 mm, 1st loading
Vertical displacement in single loading: mm
Axial displacement, u: mm

(a)

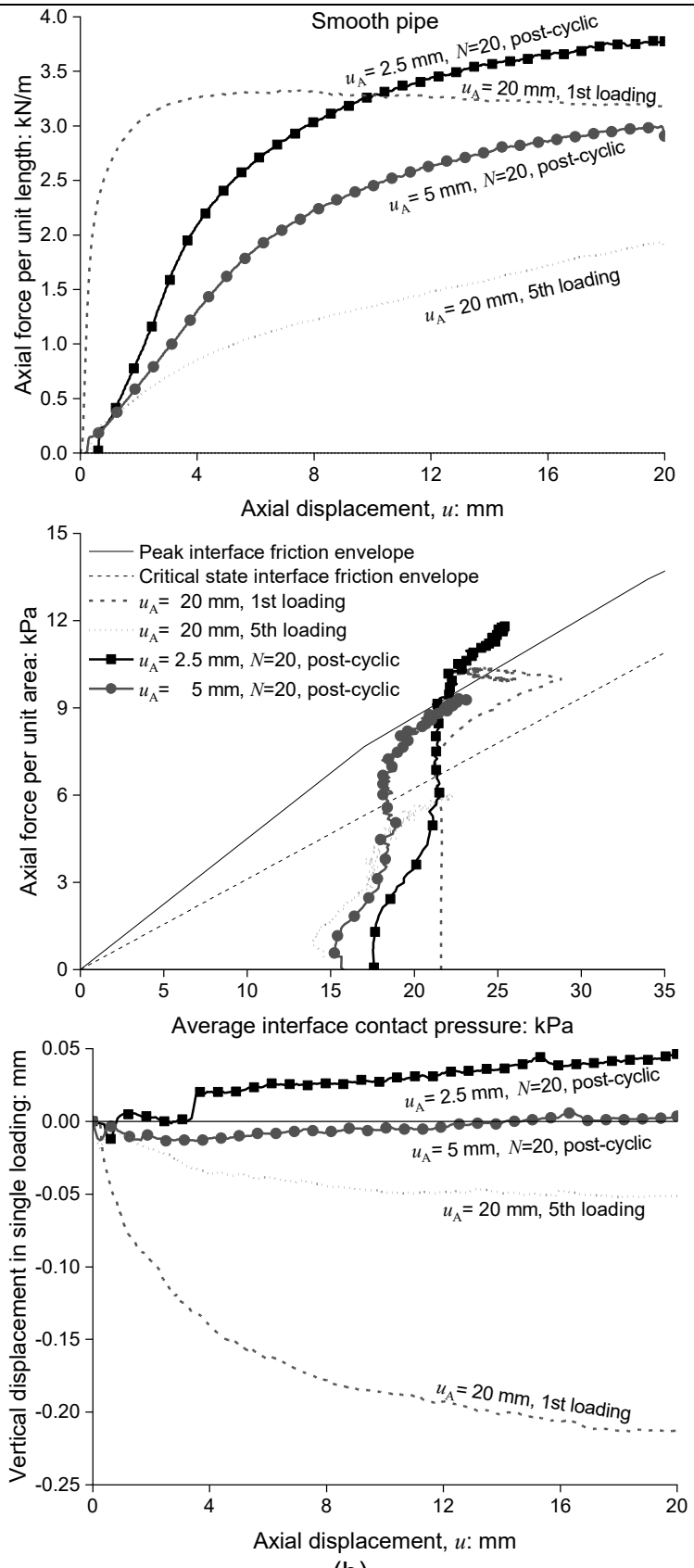

(b)

Figure 5.12 Effects of cyclic displacement amplitude on post-cyclic pullout behaviour ($\sigma_c' = 34$ kPa): (a) rough pipe and (b) smooth pipe

5.3.6 Post-cyclic pullout behaviour

Figure 5.12 illustrates the post-cyclic pullout behaviour in Series II with a nominal overburden pressure of 34 kPa. The results of the first and final loading with a displacement amplitude of 20 mm and a nominal overburden pressure of 34 kPa in Series I are also included for comparison. The former can be regarded as monotonic behaviour without cycling, as the 20 mm displacement can mobilise a stable state (see Figure 5.2). The latter can be regarded as post-cyclic behaviour after a cyclic loading with a 20 mm amplitude.

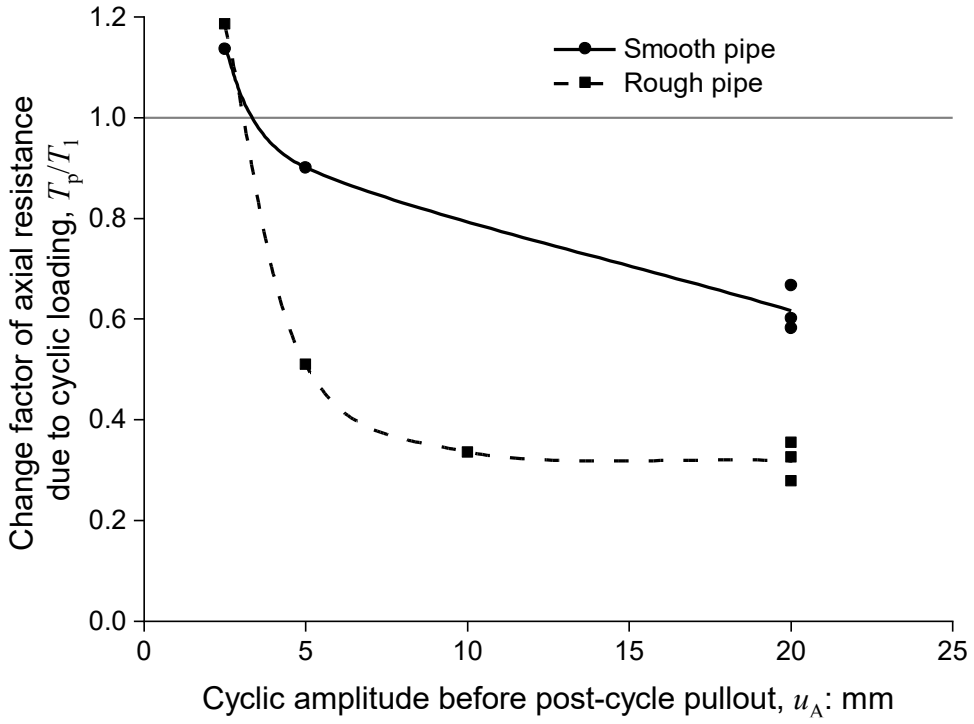

Figure 5.13 Effects of pipe roughness and cyclic amplitude on the change factors of maximum axial resistance (i.e., the ratio of post-cyclic and monotonic pullout resistances) (σ_c' =34 kPa)

An obvious displacement-softening can be seen in the post-cyclic test on the rough pipe with a 2.5 mm cyclic amplitude, while other tests on both rough and smooth pipes show displacement-hardening behaviour. This finding is likely related to the fact that the stress path in the cyclic test with a 2.5 mm amplitude has not reached the failure envelope (see Figure 5.10

(a)). Hence, its stress path during the post-cyclic pullout process resembles the monotonic behaviour, going downwards to the right after reaching the vicinity of the peak failure envelope. In contrast, only a tendency to move to the upper right can be seen in the stress paths of other tests.

To investigate the influence of cyclic loading on the post-cyclic pullout resistance, this study defines a post-cyclic change factor as the ratio T_p/T_1, where T_p is the axial resistance during the post-cyclic pullout, and T_1 is essentially the monotonic resistance without cycling. As shown in Figure 5.13, the change factor T_p/T_1 is greatly affected by the roughness and cyclic displacement amplitude. As expected, the difference between post-cyclic and monotonic resistances is consistently more significant when the pipe is rougher.

For the influence of cyclic displacement amplitude, two observations are included. On the one hand, taking the rough pipe as one example, the ratio is around 1.2 when the cyclic displacement is 2.5 mm, meaning that the post-cyclic pullout resistance is larger than the monotonic resistance by 20%. The cyclic loading-induced increase in pullout resistance is mainly attributed to larger soil-pipe interface contact pressure during pullout (see Figure 5.12 (a)). The observed effects of cyclic displacement amplitude on T_p/T_1 may result from the shear band evolution at the soil-pipe interface. According to the cyclic interface shear tests by DeJong *et al.* (2003), the shear band at a smaller cyclic amplitude might not be as fully formed as that of monotonic loading. During the post-cyclic pullout, the shear band might further develop, causing a further increase in soil-pipe interface contact pressure (see Figure 5.9) and a pipe upward movement (see Figure 5.12) due to constrained dilation. Moreover, the increase in average effective stress causes soil compression, tending to make soil denser and stronger. Furthermore, the higher values of T_p after the cyclic loading may pose risks to the pipeline system. When there is any post-cyclic relative displacement between the pipe and soil, the stress

imposed from soil to pipe may exceed the pipe strength if the pipeline design does not account for cyclic effects.

In contrast, the post-cyclic pullout resistance is smaller than the monotonic resistance because of a smaller soil-pipe interface contact pressure when the cyclic displacement is 5 mm or above. The ratio T_p/T_1 reduces significantly with an increase in roughness. The post-cyclic force-displacement curve of the rough pipe subjected to a 10 mm cyclic amplitude is very close to the final loading curve of the test at 20 mm amplitude. This proves a fully formed soil-pipe interface shear band during the cyclic stage of these tests. The maximum and minimum T_p should be considered to determine the maximum axial force and the maximum axial strain, respectively, in the pipeline system design if there is any potential post-cyclic pullout.

5.4 Summary

This chapter presents and analyses 12 tests with three levels of pipe surface roughness, three buried pressures, and four cyclic displacement amplitudes. The experimental findings led to several key conclusions:

At a given cyclic displacement of 20 mm, the maximum axial resistance during the first loading, T_1, exceeds the value predicted by the current design guidelines, using peak interface shear angle (δ_{peak}). During subsequent cycles, the axial resistance degrades and stabilises at an ultimate value, T_u, which is typically lower than the predicted value, using the critical state interface shear angle (δ_{cr}), with deviations up to 48%. Buried pressures and cyclic displacement amplitude exert a minimal influence on the ultimate degradation factor, T_u/T_1. However, smaller cyclic displacement amplitudes slow the rate at which T_u/T_1 is reached. Pipe surface roughness has a decisive impact on T_u/T_1. The average values of T_u/T_1 for pipes with normalised roughness of 0.04, 0.21, and 1.01 are about 0.62, 0.39, and 0.32, respectively.

The evolution of soil arching plays an important role in cyclic ASPI based on the results of soil-pipe interface contact pressures, vertical earth pressures around the pipes, and vertical

displacement of the pipe. Negative soil arching with constrained dilation increases interface contact pressure during the first loading, causing T_1 to be larger than predicted. In subsequent cycles, soil compression due to the interface compaction/dilation behaviour and the average effective stress variation leads to the pipe settlement. Ongoing settlement translates negative soil arching to positive soil arching on the upper part of the pipe, reducing interface contact pressure at the crown and shoulders. It causes the average interface contact pressure to be lower than predicted.

The post-cyclic pullout resistance is smaller than the monotonic resistance without cycling when the cyclic displacement is relatively large (above 5 mm in this study) due to interface contact pressure evolution, as illustrated above. In contrast, the post-cyclic pullout resistance is above the monotonic resistance when the cyclic displacement is smaller due to cyclic loading-induced soil densification. The difference between post-cyclic and monotonic resistances is consistently more significant when the pipe is rougher.

CHAPTER 6
PHYSICAL MODELLING ON AXIAL BEHAVIOUR OF BURIED PIPES BURIED IN UNSATURATED SOILS

6.1 Introduction

In this chapter, six pullout tests were conducted using a steel pipe buried in CDG, which is a clayey sand under varying saturation conditions. The main objectives are: (i) to investigate the extent to which matric suction affects pullout resistance, (ii) to examine the mechanisms of suction effects, and (iii) to propose and validate a new method for calculating pullout resistance of pipes buried in unsaturated soils.

Table 6.1 Testing program of ASPI in the unsaturated condition

Reference	Target water content: %	Target degree of saturation: %	Nominal pressure at the centre, $\sigma_{c\text{-}net}$ or σ_c': kPa
P17Wsat	20.7 (saturated)	100	17
P17W17	17.0	82.3	17
P34W17	17.0	82.3	34
P17W15	15.0	72.5	17
P34W15	15.0	72.5	34
P17W14	14.2	68.3	17

6.2 Testing programme

Considering the duration of each test, this study mainly focuses on the matric suction effect by six physical modelling tests, as summarised in Table 6.1. The target nominal pressures, $\sigma_{c\text{-}net}$, were set at 17 and 34 kPa, corresponding to burial depths of 1 and 2, respectively. The matric suction was adjusted by varying the water content during compaction. Measuring matric suction greater than 80 kPa in physical modelling is challenging. Therefore, the target water contents were 14.5%, 15%, and 17%, corresponding to 70~82% in the degree of saturation. Referring to the soil-water retention curve in Figure 3.21, matric suctions at these target water contents are

below 100 kPa, within the measurement range of tensiometers. For comparison, one test with a σ_c' of 17 kPa was conducted under saturated conditions.

Table 6.2 Measurement of matric suction and water content around pipe before pullout

Reference	Matric suction before pullout, s: kPa							Water content after testing†: %	Saturation after testing, S_r: %
	Δh^* = 0.2 m	Δh^* = 0 m				Δh^* = -0.2 m	Average		
P17Wsat	-	-	-	-	-	-	0	20.0‡	96.8
P17W17	21	17	17	18	19	15	17.8	17.2	83.3
P34W17	19	18	17	17	18	15	17.3	17.3	83.7
P17W15	52	52	48	51	50	47	50.0	15.4	74.5
P34W15	50	45	51	51	42	47	48.0	15.7	76.0
P17W14	75	74	67	68	73	64	70.2	14.1	69.2

*Δh: Buried depth of tensiometer related to that of the pipe springline.

†Measurement by five samples close to the pipe springline.

‡Estimation based on total volume of added water.

The values of matric suction measured by tensiometers before the pipe pullout are presented in Table 6.2. In each test, the distribution of suction values generally aligns with the hydrostatic conditions. During the pullout, the variation in suction is typically within ±1 kPa, allowing us to consider the average suction before pullout as constant during shearing. Additionally, the actual water content was determined by randomly collecting five soil samples, each weighing at least 40 g, from areas at the same elevation as the pipe springline after tests. The water content at the pipe springline elevation is slightly higher than the target water content used during mixing. This discrepancy is attributed to the redistribution of water content during hydrostatic equilibrium. Figure 3.21 illustrates the relationship between the measured matric suction and water content, represented by the degree of saturation. These data points are slightly lower than those obtained using the axis-translation method in element tests. This difference is primarily because the compaction process resembles a wetting path rather than the drying path observed in element tests, where the soil retains less water in the former path.

6.3 Prediction of interface shear strength

A semi-empirical model to predict the interface shear strength, τ_f, of unsaturated soil was modified by Al-Khazaali & Vanapalli (2019) based on the framework of Vanapalli *et al.* (1996), expressed as

$$\tau_f = c_{int}' + (\sigma_{n\text{-}net} + \chi_{int} s)\tan\delta' \quad (6\text{-}1)$$

where c_{int}' is the interface shear strength intercept if assuming a linear envelope, and $\sigma_{n\text{-}net} + \chi_{int}s$ is Bishop's interface stress. $\chi_{int}s$ is the additional interface stress induced by capillary forces of liquid menisci between the interface and soil particles, where χ_{int} ($=S_r^{\kappa_{int}}$) is Bishop's interface stress parameter (Bishop, 1959) and κ_{int} is an empirical exponent parameter. χ_{int} or κ_{int} might be related to interface roughness and interface material hydrophilicity, and thus should be unequal to that of the pure soil. The best fit for κ_{int} for CDG and rough steel interface used in this study is 2.5, slightly larger than the typical value of 2 for clayey and silty soils (Han & Vanapalli, 2016). The R^2 value for the prediction of shear strength results in Table 3.7 is as high as 0.99.

6.4 Experimental results and discussion

6.4.1 Axial behaviour of steel pipe buried in saturated and unsaturated soils

Figure 6.1 (a) illustrates the axial displacement-force relationship across all tests. The results indicate that pipes in both saturated and unsaturated soils exhibit clear strain-softening behaviour. This observation is consistent with the results of soil-interface direct shear tests, which demonstrate interface dilatant behaviour, as shown in Figure 3.22. Under a nominal pressure of 17 kPa, the axial pullout resistance increases from 4.44 to 11.95 kN/m as the average suction rises from 0 to 70.2 kPa. The ratio of axial resistance in unsaturated soil to that in saturated soil reaches as high as 2.69. It underscores the crucial need to account for suction effects on axial resistance during pipeline design. Failing to do so could result in the pipe experiencing stress that exceeds its design strength, potentially leading to damage when undergoing any axial displacement related to the surrounding soil.

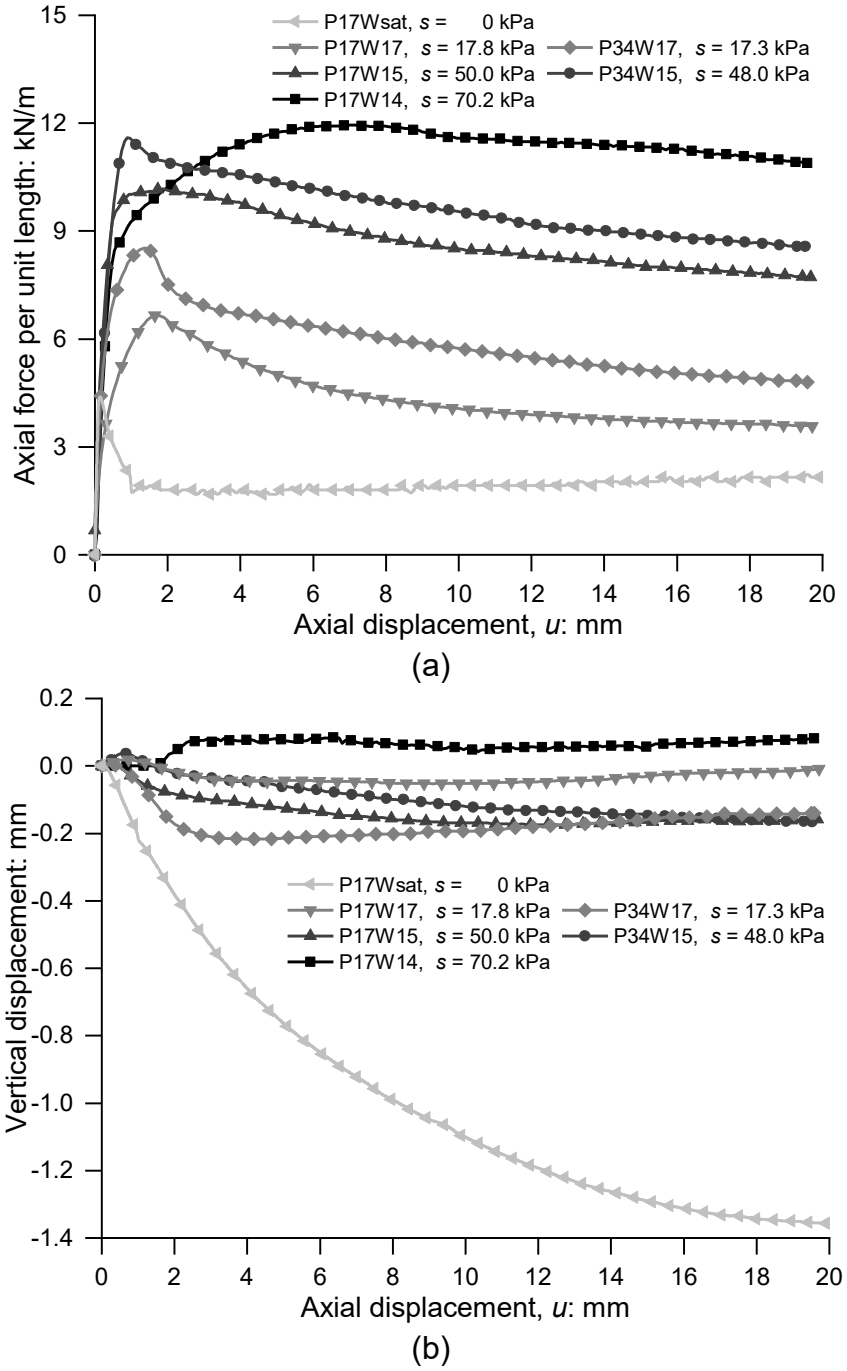

Figure 6.1 Axial behaviour of pipe: (a) axial force against axial displacement; (b) vertical displacement against axial displacement

Figure 6.1 (b) presents the vertical displacement behaviour for all tests. A clear and continuous settlement is observed in the curve for the saturated condition, with the settlement eventually reaching 1.35 mm. In contrast, the settlement under unsaturated conditions is not as evident. The maximum settlements for matric suctions ranging from 17.2 to 50.0 kPa do not exceed 0.22 mm (2.8 times d_{50}). The test with an average suction of 70.2 kPa exhibits uplifting

behaviour rather than settlement. These vertical displacement curves reflect the influence of soil-pipe interface behaviour due to two distinct mechanisms. On one hand, soil compression of the soil beneath the pipe due to variations in average effective stress tends to cause the pipe to settle. On the other hand, the dilation behaviour of the soil-pipe interface shear band below the pipe tends to lift the pipe. The stronger compression modulus of unsaturated CDG compared to saturated soil reduces the impact of the first mechanism, while its enhanced interface dilatancy leads to more pronounced pipe lifting. Consequently, the settlement of the pipe in unsaturated CDG is less than that in saturated CDG, and there is even lifting when the suction reaches 70.2 kPa.

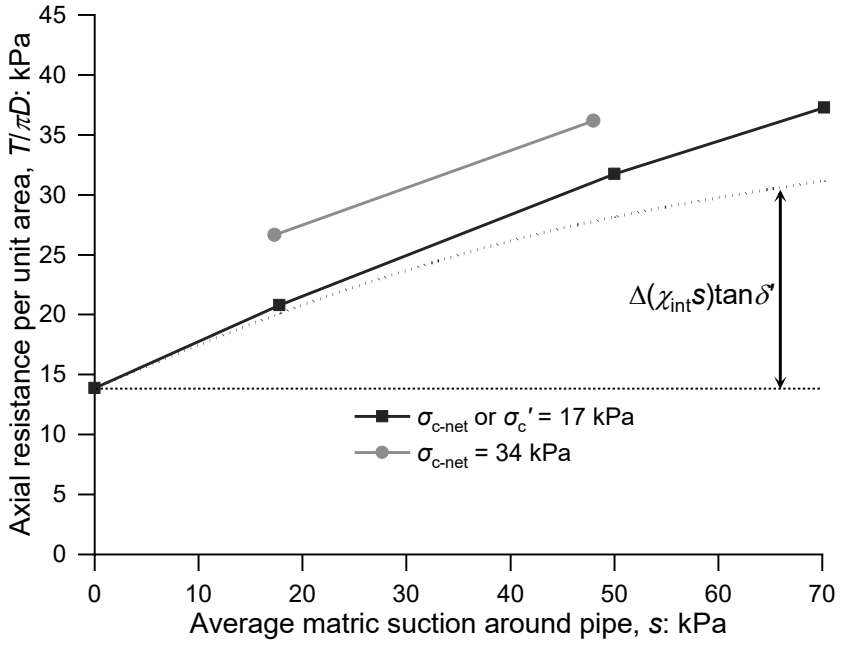

Figure 6.2 Axial resistance against average matric suction

6.4.2 Effects of suction and buried pressure on pullout resistance

Figure 6.2 illustrates the relationship between axial pullout resistance per unit area, $T/(\pi D)$, and the average matric suction around the pipe. The increase in the interface shear strength due to the additional interface contact pressure induced by capillary forces ($\Delta(\chi_{int}s)\tan\delta'$, according to Equation (6-1)) is included for comparative analysis. As matric suction rises from 0 to 70.2 kPa, axial resistance per unit area increases ($\Delta T/(\pi D)$) under $\sigma_{c\text{-}net}$ of 17 kPa is up to 25.4 kPa,

while the value of $\Delta(\chi_{int}s)\tan\delta'$ is 17.3 kPa. This indicates that around 68% of $\Delta T/(\pi D)$ is due to the increase in Bishop's interface contact pressure. As for the remaining 32%, it mainly results from the stronger constrained dilation behaviour in unsaturated soils. The presence of soil away from the interface constrains the dilation trend at the interface, leading to increased net interface contact pressures during shearing. Constrained dilation-induced interface contact pressure increase is a function of soil dilatancy and stiffness (Luo *et al.*, 2000), which is discussed later. The dilatancy of the unsaturated CDG-pipe interface is positively correlated with matric suction when suction is below at least 300 kPa (Hossain & Yin, 2015). Moreover, the stiffness of soil with fine particles is also found to generally increase with suction (Han & Vanapalli, 2016). Therefore, the difference between $\Delta T/(\pi D)$ and $\Delta(\chi_{int}s)\tan\delta'$ increases from 10 to 32% of $\Delta T/(\pi D)$ with suction increasing from 17.8 to 70.2 kPa. Furthermore, it should be acknowledged that axial resistance may not exhibit a continuous increase with further increments in matric suction. A principal limitation of the present study lies in the fact that the maximum matric suction was restricted by the limitations of the matric suction measurement technique. Consequently, uncertainties remain regarding the behavior under field conditions characterized by higher matric suctions, particularly in arid regions.

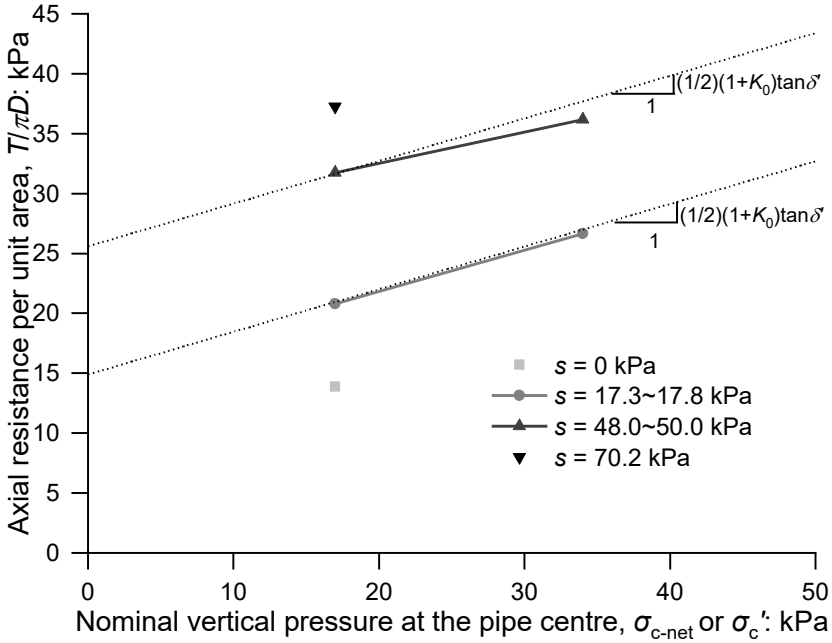

Figure 6.3 Axial resistance against nominal vertical pressure at the pipe centre

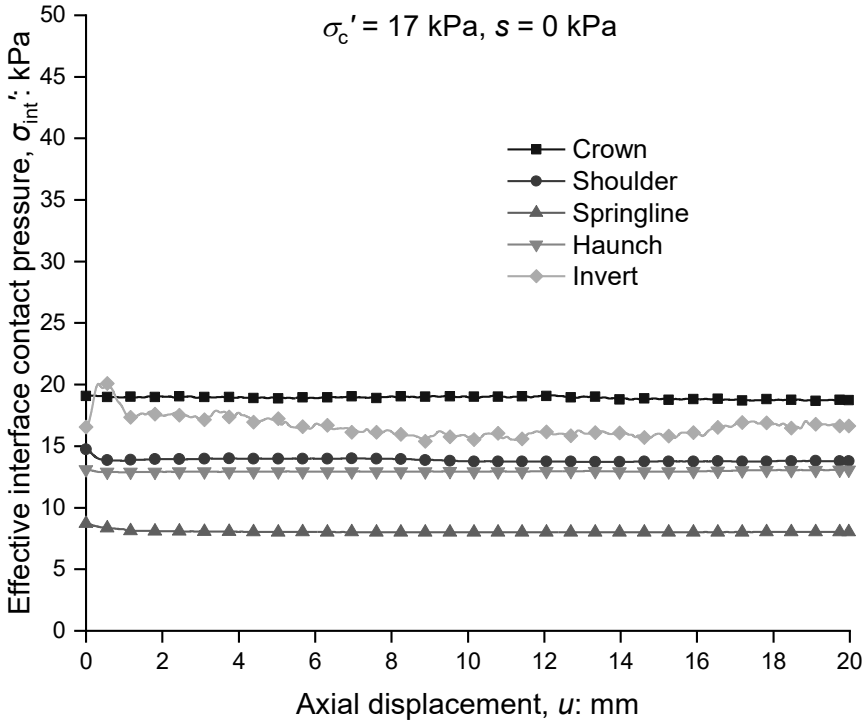

(a)

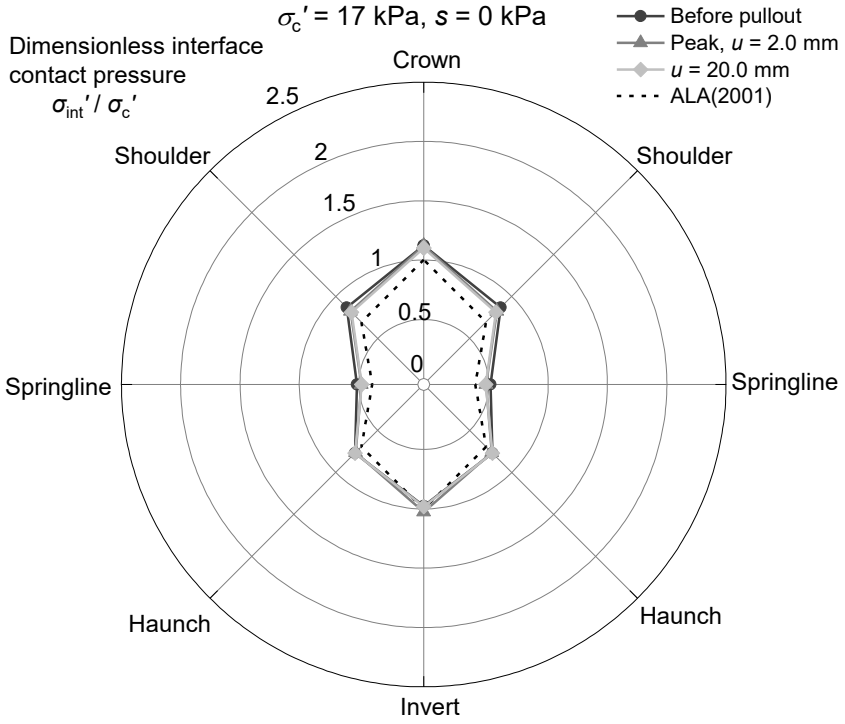

(b)

Figure 6.4 Interface contact pressure (σ_c'= 17 kPa, s = 0 kPa): (a) development; (b) distribution

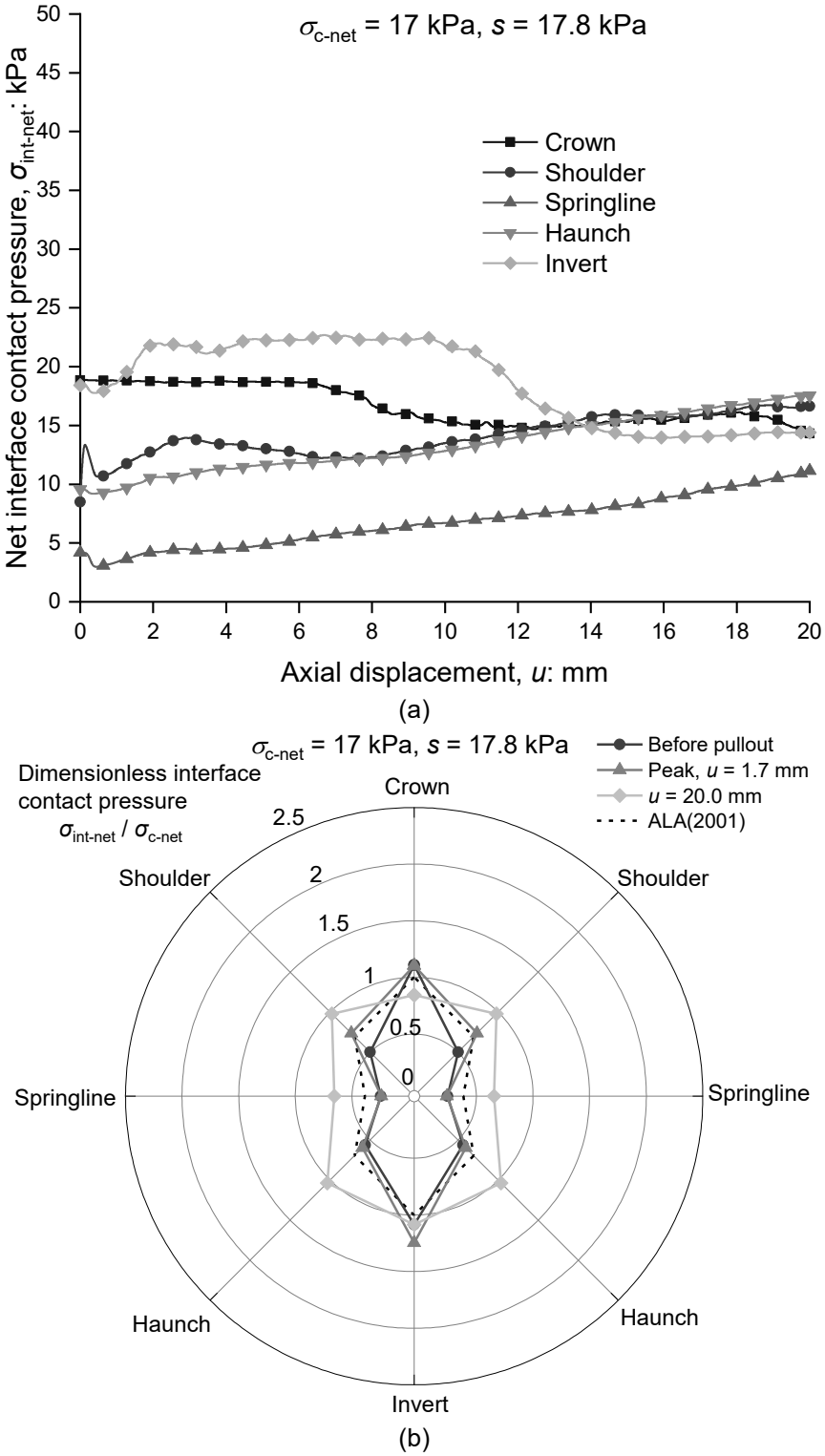

Figure 6.5 Interface contact pressure ($\sigma_{c\text{-}net}$, s = 17.8 kPa): (a) development; (b) distribution

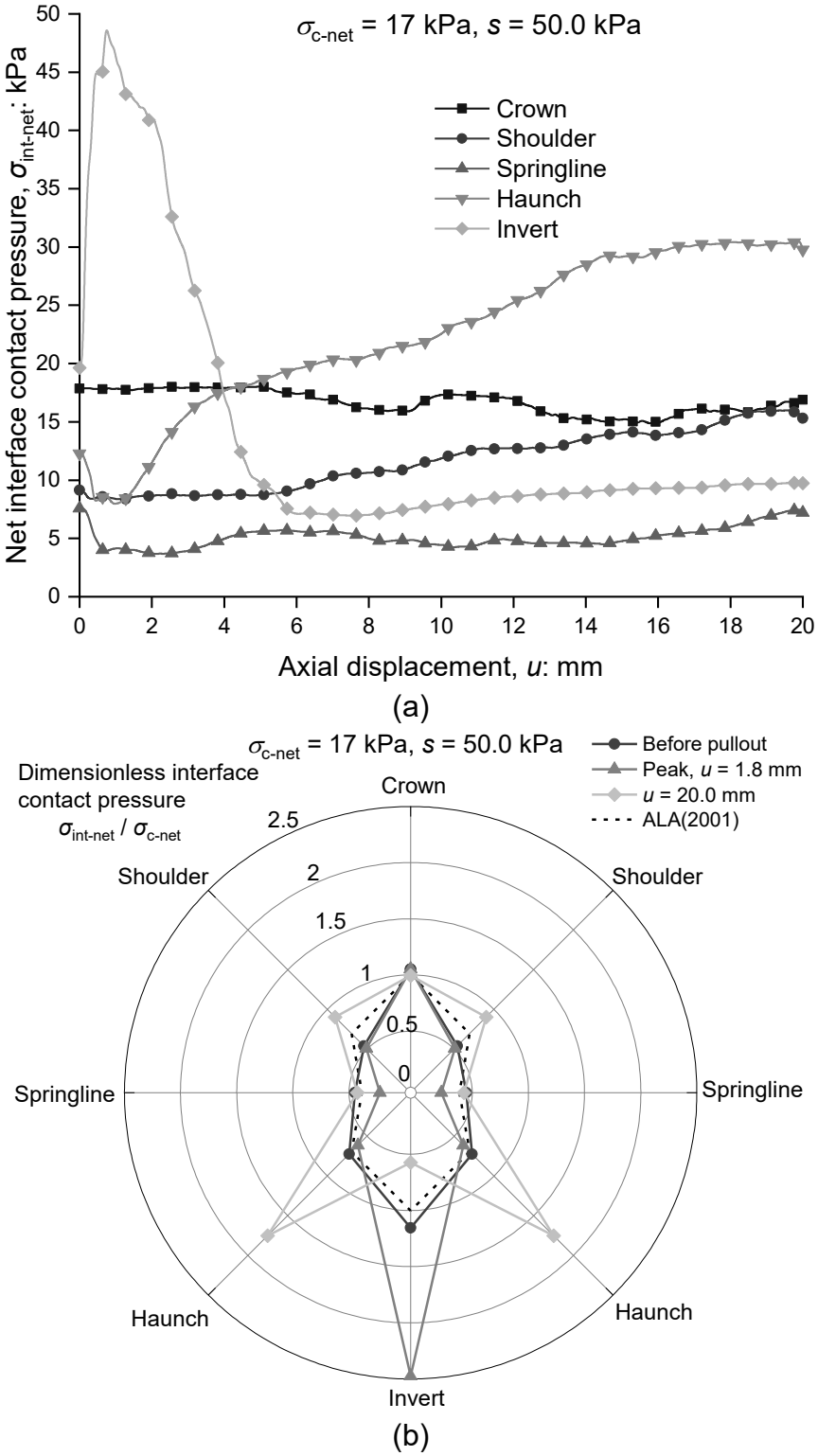

Figure 6.6 Interface contact pressure ($\sigma_{c\text{-net}}$ = 17 kPa, s = 50.0 kPa): (a) development; (b) distribution

Figure 6.3 demonstrates that axial pullout resistance increases with the nominal pressure at the pipe centre. The slopes of $T/(\pi D)$ as net nominal pressure increases from 17 to 34 kPa for

pipes subjected to suctions of 17.3~17.8 and 48.0~50.0 kPa are 0.343 and 0.261, respectively. These values are slightly smaller than $(1/2)(1+K_0)\tan\delta'$ (0.356), the theoretical slope based on Equation (2-2). Here, K_0 is typically taken as $1-\sin\varphi'$. This trend may be attributed to another interface contact pressure variation mechanism, where matric suction reduces the lateral earth pressure at rest, resulting in a decreasing trend of the above slopes as suction increases.

6.4.3 Suction effects on interface contact pressures distribution and evolution

Figure 6.4, Figure 6.5 and Figure 6.6 present the distribution and evolution of interface contact pressures for tests conducted under a nominal vertical pressure of 17 kPa, with average suction ranging from 0 to 50.0 kPa. The interface contact pressure measured by TPS, σ_{int}, is the total stress. For saturated soils, the effective interface contact pressure σ_{int}' ($=\sigma_{int}-u_w$) is used below. Here, u_w is pore pressure, which exhibits limited variation during the pipe pullout process. Hence, u_w is taken as hydrostatic pressure in this study. For unsaturated soils, the interface contact pressure can be treated as net interface contact pressure $\sigma_{int\text{-}net}$ ($=\sigma_{int}-u_a$), where u_a (= 0 kPa in this study) is the air pressure. According to guidelines, the interface contact pressures should be σ_c' or $\sigma_{c\text{-}net}$ (17 kPa) at the crown and invert, $K_0\sigma_c'$ or $K_0\sigma_{c\text{-}net}$ (6.53 kPa) at the springlines, and $(1/2)(1+K_0)\sigma_c'$ or $(1/2)(1+K_0)\sigma_{c\text{-}net}$ (11.77 kPa) at the shoulders and haunches.

Prior to pullout of the pipe buried in saturated soils, all interface contact pressures, except at the invert, are slightly higher than the expected values. This contrasts with previous findings by Sheil *et al.* (2018) and CHAPTER 4 on pipes buried in sand, where springline interface contact pressure is typically slightly lower than anticipated. This discrepancy may be attributed to the use of an earth rammer during compaction, which, combined with the pipe's stiffness, causes stress concentration across the pipe surface. During the pullout process, the interface contact pressure at the pipe invert increases by approximately 4 kPa at an axial displacement of 0.4 mm, corresponding to the peak axial force in Figure 6.1 (a) and the settlement behaviour in

Figure 6.1 (b). Changes in interface contact pressure at other locations are minimal, aligning with the limited interface dilatancy of saturated CDG shown in Figure 3.22.

Before pipe pullout in unsaturated soils, net interface contact pressures at the springline are 4.18 and 7.59 kPa for suctions of 17.8 and 50.0 kPa. These values are smaller than the value of $K_0\sigma_{c\text{-}net}$ and the value measured in the saturated condition, demonstrating the reduction of lateral earth pressure due to matric suction as discussed by Fredlund & Rahardjo (1993) and Lu & Likos (2004), and thus slightly reduces the slopes of $T/(\pi D)$ as net nominal pressure increases in Figure 6.3. However, the average initial net interface contact pressures at suctions of 0, 17.8 and 50.0 kPa are 13.59, 10.21 and 11.93 kPa, respectively. These values deviate by no more than 15.5% from the classical empirical formula $K_0=1\text{-}\sin\varphi'$, which doesn't consider the suction effect and the overconsolidation ratio (OCR). Given the absence of a reliable formula for K_0 in unsaturated soils, using this equation, which doesn't consider the suction effect, to evaluate the average initial net interface contact pressure of pipes buried in unsaturated soils is a practical approach. During the pullout process, interface contact pressures at different locations generally increase. The increase at the pipe invert is most pronounced early in the pullout, reaching maximums of 22.7 and 48.3 kPa for average matric suction of 17.8 and 50.0 kPa, respectively, playing a crucial role in axial pullout resistance. Interface contact pressures at the springline for suctions of 17.8 and 50.0 kPa decrease to 4.06 and 3.82 kPa, respectively, at the axial displacement when axial force peaks. This results from the equilibrium of initial concentration on the pipe interface disturbed during pullout, causing lateral earth pressure to approach the theoretical lateral earth pressure at rest. Late-stage pullout interface contact pressure increase concentrates on the shoulder and haunch, reaching 12.50 and 10.13 kPa for suction of 17.8 kPa and 8.65 and 10.44 kPa for suction of 50.0 kPa. The overall interface contact pressure increase is more significant for tests with higher average matric suction. It is due to stronger constrained

dilation with increasing suction, supporting the above finding where the difference between $\Delta T/(\pi D)$ and $\Delta(\chi_{int}s)\tan\delta'$ increases with suction in Figure 5.2.

Moreover, the redistribution of interface contact pressure caused by the soil arching effect (e.g., the higher pressure at the pipe crown and haunches than the predicted values) is less pronounced than in previous tests using sands by Sheil *et al.* (2018) and CHAPTER 4. This may be because the higher compression modulus of saturated and unsaturated CDG minimises the soil arching effect on the pipe.

6.4.4 Suction effects on stress path

Figure 5.6 illustrates the stress paths at the soil-pipe interfaces in physical modelling. The horizontal axis represents Bishop's interface contact pressure as $\overline{\sigma}_{int\text{-}net}+\chi_{int}s$, where $\overline{\sigma}_{int\text{-}net}$ is the average value of net interface contact pressures. The interface failure envelopes of saturated CDG, obtained through CNL interface direct shear tests, are included as references. The shapes of the stress paths are influenced by the average matric suction. In saturated conditions, due to limited variation in interface contact pressure, the stress path rises vertically towards the peak failure envelope and then descends vertically back to the critical state failure envelope.

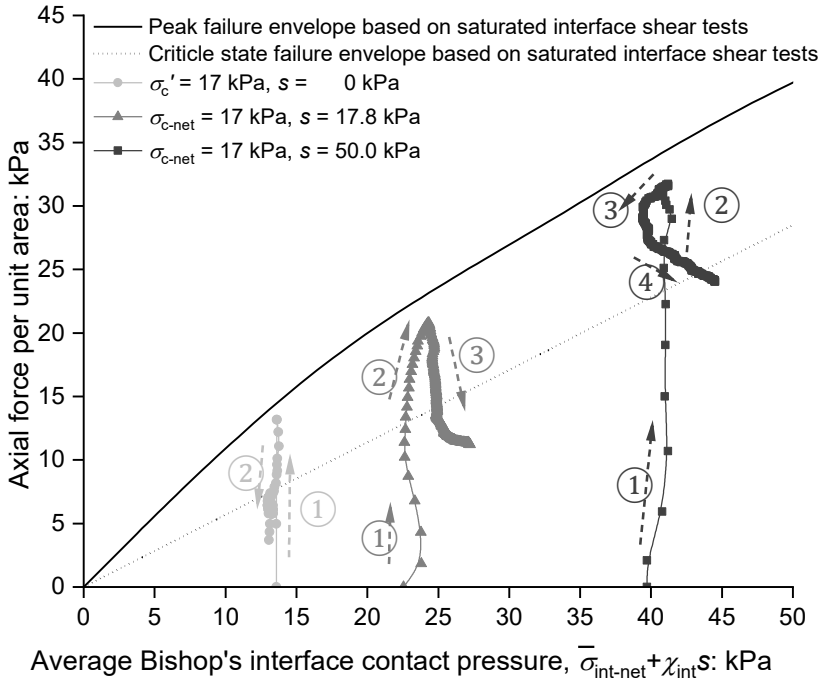

Figure 6.7 Stress path based on average interface contact pressure measured by TPS

In unsaturated conditions, the evolution of the stress path becomes more complex. For the matric suction of 17.8 kPa, the path includes three stages, resembling the typical stress path observed in CNS tests on the rough interface of dry sands (Ooi & Carter, 1987; Pra-ai & Boulon, 2016). In the first stage, the stress path rises vertically, indicating that friction angle mobilisation is dominated by elasticity. The path shape during this stage is flexural due to the dynamic equilibrium between the increment in interface contact pressure caused by constrained dilation and the decrease in lateral earth pressure caused by shear disturbance. In the second stage, the path moves towards the top right, approaching the peak failure envelope, illustrating that the increment in interface contact pressure due to constrained dilation has become dominant. Finally, the path moves to the bottom right and stops near the critical state envelope, indicating a transition of the friction angle from peak to critical state and further constrained dilation behaviour. For the suction of 50.0 kPa, the stress path during the first and second stages is similar to that of 17.8 kPa, initially rising vertically and then turning to the top right. The major difference occurs before the final stage, where the path moves to the bottom right; here, the stress path shifts towards the bottom left initially. This shift is due to the non-synchronised evolution of interface contact pressures at different surface locations, where the interface contact pressure at the invert rises sharply to 48.3 kPa and descends sharply back to 7.0 kPa.

6.5 Development of a new method for calculating the pullout resistance of pipe buried in unsaturated soils

CHAPTER 4 proposed an equation that accounts for constrained dilation and the self-weight of the pipe to calculate pullout resistance for pipes buried in dry sand in Equation (4-1). The prediction on axial pullout resistance of pipes buried in unsaturated soil can be extended by combining Equation (6-1) with Equation (4-1) as

$$T = \pi D\left[c_{\text{int}}{}' + \left(\frac{1+K_0}{2}\sigma_{\text{c-net}} + \chi_{\text{int}} s + \Delta\sigma_{\text{D}}{}' + \Delta W/\pi D \right)\tan\delta' \right] \tag{6-2}$$

K_0 is estimated by 1-sinφ', without considering the suction effects as mentioned. More details are available in CHAPTER 4. The method of Audibert & Nyman (1977) is used to determine u_c from Figure 6.1. This involves drawing a horizontal line through the maximum axial force and a secant line from the origin to the point of 70% of the maximum axial force. Their intersection determines u_c. Table 6.3 summarises the values of u_c in this study and Al-Khazaali & Vanapalli (2019), ranging from 0.09 to 2.85 mm. G and ψ_{max} depend on matric suction and degree of saturation, typically being larger in unsaturated soils than in saturated or dry soils (Hossain & Yin, 2015; Han & Vanapalli, 2016). The determination of G of unsaturated soils is as follows. The shear modulus of unsaturated soils, G_u, can be determined by replacing effective stress as Bishop's stress in the shear modulus equation for dry or saturated soils, by CHAPTER 4, as the method of Sawangsuriya *et al.* (2009), expressed as

$$G_u / p_a = \frac{A(\gamma)}{(1+e)^3}\left(\frac{\sigma_{i\text{-}net} + \chi s}{p_a}\right)^{m(\gamma)} \quad (6\text{-}3)$$

where $A(\gamma)$ and $M(\gamma)$ are the material parameter and the effective stress exponent parameter, which are functions of the shear strain γ (i.e., ratio of axial displacement to shear band thickness); p_a is the reference pressure of 100 kPa; $\sigma_{i\text{-}net}$ is the initial net stress, taken as $\sigma_{c\text{-}net}(1+K_0)/2$ in this study; χ (=S_r^{κ}) is Bishop's stress parameter for pure soils **(**Bishop, 1959**)**, where κ is an empirical exponent parameter, typically 2 for clayey and silty soils (e.g., CDG) and 1 for cohesionless soils (Han & Vanapalli, 2016). Based on the values of u_c in Table 6.3 and the empirical data in interface shear band thickness (DeJong & Westgate, 2009), the critical interface shear strains at which the axial force reaches its peak values are determined to be no less than 10%. For CDG, based on the empirical values of Wang & Ng (2005); Oztoprak & Bolton (2013); Dong *et al.* (2018); Bentil (2023), the values of $A(\gamma)$ and $M(\gamma)$ for γ =10% are 6.113 and 0.448. As for clean sand, such as Unimin 7030 quartz silica sand used by Al-Khazaali & Vanapalli (2019), Oztoprak & Bolton (2013) developed a model of G based on a database of

454 tests from the literature, where the empirical values of $A(\gamma)$ and $M(\gamma)$ are 126 and 1 for γ =10%.

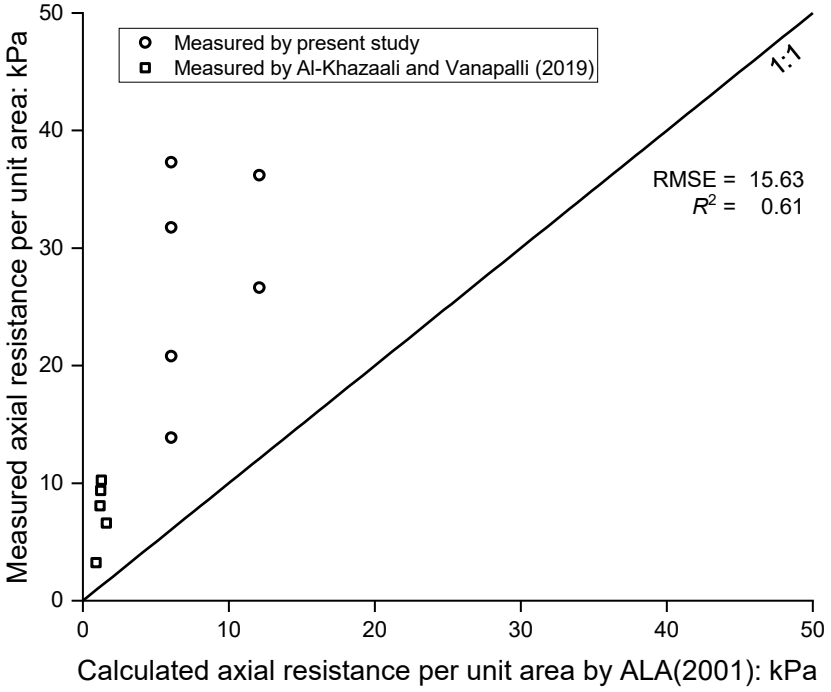

(a)

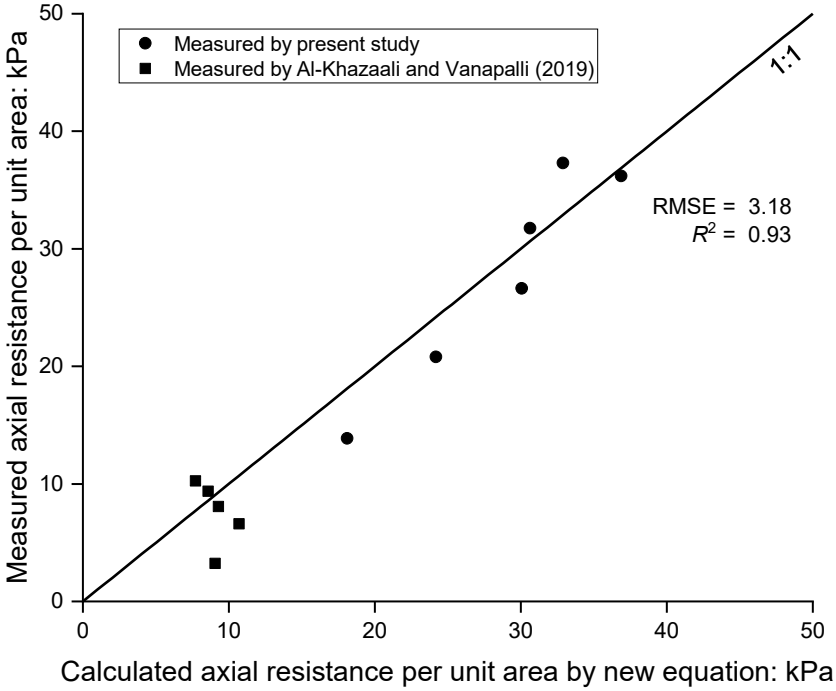

(b)

Figure 6.8 Axial pullout resistance at the unsaturated conditions predicted by (a) ALA (2001); (b) new equation

Secondly, ψ_{max} in Equation (4-5) is normally higher in unsaturated soil than that of dry or saturated soil, especially for the silty and clayey soils. However, there are limited models to predict ψ_{max} of unsaturated soil ($\psi_{max\text{-}u}$). For CDG, values of ψ_{max} and $\psi_{max\text{-}u}$ are determined as 0° and 5.71°, respectively, based on the direct shear tests of CDG by Hossain & Yin (2010). As for the sand of Al-Khazaali & Vanapalli (2019), a constant value of 6.75° from their direct shear test of dry soil is used for both saturated and unsaturated soils, considering the lack of data and minimal suction effect on $\psi_{max\text{-}u}$ of pure sand. Once a reliable model for the maximum dilation angle of unsaturated soil is developed, it is expected to be integrated into the proposed equation.

In summary, the new equation of unsaturated soil can be expressed as

$$T = \pi D\left[c_{int}{}' + \left(\frac{1+K_0}{2}\sigma_{c\text{-net}} + \chi_{int} s + 2G_u \frac{u_c}{D}\tan\psi_{max-u} + \frac{D}{4}\Delta\gamma \right)\tan\delta' \right] \quad (6\text{-}4)$$

Table 6.3 summarises the parameters for the new equation, including data from Al-Khazaali & Vanapalli (2019) and the present study. Figure 5.11 shows the calculated results based on these parameters. To evaluate the performance of the new equation, its results are compared with those of ALA (2001) and with the new equation applied without considering the matric suction effect (i.e., excluding the $\chi_{int}s$ term and using the values of G and ψ_{max} under saturated conditions). The Root Mean Square Error (RMSE) and R^2 of the new model are 3.18 and 0.93, respectively, demonstrating significantly better performance compared to the values of 15.63 and 0.61 for the prediction of ALA (2001) and 8.47 and 0.63 for the calculated results without considering matric suction.

6.6 Summary

A large-scale experimental system was employed to investigate the axial behaviour of steel pipes buried in unsaturated CDG. This study presents and analyses six tests with average matric suctions around the pipe ranging from 0 to 70.2 kPa, under nominal vertical pressures at the pipe centre of 17 and 34 kPa. The experimental findings led to several key conclusions:

The axial pullout resistance of the pipe increases with suction. Under the nominal pressure of 17 kPa, the axial resistance at an average suction of 70.2 kPa was 1.69 times greater than at 0 kPa (saturated condition), highlighting a significant underestimation of the load from soils to pipes in current design guidelines, which poses risks to pipeline systems.

The additional interface contact pressure induced by capillary forces of liquid menisci between the interface and soil particles, $\chi_{int}s$, plays a major role in axial resistance under unsaturated conditions. Of the suction-induced axial resistance increase at 70.2 kPa, 68% is attributed to the increment in $\chi_{int}s$.

The remaining increase in axial resistance in unsaturated conditions results from variations in average net interface contact pressure. Lateral earth pressure at rest decreases with increasing suction, leading to smaller initial net interface contact pressures at the springline. However, due to stress concentration on the pipe, the suction-induced reduction of lateral earth pressure is no more than 15.5% of the theoretical value, contributing minimally to axial resistance variation. In contrast, constrained dilation plays a key role in increasing net interface contact pressure. The dilatancy and stiffness of CDG, two key factors of constrained dilation, increase as matric suction rises in CDG. Consequently, the increment in axial resistance due to net interface contact pressure variation increases from 10 to 32% as suction increases from 17.8 to 70.2 kPa.

A new method for predicting axial pullout resistance in unsaturated soils was proposed, based on Bishop's stress. This method considers the suction effects on Bishop's interface contact pressure and net interface contact pressure increase caused by stronger constrained dilatancy of the unsaturated soils. Compared to the existing equation of the guideline, the new equation demonstrated better predictive capabilities, with verification of test results from both previous and current studies.

Table 6.3 Parameters for the new equation of unsaturated soils

Parameters	Present study						Al-Khazaali & Vanapalli (2019)				
Nominal pressure, $\sigma_{c\text{-}net}$ or σ_c': kPa	17	17	17	17	34	34	4.42*	4.22*	3.47*	3.35*	3.25*
Average suction, s: kPa	0	17.8	50.0	70.2	17.8	48.0	2.75	4.5	7.25	8	9.75
Unit weight difference, $\Delta\gamma$: kN/m^3	0.05	0.62	0.92	1.10	0.05	0.07	0.22	1.21	4.95	5.55	6.06
Critical displacement, u_c: mm	0.09	0.80	0.39	0.74	0.44	0.55	0.53	1.39	0.20	0.37	0.64
Maximum dilation angle, ψ_{max}: °	0	5.71	5.71	5.71	5.71	5.71	6.75	6.75	6.75	6.75	6.75
Pipe diameter, D: mm	102						114.3				
Interface friction angle, δ': °	24.8						34.5				
Interface shear strength intercept, c_{int}': kPa	10.8						0				
Exponent parameter of Bishop's stress for the interface, κ_{int}	2.5						0.1†				
Effectiver internal friction angle, φ': °	38						35.3				
Void ratio, e	0.538						0.606				
Exponent parameter of Bishop's stress for pure soils, κ	2‡						1‡				
$A(\gamma)$	6.113						126				
$M(\gamma)$	0.448						1				

*Estimation based on average suction and soil-water retention curve
†Back-fitting value based on physical modelling and recommended by Al-Khazaali & Vanapalli (2019)
‡Recommended by Han & Vanapalli (2016)

CHAPTER 7
DEM SIMULATION OF AXIAL BEHAVIOUR OF PIPES BURIED IN DRY SOILS

7.1 Introduction

This paper aims to develop a new method to simulate ASPI behaviour using YADE (Kozicki & Donzé, 2008; Šmilauer & Chareyre, 2021). Pipes with different surface roughness are generated using a clump body. Rigid-periodic-mixed boundary conditions, plane-symmetric assumption, and the particle refinement method (PRM) are adopted to eliminate the boundary effect and reduce the particle size scaling factor to get more accurate results. The main objectives are: (a) to validate the numerical model against the physical modelling database in CHAPTER 4, (b) to reveal the mechanism of ASPI behaviour with various surface roughness levels, and (c) to conduct parameter studies for better understanding the effects of interface roughness in a wide range and pipe diameter.

7.2 Numerical model and boundary conditions

Figure 7.1 presents the schematic diagram of the 3D DEM numerical model for investigating ASPI, which includes soil particles, a pipe and a domain enclosed by rigid and periodic walls. To eliminate boundary effects, the front and rear boundaries (y direction) in the simulation were a pair of parallel periodic walls (see the front view of Figure 7.1) rather than rigid walls in physical modelling in CHAPTER 4 and DEM simulation by Meidani *et al.* (2017). Particles that move through one periodic wall reappear at the corresponding location on the opposite wall. This setup creates the effect of the original zone being adjacent to identical copies of itself in the axial direction (Cundall, 1988; O'Sullivan, 2011). The pipe's axis is always perpendicular to the periodic front and rear walls, ensuring only one pipe appears. There are two main reasons for this choice in the simulation. First, computational costs limit the number

of numerical particles, and consequently, the dimensions of the numerical sample. A numerical sample with dimensions fully matching the physical modelling in CHAPTER 4 would require at least 4.4 million particles, which is nearly impossible with the current version of YADE. In contrast, the axial periodicity of the numerical model allows for a very small thickness of the periodic domain (i.e., the distance between the two periodic walls). A sensitivity analysis that will be mentioned later determines a periodic domain thickness of approximately 34 mm, which is nearly 300 times the soil sample length in the physical modelling setup, significantly reducing the numerical particle number. Second, the actual axial boundary condition in the experiments by CHAPTER 4 may lie somewhere between the rigid and periodic conditions. However, replicating the sleeves and rubber membranes in the simulation is overly complex. In contrast, periodic front and rear walls effectively eliminate boundary effects. This boundary condition makes the DEM model infinite in the pipe's axial direction, closely resembling engineering practice. Therefore, despite a slight difference from the physical modelling, using the periodic boundary could be more practical and valuable.

Additionally, the friction angles between the particles and the top and bottom walls are artificially set to 90° to ensure adequate reaction to counterbalance the axial force exerted by the pipe interface on the soil sample entirety and avoid unreasonable sliding at the top, bottom and side walls. It is consistent with the periodic boundary interface shear DEM simulation by Wang *et al.* (2022). The soil particle displacement field in the following DEM simulations on ASPI reveals that soil particle displacements in the axial direction decrease as the distance from the pipe surface increases, approaching zero near the top and bottom walls. This observation aligns with expectations, confirming the appropriateness of the boundary setting.

A plane symmetry condition along the vertical centre axis was applied using a centre wall to reduce particle number, as shown in Figure 7.1. Particles contacting the centre wall experience a normal force equivalent to contact with a particle of the same size while

experiencing no shear force by setting the friction of the centre wall to zero. This approach is common in many soil-structure interaction experiments and numerical models (Tehrani *et al.*, 2016; Zhu *et al.*, 2020; Murugathasan *et al.*, 2021). The ratio of the pipe's outer diameter, D, to $d_{50\text{-A}}$ (the mean numerical particle size near the pipe surface, i.e., in Zone A) is 68, significantly higher than 3.6 to 22 in previous 3D DEM studies on pipes, piles or penetrometers (Zhang & Wang, 2015; Meidani *et al.*, 2017; Sharif *et al.*, 2021; Guo *et al.*, 2024) ensuring minimal impact on the plane symmetry assumption. Considering the plane symmetry assumption, the horizontal translation freedom and all three rotational freedoms of the entire pipe are fixed.

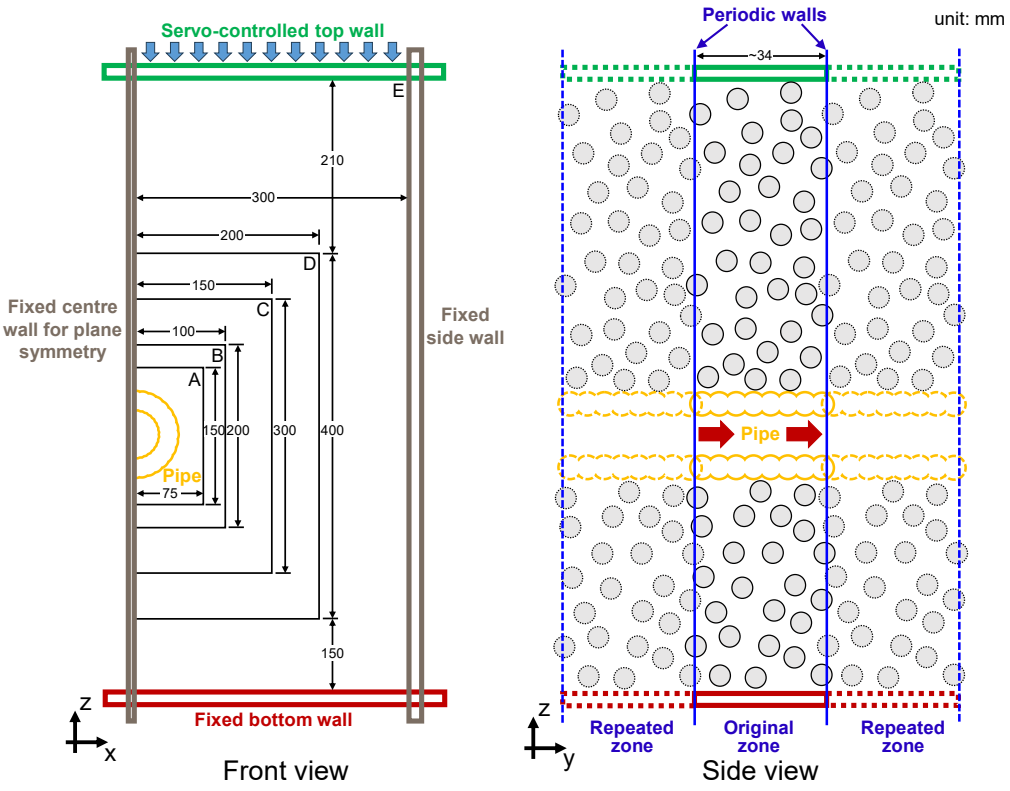

Figure 7.1 Schematic diagram of the numerical model for investigating the axial pipe-soil interaction

The dimensions of the domain space bounded by the top, bottom, centre, and side walls are initially 0.71 m in height and 0.3 m in width, with the initial height of the pipe centre at 0.35 m, corresponding to the physical modelling in CHAPTER 4 to facilitate back-calculation. The bottom, side, and centre walls are fixed. The top wall is servo-controlled to maintain the

nominal pressure at the pipe centre, σ_c', replicating the flexible pneumatic bag used in the physical modelling. The target pressure on the top wall is set to σ_c'-$\gamma' H_{c0}$, where H_{c0} is the real buried depth from the ground surface to the pipe crown.

Table 7.1. Scaling factor for soil particle size, minimum thickness and particle number of each zone

Zone	A	B	C	D	E
Scaling factor for soil particle size, f_s	4	6	9	13.5	20.25
Ratio of scaling factors to its inner zone	—	1.5	1.5	1.5	1.5
Minimum horizontal thickness, t_{min}: mm	24	25	50	50	100
t_{min}/d_{50} in the corresponding zone	16.0	11.1	14.8	9.9	11.0
Particle number: 10^3	80	27	23	10	11

7.3 Soil particles and contact model

Particles are modelled using the classical Cundall contact model to calculate the inter-particle normal and shear forces (Cundall & Strack, 1979). An incrementally formed linear elastic-perfect plastic rolling resistance model is incorporated at particle-particle and particle-rigid wall contact to account for the non-sphericity of real sand particles. Detailed formulations of this contact model can be found in the YADE user manual (Šmilauer & Chareyre, 2021).

The sand used in CHAPTER 4 ranges from 0.25 to 0.5 mm with a median diameter (d_{50}) of 0.375 mm. To reduce the number of particles, a particle refinement method (PRM) was employed (Sharif *et al.*, 2021; Guo *et al.*, 2024). In this method, the domain space is divided into five zones (A to E) (see the front view of Figure 7.1), and the scaling factor for numerical soil particle size (f_s) in these zones increases from 4 to 20.25 as the distance from the pipe's axis increases. The scaling factor (f_s), minimum thickness, and particle number for each zone are detailed in Table 7.1. As Sharif *et al.* (2021) and Guo *et al.* (2024) suggested, d_{min} of the outer zone should be smaller than d_{50} of the inner zone to prevent particle migration between

zones. Consequently, f_s increases from 4 to 20.25 from Zone A to E, with a ratio of scaling factors to the corresponding inner zone of 1.5 (d_{50}/d_{min}). The minimum thicknesses of Zones A to E (t_{min}) are 24, 25, 50, 50, and 100 mm, respectively, corresponding to approximately 0.25 to 1 D. The ratio of t_{min} to d_{50} for each zone is no less than 9.9, which is larger than the 3.8 to 8 range found in previous studies (Butlanska *et al.*, 2009; Zhang & Wang, 2015; Guo *et al.*, 2024).

Table 7.2. DEM model parameters of ASPI at the dry condition

Parameters	Soil particles	Pipe particles
Normal stiffness to particle radius, k_n/r: MPa	60	300
Shear to normal stiffness ratio, k_s/k_n	0.3	0.3
Inter-particle friction angle, φ_{micro}: °	22	20
Dimensionless rolling strength	0.8	0.8
Dimensionless rolling stiffness	0.8	0.7
Particle size: mm	$0.25\times f_s \sim 0.5\times f_s$	4.5 ($3\times f_{s\text{-}A} \times 0.375$)
Local non-viscous damping ratio	0.2	
Pipe axial velocity: mm/s	2	
Relative density: %	85	
Gravity, m/s^2	9.8	

The contact model parameters were calibrated to match the results of CNL interface direct shear tests conducted with Fujian medium sand. Specimens of 60 × 60 × 20 mm^3 with a relative density of 85% were placed above a roughness-controllable interface and enclosed by five frictionless rigid walls. The maximum and minimum porosities of the soil in the simulation are 0.499 and 0.373, determined by the method of Macaro (2015). The interface was created by overlapping particles using the same approach and particle size as the pipe discussed later. The top wall is servo-controlled to apply effective normal stresses, σ_n', of 17, 34, 50, and 100 kPa on the specimens, corresponding to the target nominal pressure at the pipe centre. More details

of the interface direct shear tests can be found in CHAPTER 4. The scaling factor for the soil particle size in the interface direct shear simulation is four, consistent with that of the zone adjacent to the pipe (i.e., Zone A, as discussed later). Consequently, the ratio of specimen height to d_{50} is 13.3, larger than the typical range of 7.1 to 12 found in previous interface shear 3D DEM simulations (Jing *et al.*, 2017; Feng *et al.*, 2018; Liu *et al.*, 2021b). The calibrated parameter values are summarised in Table 7.2. Figure 7.2 compares the simulation results for rough and smooth interfaces using these parameters with experimental data. Both shear stress and vertical displacement demonstrate a high degree of accuracy. Compared to the experimental results, regular fluctuations are observed in the curves for the smooth interface. This is common in previous simulations of smooth interfaces, as the shear on a smooth interface is primarily due to sliding along the interface, which is regular in shape in the simulation, rather than the complex relative displacement occurring in the soil-interface shear band (Jing *et al.*, 2017). The computed maximum vertical displacements of the rough interface are 32~57% larger than the measured values. This discrepancy is likely attributed to the larger particle in the DEM model, which increases the volumetric expansion of the interface shear band. This difference may lead to a slightly higher increase in interface contact pressure due to the limitation of the surrounding soils on the trend of interface shear band volumetric expansion (i.e., constrained dilatancy, as discussed in detail later) in the simulation. The thickness of the shear band, determined by the inflexion point in the gradient of the curves of average horizontal soil displacement and the vertical distance from the interface, is 4.5~6.5 mm. It corresponds to 2.7~4.3 $d_{50\text{-A}}$ in this rigid boundary interface shearing simulation, within the empirical interface shear band thickness of 2~5 d_{50} observed in previous experimental studies (Uesugi *et al.*, 1988; DeJong *et al.*, 2003; DeJong & Westgate, 2009).

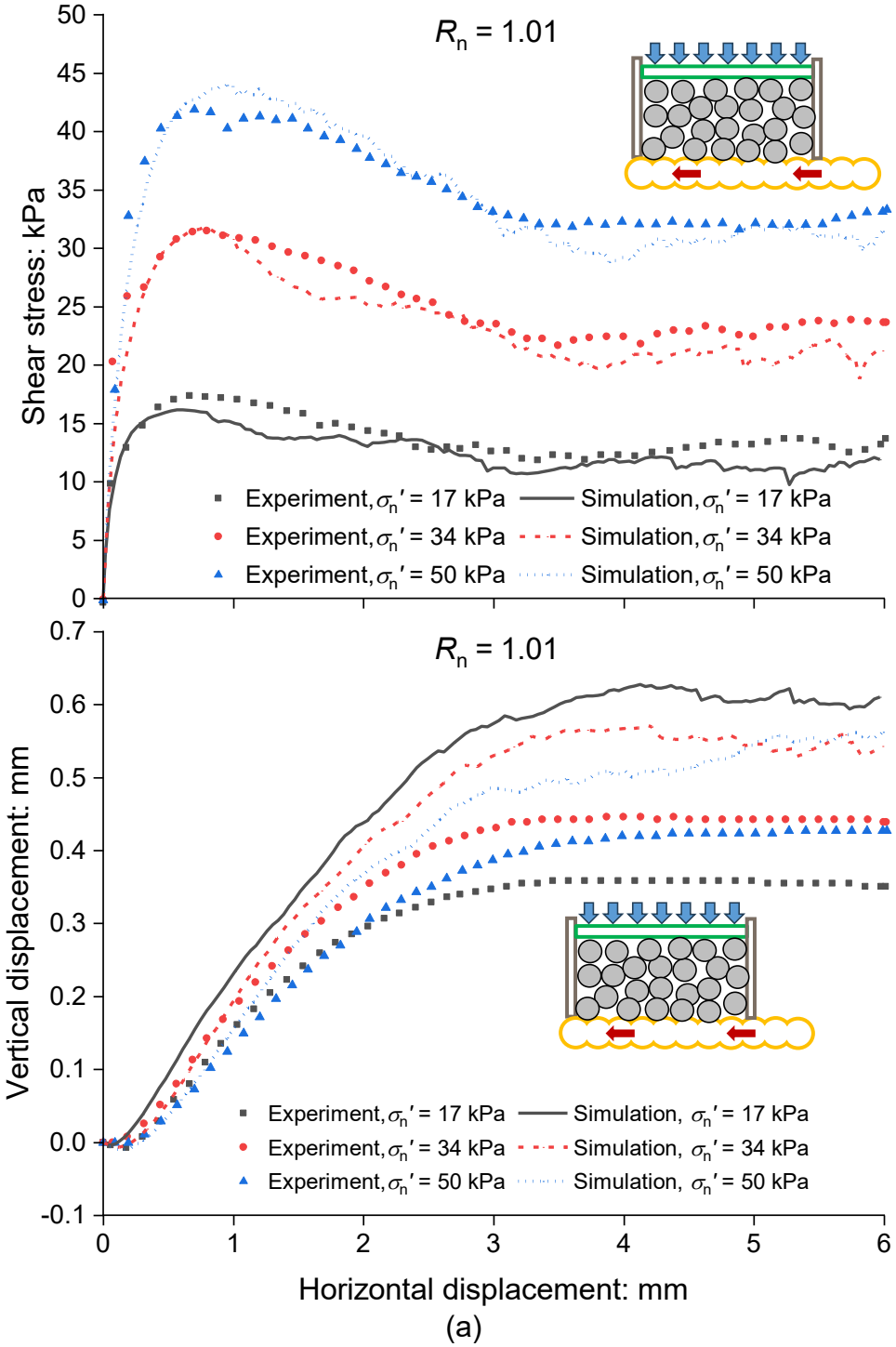
R_n = 1.01
Shear stress: kPa
Experiment, σ_n' = 17 kPa
Simulation, σ_n' = 17 kPa
Experiment, σ_n' = 34 kPa
Simulation, σ_n' = 34 kPa
Experiment, σ_n' = 50 kPa
Simulation, σ_n' = 50 kPa
R_n = 1.01
Vertical displacement: mm
Horizontal displacement: mm
(a)

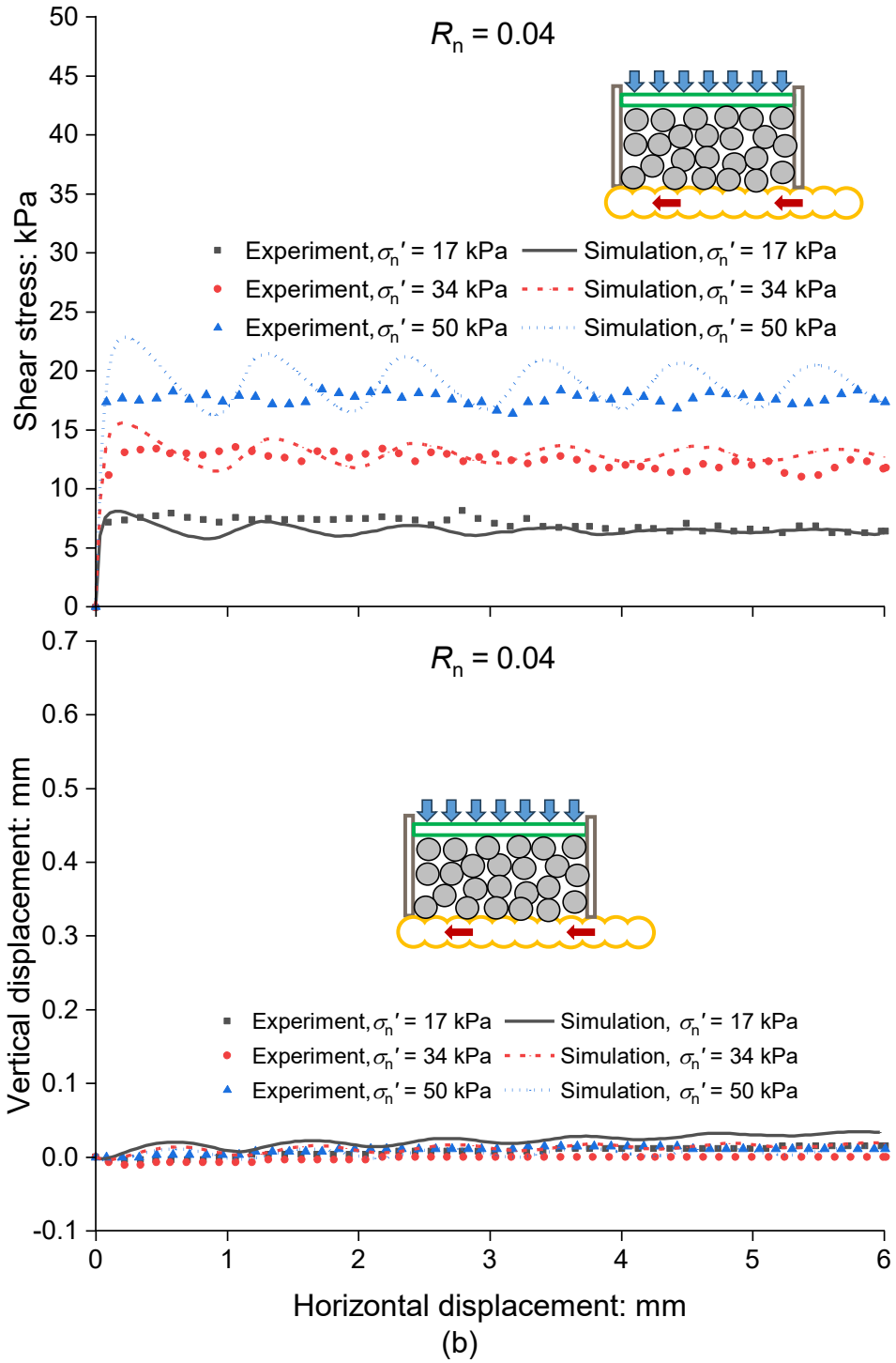

Figure 7.2 Validation of the contact model parameters using interface direct shear tests with rigid boundary (scaling factor for particle size, f_s = 4): (a) rough interface (normalised roughness, R_n = 1.01); (b) smooth interface (R_n = 0.04)

7.4 Modelling of pipe with various roughness conditions

The pipe was modelled by clumping overlapping particles, as illustrated in Figure 7.3. This method allows for control over the surface roughness by adjusting the diameter of the pipe particles, d_{pipe}, and the distance between two adjacent and touching pipe particles, Δl (where $\Delta l < d_{pipe}$. In line with physical modelling, the pipe surface roughness is evaluated using the normalised surface roughness (R_n) and can be numerically calculated by (d_{pipe}-$\sqrt{d_{pipe}^{\ 2} + \Delta l^2}$)/2. d_{pipe} is chosen to be 4.5 mm (3 × $d_{50\text{-A}}$) to prevent gaps between particles.

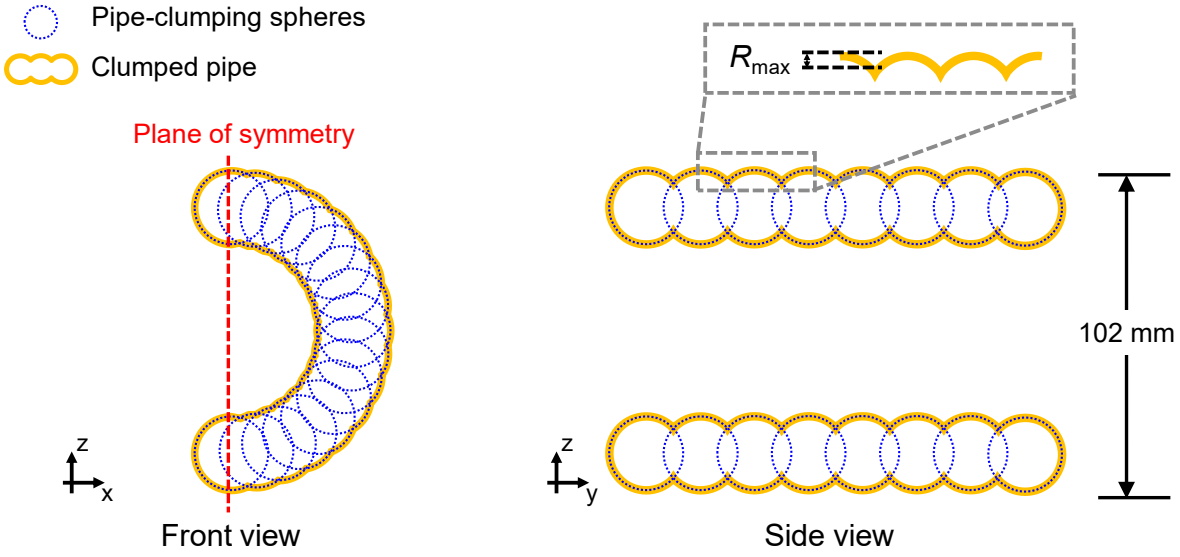

Figure 7.3 Schematic diagram of pipe

In the side view of the pipe shown in Figure 7.3, pipe particles are evenly distributed at a distance of (D-d_{pipe})/2 from their centre points to the target pipe centre axis, ensuring a consistent outer diameter (D) with the physical model. In the physical modelling in CHAPTER 4, the pipe surfaces were circumferentially treated using a turning method, resulting in different values for axial and circumferential roughness. In the simulation, the target values for axial R_n are 1.01 (rough) and 0.04 (smooth), aligning with the physical model. Circumferentially, pipe particles are arranged around the pipe centre with an angular gap of 1.2°, resulting in a circumferential R_n of approximately 0.04, which matches the R_n of untreated raw seamless steel pipe in CHAPTER 4.

To account for particle overlapping and the difference between the real pipe thickness and the size of the pipe particles, the material density input for the pipe particles is set as $m_{real}/(N_{pipe} \cdot V_{pipe})$ to achieve the same pipe mass as the physical model. Here, m_{real} ($=\rho_{steel}\pi(t_{pipe}^2 - 2Dt_{pipe})/4$) represents the pipe mass per meter; N_{pipe} is the number of pipe particles per meter; and V_{pipe} ($=\pi d_{pipe}^3/6$) is the volume per pipe particle.

This method of modelling the pipe doesn't consider pipe deformation. It is acceptable for the simulation of steel pipes buried in shallow ground, as used in CHAPTER 4, due to its minimal deformation. For instance, the axial strain of a smooth pipe subjected to a surcharge of 34 kPa is no more than 35 microstrains as measured by an optical fibre with the optical frequency domain reflectometry method.

7.5 Effectiveness of the periodic boundary and determination of periodic domain thickness

Before the formal simulation, two issues related to the use of the periodic boundary in the pipe's axial direction were addressed. The first issue concerns the effectiveness of using periodic front and rear walls. A comparison between periodic and rigid boundaries was made using the CNL interface shear simulation. The specimen size, scaling factor and relative density in the periodic boundary interface shear simulation were identical to those in the rigid boundary one for parameter calibration. The only difference was the periodic left and right walls (corresponding to the rear and front walls in ASPI). The results for the rough interface under 34 kPa are presented in Figure 7.4. The shear strength of the periodic boundary setup is 17.9 % lower than that of the rigid boundary, and the horizontal displacement at which the shear strength is 126.9 % larger. It indicates a reduction in soil-interface shear strength and stiffness.

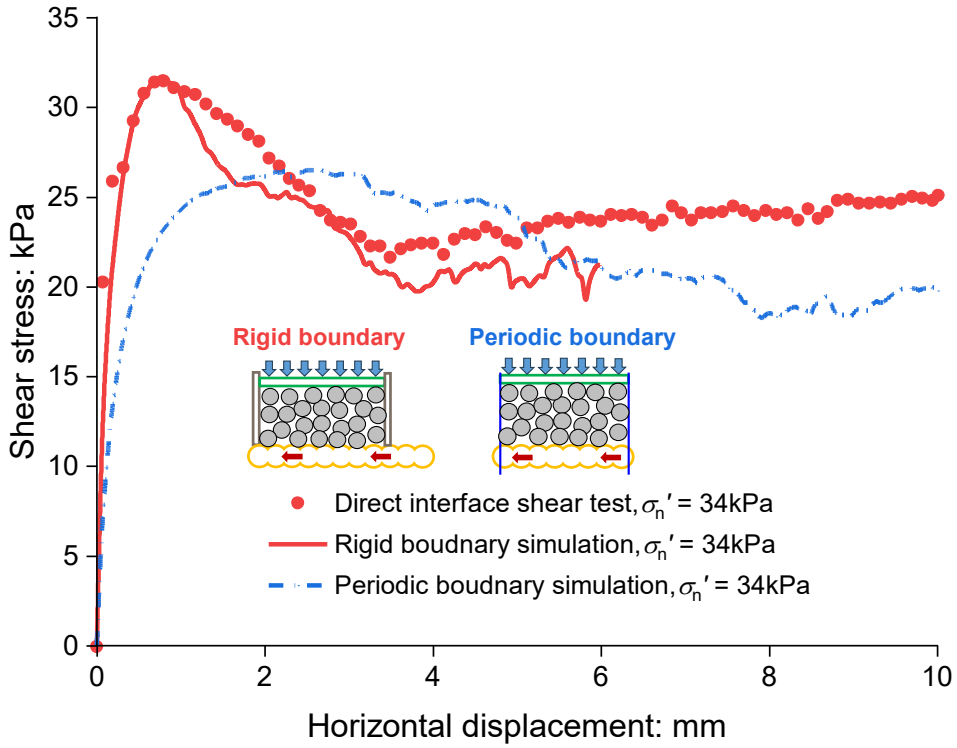

Figure 7.4 Comparison of interface shear stress in DEM interface shear simulations with different horizontal boundaries (σ_n' = 34 kPa, f_s = 4, R_n = 1.01)

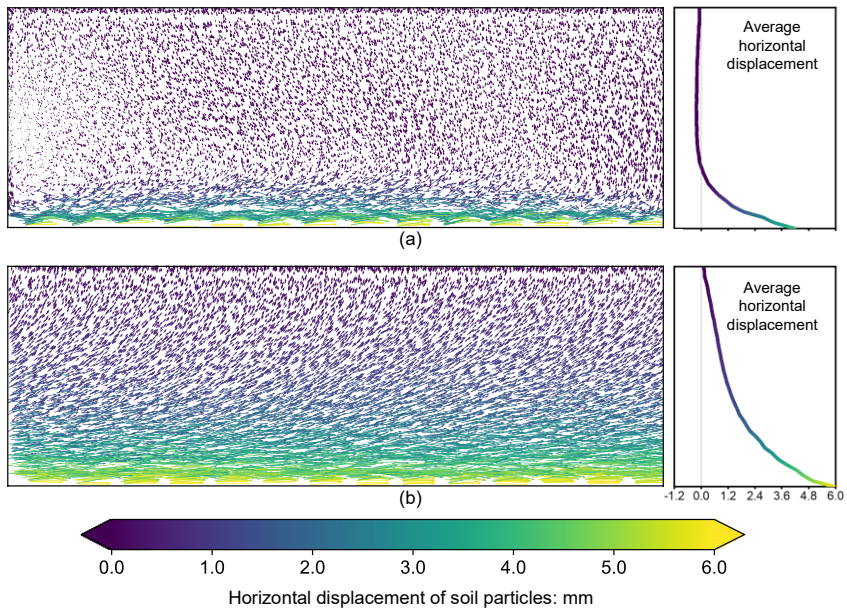

Figure 7.5 Soil particle displacement fields in DEM interface shear simulations with different horizontal boundaries (σ_n' = 34 kPa, f_s = 4, R_n = 1.01, horizontal displacement of interface = 6.0 mm): (a) rigid boundary; (b) periodic boundary

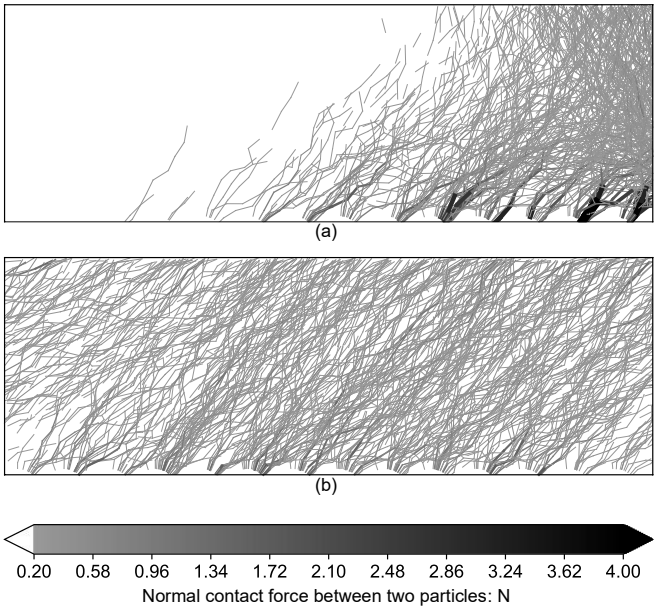

Figure 7.6 Force chain in DEM interface shear simulations with different horizontal boundaries (σ_n' = 34 kPa, f_s = 4, R_n = 1.01, horizontal displacement of interface = 1.2 mm): (a) rigid boundary (maximum normal contact force = 5.78 N); (b) periodic boundary (maximum normal contact force = 1.84 N)

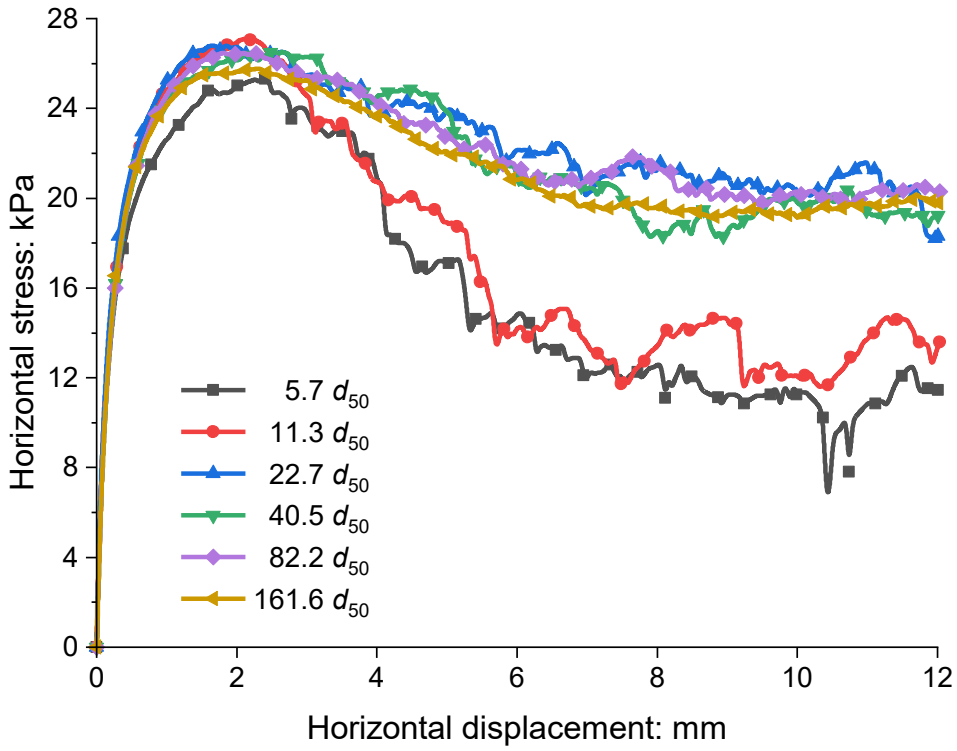

Figure 7.7 Effects of DEM periodic domain thickness ($n_p \times d_{50}$) on the soil-interface shear behaviour (σ_n' = 34 kPa, f_s = 4, R_n = 1.01)

Figure 7.5 compares soil particle displacement vectors under different boundary conditions. The vector colours represent the projected length in the horizontal direction. The rigid right wall significantly restricts particle displacement (see Figure 7.5 (a)). The average horizontal displacement of particles in contact with the interface is merely 70% of the interface displacement. Due to limited space near the rigid right wall, particles in the upper section of the specimen exhibit reverse horizontal displacement. Consequently, some particles near the left wall move downward. This results in non-uniform vertical displacement of soil particles along the horizontal direction. In contrast, the soil particle field for the periodic boundary is more uniform, as shown in Figure 7.5 (b). Here, the average horizontal displacement of particles in contact with the interface matches the interface displacement and decreases with distance from the interface. All displacement vectors along the horizontal direction are consistent.

Figure 7.6 (a) indicates that the force chains of the rigid boundary condition are nonuniform. The inter-particle contact force diminishes from right to left, with the maximum normal inter-particle contact force reaching 5.78 N at the rightmost soil-interface inter-particle contact. Many force chains originate from the right rigid wall rather than the interface. In contrast, the force chains of the periodic boundary specimen in Figure 7.6 (b) grow uniformly from the interface to the top right, with a maximum normal inter-particle contact force of only 1.84 N.

The above discussion proves the effectiveness of periodic walls in eliminating boundary effects. Considering computational costs, no further comparison between these two boundary conditions in the ASPI simulation is provided. Furthermore, it is important to note that contact model parameter calibration continues to be based on the rigid boundary interface direct shear rather than the periodic boundary one. It ensures the reliability of parameters by maintaining consistent boundary conditions with the interface direct shear tests. Any differences in the axial behaviour of the pipe between the computed and measured results could then be attributable to the periodic boundary setting rather than the parameters themselves.

The second issue pertains to the thickness of the periodic domain, denoted as $n_p \times d_{50\text{-A}}$ (i.e., the distance between the two periodic boundary walls). Although $n_p \times d_{50\text{-A}}$ should be minimised to reduce the number of particles, it is essential to ensure the simulation validity. Hence, a sensitivity analysis of the domain thicknesses is conducted based on periodic boundary interface shear simulations. The values of $n_p \times d_{50\text{-A}}$ range from 8.4 to 238.0 mm, corresponding to n_p values of around 5.7 to 161, which are integral multiples of Δl. Figure 7.7 compares the typical shear stress curves of the interface with an R_n of 1.01 under 34 kPa. A critical n_p value of 23 was identified, where curves for n_p greater than or equal to this value exhibit high consistency, whereas those for n_p smaller than this value do not, particularly concerning the critical state shear strength. This critical n_p is also 23 for the interface with an R_n of 1.01 under 17 and 50 kPa, and 5.7 for the interface with an R_n of 0.04 under 17 to 50 kPa. Therefore, it is a reasonable choice to use a domain thickness of no less than $23 \times d_{50\text{-A}}$ (34.0 mm), which can be considered the minimum acceptable size for a representative volume element (RVE) (O'Sullivan, 2011). Consequently, in the formal axial soil-pipe interaction simulation, the thickness of the periodic domain is approximately 34 mm.

7.6 Sample generation and simulation procedures

The soil particles were prefabricated using the radius expansion approach. In the approach, walls and pipe particles are frictionless, and the pipe is fixed. Smaller soil particles that do not initially touch each other are then randomly generated within the space. The particle number of each zone, as listed in Table 7.1, is pre-calculated based on the target particle size and relative density. Subsequently, these particles are incrementally enlarged until reaching the target size and, thus, the relative density.

In the formal simulation, the friction angles of the top and bottom walls are set to 90°, as mentioned. The target pressure for the servo-controlled top wall is set, the restriction on vertical translation freedom of the pipe is released, and a gravity of 9.8 m/s² is applied. Once the model

reaches stability (with an unbalanced force of less than 0.01 and a vertical velocity of the top wall below 0.01 mm/s), the axial velocity of the entire pipe is set to 2 mm/s, which is 100 times the value used in physical modelling for speeding up the simulation. The unbalanced force remains below 0.003 throughout the simulations, ensuring a quasi-static simulation at this axial velocity. The target axial displacement is 20 mm, consistent with the physical modelling. Each simulation with approximately 151,000 soil particles requires approximately 200 hours of computational time on a workstation equipped with a 16-core AMD Ryzen 9 7950X processor.

7.7 Validation of the DEM model and analysis of the macro-behaviour

7.7.1 Comparisons between the measured and computed pullout force and vertical displacement

Figure 7.8 (a) compares the computed and measured axial pullout force of pipes with R_n of 1.01 and 0.04, as observed in CHAPTER 4 and the simulation. The nominal pressure at the pipe centre, σ_c', is 34 kPa. The curves of the simulation align closely with the experimental data. The rough pipe exhibits a significant strain-softening behaviour, as shown in the interface shear behaviour in Figure 7.2. However, the extent of softening, i.e., the difference between the axial pullout resistance (the maximum axial force per unit length) and the axial force per unit length at an axial displacement of 20 mm, is less pronounced in the simulation compared to the physical model. In the DEM simulation, the axial resistance of the rough pipe is approximately 8.24 kN/m, which is 14% lower than the experimental value. The axial force per unit length at 20 mm is about 7.10 kN/m, matching the experimental results. The critical displacement at which peak axial resistance is reached is around 5.96 mm, slightly less than the 5.32 mm observed experimentally. Smaller axial resistance and larger critical displacement in DEM simulation, consistent with lower shear strength and stiffness during the comparison between the rigid and periodic boundary in the interface shearing simulation of Figure 7.4, is due to its idealised boundary conditions. Although efforts were made to minimise boundary effects

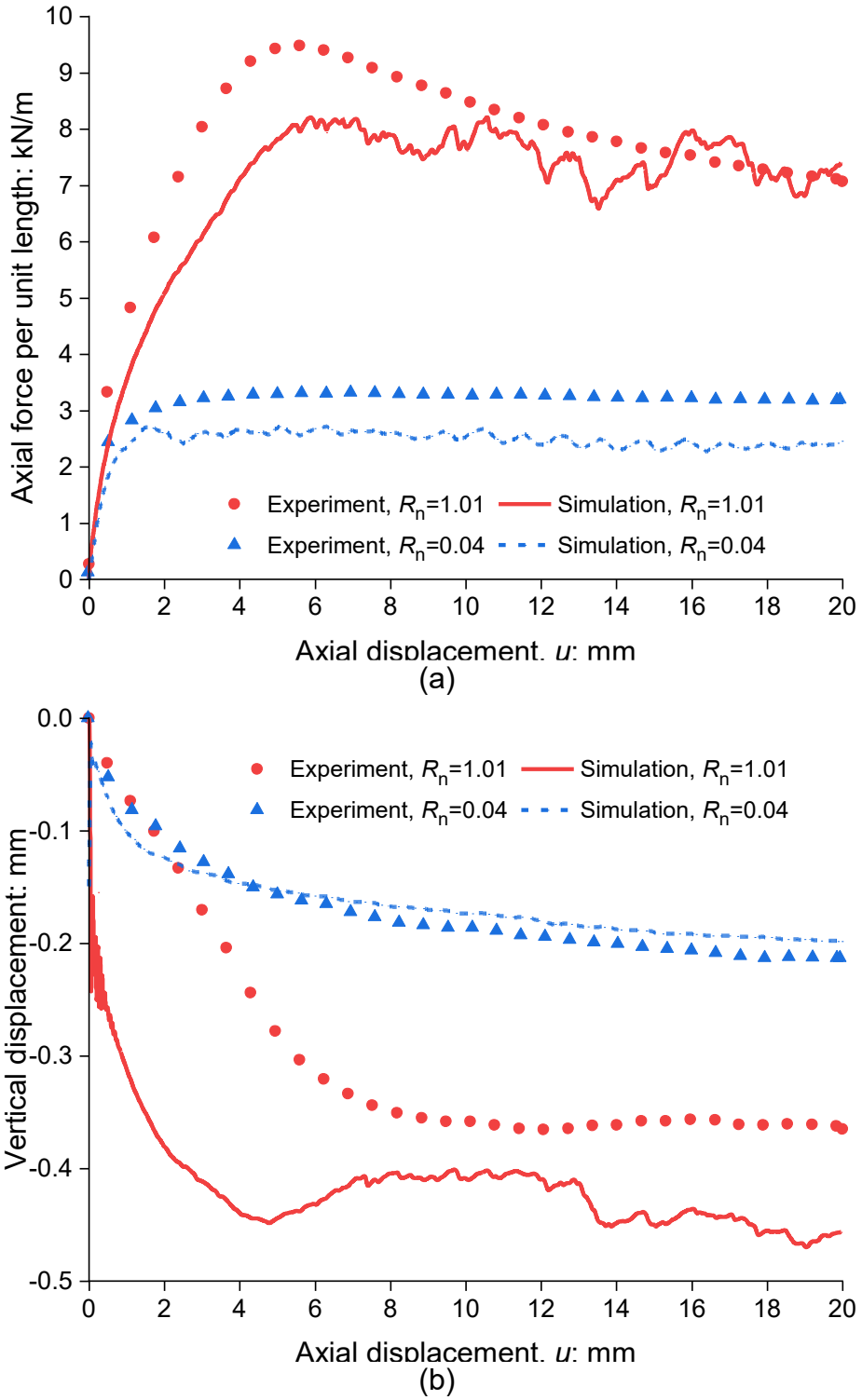

Figure 7.8 Comparisons between the measured and computed pipe pullout behaviour at various roughness (nominal vertical pressure at the pipe centre, $\sigma_c' = 34$ kPa): (a) axial force; (b) pipe settlement

using sleeves and flexible rubber membranes in physical modelling, the presence of a rigid front wall in the experiments may have redistributed the force chains, as illustrated in Figure 7.6. As

the surface roughness decreases, so does axial resistance; the rough pipe's resistance is 2.03 times greater than the smooth pipe, slightly smaller than that in physical modelling. In the smooth pipe simulation, the extent of softening is approximately 0.27 kN/m, which is slightly more pronounced than in the physical model. This is due to more significant negative soil arching degradation in the simulation, as discussed later.

Figure 7.8 (b) depicts the rough and smooth pipes' computed and measured vertical displacement. The curves reveal a settlement behaviour consistent with experiments. The experimental and simulation curves for the smooth pipe align well. The pipe continues to settle with a decreasing slope, reaching a total settlement of 0.20~0.21 mm at an axial pullout displacement of 20 mm. For the rough pipe, the settlement curve shape closely resembles the experimental results, where the pipe initially settles rapidly and then fluctuates slightly. The maximum settlement is approximately 0.47 mm, 30% larger than the observation in the physical model. This is due to the higher interface contact pressures at the pipe invert and haunches in the simulation, as illustrated later, which induced compression of the soil beneath the pipe.

Figure 7.9 presents the axial force-displacement curves for the rough pipe under different buried pressures. As noted in the discussion of Figure 7.8 (a), the extent of softening in the rough pipe simulation is consistently less than in the physical model. The axial resistance values under the surcharge of 17, 34, and 50 kPa in the simulation are 5.06, 8.24, and 12.02 kN/m, respectively, which are lower than 5.63, 9.49, and 14.02 kN/m in the physical model.

7.7.2 Comparisons between the measured and computed interface contact pressure at the soil-pipe interface

Figure 7.10 presents the distribution and evolution of interface contact pressures for smooth and rough pipes under a nominal vertical pressure of 34 kPa, compared with experimental data. In the simulation, interface contact pressure at a specific position on the pipe surface (e.g., crown) is calculated by the sum of soil-pipe inter-particle contact forces within a ±5° cross-

sectional area around this position. The soil-pipe inter-particle contact force is numerically the projection length of a contact force vector between a soil particle and a pipe particle onto the pipe's cross-sectional plane. According to the ALA (2001) assumptions, the interface contact pressure is σ_c' (34 kPa) at the crown and invert, $K_0\sigma_c'$ (12.3 kPa, where K_0 is 1-sin φ'), at the springlines, and $(1+K_0)\sigma_c'/2$ (23.2 kPa) at the shoulders and haunches.

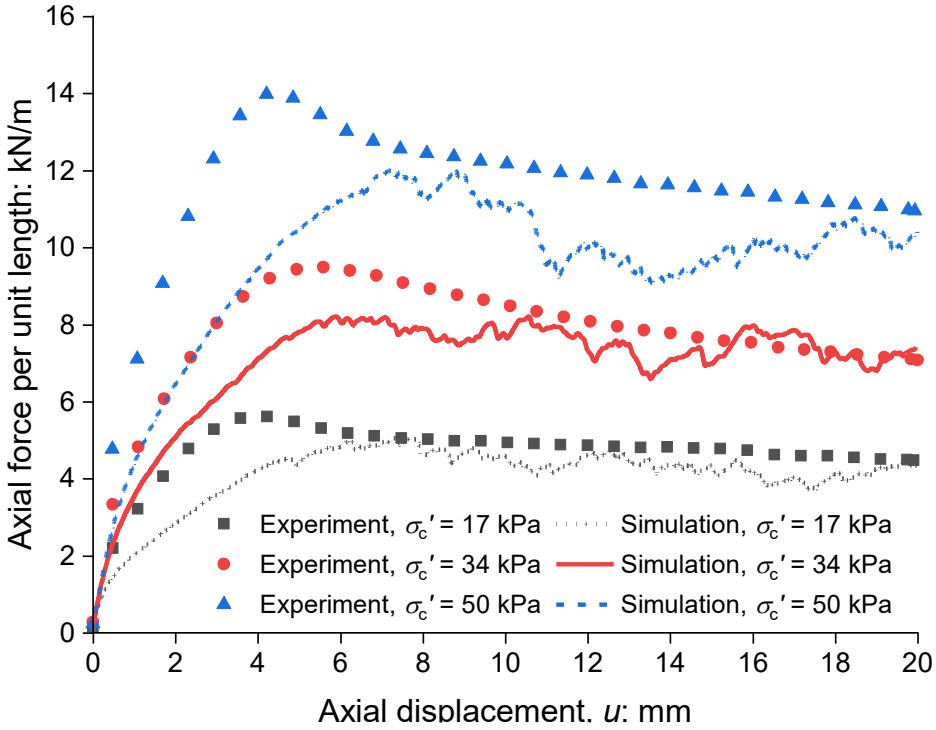

Figure 7.9 Comparisons between the measured and computed pipe pullout with different nominal pressures (σ_c') (R_n = 1.01)

Before pullout, the initial interface contact pressure distribution aligns with the experimental results of Wijewickreme *et al.* (2009), Sheil *et al.* (2018) and CHAPTER 4 and the simulation results of Murugathasan *et al.* (2021). For the rough pipe, interface contact pressures at the invert and shoulder exceed the guideline-assumed values. At the same time, those at the springline and haunch are slightly lower, consistent with the physical modelling in CHAPTER 4. In contrast, the smooth pipe shows larger interface contact pressures at the springline and haunch than the guideline-assumed values and the rough pipe simulation. This is attributed to the negative soil arching effect, where the stiffer pipe induces uneven soil

deformation, concentrating more pressure on the pipe. Both distributions are considered reliable. The similarity in distribution for the rough pipe suggests that the radius expansion approach effectively reproduces the initial conditions of physical modelling using the sand pluviation method in CHAPTER 3. In engineering practice, the initial distribution observed in the smooth pipe simulation might occur due to complex installation environments, such as cyclic loading on embankments (Meguid & Ahmed, 2020).

Figure 7.8 (a) shows that the evolution of the rough pipe's interface contact pressures closely matches experimental results. The pressure curves at the crown and springline align with physical modelling observations, with the former increasing from around 30 kPa to 58 kPa before stabilising at 40 kPa, and the latter rising from 10 kPa to 19 kPa. Pressures at other positions in the simulation exhibit similar trends. The pressure at the invert increases, followed by a decrease, while that of the shoulder and haunch shows an overall increasing trend. The significant increase in interface contact pressure for the rough pipe mainly results from constrained dilatancy, as inferred in CHAPTER 4 and confirmed by subsequent microscopic analysis: the dilation trend at the interface is limited by the surrounding soil, increasing interface contact pressures during shearing.

For the smooth pipe, before the axial displacement reaches 4 mm, all interface contact pressures show slight decreasing trends in the simulation, contrary to the increase observed in physical modelling, but consistent with the relatively pronounced softening of the smooth pipe simulation in Figure 7.8 (a). This is due to differences in initial interface contact pressure distribution, as mentioned, and the degradation of the initial negative soil arching effect. Afterwards, the pressures remain stable, showing high consistency in peak interface contact pressure distribution with experimental observations in Figure 7.10 (b).

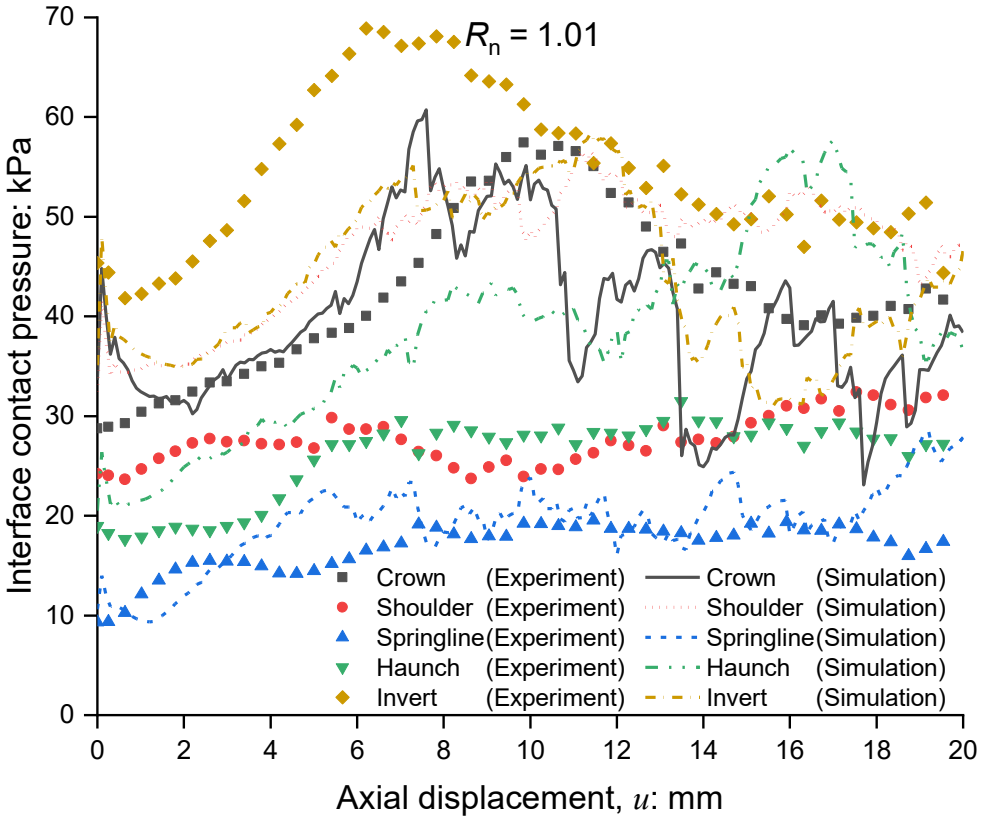
R_n = 1.01
Interface contact pressure: kPa
Axial displacement, u: mm
Crown (Experiment)
Shoulder (Experiment)
Springline (Experiment)
Haunch (Experiment)
Invert (Experiment)
Crown (Simulation)
Shoulder (Simulation)
Springline (Simulation)
Haunch (Simulation)
Invert (Simulation)

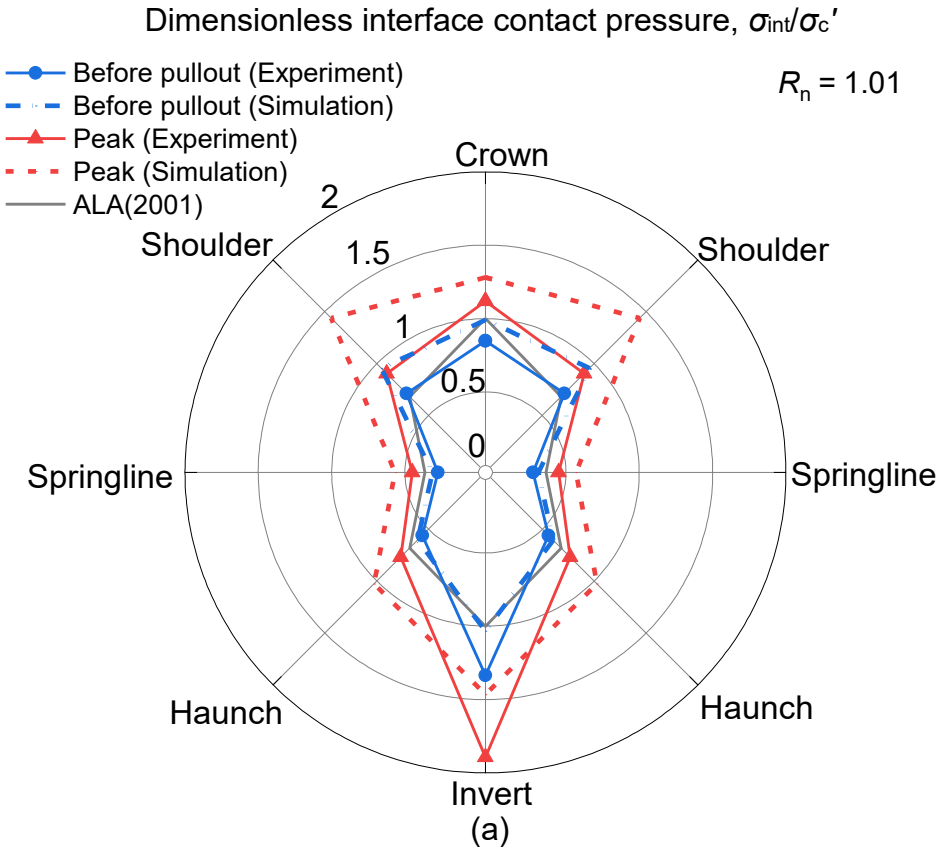
Dimensionless interface contact pressure, σ_{int}/σ_c'
Before pullout (Experiment)
Before pullout (Simulation)
Peak (Experiment)
Peak (Simulation)
ALA(2001)
R_n = 1.01
Crown
Shoulder
Shoulder
Springline
Springline
Haunch
Haunch
Invert
(a)

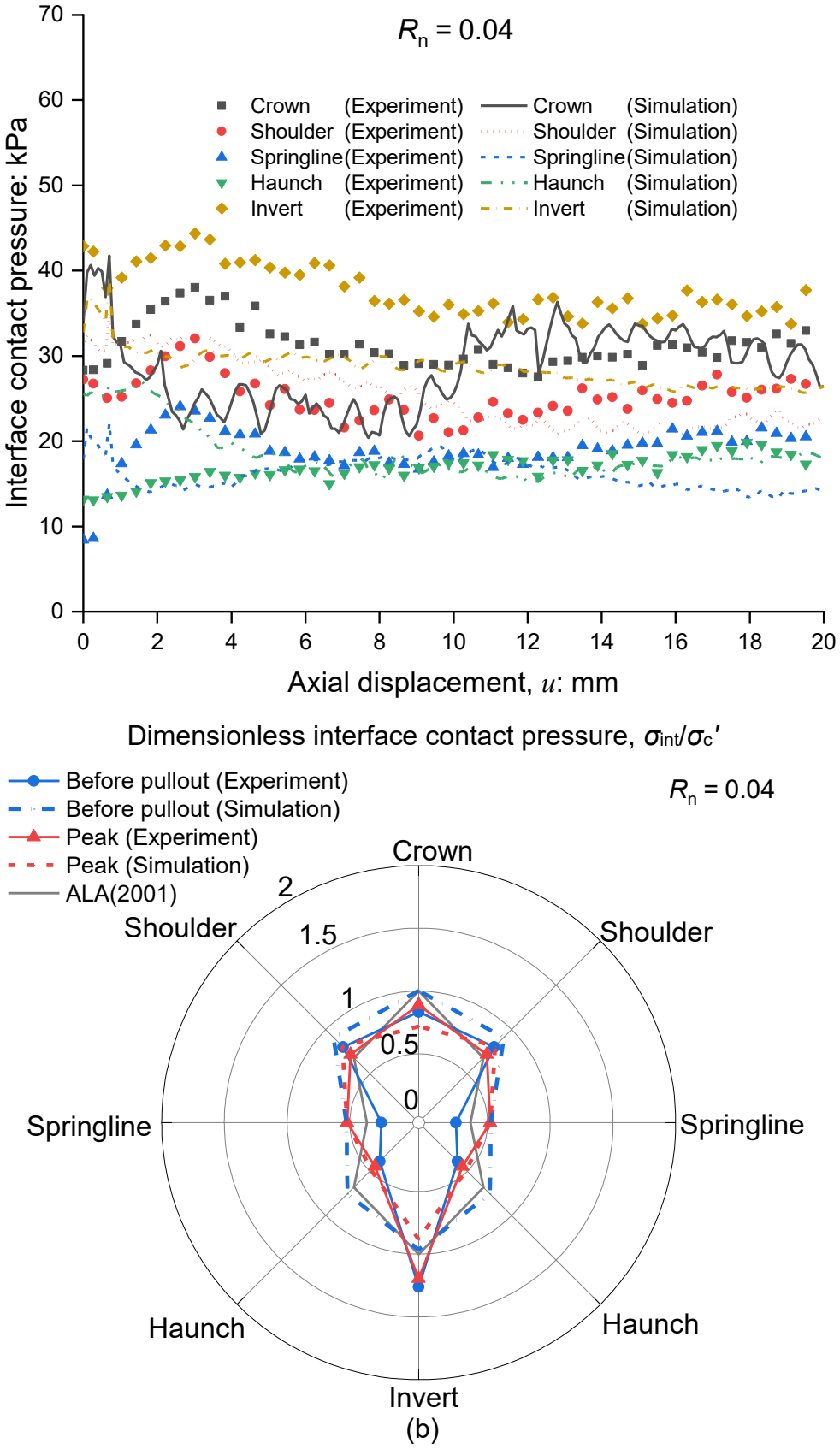

Figure 7.10 Validation of interface contact pressure development and distribution (σ_c' = 34 kPa): (a) rough pipe (R_n = 1.01); (b) smooth pipe (R_n = 0.04)

7.7.3 Comparisons between the measured and computed stress path at the soil-pipe interface

Figure 7.11 (a) compares the average stress path of the rough pipe at the soil-pipe interfaces in the simulation with the observation in physical modelling. The average interface contact pressure from the simulation is determined by summing all soil-pipe inter-particle contact forces acting on the pipe particles. In contrast, the average interface contact pressure from the physical modelling is derived from the mean of discrete data collected by single-point interface contact pressure sensors, as reported in CHAPTER 4. The failure envelopes of soil-interface shear are determined through CNL rigid boundary interface direct shear tests and periodic boundary interface shear simulations and are included as references. The average stress path shape of the simulation in Figure 7.11 (a) resembles that of the physical modelling in CHAPTER 4 and typical stress paths observed in CNS tests on rough interfaces (Ooi & Carter, 1987; Pra-ai & Boulon, 2016). It mainly comprises three stages. The stress path rises vertically in the first stage, representing elastic friction angle mobilisation. Then, it transitions to the second stage, moving towards the top right, illustrating an increase in average interface contact pressure due to constrained dilatancy. In the ultimate stage, the stress path turns to the bottom right and finally touches the critical state envelope. Moreover, the computed average stress path never exceeds the peak failure envelope, which appears better than the experimental observation. It is because it is calculated from the sum of all contact forces on the pipes rather than from discrete data.

Figure 7.11 (b) illustrates the local stress paths at various locations on the pipe surface. The local interface contact pressures correspond to those shown in Figure 7.10. The local shear stress in the axial direction is determined by projecting the contact force vector between a soil particle and a pipe particle onto the pipe's axis within the same regions as the local interface contact pressure. The shapes of these local paths at different locations resemble their average path, as shown in Figure 7.9 (a), featuring three distinct stages, as previously mentioned.

Notably, only the path at the pipe crown reaches the peak interface envelope, as determined by CNL interface shear tests during the pipe pullout. In contrast, the pipe invert and haunch paths are closer to the critical state envelope. This trend is more clearly observed when considering the local stress ratio (interface shear stress/interface contact pressure) depicted in Figure 7.11 (c). The stress ratio generally decreases with increasing depth from the pipe crown to the invert. The peak stress ratio at the pipe crown reaches 0.79, while at the pipe haunch, it is only 0.65. Except for the transient peak phase at the pipe's axial displacement of 4.0 to 4.8 mm, the stress ratio at the pipe invert is generally lower than those at the crown, shoulder, and springline. This observation aligns with the experimental findings from CNS interface shear tests by DeJong & Westgate (2009), which showed that the dense soils' interface shear stress ratio decreases as normal stiffness increases. In the ASPI, the stiffness of the soils surrounding the pipe increases with depth due to reduced restriction from the top boundary compared to the fixed side and bottom walls. Hence, from the pipe crown to invert, the local stress ratio decreases with their stress path far away from the peak interface shear envelope based on CNL interface shearing.

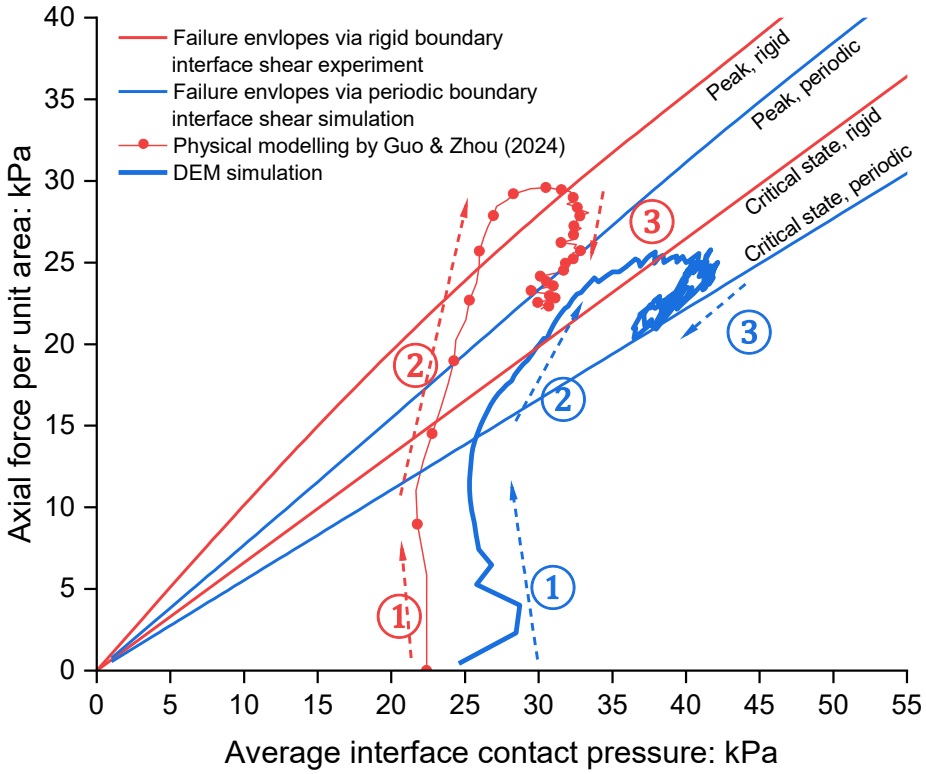

(a)

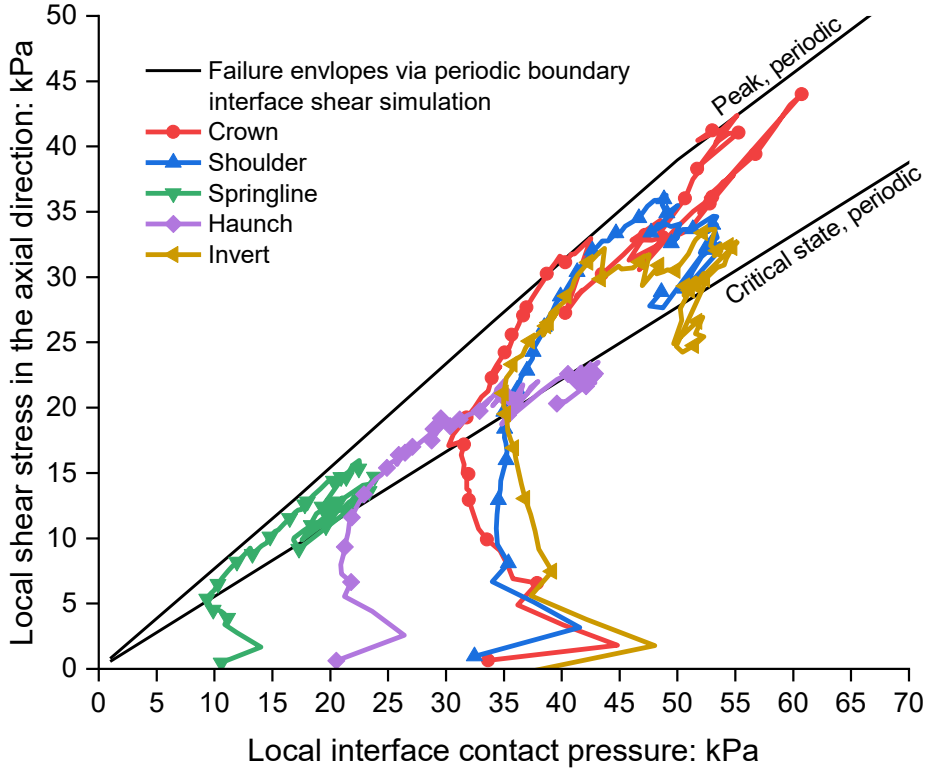

(b)

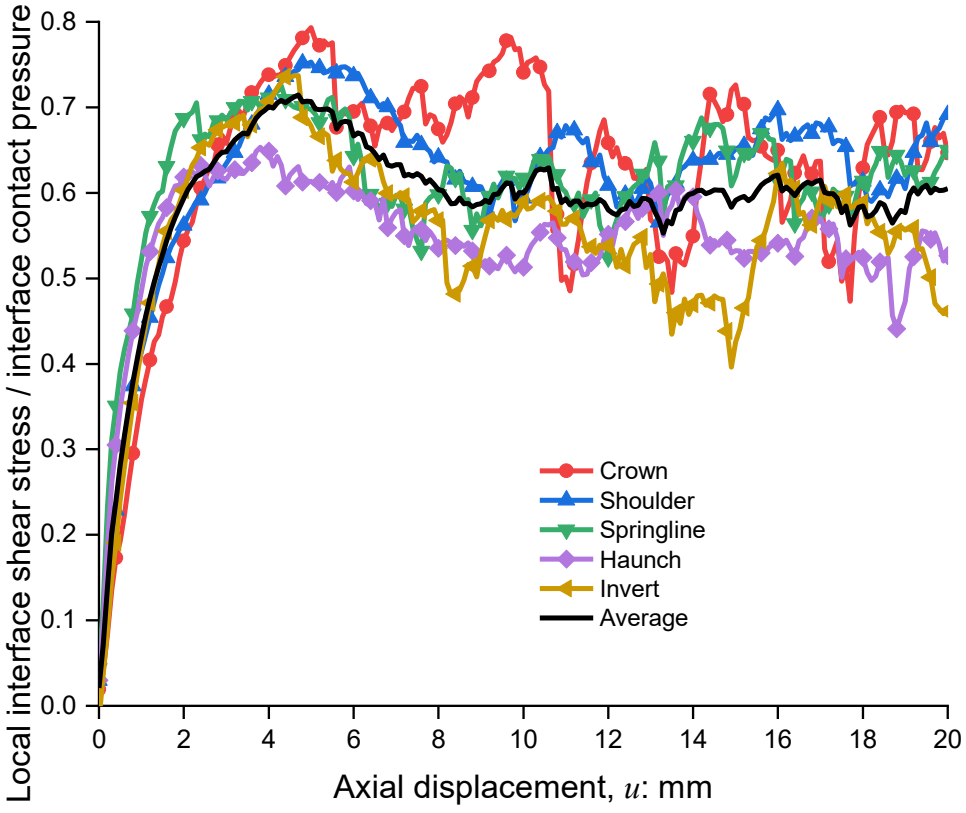

(c)

Figure 7.11 Stress path of rough pipe (R_n = 1.01): (a) measured and computed average stress paths; (b) computed stress paths of local positions at the pipe surface (axial displacement, u, 0~10 mm); (c) computed local stress ratio

7.8 Micro-mechanical analysis of axial soil-pipe interaction

7.8.1 Soil-pipe interface shear band

Figure 7.12 (a) illustrates the average soil particle displacement in the *y* (axial) direction as the distance from the soil particles to the pipe surface increases. Data for distances greater than 100 mm are not shown due to minimal axial displacement. A clear trend is observed: the axial displacement of soil particles decreases as their distance from the pipe surface increases. Soil particles adjacent to the rough pipe surface move axially generally in sync with the pipe, with the average axial displacement of soil particles exceeding 90% of the pipe's axial displacement. In contrast, the axial displacement of soil particles further away typically does not exceed 15%. Greater axial displacement of soil particles results in higher shear strain, leading to more significant volumetric expansion in dense soils. Conversely, lower shear strain associated with limited soil particle displacement may result in a minimal volumetric expansion or even a volumetric compression. It corresponds to the soil particle displacement field in the *x*-*z* plane.

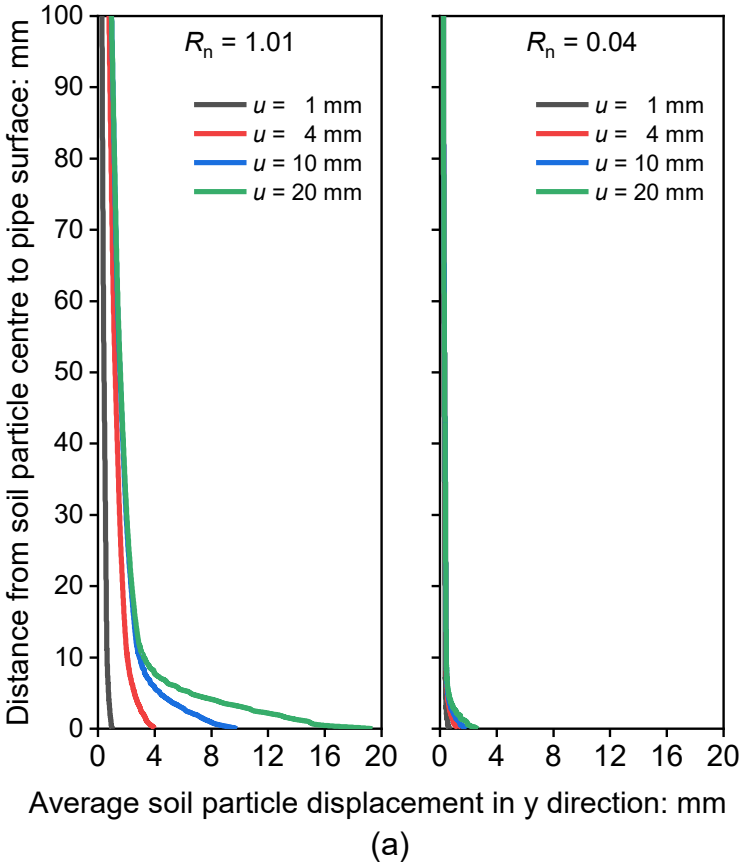

(a)

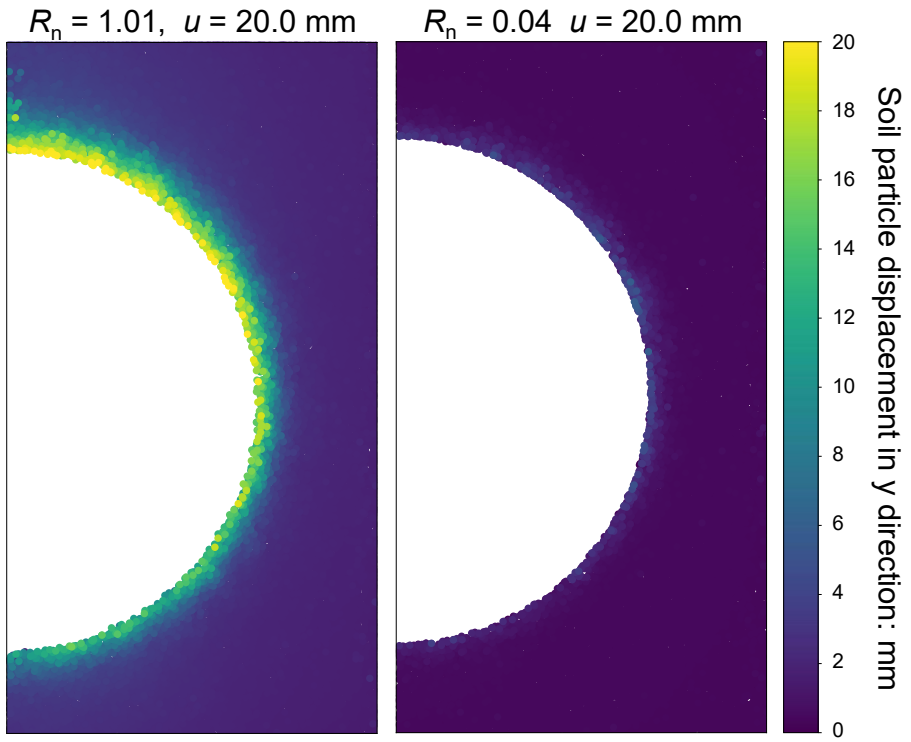

(b)

Figure 7.12 Soil particles in *y* direction: (a) development of average soil particle displacement against distance from soil particle centre to pipe surface; (b) displacement field within Zone A (σ_c' = 34 kPa, u = 20 mm)

There is a noticeable inflexion point in the gradient of the curves in Figure 7.12 (a). The region below this point represents the shear band at the soil-pipe interface (Sadrekarimi & Olson, 2010; Gu *et al.*, 2017). With the interface roughness dropping, the shear band thickness decreases from 8.6 to 3.6 mm, 5.7 to 2.4 $d_{50\text{-A}}$. These trends align with previous experimental and numerical findings (Zhang *et al.*, 2011; Martinez & Frost, 2017; Grabowski *et al.*, 2020). The thicker shear band of the rigid pipe represents a stronger trend of volumetric expansion, corresponding to the higher interface contact pressure increase in Figure 7.10 and additional negative soil arching, as discussed later. Furthermore, the displacements in the *y* direction for particles in Zones B~E do not exceed 1.4 $d_{50\text{-A}}$, indicating limited effects on the formation of the soil-pipe interface shear band.

Figure 7.12 (b) depicts the axial displacement field of soil particles. For clarity, only results for the rough pipe within Zone A at a pipe displacement of 20 mm are shown. The shear band exhibits a decreasing trend in thickness from the pipe crown to the invert rather than being uniformly distributed along the pipe surface. The soil particle displacements also decrease from 100% of the pipe's axial displacement at the pipe crown to less than 65% at the pipe invert. This is consistent with the local stress path and the stress ratio in Figure 7.11 (b) and (c), where the higher restriction from the fixed side and bottom walls limits the formation of the interface shear band close to the pipe invert and haunch.

7.8.2 Soil particle displacement field in the *x-z* plane

Figure 7.13 illustrates the displacement vectors of soil particles in the x-z plane when the pipe is displaced by 6 mm. These vectors, originating from points prior to the pipe pullout, are magnified five times for clarity. The displacement fields of soil particles around pipes with varying surface roughness exhibit distinct behaviours. Around the rough pipe, the shear band shows significant volumetric expansion: inner particles move towards the pipe, while outer particles move away. This behaviour aligns with the CNL rough interface characteristics depicted in Figure 7.2 (a). The expansion of the shear band causes soil particles beyond it to also move away from the pipe, demonstrating constrained dilation around the rough pipe. This dilation increases the soil-pipe interface contact pressure, as shown in Figure 7.10 (a), which in turn compresses the surrounding soil. The restriction of the surrounding soil is most pronounced at the invert due to the fixed bottom and side boundaries, as previously shown in Figure 7.11 (b), Figure 7.11 (c), and Figure 7.12 (b). Consequently, the volumetric expansion in the shear band beneath the pipe is reduced, and the settlement of the rough pipe during pullout (see Figure 7.8 (b)) is primarily due to the compression of soil beneath the pipe caused by increased interface contact pressure. Moreover, the outward movement of surrounding soils exhibits a rightward trend related to forming a lateral force chain during shearing, which is discussed later.

In contrast to the smooth pipe, nearly all particles within the shear band move towards the pipe, corresponding to the slight contraction behaviour at the smooth interface shown in Figure 7.2 (b). This contraction decreases interface contact pressure, as seen in Figure 7.10 (b). Soil particles beyond the shear band move towards the pipe over a limited distance, disrupting the initial soil arching, as discussed later. Due to the higher restriction of the surrounding soil at the invert, the movement of soil particles beneath the pipe is minimal, indicating that the settlement of the smooth pipe (see Figure 7.8 (b)) is due to the contraction at the soil-pipe interface.

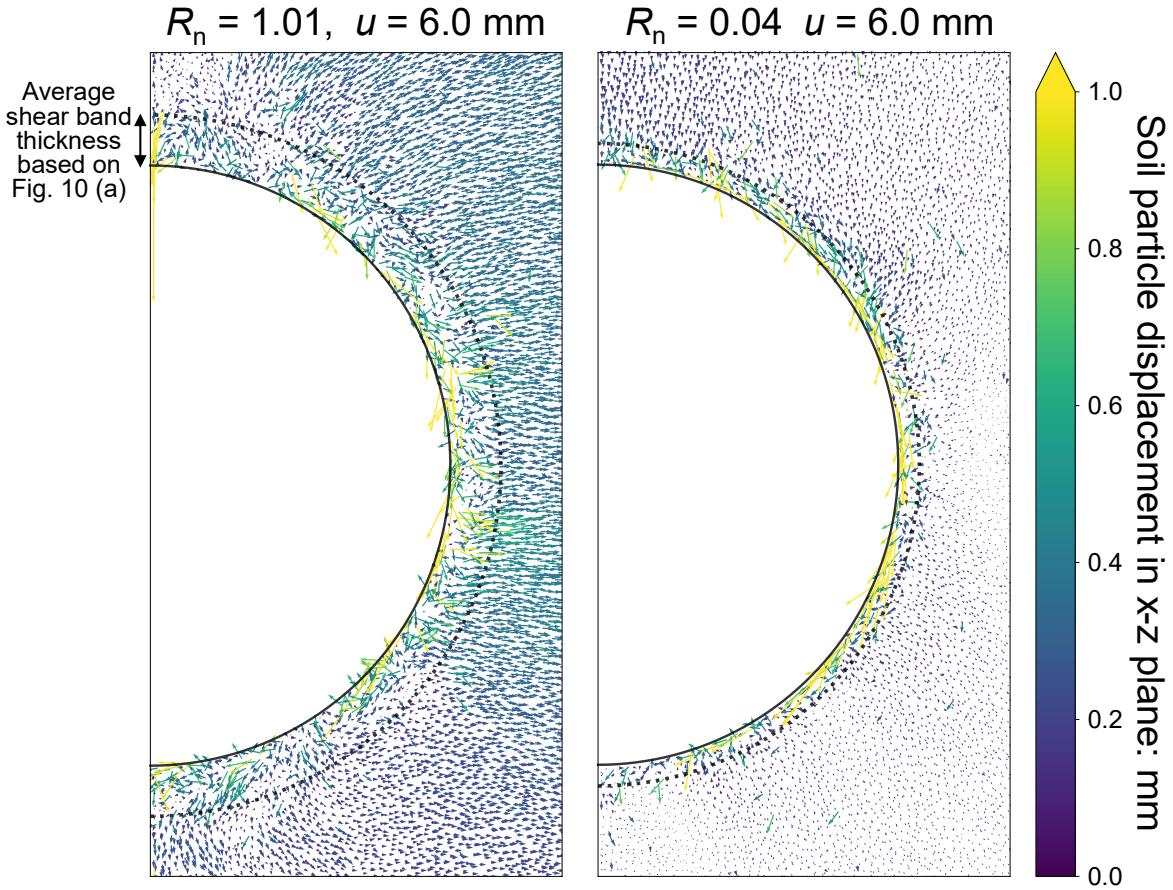

Figure 7.13 Soil particle displacement in the *x*-*z* plane within Zone A (five times in vector length)

Figure 7.14 displays the vertical displacement fields within Zone C during shearing, providing strong evidence of soil arching evolution. For the rough pipe, soils above the pipe move upwards and soils below the pipe move downwards, due to the thick and expanding shear band at the interface, as shown in Figure 7.12 (a). The magnitudes of these upward and

downward movements are consistently greater than those of the soil at the sides of the pipe, indicating an additional negative soil arching effect during shearing. Consequently, the pressure increase is more pronounced at the crown and invert of the rough pipe in Figure 7.10 (a) due to the soil resistance limiting the relative displacement. In contrast, an opposite trend is observed around the smooth pipe, where soils above the pipe, especially near the pipe haunch, move downwards, and soils below the pipe move upwards. It demonstrates a volumetric contraction trend at the pipe interface, corresponding to the decrease in interface contact pressures in Figure 7.8 (b) and the slight movement of soil particles toward the pipe in Figure 7.13.

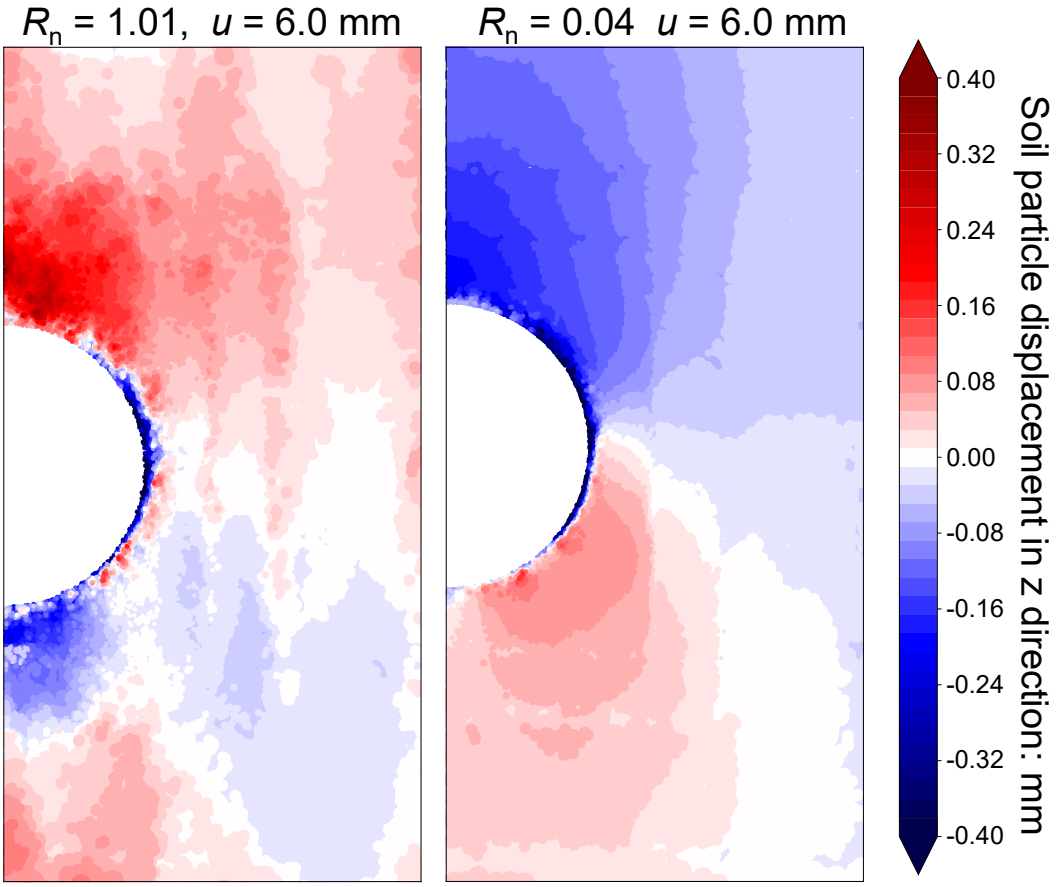

Figure 7.14 Soil particle displacement in *z* direction within Zone C (positive: upward)

7.8.3 Force chain evolution

Figure 7.15 illustrates the evolution of force chains using the normal forces of inter-particle contacts. For clarity, only inter-particle contact forces greater than 0.2 N are displayed. As previously mentioned, the force chains around the rough pipe before pullout exhibit slight initial

negative soil arching. Vertical force chains develop from the pipe's crown, shoulder, haunch, and invert, with maximum inter-particle contact forces not exceeding 2.1 N. In contrast, there are few inter-particle contact normal forces greater than 0.2 N near the pipe springline. This is consistent with the interface contact pressure distribution observed before pullout in both experimental and simulation results shown in Figure 7.10, as well as in previous studies (Wijewickreme *et al.*, 2009; Sheil *et al.*, 2018; Murugathasan *et al.*, 2021). In the region adjacent to the pipe springline, force chains extend vertically from top to bottom to transfer overburden pressure rather than connecting to the pipe surface, indicating a limited effect of negative soil arching in this area.

When the rough pipe is pulled out to 6 mm, stronger force chains, with maximum forces exceeding 4 N, emerge from the pipe due to constrained dilation. It is consistent with the increase in interface contact pressure shown in Figure 7.10 (a) and the particle displacement in Figure 7.13. The strengthening of force chains is pronounced at the pipe's crown, shoulder, haunch, and invert but remains minimal at the springline. It indicates additional negative soil arching on the pipe due to the volumetric expansion of the soil-pipe interface shear band, as in the vertical displacement of soil particles in Figure 7.14. The development of force chains in the horizontal direction corresponds to the rightward trend of soil particle displacement shown in Figure 7.13.

For the smooth pipe at a displacement of 6 mm, limited force chains develop from the pipe surface, and their distribution no longer focuses on the pipe's crown, shoulder, haunch, and invert, corresponding to interface contact pressures decrease in Figure 7.10 (b) and soil particles displacement in Figure 7.13 and Figure 7.14. In contrast to the rough pipe, a force chain loop forms around the smooth pipe, indicating the disturbance of the initial negative soil arching and establishing a new stress equilibrium between the pipe and the surrounding soils.

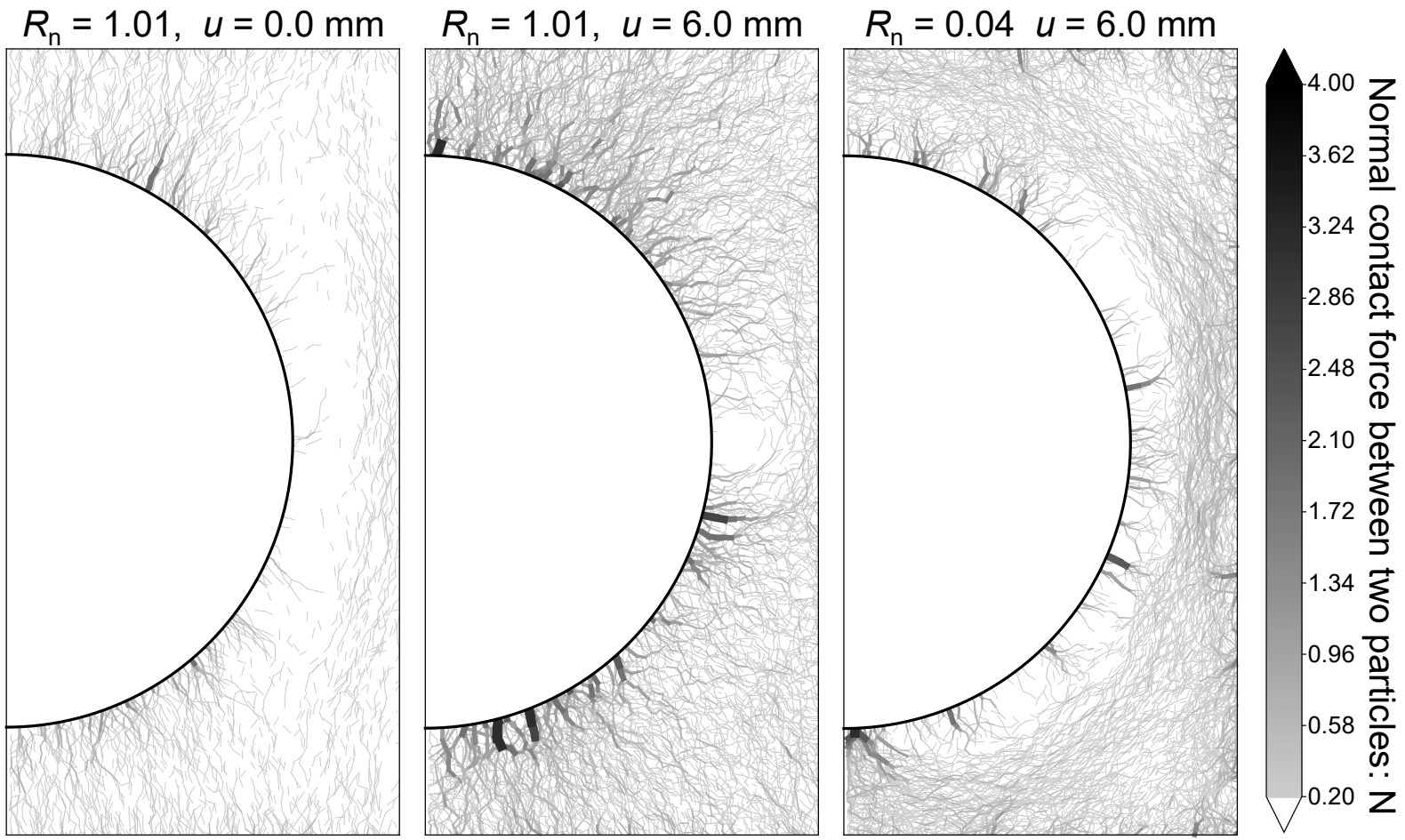

Figure 7.15 Force chain evolution within Zone A

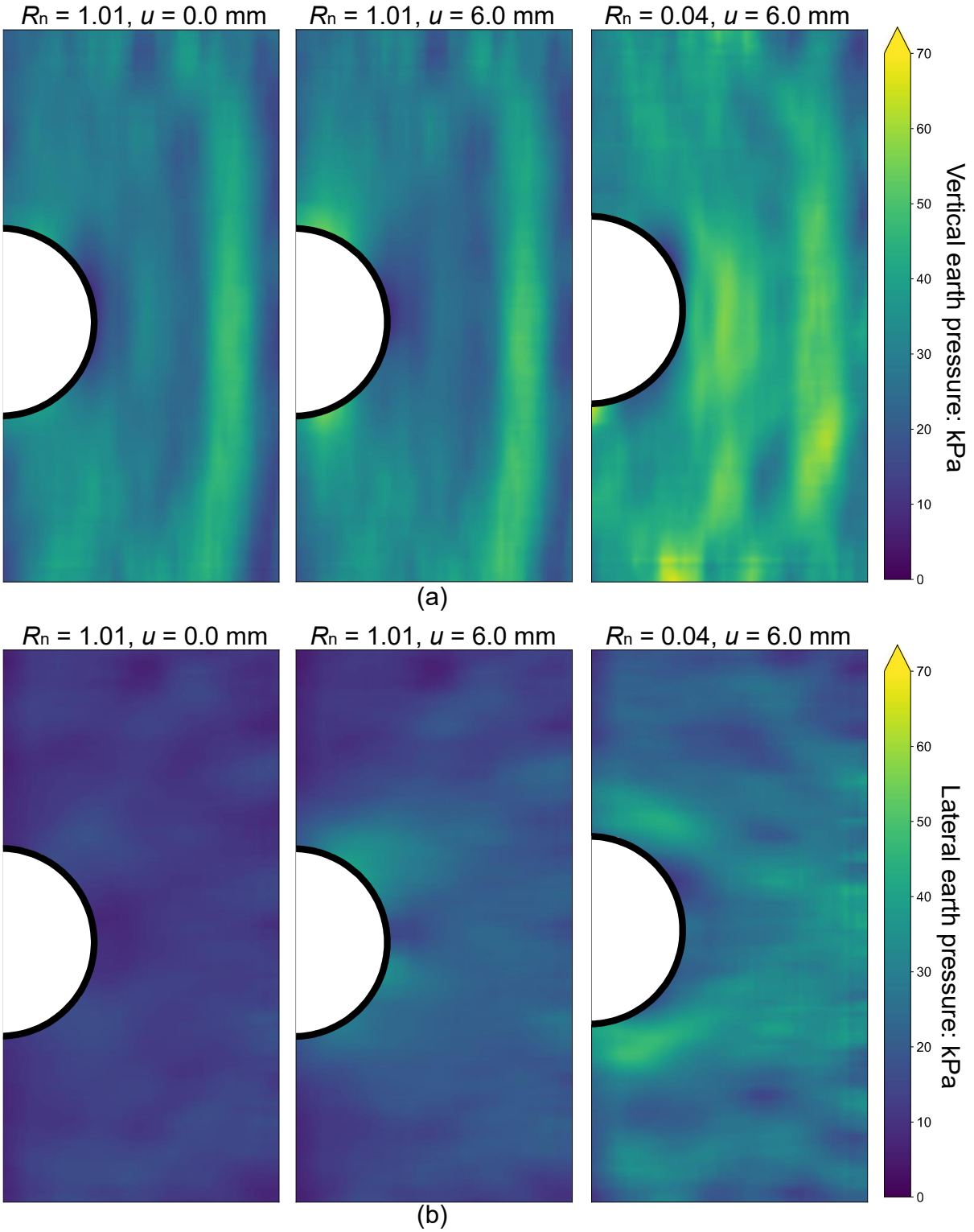

Figure 7.16 Stress field within Zone C: (a) vertical earth pressure; (b) lateral earth pressure

7.8.4 Earth pressure evolution around the pipe

Figure 7.16 illustrates the evolution of vertical and lateral earth pressures around the pipe, calculated using a homogenisation approach (Nicot *et al.*, 2013; Duriez & Wan, 2016) after numerically dividing the soil area into 10×10 mm² meshes. The evolution of vertical earth pressure in Figure 7.16 (a) reflects the negative soil arching effect. Before the pipe pullout, the pipe bears more overburden pressure than the soil adjacent to its sides. During pipe pullout, the concentration of vertical pressure on the rough pipe becomes more pronounced, with a larger area of low vertical earth pressure near the pipe sides, consistent with the additional negative soil arching effect previously mentioned. In contrast to the smooth pipe, the concentration of vertical pressure weakens, with a larger area near the pipe sides where the soil bears more overburdened pressure, aligning with the disturbance of negative soil arching, as discussed.

Regarding the lateral earth pressure shown in Figure 7.16 (b), values before pullout are generally less than 25 kPa. However, when the rough pipe is pulled out to 6 mm, the lateral pressure near the pipe increases to over 40 kPa due to constrained dilation, as evidenced in Figure 7.10 (a) and Figure 7.13. In contrast, for the smooth pipe, the increase in lateral pressure is mainly observed in areas above and below the pipe, corresponding to the force chain loop depicted in Figure 7.15.

7.9 Parametric studies

7.9.1 Relationship between axial resistance and surface roughness

A parametric study of interface normalised roughness over a wider range of 0.01 to 1.40 on the axial behaviour of buried pipes ($\sigma_c' = 34$ kPa) was conducted in this section. The objective is to achieve a more general conclusion about the relationship between axial resistance and surface roughness, extending the findings in the above simulation and the physical modelling in CHAPTER 4.

Figure 7.17 (a) illustrates the relationship between axial force and axial displacement of pipes with different roughness levels. The curves for pipes with normalised roughness levels of 0.50, 1.01, and 1.40 are generally consistent, while those for levels of 0.01 and 0.04 also show consistency. The axial resistances for pipes with normalised roughness levels of 0.10 and 0.21 are 4.05 and 5.74 kN/m, respectively. The extent of softening at these two roughness levels is 0.55 and 0.64 kN/m, respectively, increasing with roughness due to higher dilatancy.

Figure 7.17 (b) depicts the relationship between axial resistance and roughness. To facilitate comparison with the interface friction coefficient (the tangent of the interface friction angle) determined by periodic boundary soil-interface shear simulations under a normal pressure of 17~100 kPa, the axial resistance is presented as a dimensionless value, $T/[\pi D(1/2)(1+K_0)\sigma_c']$, where $\pi D(1/2)(1+K_0)\sigma_c'$ represents the theoretical average soil-pipe interface contact force per unit length assumed by ALA (2001). Consistent with the interface friction coefficient, there are two critical roughness levels of 0.06 and 0.5 for the axial resistance of buried pipes. Within these levels, the axial pullout resistance increases with the natural logarithm of the normalised roughness level. Beyond these levels, the axial pullout resistance remains almost unchanged despite variations in roughness. Furthermore, when R_n exceeds 0.09, $T/[\pi D(1/2)(1+K_0)\sigma_c']$ surpasses the interface friction coefficient, with the difference increasing as R_n increases. This is attributed to the increase in soil-pipe interface contact pressure caused by constrained dilation and additional soil arching, as illustrated in Figure 7.10, Figure 7.15 and Figure 7.16.. In contrast, when R_n is less than 0.09, $T/[\pi D(1/2)(1+K_0)\sigma_c']$ is lower than the interface friction coefficient, due to the decrease in soil-pipe interface contact pressure caused by the disturbance of the initial soil arching, as shown in Figure 7.10, Figure 7.15 and Figure 7.16.

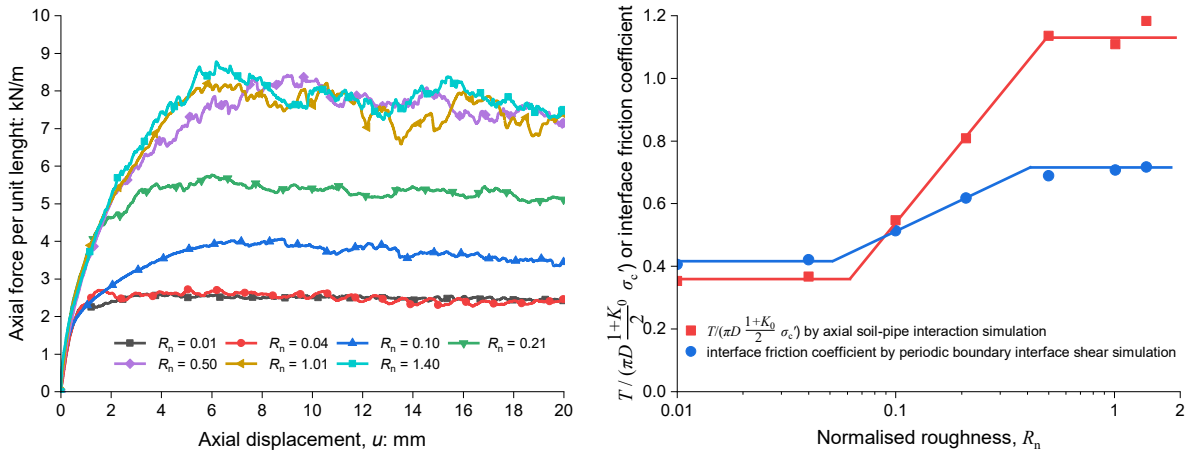

Figure 7.17 Computed axial pullout behaviour of pipes with normalised roughness levels of 0.01~1.40 (σ_c' = 34 kPa): (a) axial force-displacement relationship; (b) normalised roughness against axial pullout resistance

7.9.2 Effect of pipe outer diameter

In practice, the pipe diameter varies with the different flow rate requirements of the internal fluids (WSD, 2020). Therefore, another parametric study of pipe diameter on the axial behaviour of buried pipes (σ_c' = 34 kPa, R_n = 1.01) is conducted. The selected outer diameters are 51, 102 and 153 mm (2, 4, and 6 inches), which comply with the maximum allowable pipe diameter for a trench width of 0.6 m (USBR, 1996; BSI BS EN 1610, 2015). The thickness of the pipe wall is consistently maintained at 4 mm. The particle size scaling factors for Zones A to E for pipes with different outer diameters are consistent with those in Table 7.2. The minimum thicknesses for Zones A to E (t_{min}) are 25, 50, 50, 50, and 100 mm for pipes with an outer diameter of 51 mm, and 19, 25, 35, 50, and 100 mm for pipes with an outer diameter of 153 mm, ensuring that the ratio of t_{min} to d_{50} for each zone is no less than 9.9.

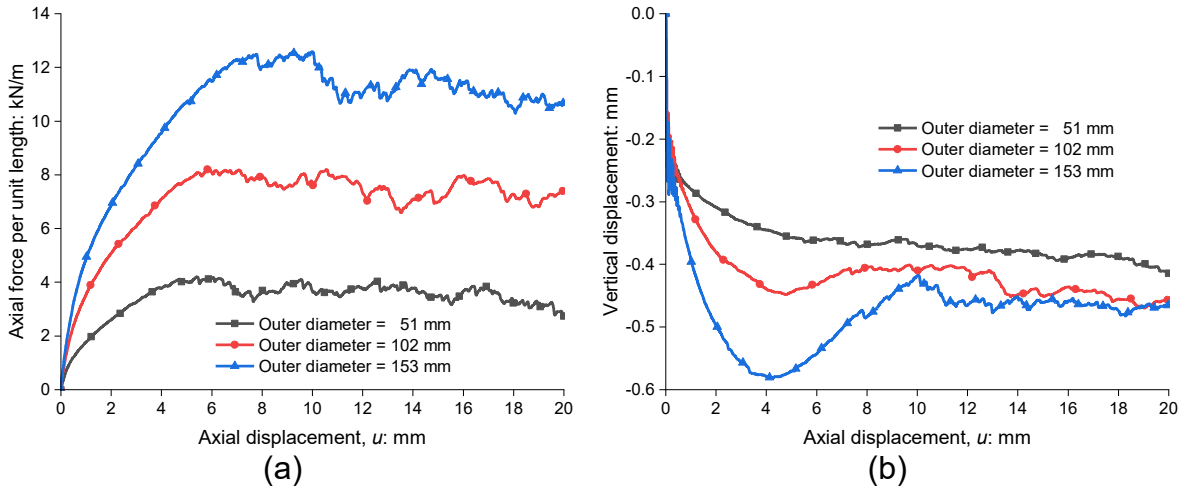

Figure 7.18 Computed axial pullout behaviour of pipes with different outer diameters (σ_c' = 34 kPa, R_n = 1.01): (a) axial force; (b) vertical displacement

Figure 7.18 (a) illustrates the axial force-displacement relationship computed in this parametric study. Pipes with varying outer diameters exhibit consistent strain-softening behaviour. The axial resistances are 4.11, 8.24, and 12.59 kN/m, increasing almost linearly as the pipe's outer diameter increases from 51 to 153 mm. The corresponding axial resistances per unit area range from 25.65 to 26.19 kPa, with a margin of error no greater than 2%, suggesting that pipe diameter has a minimal effect on axial resistance. Settlement behaviour is also observed for pipes with different outer diameters (see Figure 7.18 (b)). However, the settlement value increases with the pipe's outer diameter. The ultimate settlement values at an axial displacement of 20 mm are 0.41, 0.46 and 0.47 mm for outer diameters of 51, 102 and 153 mm, respectively. Additionally, the pipe with a 153 mm outer diameter initially settles rapidly to 0.58 mm before rising and stabilising at the ultimate value, clearly reflecting the behaviour of the soil beneath the pipe, which initially contracts and then dilates during the soil-pipe interface shear. In contrast, the pipe with a 51 mm outer diameter shows continuous settling. This difference is likely due to the larger soil-pipe interaction area of the thicker pipe, making its vertical displacement more sensitive to volumetric changes at the soil-pipe interface during pullout.

7.10 Summary

This study explores the behaviours of steel pipes buried in dry sand and subjected to axial displacement using the 3D DEM software YADE. The simulation employs a Cundall linear contact law that accounts for normal and shear forces and rolling torque. A novel method has been developed to analyse the ASPI behaviour. The pipe is modelled as a clump of overlapping particles to simulate varying roughness. A pair of periodic boundary walls with an optimised domain thickness is used in the pipe's axial direction to minimise boundary effects. A particle refinement method and plane symmetry assumption are employed to enhance computational efficiency. The physical modelling of ASPI in CHAPTER 4 was back-calculated and analysed on both macro and micro scales. Key conclusions are as follows:

The consistency between computed and experimental macro-mechanical behaviours, including displacement-softening behaviours, axial resistance values with varying roughness and burial pressure, settlement behaviours, the evolution and distribution of soil-pipe interface contact pressure, and the stress path, confirms the reliability of the new method.

The ASPI mechanisms differ significantly between pipes with different roughness values, primarily due to the distinct movement behaviours of soil particles around the pipe. Soil particles adjacent to the rough pipe surface move axially in sync with the pipe, with the average axial displacement of soil particles (in the y direction) exceeding 90% of the pipe's axial displacement. It induces significant volumetric expansion of the soil-pipe interface shear band, increasing the interface contact pressure and compressing the surrounding soils as particles move away from the pipe in the x-z plane. In contrast, the average axial displacement of soil particles around the smooth pipe is no more than 15% of the pipe's axial displacement. The limited shear strain results in a slight volumetric contraction in the soil-pipe interface shear band, causing a slight inward movement of the surrounding soil particles and reducing interface contact pressures.

Interestingly, despite the different soil particle displacement modes, both rough and smooth pipes experience settlement, with maximum settlements of 0.47 and 0.21 mm, respectively, during pullout. However, the underlying reasons differ. For the rough pipe, settlement is primarily due to the compression of surrounding soils beneath the pipe invert caused by increased interface contact pressure. The volumetric expansion of the shear band at the pipe invert, which tends to lift the pipe, is limited by the higher restriction from the fixed side and bottom boundaries, as evidenced by the stress path, stress ratio, and soil particle displacement results. In contrast, the settlement of the smooth pipe is due to the volumetric contraction of the shear band at the invert rather than a significant movement of the surrounding soils.

The different particle displacement fields around rough and smooth pipes lead to distinct mechanical responses in the surrounding soils. During the rough pipe pullout, soil particles above the pipe move upward while those beneath move downward. Stronger force chains develop from the pipe's crown, shoulder, haunch, and invert, enhancing the soil arching effect during sampling and causing a noticeable concentration of vertical earth pressure around the pipe surface. The horizontal displacement of soil particles also increases lateral earth pressure around the pipe surface. For the smooth pipe, the opposite trend of soil particle displacement in the *x*-*z* plane disrupts the initial soil arching effect. Instead, a force chain loop forms outside the pipe interface shear band, increasing vertical and lateral earth pressure within the surrounding soils rather than at the soil-pipe interface.

The parametric study on surface roughness reveals a three-sectional axial resistance-normalised roughness relationship, akin to the pattern observed in interface shear strength. Within the normalised roughness range of 0.06 to 0.5, axial resistance increases with roughness. Outside this range, axial resistance remains almost constant regardless of roughness variations. Furthermore, the parametric study on the pipe's outer diameter confirms a minimal effect on axial resistance for pipes subjected to a constant nominal buried pressure.

CHAPTER 8
DEM SIMULATION OF AXIAL BEHAVIOUR OF PIPES BURIED IN UNSATURATED SOILS

8.1 Introduction

In this chapter, a new DEM code was developed to simulate a pipe buried in unsaturated soil based on the methodology in CHAPTER 7. The primary objectives are: (i) to address and verify the scaling law related to inter-particle capillary forces in the DEM simulation, (ii) to conduct a back-analysis of the physical modelling tests of unsaturated CDG presented in CHAPTER 6, and (iii) to investigate the micro-level mechanisms underlying the pullout behaviour of a pipe buried in unsaturated soils.

8.2 Numerical model, boundary conditions and pipe generation

The model, boundary conditions and pipe generation are generally consistent with those described in CHAPTER 7. It comprises soil particles and a pipe within a domain, featuring two periodic walls along the pipe's axial direction (*y* direction) and four rigid walls in the other two directions, as illustrated in Figure 7.1.

The dimensions enclosed by rigid walls in the *x*-*z* plane of the domain are 0.71 m in height (*z* direction) and 0.3 m in width (*x* direction), corresponding to the physical modelling in CHAPTER 3 to CHAPTER 6. The left rigid wall (centre wall) in the *x* direction serves as the centre axis to apply plane symmetry. Considering the plane symmetry assumption, the pipe's rotation and horizontal displacement are restricted, and the friction angle of contact with the centre wall is set to 0°. The top wall is servo-controlled to apply the burial pressure as the top boundary in the physical modelling. The use of periodic walls is intended to minimise boundary effects. The thickness of the periodic domain (i.e., the distance between these two periodic walls)

is approximately 34 mm (23 times the average particle size of soils in Zone A). The friction angles of the top and bottom walls are set to 90° to ensure adequate reaction to the axial force.

To simulate pipe surface roughness, the pipe was constructed by clumping overlapping particles with a diameter of 3 times the average particle size of soils in Zone A. The normalised surface roughness ($R_n = R_{max}/d_{50}$) in the axial direction was controlled by adjusting the distance between two adjacent and touching pipe particles. The target value of R_n is 1.01, consistent with the rough pipe in the DEM simulation of CHAPTER 7 and close to 1.02 in the physical modelling of unsaturated CDG in CHAPTER 6.

8.3 Inter-particle contact model with capillary force

The classical Cundall linear contact model is employed to calculate the inter-particle linear normal force and the incrementally-formed linear elastic-perfect plastic shear force (Cundall & Strack, 1979), while an incrementally-formed linear elastic-perfect plastic model is used to determine the rolling torque (Šmilauer & Chareyre, 2021), as the same to dry conditions in CHAPTER 7.

To account for unsaturated conditions between particles, the capillary model developed by Scholtès *et al.* (2009); Duriez & Wan (2017a) for YADE is used to calculate the capillary force (F_{cap}) between particles. The key parameters related to the capillary model are given in Table 8.1. With this capillary force, the resultant force vector between two particles, p and q, denoted as $\boldsymbol{F}^{q,p}$, can be calculated using

$$\boldsymbol{F}^{q,p} = \boldsymbol{F}^{q,p}_{\text{contact}} + \boldsymbol{F}^{q,p}_{\text{cap}} \tag{8-1}$$

where $\boldsymbol{F}_{\text{contact}}$ is the contact force vector calculated via the Cundall linear model with the rolling resistance.

Figure 8.1 (a) illustrates a schematic diagram of an inter-particle liquid bridge. The shape of the bridge surface follows the Laplace-Young equation as

$$s = \frac{\gamma_t}{C} = \gamma_t \left[\frac{y''(z)}{(1+y'^2(z))^{3/2}} - \frac{1}{y(z)(1+y'^2(z))^{1/2}} \right] \tag{8-2}$$

where s is the matric suction and γ_t is the surface tension coefficient. The curvature C of the liquid bridge surface can be expressed as a function of the liquid bridge profile curve $y(z)$, as given in the equation. Here, the z-axis is the symmetry axis of the bridge, and y is the distance between the liquid bridge surface and the z-axis. The function $y(z)$ is solved using FDM with a second-order Taylor series expansion of $y(z)$ and boundary conditions of $y(z_i) = R_i \sin\delta_i$ and $y'(z_i) = -R_i/\tan(\delta_i+\theta)$, where R_i is the particle radius, δ_i is the filling angle on the particle, θ is the solid-liquid contact angle, z_i is the minimum or maximum z of the liquid profile ($z_2 - z_1 = d + R_1 + R_2 - R_1\cos\delta_1 - R_2\cos\delta_2$), d is the inter-particle distance, and i is the index of 1 and 2. More details on the finite difference approximation can be found in Duriez & Wan (2017a). With the solved $y(z)$, the capillary force, F_{cap}, and the water volume of the liquid meniscus, V_{cap}, can be obtained using

$$F_{cap} = \pi R_i^2 \sin\delta_i^2 s + 2\pi R_i \sin\delta_i \sin\left(\delta_i + \theta\right)\gamma_t \tag{8-3}$$

$$V_{cap} = \pi \int_{z_1}^{z_2} y^2(z)dx - \pi R_1^3 \left(\cos^3\delta_1 - 3\cos\delta_1 + 2\right) - \pi R_2^3 \left(\cos^3\delta_2 - 3\cos\delta_2 + 2\right) \tag{8-4}$$

Given the values of s, θ, R_i, γ_t and d, the results for F_{cap}, $V_{cap,}$ and δ_i can be determined. To enhance the calculation efficiency, all dimensionless solutions with specified values of θ and R_1/R_2 are pre-calculated and stored in ASCII files for direct retrieval via linear interpolation during the DEM simulation. In this study, the specific θ is assumed to be zero.

Figure 8.1 (b) depicts the relationship between F_{cap} and d. When $d<0$, F_{cap} is treated as a constant at the value for $d=0$, as the penetration depth is minimal in DEM simulations. When $d>0$ and the numerical capillary bridge is active, F_{cap} decreases as d increases until reaching $d_{rupture}$, beyond which there is no solution for $y(z)$. For conditions where $d>0$ but the numerical capillary bridge is not yet active, the capillary force is generally not added until d is smaller

than $d_{creation}$ rather than $d_{rupture}$. This study, following Scholtès *et al.* (2009), treats $d_{creation}$ as zero to simulate wetting conditions closer to the compaction during the sampling of physical models.

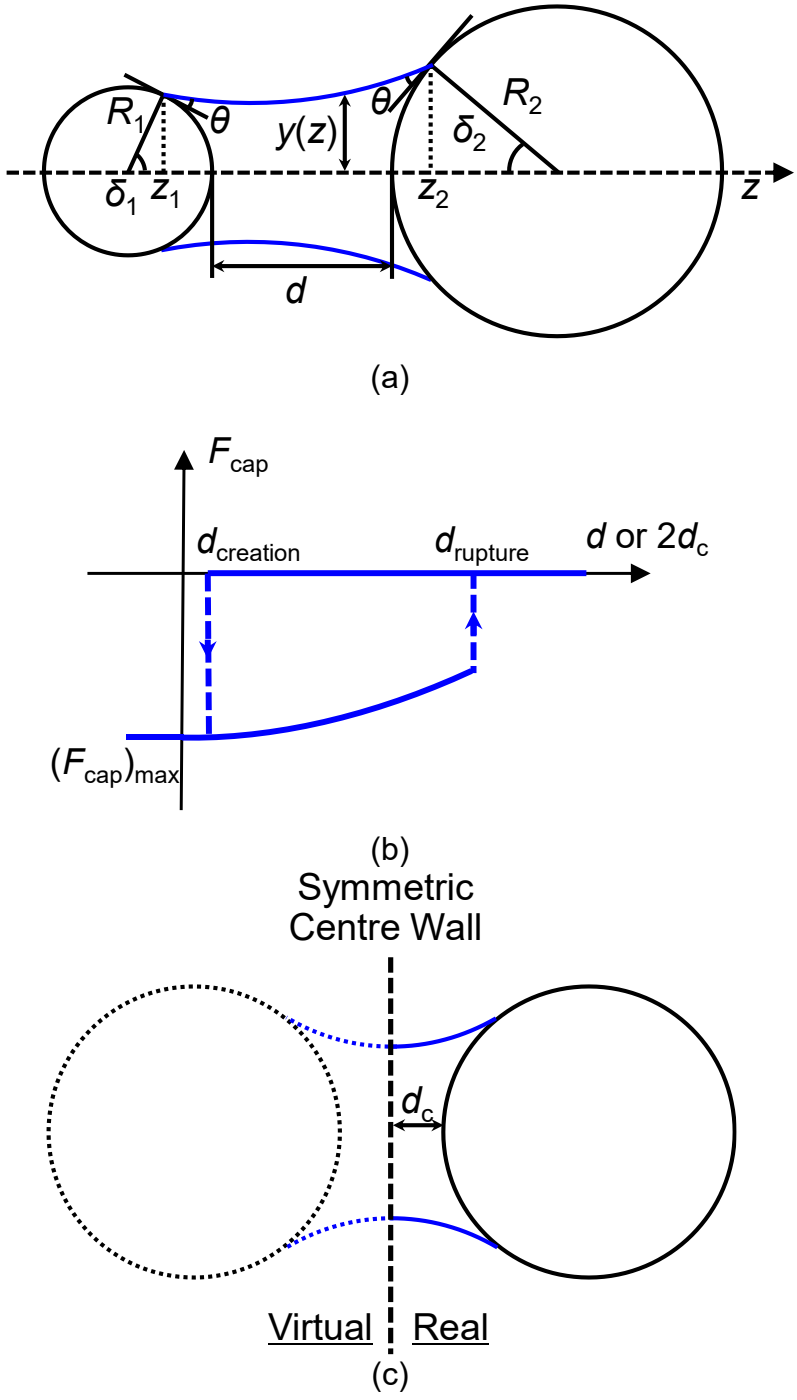

Figure 8.1 Schematic diagram of capillary model: (a) liquid bridge between particles; (b) the relationship between capillary force, F_{cap}, and inter-particle normal distance,d, or particle-centre wall normal distance, d_c; (c)liquid bridge through the symmetric centre wall

To ensure compatibility with the proposed model and boundary conditions, the existing YADE source code was enhanced to address three specific limitations. First, the capillary model in the existing code was not compatible with the Cundall contact model with rolling resistance by the previous developer. The new code combined the capillary model with the Cundall contact model with rolling and bending moments (i.e., class *Law2_ScGeom6D_CohFrictPhys_CohesionMoment* in YADE). Second, the existing code did not apply to particles contacting the symmetric centre wall, because there was no algorithm to build capillary force interaction between a particle and a wall and to calculate capillary force and liquid meniscus volume based on the plane-symmetric assumption. To resolve this, a F_{cap} is added to the interaction between any particle and the centre wall, as shown in Figure 8.1 (c), by treating the values of R_1/R_2, d and $V_{cap\text{-}c}$ as 1, $d_c \times 2$ and $V_{cap}/2$, respectively, where $V_{cap\text{-}c}$ is the water volume of the liquid meniscus between a particle and the centre wall, and d_c is the distance between a particle and the centre wall. Third, as discussed in the following section, the surface tension coefficient should vary for soils with different particle size scaling factors. To achieve this, the YADE source code was enhanced to allow the assignment of different target surface tension coefficients to particles in different zones within a single simulation. For any liquid meniscus formed between particles from different zones, the mean value of their respective target coefficients is used in the calculations.

8.4 Derivation and verification of scaling law for capillary force

In DEM simulations, particle sizes are often scaled up relative to real soil materials to reduce computation time. With an increase in particle size, the significance of suction effects couldn't remain unchanged, compared to that on real soil behaviour, if keeping constant matric suction (s) and surface tension coefficient (γ_t). The liquid bridge profile curve may become dissimilar due to the change in boundary conditions. To address these issues, a scaling law

related to capillary force is derived. The target is to keep the stress induced by capillary forces of liquid menisci (σ_{cap}) constant with the particle size scaling.

The stress tensor of a soil sample with volume V can be calculated using the extended Love-Weber formula, incorporating all inter-particle forces within the volume (Nicot *et al.*, 2013). Scholtès *et al.* (2009) extended this formula to compute the tensor of σ_{cap} as

$$\boldsymbol{\sigma}_{\text{cap}} = \frac{1}{V}\sum_{p=1}^{m}\sum_{q=1}^{p-1} \boldsymbol{f}_{\text{cap}}^{\,q,p} \otimes \boldsymbol{l}^{q,p} \tag{8-5}$$

where m is the number of particles and $\boldsymbol{l}^{q,p}$ is the distance vector between the centres of two particles. By combining with Equation (8-3), it can be rewritten as

$$\boldsymbol{\sigma}_{\text{cap}} = \pi\sum_{p=1}^{m}\sum_{q=1}^{p-1}\left[\sin\delta_q^{\,2}\,\frac{sR_q^{\,2}l^{q,p}}{V} + 2\sin\delta_q\sin\left(\delta_q+\theta\right)\frac{\gamma_{\text{t}}R_q l^{q,p}}{V}\right]\boldsymbol{n}^{q,p}\otimes\boldsymbol{n}^{q,p} \tag{8-6}$$

where $l^{q,p}$ ($=|\boldsymbol{l}^{q,p}|$) is the length of the distance vector and $\boldsymbol{n}^{q,p}$ ($=\boldsymbol{l}^{q,p}/l^{q,p}=\boldsymbol{f}_{\text{cap}}^{\,q,p}/f_{\text{cap}}^{\,q,p}$) is the unit vector of both the capillary force vector and the distance vector. Assume a soil sample model (with parameters denoted by the subscript 'mod') where the particle size is scaled up from a prototype (with parameters denoted by the subscript 'proto') by a factor of f_s. The scaling factors for particle size, inter-particle length, and sample volume can be expressed as

$$\frac{\left(R_q\right)_{\text{mod}}}{\left(R_q\right)_{\text{proto}}} = \frac{\left(l^{q,p}\right)_{\text{mod}}}{\left(l^{q,p}\right)_{\text{proto}}} = \frac{\sqrt[3]{V_{\text{mod}}}}{\sqrt[3]{V_{\text{proto}}}} = f_{\text{s}} \tag{8-7}$$

The scaling factor for the stress induced by capillary forces of liquid menisci should be equal to one for similarity, expressed by cancelling out dimensionless items and summation as

$$\frac{\left(\boldsymbol{\sigma}_{\text{cap}}\right)_{\text{mod}}}{\left(\boldsymbol{\sigma}_{\text{cap}}\right)_{\text{proto}}} = \frac{V_{\text{proto}}}{V_{\text{mod}}}\frac{\left(R_q\right)_{\text{mod}}}{\left(R_q\right)_{\text{proto}}}\frac{\left(l^{q,p}\right)_{\text{mod}}}{\left(l^{q,p}\right)_{\text{proto}}}\frac{\sin\delta_q s_{\text{mod}}\left(R_q\right)_{\text{mod}} + 2\sin\left(\delta_q+\theta\right)\left(\gamma_{\text{t}}\right)_{\text{mod}}}{\sin\delta_q s_{\text{proto}}\left(R_q\right)_{\text{proto}} + 2\sin\left(\delta_q+\theta\right)\left(\gamma_{\text{t}}\right)_{\text{proto}}} = 1 \tag{8-8}$$

The common solution for Equation (8-8) with different values of R and δ is

$$\frac{\left(s\right)_{\text{mod}}}{\left(s\right)_{\text{proto}}} = 1, f_\gamma = \frac{\left(\gamma_{\text{t}}\right)_{\text{mod}}}{\left(\gamma_{\text{t}}\right)_{\text{proto}}} = f_{\text{s}} \tag{8-9}$$

where f_γ is the scaling factor for the surface tension coefficient. Thus, the stress induced by capillary forces of liquid menisci in the model can match that of the prototype by using the same matric suction and a scaled surface tension coefficient with the same factor as the particle size scaling factor.

Furthermore, the scaling factors for the liquid bridge surface curvature ($C_{\text{mod}}(z_{\text{mod}})$ / $C_{\text{proto}}(z_{\text{proto}})$) and the boundary conditions of $y(z)$ ($y_{\text{mod}}((z_i)_{\text{mod}})$ / $y_{\text{proto}}((z_i)_{\text{proto}})$ and $y'_{\text{mod}}((z_i)_{\text{mod}})$ / $y'_{\text{proto}}((z_i)_{\text{proto}})$) are all equal to f_s. Therefore, the solution for $y(z)$ has a scaling factor as

$$\frac{y_{\text{mod}}(z_{\text{mod}})}{y_{\text{proto}}(z_{\text{proto}})} = f_s \tag{8-10}$$

ensuring the liquid bridge surface profile is fully similar. Consequently, the scaling factor for the sum volume of liquid menisci, $(V_{\text{cap}})_{\text{mod}}$ / $(V_{\text{cap}})_{\text{proto}}$, equals f_s^3, consistent with that of V. Thus, the degree of saturation remains unchanged, expressed as

$$\frac{(S_r)_{\text{mod}}}{(S_r)_{\text{proto}}} = \frac{\sum(V_{\text{cap}})_{\text{mod}} / (V)_{\text{mod}}}{\sum(V_{\text{cap}})_{\text{proto}} / (V)_{\text{proto}}} = 1 \tag{8-11}$$

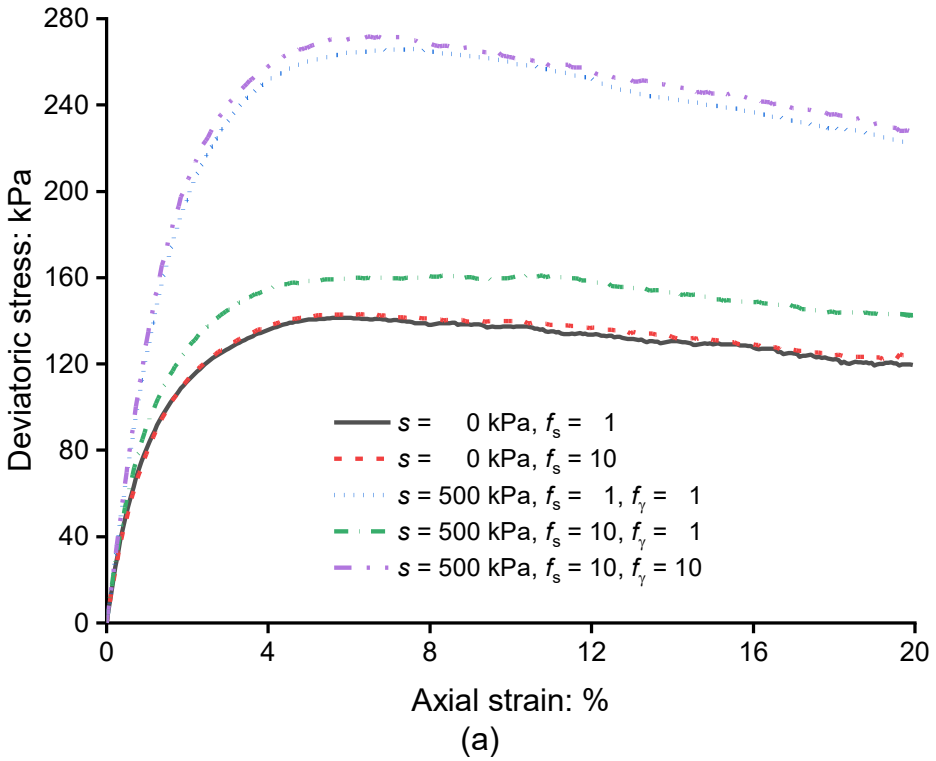

(a)

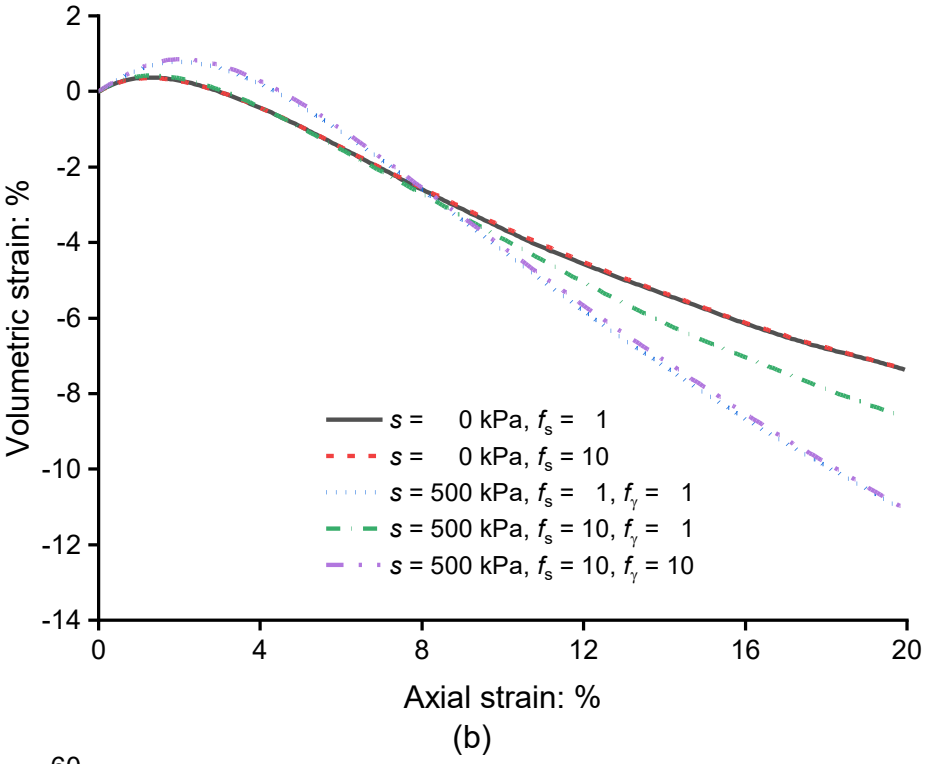
Volumetric strain: %
2
0
-2
-4
-6
-8
-10
-12
-14
0
4
8
12
16
20
Axial strain: %
s = 0 kPa, fs = 1
s = 0 kPa, fs = 10
s = 500 kPa, fs = 1, fγ = 1
s = 500 kPa, fs = 10, fγ = 1
s = 500 kPa, fs = 10, fγ = 10

(b)

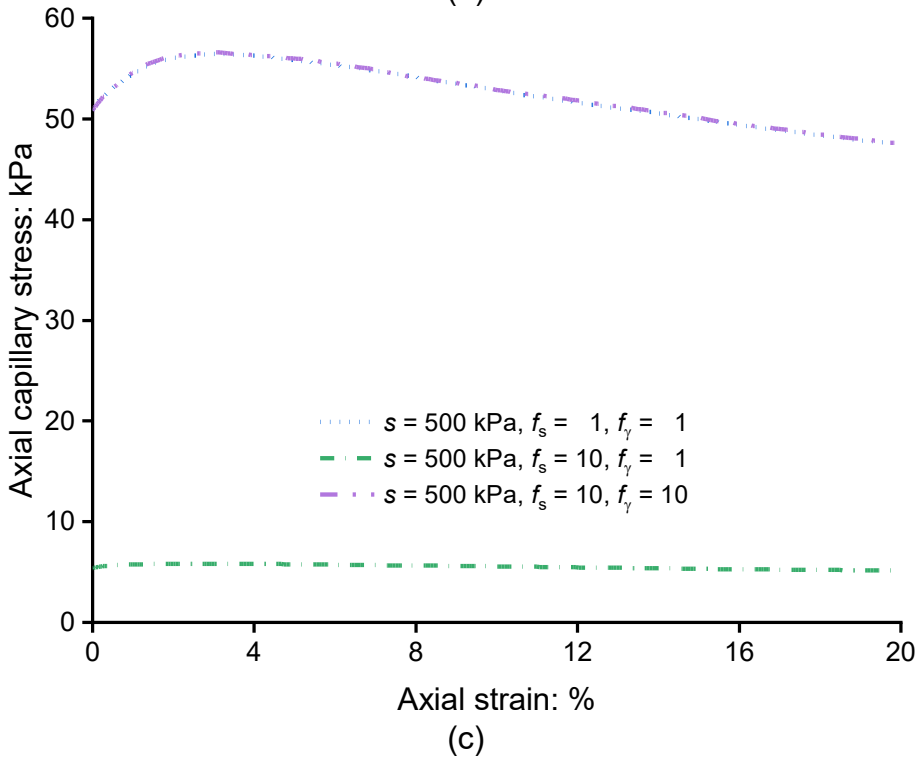
Axial capillary stress: kPa
60
50
40
30
20
10
0
0
4
8
12
16
20
Axial strain: %
s = 500 kPa, fs = 1, fγ = 1
s = 500 kPa, fs = 10, fγ = 1
s = 500 kPa, fs = 10, fγ = 10

(c)

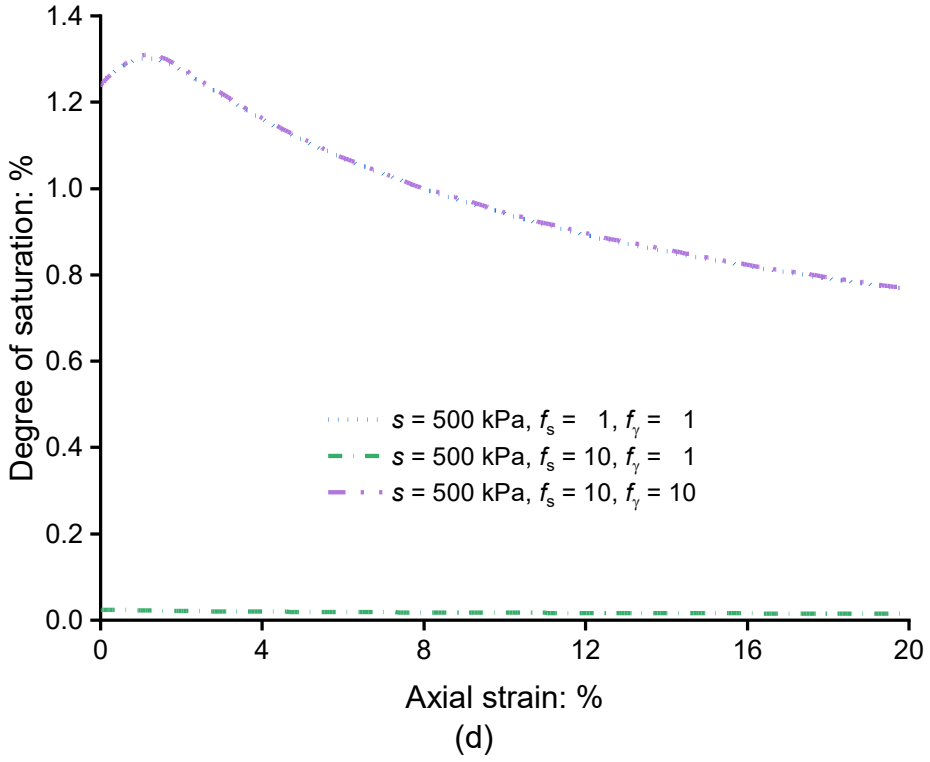

Figure 8.2 Validation of scaling law for the stress induced by capillary forces of liquid menisci using triaxial compaction simulation (confining pressure = 34 kPa, axial strain rate = 0.01/s, particle size of the prototype = 0.0025~0.005 mm): (a) deviatoric stress; (b) volumetric strain; (c) axial stress induced by capillary forces of liquid menisci; and (d) degree of saturation

To verify this scaling law, five triaxial compaction simulations were conducted. A total of 20,000 particles were randomly generated and compacted to a relative density of 85% using the radius expansion method (Scholtès *et al.*, 2009) within a cube enclosed by six frictionless rigid walls. An axial strain with a rate of 0.01/s was applied after the capillary forces application and the isotropic compaction to a confining pressure of 34 kPa. The contact model and its parameter values are consistent with subsequent soil-pipe interaction modelling. The particle size of the prototype and the target matric suction are set between 0.0025 and 0.005 mm and 500 kPa, respectively, to highlight differences in soil behaviour. Three simulations with $f_s = 10$ compare the behaviour of model soil samples with and without scaling law control, while two with $f_s = 1$ represent the prototype soil samples. Figure 8.2 illustrates the deviatoric stress, volumetric

strain, axial stress induced by capillary forces of liquid menisci, and degree of saturation with increasing axial strain. For the prototype sample simulation (f_s = 1), as matric suction increases to 500 kPa, the peak deviatoric stress rises sharply from 140 to 266 kPa, and dilatancy becomes more pronounced. The stress and strain curves of the model sample under dry conditions (f_s = 10 and s = 0 kPa) align well with those of the dry prototype, indicating no scaling effect on the Cundall model. However, significant differences exist between unsaturated model samples with and without the scaling law. The four curves of the unsaturated model with f_s = 10 closely match those of the prototype, validating the scaling law. In contrast, the peak deviatoric stress with f_s = 1 is only 160 kPa. The axial stress induced by capillary forces of liquid menisci and degree of saturation for the model with f_s = 1 are 5.1~5.8 kPa and 0.01~0.02%, much lower than the 47~56 kPa and 0.77~1.31% for f_s = 10.

The YADE source code was enhanced to achieve different target values of f_s in a single simulation for subsequent soil-pipe interaction simulations. Here, f_γ for interactions between any pair of particles with target values of f_γ is used as the mean value of the target.

8.5 Soil particles and parameters calibration

The particle size of CDG used in CHAPTER 3 ranges from around 0.0015 mm to 2 mm. Using such a high d_{max}/d_{min} ratio (> 1333) in DEM simulations is impractical because it would result in an excessively large number of particles, regardless of the particle size scaling factor. Therefore, a d_{max}/d_{min} ratio of 2 was adopted in this study for simplification. It is recognised that this simplification may influence both the soil-water retention curve and the shear behaviour, which is acceptable in DEM as it has minimal impact on axial resistance and the analysis of microscopic mechanisms. Furthermore, with the different d_{max}/d_{min} ratio, the prototype particle size (the quotient of the numerical particle size to the soil particle size scaling factor) is 0.01~0.02 mm, with a d_{50} value close to the d_{30} of the CDG, determined by the following calibration simulation.

The contact model parameters were calibrated to match the experimental results from constant normal loading (CNL) interface direct shear tests in CHAPTER 6. The experimental apparatus for soil-interface shearing was modified from the direct shear testing apparatus, featuring specimens of 60 × 60 × 20 mm^3. These specimens were placed above steel interfaces matching the pipe's surface roughness, enclosed by a steel box with four smooth, rigid walls, and covered by a pressure-controlled top cap wall. The calibration simulation employed the same boundary conditions as the interface direct shear tests. The interface was created by overlapping particles using the same approach and particle size as the pipe. Around 23,500 particles with a numerical size of 1~2 mm (consistent with the numerical particle size in Zone A) are used in the calibration. The dry density is 1.62 kg/m^3, which corresponds to 95% relative compaction, identical to that in CHAPTER 6. The maximum dry density is 1.71 kg/m^3, determined by isotropic compaction to 500 kPa using 30,000 frictionless particles.

The parameters for the Cundall linear contact model and rolling torque were first calibrated at a 0 kPa suction (i.e., the dry or saturated condition without the calculation of capillary force). The calibration results are shown in Table 8.1. Figure 8.3 (a) compares the computed interface shear stress of saturated soils using these parameters to the measured results. Computed curves align well with the experimental results, demonstrating the feasibility of these parameters.

With the calibrated parameters for the Cundall linear contact model and rolling torque, the prototype particle size was back-calculated by adjusting the surface tension coefficient at a matric suction of 70 kPa. Figure 8.3 (b) compares the measured and computed interface shear stress of unsaturated soils with a surface tension coefficient of 0.73 N/m (i.e., f_γ = 100). The computed interface shear strength and the critical displacement at which the interface shear strength is reached match the measured values. The displacement-softening in the computed results is not as rapid as in the measured results, possibly due to differences in particle distribution and soil-water retention capability. Given that there are no additional parameters

available to further adjust the soil response, the current validation should be considered acceptable. This limitation is expected to be addressed in the future when a higher d_{max}/d_{min} ratio becomes available in DEM simulations.

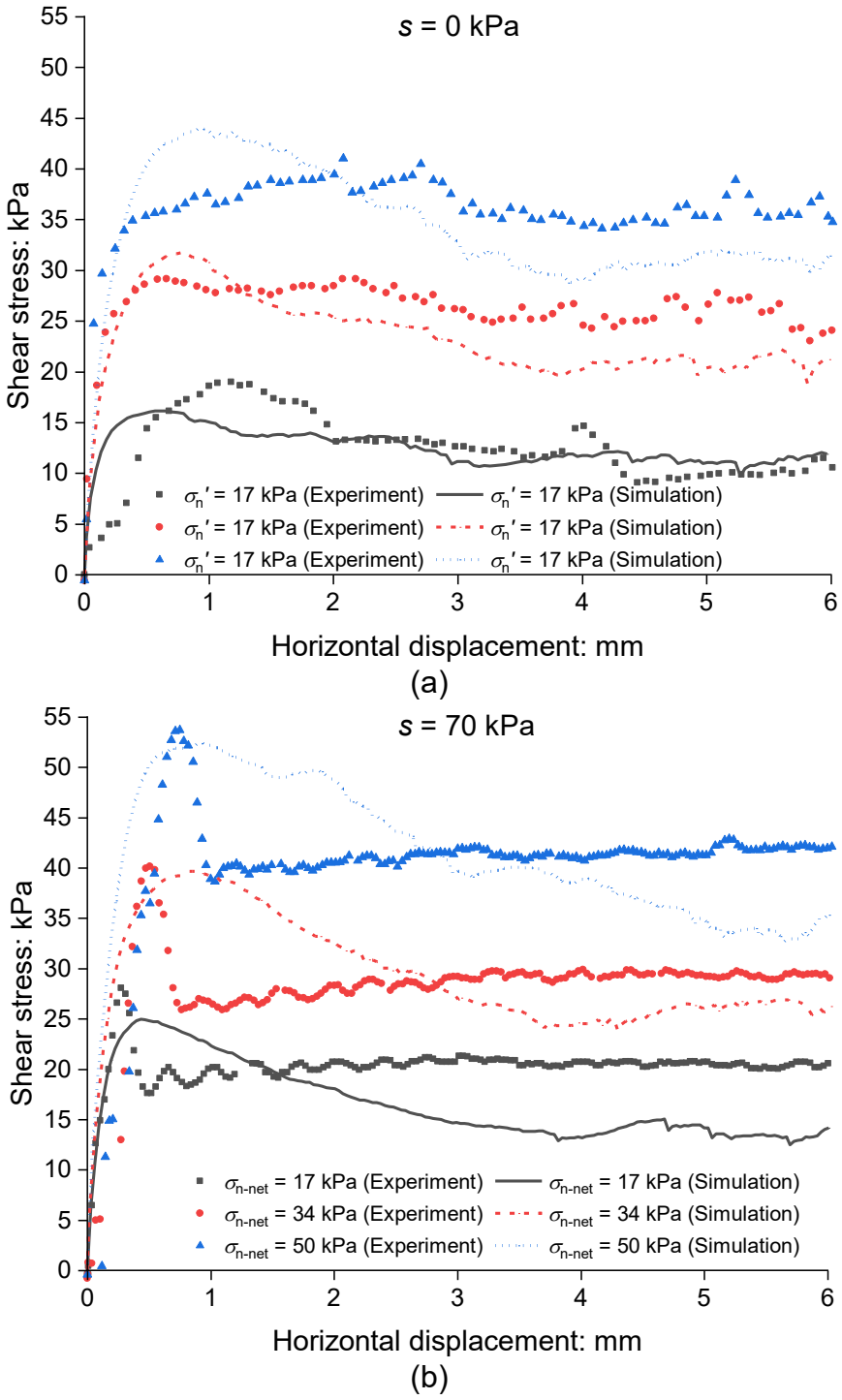

Figure 8.3 DEM parameter validation using interface direct shearing: (a) matric suction, s = 0 kPa; (b) s = 70 kPa

Table 8.1 DEM model parameters of ASPI at the unsaturated condition

Categories	Parameters	Values
Soil and pipe setting	Particle specific gravity	2.68
	Soil particle size: mm	$0.01\times f_s \sim 0.02\times f_s$
	Scaling factor of particle size, f_s	100(A), 150(B), 225(C), 337.5(D), 506.25(E)*
	The ratio of scaling factors to its inner zone	1.5
	Relative compaction: %	95
	Pipe particle size: mm	$3\times f_{s\text{-}A}^{\dagger} \times 0.015$
	Pipe normalised surface roughness, R_n	1.01
	Pipe axial velocity: mm/s	2
Cundall linear contact model	Normal stiffness to the radius of soil particles, k_n/r: MPa	60
	Normal stiffness to the radius of pipe particles, k_n/r: MPa	300
	Shear to normal stiffness ratio of soil particles, k_s/k_n	0.3
	Shear to normal stiffness ratio of pipe particles, k_s/k_n	0.3
	Inter-particle friction angle of soil particles, φ_{micro}: °	22
	Inter-particle friction angle of pipe particles, φ_{micro}: °	20
	Dimensionless rolling strength of soil particles	0.8
	Dimensionless rolling strength of pipe particles	0.8
	Dimensionless rolling stiffness of soil particles	0.8
	Dimensionless rolling stiffness of pipe particles	0.7
Capillary model	Surface tension coefficient, γ_t: N/m	$0.073\times f_c$
	Scaling factor of surface tension coefficient, f_γ	100(A), 150(B), 225(C), 337.5(D), 506.25(E)*
	Solid-liquid contact angle, θ: °	0
	Normal distance to create capillary force, $d_{creation}$	0
Others	Local non-viscous damping ratio	0.2
	Gravity, m/s^2	9.8

*Scaling factors within Zones A to E

†$f_{s\text{-}A}$: particle size scaling factor within Zone A

8.6 Simulation procedures

Considering that the capillary model is only applicable to soils in the pendular regime (degree of saturation < 15% as per Duriez & Wan (2017a)), the matric suction in the simulation is set to 70 kPa with a degree of saturation < 3% during pipe pullout to back-analyse the physical

modelling test with an average matric suction of 70.2 kPa. The water content in the simulation is obviously different from the physical model in CHAPTER 6 due to the differences in particle size distribution and the existence of combined water. The matric suction is then set to 200~1000 kPa to conduct a parametric study on suction effects. Assuming a hydrostatic distribution, the variation of matric suction along the depth of the pipe surface is minimal. Thus, for simplification, a constant matric suction is set along the depth in the simulation.

After incorporating the soil particle sample, which was prefabricated using the radius expansion approach, along with mixed boundaries and a pipe with free vertical displacement, a standard acceleration of gravity of 9.8 m/s² is applied. The sample is then compacted to achieve a target pressure on the top wall of $\sigma_{c\text{-}net}$ - $\gamma_{dry}H_{c0}$, where γ_{dry} is the dry unit weight, rather than the bulk unit weight of the soil and water mixture, due to the limited water content (<1.0%). Once stability is achieved (with an unbalanced force < 0.01 and vertical velocity of the top wall < 0.01 mm/s), the axial velocity of the pipe is set to 2 mm/s, and the target axial displacement is 20 mm, consistent with the physical modelling.

8.7 Interpretations of the simulation results

8.7.1 Comparison between the measured and computed axial behaviours at the unsaturated condition

Figure 8.4 (a) compares the computed axial pullout forces of pipes buried in soils with matric suctions of 70 kPa with the measured results in the physical modelling of CHAPTER 6. The axial force curves from the simulation exhibit significant strain-softening behaviour, similar to that observed in the physical modelling. In the simulation, the axial pullout resistance at a suction of 70 kPa is 13.37 kN/m, slightly larger than the measured value of 1.95 kN/m. The extent of softening, defined as the difference between the maximum axial force per unit length and the residual axial force per unit length, is approximately 1.72 kN/m in the DEM simulation, which is close to the values of 1.06 kN/m observed in physical modelling. Although the axial

stiffness in the DEM simulation is slightly smaller than the experimental results before 3 mm, the critical displacement required to reach the axial resistance in the simulation is between 6 and 8 mm, close to that in the physical model.

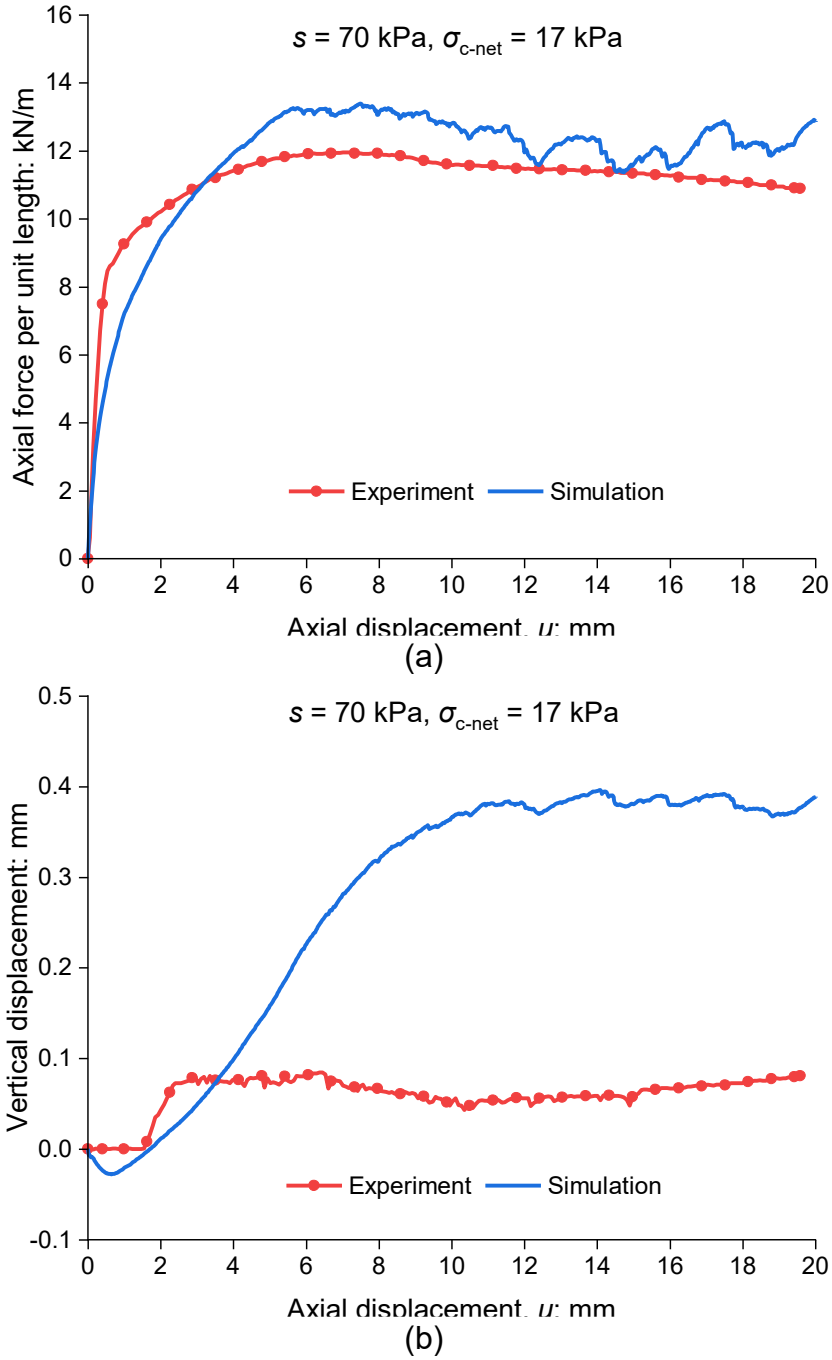

Figure 8.4 Comparisons between the measured and computed axial behaviour (net nominal vertical pressure at the pipe centre, σc-net = 17 kPa): (a) axial force; (b) vertical displacement

Figure 8.4 (b) illustrates the computed and measured vertical displacements of the pipe during the pullout process. In the numerical simulation, the pipe buried in unsaturated soils settles and then rises to stabilise at approximately 0.4 mm. The experimental result shows a similar trend, although the pipe stabilised at around 0.08 mm. The difference in the vertical displacement is possibly due to variations in the d_{max}/d_{min} ratio, particle scaling and water content.

8.7.2 Matric suction and buried pressure effects on axial behaviours

Figure 8.5 compares the axial behaviour of pipes under different matric suctions. The initial degrees of saturation are 2.69%, 0.34%, and 0.02% for matric suctions of 70, 200, and 1000 kPa, respectively. All axial force-displacement curves exhibit clear displacement-softening behaviour, as shown in Figure 8.5 (a). The axial resistance under unsaturated conditions is consistently greater than the 5.01 kN/m observed under dry conditions. In the DEM simulation, the ratio of axial resistance at 70 kPa suction to that at 0 kPa is 2.67, which closely matches the experimental ratio of 2.69 in CHAPTER 6. As matric suction increases from 70 to 1000 kPa, the axial resistance decreases. At a matric suction of 1000 kPa with a degree of saturation of 0.02%, the axial resistance is 8.81 kN/m. Although the maximum axial resistance cannot yet be determined numerically, the results indicate a trend in which axial resistance first increases and then decreases as matric suction rises from 0 kPa to very high levels in the pendular zone.

Under unsaturated conditions, the pipe exhibits upward movement at various matric suctions, although the final elevation decreases as matric suction increases from 70 to 1000 kPa (see Figure 8.5 (b)). In contrast, the pipe buried in dry soils undergoes continuous settlement, eventually stabilising at around -0.4 mm. The vertical displacement of the pipe is influenced by volumetric changes at the soil-pipe interface and in the soil beneath the pipe. Dilatancy at the bottom part of the soil-pipe interface can cause the pipe to rise, whereas compression of the soil beneath the interface, due to increased contact pressure, can lead to pipe settlement. For pipes

buried in dry soils, the compression effect dominates over dilatancy, resulting in net settlement. Conversely, in unsaturated soils, stronger soil-interface dilatancy and higher soil stiffness promote more dilatancy-induced pipe uplift and reduce compression-induced settlement, leading to the observed upward movement of the pipe. This interpretation is further supported by the particle displacement data presented later.

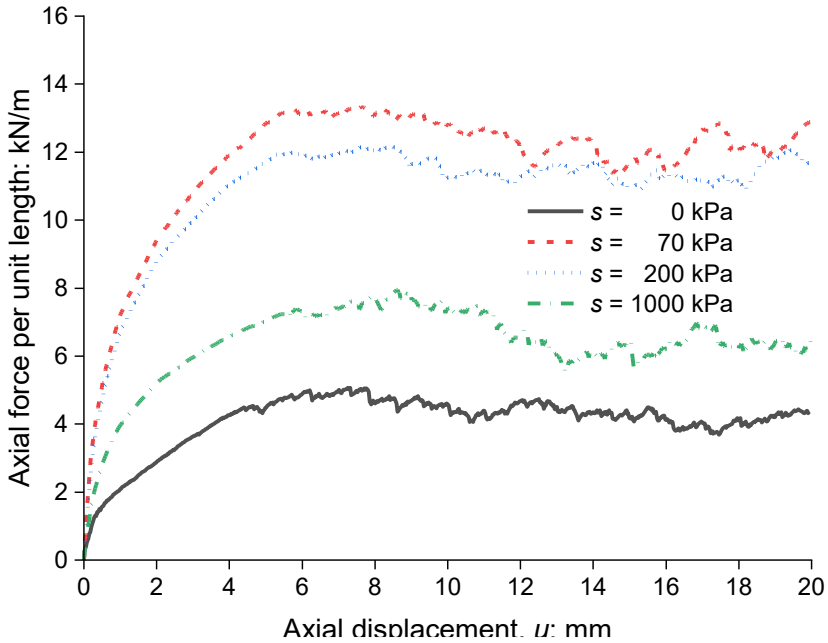

(a)

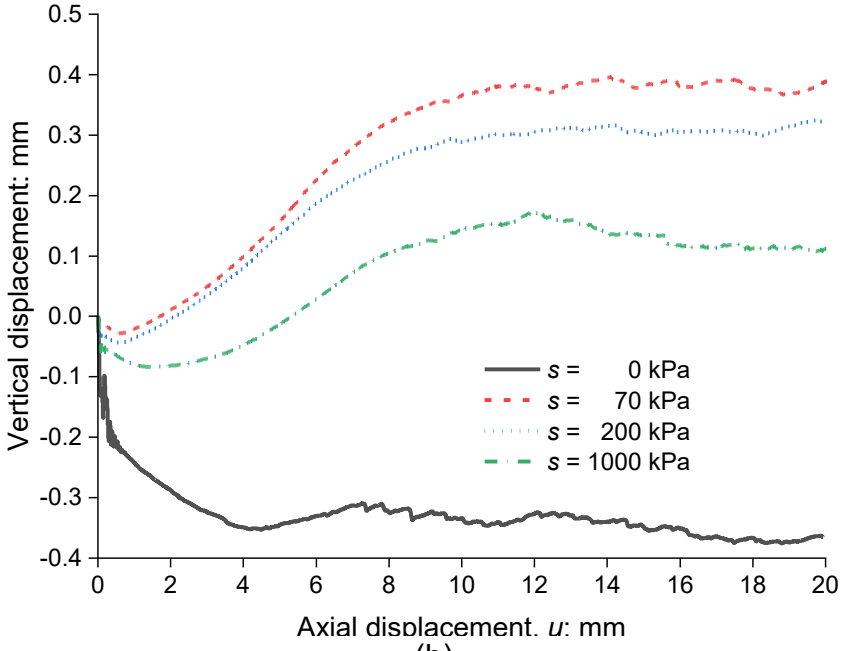

(b)

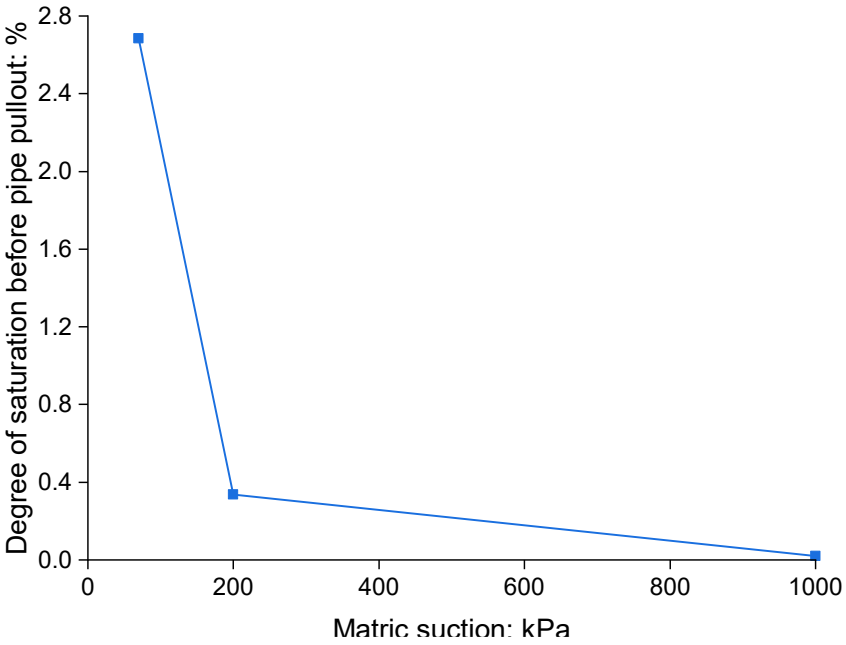

(c)

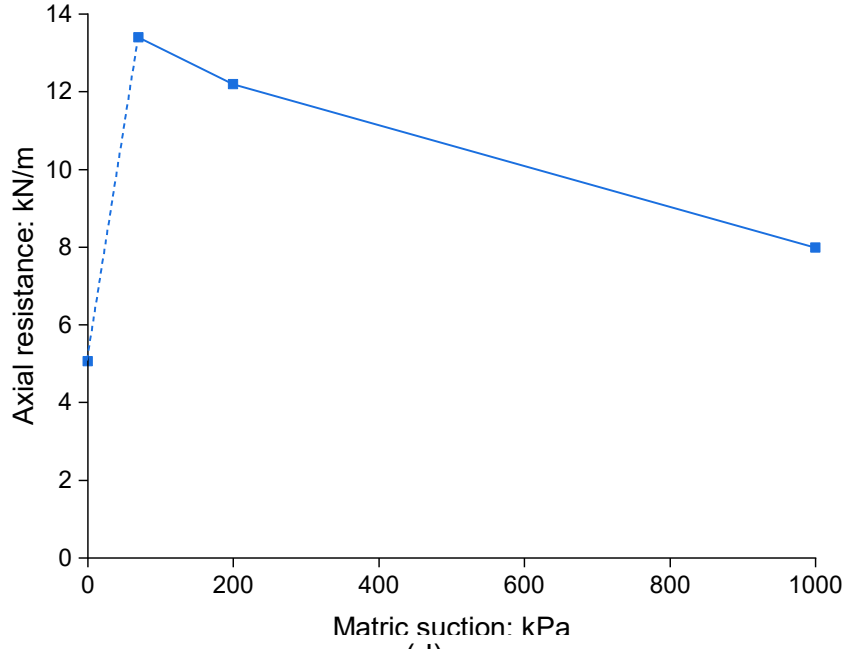

(d)

Figure 8.5 The computed axial behaviour at dry and unsaturated conditions ($\sigma_{c\text{-net}}$ or σ_c ′= 17 kPa): (a) axial force; (b) vertical displacement; (c) soil-water retention curve based on data before the pipe pullout; (d) matric suction effect on axial resistance

Figure 8.6 (a) presents the computed axial force-displacement curves under suction of 70 kPa and nominal buried pressures of 17, 34 and 50 kPa. The curve shapes are similar across different buried pressures. The axial resistance of unsaturated soils increases with increasing buried pressures, consistent with the findings in CHAPTER 6. Figure 8.6 (b) shows that the

relationship between the computed axial resistance of unsaturated soils and net buried pressure is linear, with a slope of 0.616, similar to that of dry soils, indicating no suction effect on the resistance-pressure relationship.

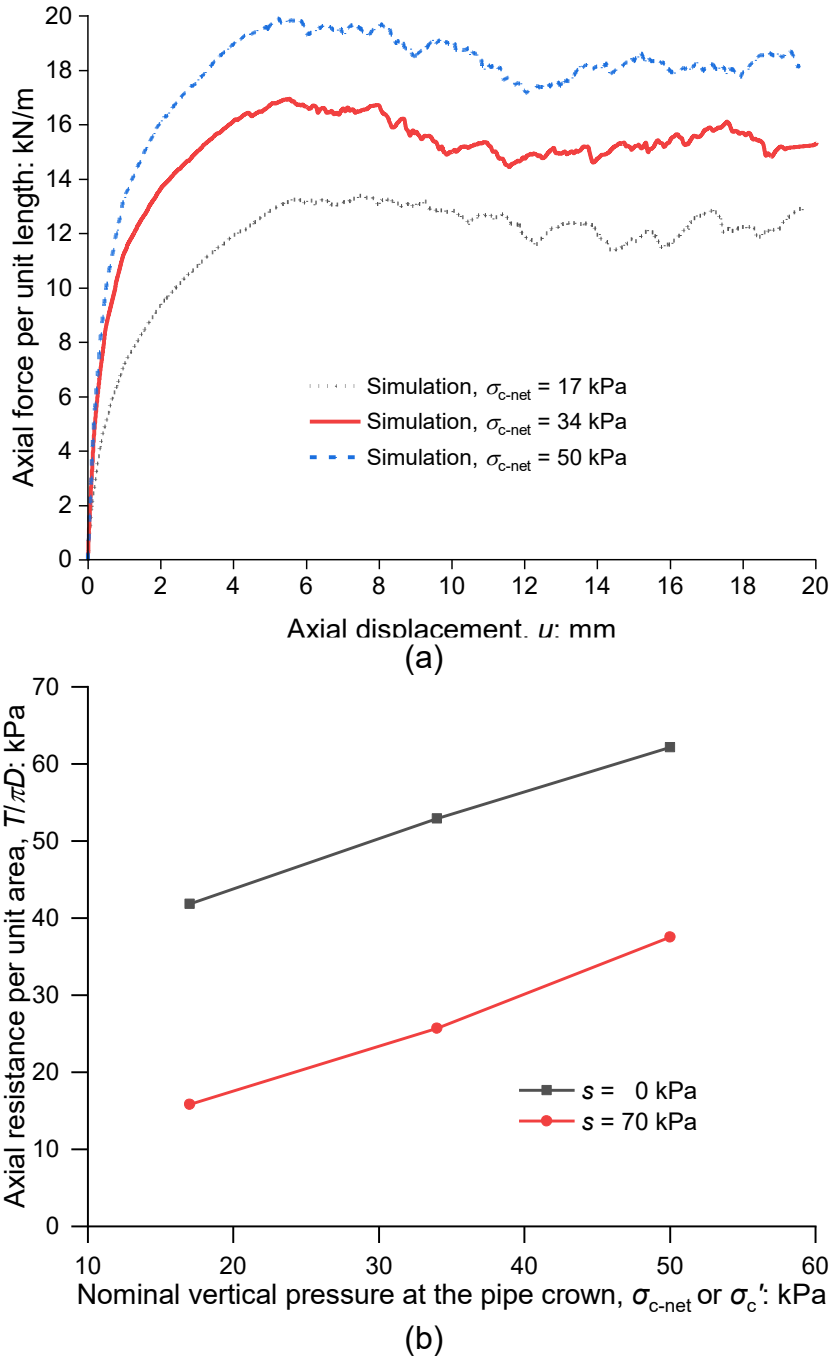

Figure 8.6 Buried pressure effect on the computed pipe pullout behaviour: (a) axial force (s = 70 kPa); (b) axial resistance against nominal pressure at the pipe centre

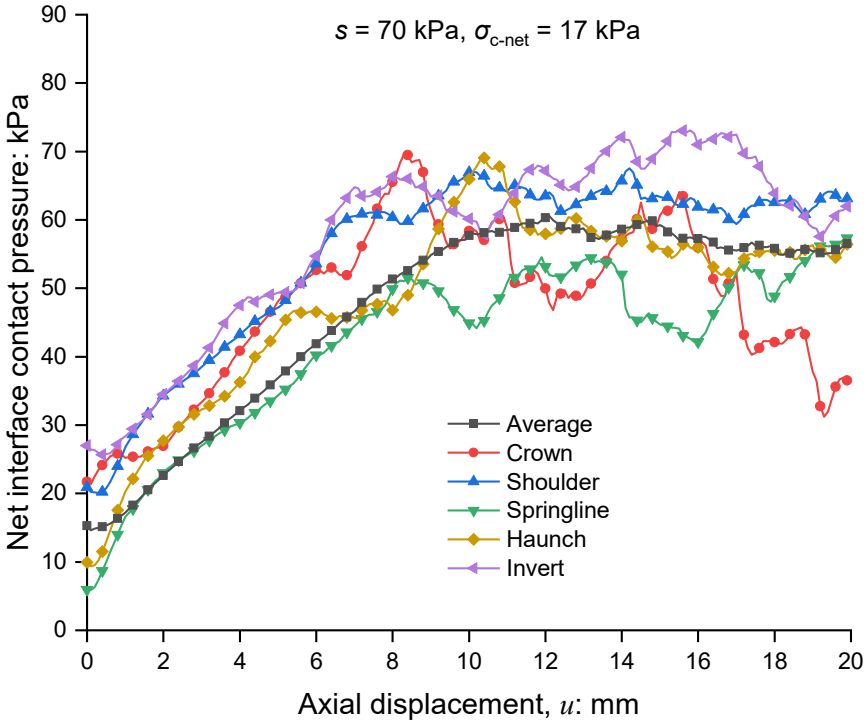
s = 70 kPa, σc-net = 17 kPa
Net interface contact pressure: kPa
Axial displacement, u: mm
Average
Crown
Shoulder
Springline
Haunch
Invert

(a)

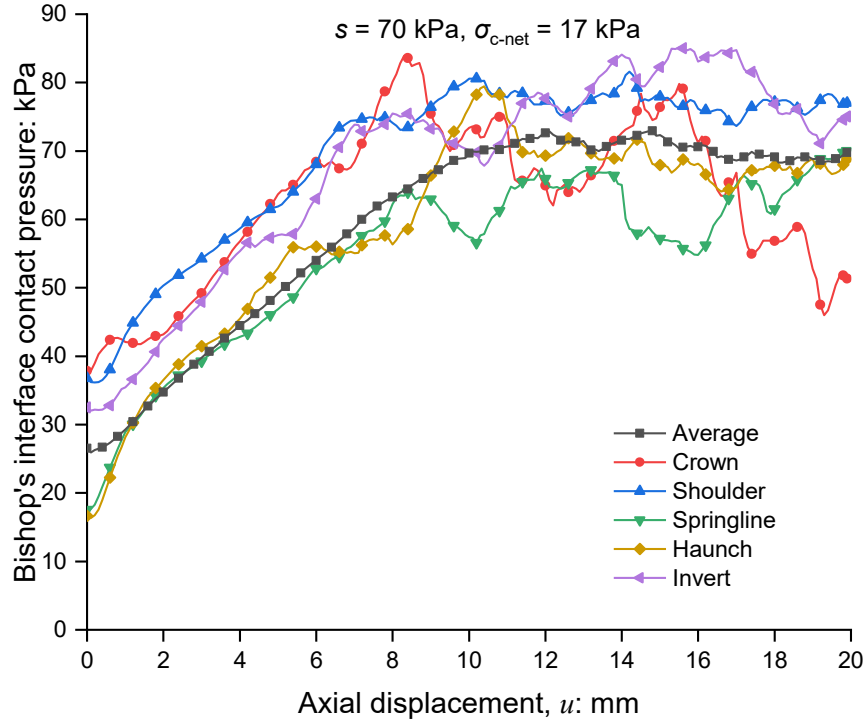
s = 70 kPa, σc-net = 17 kPa
Bishop's interface contact pressure: kPa
Axial displacement, u: mm
Average
Crown
Shoulder
Springline
Haunch
Invert

(b)

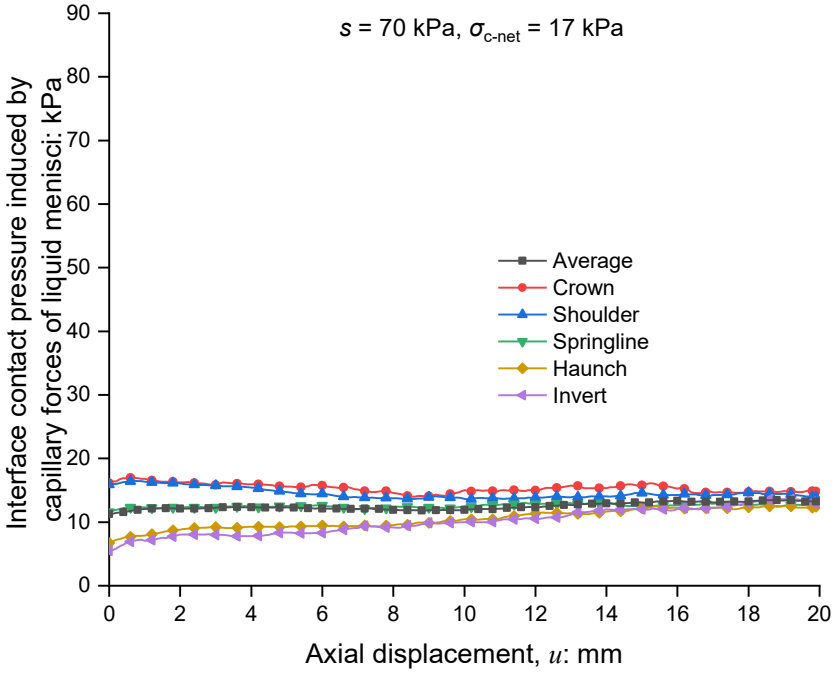

(c)

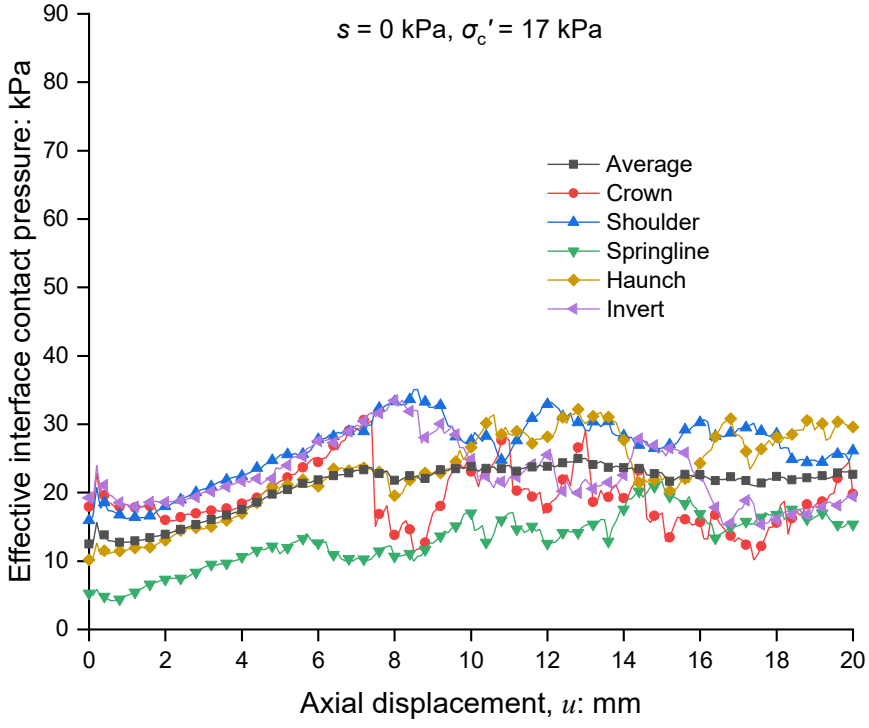

(d)

Figure 8.7 Interface contact pressure ($\sigma_{c\text{-net}}$ or σ_c' = 17 kPa;): (a) net interface contact pressure (s = 70 kPa); (b) Bishop's interface contact pressure (s = 70 kPa); (c) the interface contact pressure induced by capillary forces of liquid menisci (s = 70 kPa) and (d) effective interface contact pressure (s = 0 kPa)

8.7.3 Interface contact pressure at the soil-pipe interface

Figure 8.7 illustrates the evolution of soil-pipe interface contact pressures (σ_{int}) under a nominal vertical pressure of 17 kPa and matric suction of 70 kPa. In the simulation, the interface contact pressure at a specific position on the pipe surface is calculated by summing the soil-pipe inter-particle contact forces within a ±5° cross-sectional area around that position. Net and Bishop's interface contact pressures ($\sigma_{int\text{-}net}$ and $\sigma_{int\text{-}bishop}$) are calculated using $\boldsymbol{F}_{contact}$ and $\boldsymbol{F}$. And the component of interface contact pressure induced by capillary forces of liquid menisci, $\sigma_{int\text{-}cap}$, is calculated based on $-\boldsymbol{F}_{cap}$.

Figure 8.7 (a) compares $\sigma_{int\text{-}net}$ at different surface locations. Before pullout, the initial values of $\sigma_{int\text{-}net}$ at the crown, springline, and haunch are 21.7, 6.0, and 9.9 kPa, respectively. During pipe pullout, an overall increasing trend is evident in all curves of $\sigma_{int\text{-}net}$ due to constrained dilatancy. Specifically, at the pipe crown, $\sigma_{int\text{-}net}$ decreases after initially increasing to around 70 kPa. The values of $\sigma_{int\text{-}net}$ at the shoulder, springline, and haunch show a slight decrease before subsequently increasing.

Figure 8.7 (b) shows the evolution of $\sigma_{int\text{-}bishop}$ and $\sigma_{int\text{-}cap}$. The presence of $\sigma_{int\text{-}cap}$ strengthens the contact force between soil particles and the interface (i.e., $\sigma_{int\text{-}bishop}$), sharply increasing the axial resistance shown in Figure 8.5. The magnitude of $\sigma_{int\text{-}cap}$ could be linked to the void ratio at the interface, which is negatively related to the soil-interface contact number and distance between soil and pipe particles. The values of $\sigma_{int\text{-}cap}$ are not constant along the pipe surface. Instead, before pipe pullout, the values of $\sigma_{int\text{-}cap}$ at the pipe crown, shoulder, springline, haunch and invert are 16.2, 15.9, 11.6, 6.7 and 5.5 kPa, decreasing with the depth. During the axial displacement of the pipe, the values of $\sigma_{int\text{-}cap}$ do not vary with $\sigma_{int\text{-}bishop}$. Instead, the average value of $\sigma_{int\text{-}cap}$ remains 11~13 kPa. It contributed at least 20% of Bishop's interface contact pressure during the pipe pullout, increasing the axial resistance at the unsaturated condition. Pressures at different pipe surfaces converge to this average value, reflecting that the void ratio

tends to become uniform along the pipe surface due to the disturbance of soil contact structure and interface dilatancy during pipe pullout.

8.7.4 Stress path at the soil-pipe interface

Figure 8.8 illustrates the stress path at the soil-pipe interfaces in the simulation using both net stress and Bishop's stress. The average stress paths for tests under matric suctions of 0 and 70 kPa, as well as local stress paths at different positions under a matric suction of 70 kPa, are presented. For clarity, only data from local paths at axial displacements of 0~10 mm are shown. The failure envelopes for soil-interface shear are determined through CNL periodic boundary interface shear simulations at normal stresses of 1, 17, 34, 50, and 100 kPa and matric suctions of 0 and 70 kPa, and are included as references. The shapes of the average and local interface stress paths for unsaturated soils, in terms of both net and Bishop's stress, resemble those from the simulation of dry soils, the physical modelling inCHAPTER 4 and CHAPTER 6, and constant normal stiffness (CNS) tests on soil elements at rough interfaces by Ooi & Carter (1987); Pra-ai & Boulon (2016). These paths generally include three stages. First, the path rises vertically with elastic friction angle mobilisation. Second, it moves towards the top right due to constrained dilatancy-induced increases in the interface contact pressure and thus shear stress. Third, the stress path turns to the bottom right and even the bottom left, sliding along the critical state envelope.

In terms of net stress (see Figure 8.8 (a)), the initial average interface contact pressure under unsaturated conditions is 15.3 kPa, similar to that under dry conditions with the same nominal buried pressure. Subsequently, the average path for unsaturated soils approaches the peak failure envelope for s = 70 kPa in the second stage and stabilises at the critical state failure envelope for s = 70 kPa, rather than yielding to the failure envelopes for s = 0 kPa, as seen in the dry condition path. In contrast, Bishop's interface stress path for unsaturated soils yields the failure envelopes for s = 0 kPa (see Figure 8.8 (b)). Moreover, the increases in average interface

contact pressure from the beginning to the point of touching the critical state failure envelope for net and Bishop's stresses are 45.3 and 50.0 kPa, respectively, which are significantly higher than the 11.72 kPa observed for dry soil. This is attributed to the stronger interface dilatancy in unsaturated soil, as demonstrated later.

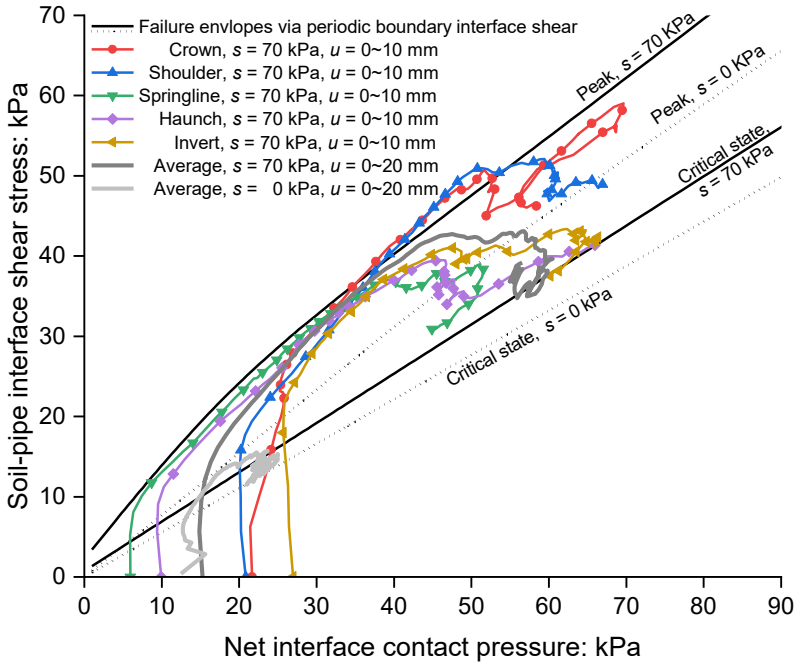

(a)

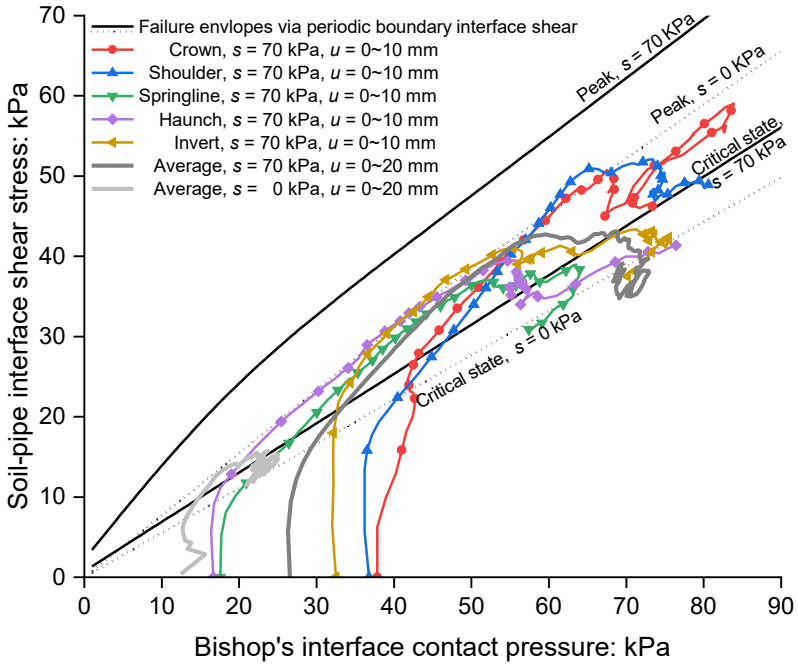

(b)

Figure 8.8 The computed soil-pipe interface stress path ($\sigma_{c\text{-net}}$ or $\sigma_c' = 17$ kPa): (a) net stress; (b) Bishop's stress

All of the local interface stress paths normally touched the peak failure envelope and stabilised at the critical state envelope in terms of both net and Bishop's stresses, demonstrating full mobilisation of interface shear at the entire soil-pipe interface. It corresponds to the distribution of the interface contact pressure induced by capillary forces of liquid menisci in Figure 8.7 (c) and soil particle displacement and force chain in the following parts.

8.7.5 Soil particle displacement around the pipe

Figure 8.9 (a) illustrates the average soil particle displacement in the *y* (axial) direction at matric suctions of 70 and 0 kPa. Both curves exhibit a similar shape, where soil particle displacement in the *y* direction decreases as the distance from the pipe surface increases. The interface shear band thicknesses, identified by the noticeable inflexion point of the curves, are 7.9 mm and 8.7 mm for suctions of 70 and 0 kPa, respectively. The differences in interface shear band thickness and displacement within the shear band between unsaturated and dry soils are minimal. However, the axial displacements of unsaturated soil particles outside the shear band are slightly larger than those of dry soils, with the maximum difference being around 10% of the axial displacement of the pipe, *u*. The soil-interface distance at the point of maximum soil displacement difference is between 11 and 15 mm, 40~90% larger than the shear band. This larger axial displacement of soil particles in unsaturated conditions outside the shear band is due to inter-particle adhesions from capillary forces, leading to more pronounced dilatancy of the entire soil sample and thus a higher increase in interface contact pressure, as shown in Figure 8.8.

Figure 8.9 (b) compares the axial displacement field of soil at a pipe displacement of 20 mm between dry and unsaturated soils. The unsaturated soil-interface shear band is uniformly distributed along the pipe surface, rather than decreasing in thickness from the pipe crown to the invert under the saturated conditions. This results from the full mobilisation of interface shear along the entire soil-pipe interface, as indicated by the local stress paths in Figure 8.8.

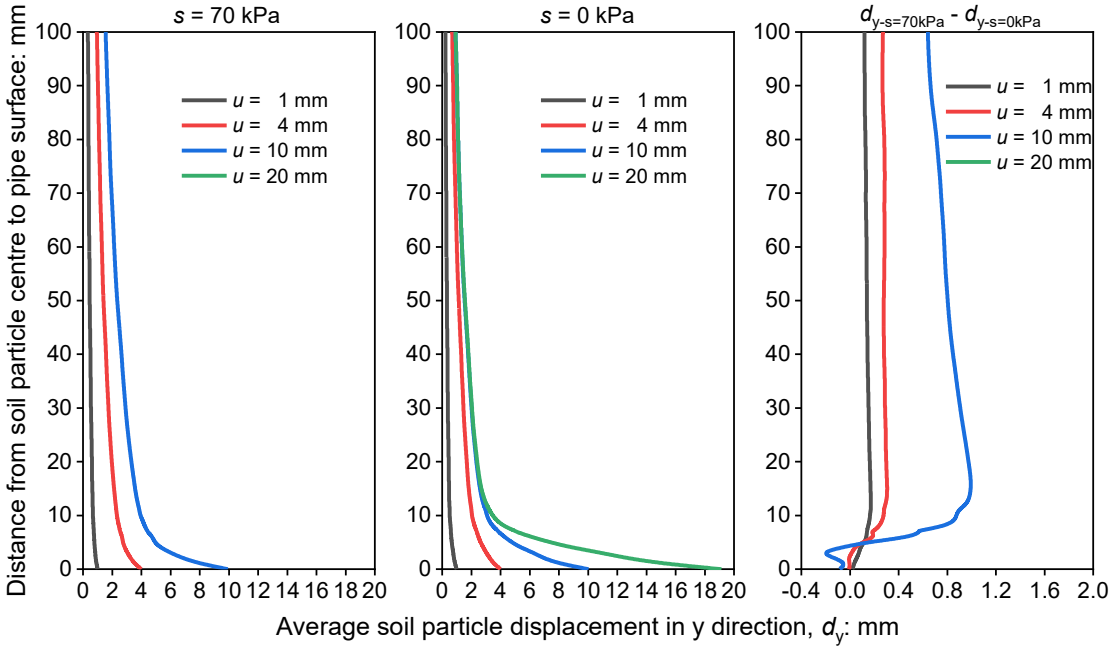

(a)

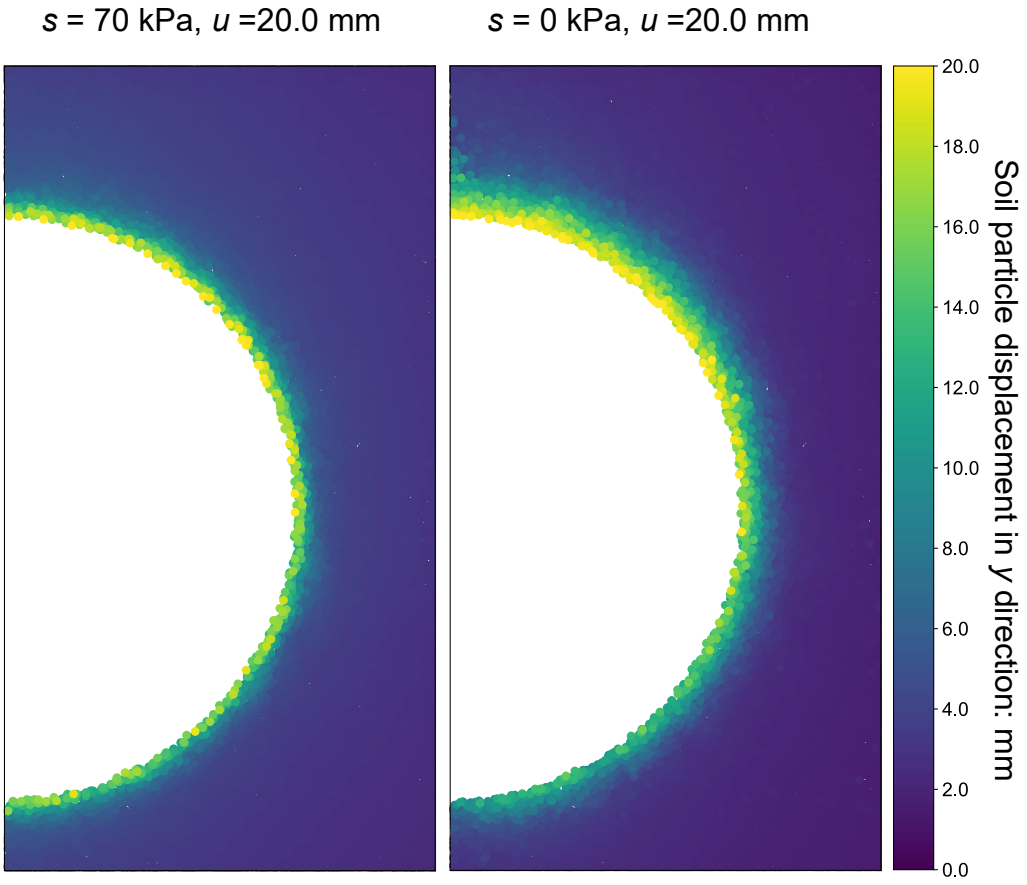

(b)

Figure 8.9 Soil particle displacement in *y* direction: (a) development of average soil particle displacement against distance from soil particle centre to pipe surface; (b) displacement field within Zone A ($\sigma_{c\text{-net}}$ or σ_c' = 17 kPa, u = 20 mm)

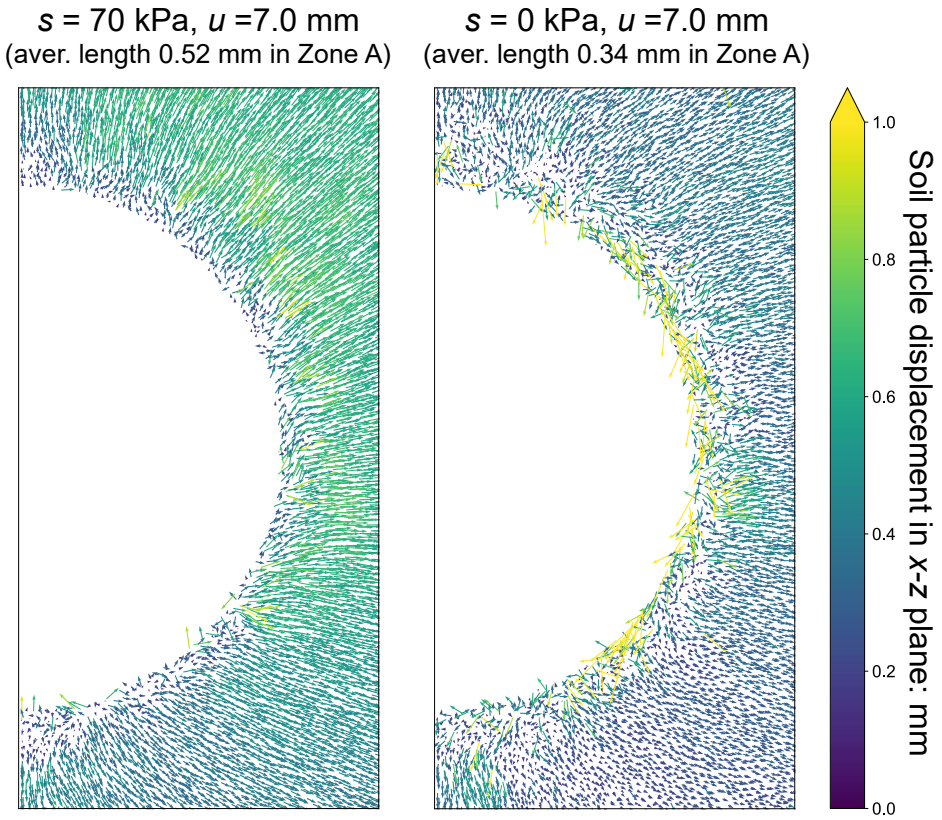

Figure 8.10 Soil particle displacement in *x-z* plane within Zone A ($\sigma_{c\text{-net}}$ or $\sigma_c' = 17$ kPa, five times in vector length)

Figure 8.10 shows the soil particle displacement vectors in the *x-z* plane at a pipe displacement of 7 mm with matric suctions of 70 and 0 kPa. The vectors originate from their initial positions before the pipe pullout, and their lengths are magnified five times for clarity. Soil particles outside the shear band in both dry and unsaturated soils move away from the pipe due to the dilation behaviour within the interface shear band. The volumetric expansion of the soil is constrained by the boundary walls, which in turn increases the soil-pipe interface contact pressure, as shown in Figure 8.7. The average soil displacement vector length in the *x-z* plane at a suction of 70 kPa is 0.52 mm within Zone A, noticeably higher than at a suction of 0 kPa. This is due to three reasons: first, the dilatancy of the unsaturated soil interface shear band is stronger than that of the dry soil; second, the larger shear displacement of soil outside the interface shear band, as shown in Figure 8.9 (a), induces more volumetric expansion of soil

outside the shear band; third, the higher increase in unsaturated soil-pipe interface contact pressure, as seen in Figure 8.7, leads to greater soil compression.

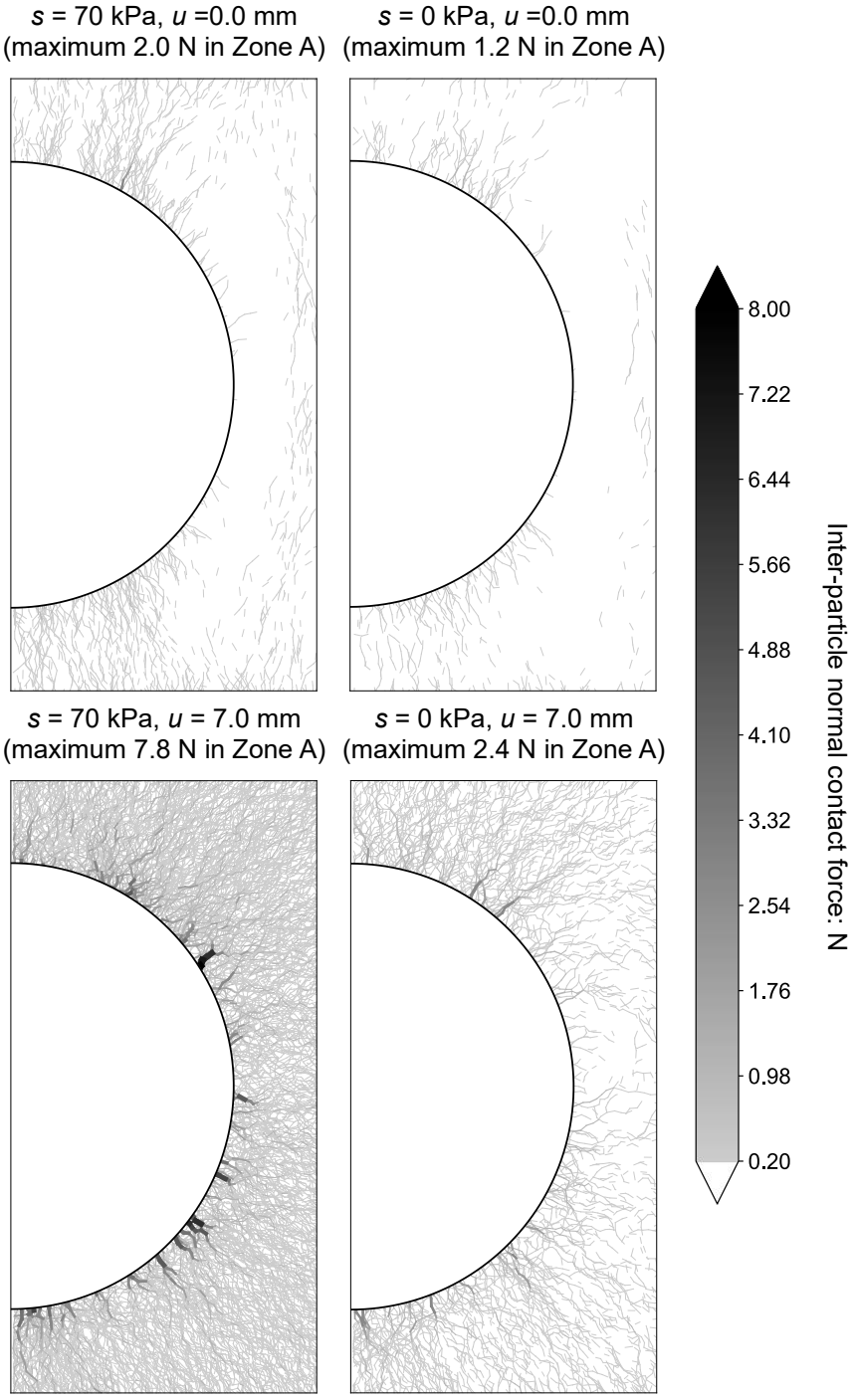

Figure 8.11 Inter-particle contact normal force chain evolution within Zone A ($\sigma_{c\text{-net}}$ or $\sigma_c' = 17$ kPa)

Moreover, the soil displacement vectors in the *x-z* plane also explain the pipe rising behaviour during shearing, as shown in Figure 8.5. The movement of unsaturated soil particles

beneath the interface shear band is more pronounced than in dry soil, yet the pipe buried in unsaturated soils rises during pullout rather than settling, as it does in dry soils. This demonstrates that the pipe rising caused by the volumetric expansion of the soil-pipe interface shear band is greater than the settlement of the soil beneath the pipe at the unsaturated condition.

8.7.6 Inter-particle normal contact force chain evolution

Figure 8.11 illustrates the evolution of force chains using inter-particle normal contact forces. For clarity, only contact forces greater than 0.2 N are displayed. Before the pipe pullout, the force chain distributions under both dry and unsaturated conditions are similar. Stronger vertical force chains develop from the pipe's crown, shoulder, haunch, and invert, while there are few contact normal forces greater than 0.2 N near the pipe springline. This demonstrates the passive soil arching effect due to stress concentration on the stiffer pipe, as discussed in CHAPTER 4, CHAPTER 6 and CHAPTER 7, and in previous studies (Wijewickreme *et al.*, 2009; Sheil *et al.*, 2018; Murugathasan *et al.*, 2021). The contact forces under unsaturated conditions are stronger, with more contacts exceeding 0.2 N and a maximum contact force of 2 N within Zone A, which is 67% higher than the 1.2 N observed under dry conditions. This is because the presence of capillary forces strengthens the inter-particle contact forces.

At a pipe axial displacement of 7 mm, more and stronger force chains develop from the pipe surface due to the constrained dilation mentioned earlier. There are two key differences between the dry and unsaturated conditions. First, the force chains in unsaturated soil are much stronger. The maximum contact force in Zone A for unsaturated soils is 7.8N, 290% higher than the initial condition, compared to only a 100% increase in dry soils. This corresponds to the higher increase in soil-pipe interface contact pressure due to constrained dilatancy in unsaturated soils. Second, under dry conditions, force chains are still primarily developed from the pipe crown, shoulder, haunch, and invert, demonstrating the continuous effect of passive soil arching on the soil-pipe interface contact pressure redistribution. In contrast, under

unsaturated conditions, the force chains are distributed uniformly along the pipe surface. This corresponds to the uniform distribution of interface contact pressure induced by capillary forces of liquid menisci shown in Figure 8.7 (c) and the full mobilisation of interface shear across the entire soil-pipe interface, as shown in Figure 8.8.

8.7.7 Earth pressure evolution

Figure 8.12 and Figure 8.13 depict the evolution of vertical and lateral earth pressures around the pipe, calculated using a homogenization approach. This method involves dividing the soil area into 10×10 mm² meshes in the *x*-*z* plane. Both net stress and Bishop's stress are considered. Before the pipe is pulled out, the net vertical earth pressure field under unsaturated conditions closely resembles the effective vertical earth pressure under dry conditions, with average values in Zone C of 21.8 kPa and 19.1 kPa, respectively. These values are slightly higher than the nominal buried pressure due to the passive soil arching effect, where the pipe supports more overburden pressure than the adjacent soil. Bishop's vertical earth pressure field, with an average value of 32.8 kPa in Zone C, is significantly higher than the net stress field due to the stress induced by capillary forces of liquid menisci, which is uniformly distributed. When the pipe moves 7 mm, an increase in vertical earth pressure is observed at the top and bottom of the pipe. This increase is more pronounced in unsaturated soil due to its stronger constrained dilatancy, with values near the pipe crown, springline, and invert exceeding 60 kPa, which is 3.5 times the nominal pressure. The average variation in vertical earth pressure within Zone C is minimal because the pressure at the pipe sides decreases while the pressure above and below the pipe supports more of the overburden.

Regarding lateral earth pressure, as shown in Figure 8.13, the average lateral effective stress within Zone C for dry soils is 7.4 kPa, corresponding to a lateral pressure coefficient at rest, K_0, of 0.387, which is close to the empirical value of 0.362 based on 1-sinφ'. Under a matric suction of 70 kPa, the average net lateral stress is 5.1 kPa, resulting in a K_0 value of 0.234, which is 40%

lower than that of dry soil, consistent with previous studies on the suction effect on K_0 (Lu & Likos, 2004). During pipe pullout, lateral pressure increases significantly, with the average net lateral earth pressure in unsaturated soil rising by 110%, compared to a 28% increase in dry soil. The earth pressure coefficients increase to 0.514 and 0.455 at matric suctions of 70 kPa and 0 kPa, respectively. Bishop's lateral pressure near the pipe also exceeds 60 kPa.

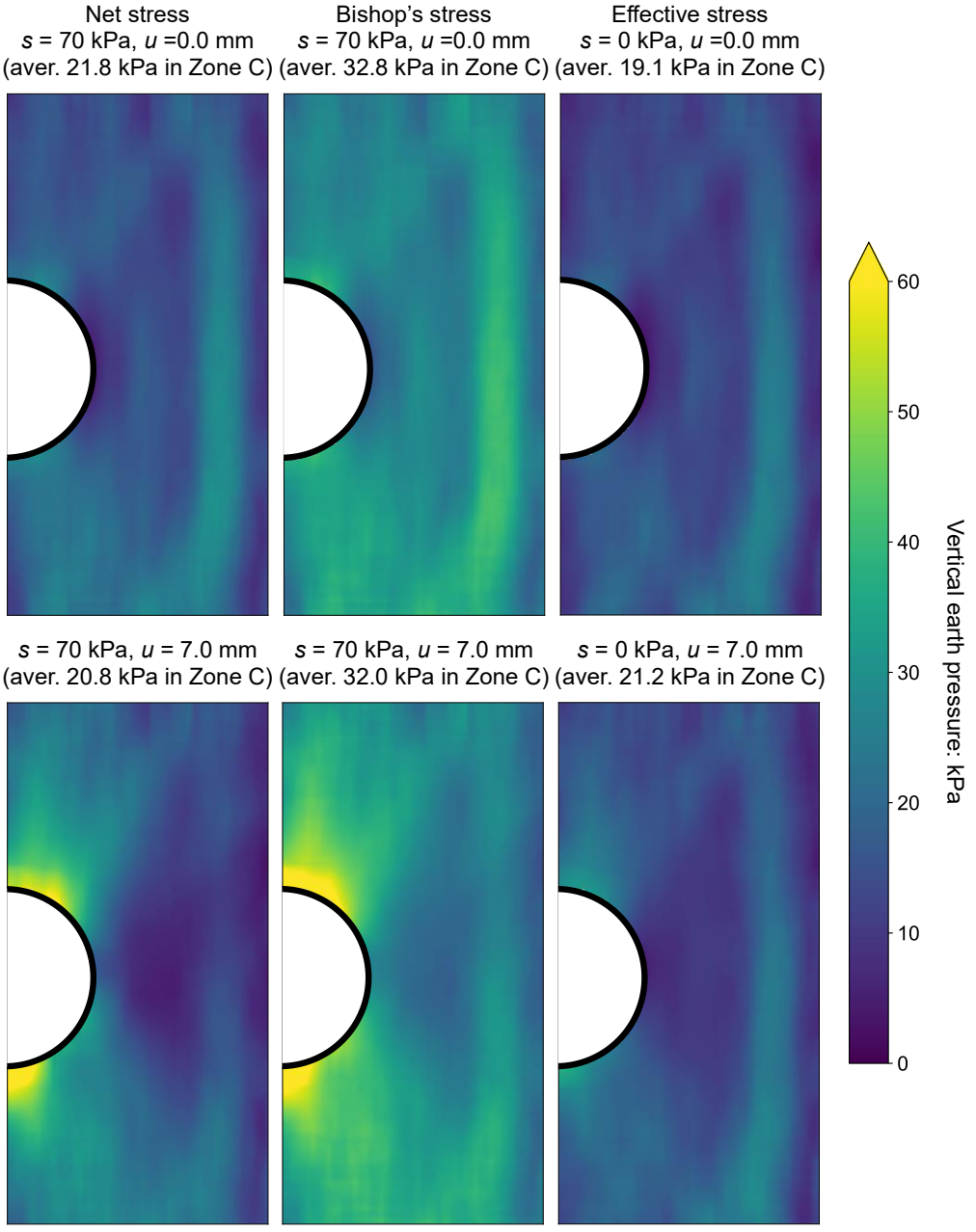

Figure 8.12 Vertical earth pressure field within Zone C ($\sigma_{c\text{-net}}$ or $\sigma_c' = 17$ kPa)

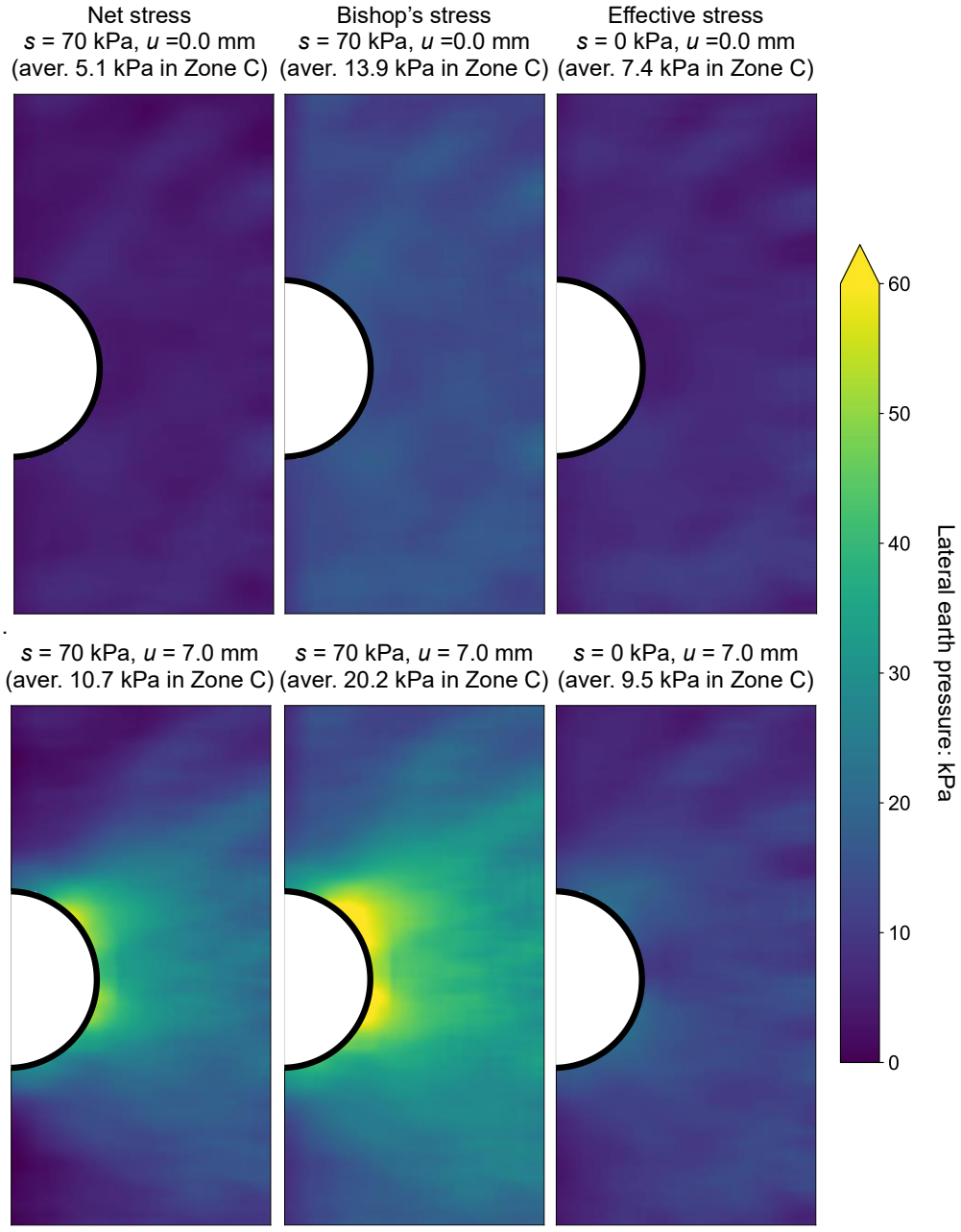

Figure 8.13 Lateral earth pressure field within Zone C ($\sigma_{c\text{-net}}$ or $\sigma_c' = 17$ kPa)

8.8 Summary

This chapter explores the microscopic mechanisms governing the axial behaviour of steel pipes buried in unsaturated soils using the 3D DEM software, YADE. The capillary model is employed to calculate inter-particle capillary forces in the pendular zone. A scaling law related to capillary force was derived to address particle size scaling effects by using the scaling factor for surface tension coefficient equal to the one for particle size, to obtain the same stress induced

by capillary forces of water menisci. It was then validated through triaxial compaction simulations. Three modifications of the YADE source code were made to accommodate the new method, including integrating the capillary model with the Cundall contact model that incorporates rolling resistance, ensuring compatibility with plane-symmetric conditions, and enabling multiple surface tension coefficients within a single simulation. Using the improved code and method, the physical modelling of ASPI at a matric suction of 70 kPa was back-analysed, and parametric studies in the range of 0 to 1000 kPa were carried out. The analysis of the simulation results revealed several findings as follows:

Key macro-level behaviour, such as the displacement-softening and the characteristic shapes of the axial pullout force and vertical displacement curves, confirms the validity of the new method and parameters. The computed axial resistance at a suction of 70 kPa is 13.37 kN/m, which is slightly higher than the measured value. The computed ratio of axial resistance at 70 kPa suction to that at 0 kPa in the DEM simulation is 2.67, closely matching the experimental value of 2.69.

One important reason for the suction-induced change in axial resistance is interface contact pressure induced by capillary forces of liquid menisci between soil particles and interface particles, denoted as $\sigma_{\text{int-cap}}$. It ranges from 6 to 17 kPa at the pipe interface, which contributes at least 20% of Bishop's interface contact pressure and thus enhances axial resistance. Interestingly, $\sigma_{\text{int-cap}}$ is not uniform along the pipe surface. Instead, before pipe pullout, the values of $\sigma_{\text{int-cap}}$ decrease from 16.2 to 5.5 kPa from the pipe crown to the invert. During the pipe pullout, pressures at different pipe surfaces converge to this average value, reflecting that the contact at the pipe surface tends to become uniform along the pipe surface due to the disturbance of soil contact structure and interface dilatancy during pipe pullout. Axial resistance initially increases and then decreases as matric suction rises from 0 to 1000 kPa.

Another reason for the higher axial resistance in the unsaturated conditions is the stronger dilatancy at the unsaturated soil-pipe interface. The capillary force does not increase the thickness of the interface shear band. Instead, it enhances the axial displacement of soil particles outside the shear band, leading to volumetric expansion in that area. Combined with the greater volumetric expansion at the unsaturated soil-pipe interface, soil particles move away from the pipe, which, in turn, sharply increases the net interface contact pressure due to the constraint of the surrounding soils. The interface stress paths in terms of the net and Bishop's stress yield the peak and critical state interface failure envelopes under matric suction of 70 and 0 kPa, respectively, showing the uniformity of interface contact pressure in the views of two different stresses.

The effects of suction and capillary force can also be observed in the surrounding soil. The constrained dilation-caused force chains are significantly stronger than those in the dry condition, and their distribution is uniform along the pipe surface. Moreover, capillary forces induce a higher Bishop's lateral earth pressure and a lower net lateral earth pressure. Within an area of 3×3 pipe diameters squared, the earth pressure coefficient at rest for soils with a matric suction of 70 kPa is 40% less than that of dry conditions before pipe pullout. During pipe pullout, lateral pressure increases significantly, with the average net lateral earth pressure in unsaturated soil rising by 110%, outstripping the pressure in dry soil.

CHAPTER 9
CONCLUSIONS AND SUGGESTIONS FOR FUTURE RESEARCH

Understanding ASPI is crucial for improving the resilience of onshore buried pipeline systems. This thesis presents advanced methodologies in both physical modelling and DEM simulations to thoroughly investigate ASPI. The study focuses on key factors such as surface roughness, coating hardness, cyclic loading, and partial saturation. This chapter summarises the major conclusions of the thesis and offers suggestions for future research.

9.1 Summary and major conclusions

9.1.1 A novel single-point-type tactile pressure sensor for earth and soil-structure interface contact pressure measurement

A new earth pressure cell (TPS-EPC) with limited thickness and thickness and a soil-structure interface contact pressure transducer (TPS-ICPT) conforming to curved interfaces was developed based on a single-point-type TPS with a comprehensive methodology encompassing sensor design, signal processing, and calibration. A non-linear signal conversion method is recommended to enhance measurement accuracy. Compared to traditional earth pressure cells, TPS-EPCs with the suggested methodology offer more precise earth pressure measurements due to reduced arching effects resulting from their limited thickness and stiffness. The feasibility of new sensors was validated for the first time in the physical modelling of axial soil pipe interaction, providing a new and highly sensitive method for soil pressure measurement and yielding valuable insights into soil-pipe interaction behaviours.

9.1.2 A new experimental system for physical modelling of ASPI

A new experimental apparatus has been developed to conduct physical modelling tests on ASPI for soils under varying moisture contents. This apparatus offers comprehensive

functionality for ASPI, including applying cyclic axial displacement at a constant speed, control of buried pressure, and measurement of key parameters such as axial force, axial and vertical displacements, interface contact pressure, earth pressure, and matric suction. Compared to previous studies, a key feature of this system is its ability to effectively minimise boundary effects from the front and rear walls by incorporating a pair of sleeves mounted on the walls and rubber membranes between the pipe and sleeves.

9.1.3 An advanced DEM code to simulate ASPI under unsaturated conditions

A new methodology has been developed to simulate ASPI using a capillary model capable of calculating inter-particle capillary forces in 3D DEM. Key features are as follows. The pipe is modelled as a clump of overlapping particles to simulate real surface roughness and facilitate capillary force calculations between the pipe and soil particles. Boundary effects are eliminated by employing parallel periodic walls in the pipe's axial direction. Computational efficiency is enhanced through particle refinement, plane symmetry assumptions, and optimal periodic domain thickness. A scaling factor for the surface tension coefficient, equal to that for particle size, is used based on the derivation of scaling laws for capillary force to address particle size scaling effects in unsaturated soils. The YADE source code has been improved to support these features.

9.1.4 Surface roughness and hardness effects on ASPI subjected to the monotonic loading

Surface roughness significantly influences the pipe pullout resistance during monotonic loading. The pullout resistance of a rough pipe is 1.70 to 1.85 times greater than that of a smooth pipe under identical burial conditions, far exceeding the 0.17 value specified in current design guidelines. This increase arises from different mechanisms: 72~79% is due to increased interface friction coefficient, while 21~28% results from increased interface contact pressure caused by constrained dilation and negative soil arching.

Negative soil arching affects the interface contact pressure between soil and pipes during backfilling and monotonic pullout processes. During backfilling, vertical force chains develop from the pipe's crown, shoulder, haunch, and invert, concentrating interface contact pressure at these points, indicating initial negative soil arching. Near the pipe springline, force chains extend vertically from top to bottom to transfer overburden pressure rather than connecting to the pipe surface, indicating limited soil arching in this area. During axial displacement, the displacement fields of soil particles near pipes with different roughness values differ, leading to distinct ASPI evolution mechanisms. Soil particles at the soil-pipe interface move with the pipe, forming a thicker interface shear band and causing volumetric expansion due to dilatancy. This movement is constrained by the surrounding soils, increasing interface contact pressure. Moreover, soil particles above the pipe move upward, while those below move downward, forming force chains from the pipe crown, shoulder, haunch and invert, indicating additional negative soil arching. For smooth pipes, the maximum soil particle axial displacement is no more than 15% of the pipe's axial displacement, resulting in a thinner interface shear band and volumetric contraction. Soil particles move inward, reducing interface contact pressure, and a force chain loop forms around the smooth pipe, disturbing the initial negative soil arching.

Axial resistance during monotonic loading decreases as coating hardness increases. A critical coating hardness of approximately 35 HRA was identified. Pipes behave similarly to rough pipes below this threshold (e.g., EA-coated pipes) due to equivalent roughness from particle embedment. Above this threshold (e.g., FBE-coated and raw steel pipes), the hardness influence appears limited.

9.1.5 Cyclic and post-cyclic ASPI behaviour

During cyclic axial displacement, axial resistance degrades and stabilises at an ultimate value, typically lower than predicted using the critical state interface shear angle, with deviations up to 48%. Buried pressures and cyclic displacement amplitude minimally influence

the ultimate degradation factor, though smaller cyclic displacement amplitudes slow the rate at which this factor is reached. The ultimate degradation factor increases from 0.32 to 0.62, with normalised roughness decreasing from 1.01 to 0.04.

Soil arching evolution plays a crucial role in cyclic ASPI. With cycles, soil compression due to interface compaction/dilation and average effective stress variation leads to pipe settlement. This ongoing settlement shifts negative soil arching in the first loading to positive soil arching on the pipe's upper part, reducing interface contact pressure at the crown and shoulders and resulting in lower average interface contact pressure than predicted.

Post-cyclic pullout resistance is lower than monotonic resistance without cycling when cyclic displacement is relatively large (above 5 mm in this study) due to interface contact pressure evolution. Conversely, post-cyclic pullout resistance exceeds monotonic resistance when cyclic displacement is smaller due to cyclic loading-induced soil densification. The difference between post-cyclic and monotonic resistances is more pronounced with rougher pipes.

9.1.6 Matric suction effect on ASPI behaviour

Monotonic axial pullout resistance increases with matric suction. Under a nominal pressure of 17 kPa, the axial resistance of pipes buried in completely decomposed granite (CDG) at an average suction of 70.2 kPa was 1.69 times greater than at 0 kPa (saturated condition), highlighting a significant underestimation of soil load on pipes in current design guidelines.

Increased interface contact pressure due to Bishop's stress increment at the interface plays a major role in axial resistance under unsaturated conditions. Bishop's interface contact pressure is not uniform along the pipe surface. Of the suction-induced axial resistance increase at 70.2 kPa, 68% is attributed to Bishop's interface contact pressure. During pipe pullout, pressures at different pipe surfaces converge to their average value with minimal variation.

The remaining increase in axial resistance under unsaturated conditions is attributed to average net interface contact pressure changes. In unsaturated conditions, soil particles experience more significant axial displacement than in saturated conditions, moving away from the pipe with an average displacement in the *x*-*z* plane that is 53% higher. This suggests a more significant volumetric expansion of unsaturated soils around the pipe. The higher stiffness of unsaturated soil results in stronger constrained dilatancy with stronger force chains from the entire pipe surface. As a result, the increase in axial resistance due to variations in net interface contact pressure rises from 10% to 32% as suction levels increase from 17.8 to 70.2 kPa.

9.1.7 A new design equation to predict axial resistance for soils with varying water contents

A new and simple method was proposed for calculating axial resistance under dry, unsaturated, and saturated conditions. The increase in interface contact pressure due to constrained dilation is considered based on elastic expanding cylinder theory. The effect of surface roughness on the interface friction angle is quantitatively estimated using a linear relationship with the logarithmic roughness value. Suction effects on Bishop's stress, stiffness, and dilatancy are incorporated to calculate axial resistance under unsaturated conditions. The new equation demonstrated a good predictive capability, verifying 28 test results under different water contents from previous and current studies.

9.2 Recommendation for further work

9.2.1 DEM simulation of ASPI under a higher degree of saturation

The capillary model employed in this thesis is only available for simulating soil in the pendular regime, where only the capillary forces between two particles are considered. As a result, the degree of saturation typically remains below 15% (Duriez & Wan, 2017a). Beyond the pendular regime, soil-interface shear behaviour would change due to the non-linear variation of stress caused by capillary forces from liquid menisci with suction varying. Consequently, the mechanism of ASPI at higher degrees of saturation differs. A significant

limitation in simulating soils with a higher degree of saturation is the computational cost, as outlined in Table 2.6. To address this challenge, an enhanced capillary model utilising Graphical Processing Unit (GPU) acceleration is expected to solve this issue.

9.2.2 Thermal effects on ASPI

Periodic temperature variations in both pipes and the surrounding ground can induce cyclic displacements of the pipe relative to the surrounding soils. This thesis simplifies the problem by neglecting the thermal effects on ASPI. However, thermo-hydraulic-mechanical behaviour is crucial, particularly for plastic pipes with high thermal expansion coefficients. The impact of temperature could be examined, focusing on variations in interface contact pressure due to thermal expansion or contraction of the pipe and soils, as well as changes in Bishop's stress, soil dilatancy, and interface shear behaviour due to temperature and stress-dependent water retention in the surrounding soil. Moreover, investigating thermal energy transfer around buried pipes, which depends on stress and water content, is essential for optimising temperature drop calculations in pipeline system design. Future physical modelling could involve controlling pipe temperature by circulating temperature-controlled water. The DEM code could be enhanced for thermal-dependent soil and pipe size, surface tension coefficient and hydrophilicity.

9.2.3 Soil-pipe interaction behaviour under multidirectional loading

In practice, pipes are typically subjected to multidirectional rather than unidirectional loading. Previous studies and design codes have often overlooked the coupling behaviours of pipes subjected to simultaneous axial and other directional loads. The potential effects of multidirectional loading may influence average net interface contact pressure, interface shear strength, water retention ability and Bishop's stress. Enhancements to the DEM code are needed to investigate these effects by incorporating multidirectional displacement settings.

9.2.4 Suction effect on lateral earth pressure

A limited understanding of suction effects on lateral earth pressure constrains the comprehension of suction impacts on ASPI and the development of related equations in this thesis. This is a fundamental issue in soil mechanics. Element tests and DEM simulations could be conducted to explore this problem further.

9.2.5 Influence of surface roughness, hardness and hydrophilicity on unsaturated soil-interface shear behaviour

The soil-interface shear behaviour is critical to ASPI. The interface material's surface roughness, hardness, and hydrophilicity could significantly affect capillary forces and Bishop's interface normal pressure. More unsaturated soil interface shear tests are needed. An improved capillary model could be developed, considering different surface contact angles within a single liquid bridge.

References

Abuel-Naga, H. M., Shaia, H. A. & Bouazza, A. (2018) Effect of surface roughness and hardness of continuum materials on interface shear strength of granular materials. *Journal of Testing and Evaluation* **46(2)**:826-831, https://doi.org/10.1520/jte20160375.

Al-Khazaali, M. & Vanapalli, S. K. (2018) Modelling the elastic axial force-displacement behaviour of a buried pipeline subjected to permanent ground deformation in the axial direction In *Proceedings of the 7th International Conference on Unsaturated Soil Mechanics*, HK.

Al-Khazaali, M. & Vanapalli, S. K. (2019) Axial force–displacement behaviour of a buried pipeline in saturated and unsaturated sand. *Géotechnique* **69(11)**:986-1003, https://doi.org/10.1680/jgeot.17.P.116.

ALA (American Lifeline Alliance) (2001) Guidelines for design of buried steel pipes. American Lifelines Alliance in Partnership with the Federal Emergency Management Agency (FEMA) and American Society for Civil Engineers (ASCE), Reston, VA, US.

Alonso, E. E., Pereira, J. M., Vaunat, J., *et al.* (2010) A microstructurally based effective stress for unsaturated soils. *Géotechnique* **60(12)**:913-925, https://doi.org/10.1680/geot.8.P.002.

Anderson, C., Wijewickreme, D., Ventura, C. E. H., *et al.* (2004) Full-scale laboratory testing of buried polyethylene gas distribution pipelines subject to lateral ground displacements In *Proceedings of the 13th World Conference on Earthquake Engineering*, BC, Canada.

ASCE (American Society of Civil Engineers) (1984) Guidelines for the seismic design of oil and gas pipeline systems. Committee on Gas and Liquid Fuel Lifelines, American Society for Civil Engineering, New York, NY, US.

ASME (American Society of Mechanical Engineers) (2018) ASME B36.10M - 2018: Welded and seamless wrought steel pipe. American Society of Mechanical Engineers, New York, NY, US.

ASTM (American Society for Testing Materials) (2017) ASTM D2487-17(2025): Standard practice for classification of soils for engineering purposes (unified soil classification system). ASTM International, West Conshohocken, PA, US.

ASTM (American Society for Testing Materials) (2021) ASTM D698-12: Standard test methods for laboratory compaction characteristics of soil using standard effort. ASTM International, West Conshohocken, PA, US.

ASTM (American Society for Testing Materials) (2022) ASTM E18: Standard test methods for Rockwell hardness of metallic materials. ASTM International, West Conshohocken, PA, US.

ASTM (American Society for Testing Materials) (2023) ASTM D785: Standard test method for Rockwell hardness of plastics and electrical insulating materials. ASTM International, West Conshohocken, PA, US.

Audibert, J. M. E. & Nyman, K. J. (1977) Soil restraint against horizontal motion of pipes. *Journal of the Geotechnical Engineering Division* **103(10)**:1119-1142, https://doi.org/10.1061/AJGEB6.0000500.

Bahadori, A. (2017) *Oil and Gas Pipelines and Piping Systems. Design, Construction, Management, and Inspection.* Gulf Professional Publishing, MA, US.

Bartlett, S. F., Lingwall, B. N. & Vaslestad, J. (2015) Methods of protecting buried pipelines and culverts in transportation infrastructure using EPS geofoam. *Geotextiles and Geomembranes* **43(5)**:450-461, https://doi.org/10.1016/j.geotexmem.2015.04.019.

Bentil, O. T. (2023) *Small strain stiffness of a compacted clay with different initial structures under cyclic thermo-hydro-mechanical loads*. Ph.D. thesis, The Hong Kong Polytechnic University, HK.

Bilgin, Ö. & Stewart, H. E. (2009a) Design guidelines for polyethylene pipe interface shear resistance. *Journal of Geotechnical and Geoenvironmental Engineering* **135(6)**:809-818, http://doi.org/10.1061/(ASCE)GT.1943-5606.0000030.

Bilgin, Ö. & Stewart, H. E. (2009b) Pullout resistance characteristics of cast iron pipe. *Journal of Transportation Engineering* **135(10)**:730-735, https://doi.org/10.1061/(ASCE)0733-947X(2009)135:10(730).

Bishop, A. W. (1959) The principle of effective stress. *Teknisk Ukeblad* **39**:859-863.

Bolton, M. D. (1986) The strength and dilatancy of sands. *Géotechnique* **36(1)**:65-78, https://doi.org/10.1680/geot.1986.36.1.65.

Borana, L., Yin, J. H., Singh, D. N., *et al.* (2016) Interface behavior from suction-controlled direct shear test on completely decomposed granitic soil and steel surfaces. *International Journal of Geomechanics* **16(6)**:D4016008, https://doi.org/10.1061/(ASCE)GM.1943-5622.0000658.

BSI (British Standards Institution) (2002) BSI EN 10220:2002: Seamless and welded steel tubes. Dimensions and masses per unit length. BSI Group, London, UK.

BSI (British Standards Institution) (2003) EN-14161: Petroleum and natural gas industries — Pipeline transportation systems. BSI Group, London, UK.

BSI (British Standards Institution) (2015) BSI EN 1610:2015: Construction and testing of drains and sewers. BSI Group, London, UK.

Burland, J. (1973) Shaft friction of piles in clay - A simple fundamental approach. *Ground Engineering* **6**:30-42, https://cdn.ca.emap.com/wp-content/uploads/sites/13/1973/05/1973-05_Pages_30_32_37_41-42.pdf.

Butlanska, J., Arroyo, M. & Gens, A. (2009) Homogeneity and symmetry in DEM models of cone penetration In *Proceedings of the 6th International Conference on Micromechnics of Granular Media*, HK.

Calvetti, F., di Prisco, C. & Nova, R. (2004) Experimental and numerical analysis of soil–pipe interaction. *Journal of Geotechnical and Geoenvironmental Engineering* **130(12)**:1292-1299, https://doi.org/10.1061/(asce)1090-0241(2004)130:12(1292)

CEDD (Civil Engineering and Development Department) (2020) General specification for civil engineering works (GS), volume 2. Civil Engineering and Development Department, The Government of the Hong Kong Special Administrative Region, HK.

Chakraborty, T. & Salgado, R. (2010) Dilatancy and shear strength of sand at low confining pressures. *Journal of Geotechnical and Geoenvironmental Engineering* **136(3)**:527-532, https://doi.org/10.1061/(asce)gt.1943-5606.0000237.

Chareyre, B., Cortis, A., Catalano, E.*, et al.* (2012) Pore-scale modeling of viscous flow and induced forces in dense sphere packings. *Transport in Porous Media* **92(2)**:473-493, https://doi.org/10.1007/s11242-011-9915-6.

Costa, Y. D. J. & Zornberg, J. G. (2020) Active and passive arching stresses outside a deep trapdoor. *Acta Geotechnica* **15(11)**:3211-3227, https://doi.org/10.1007/s11440-020-00969-x.

Cui, S., Zhou, C., Mu, Q.*, et al.* (2024) Coupled effects of temperature and suction on the shear behaviour of saturated and unsaturated clayey sand–structure interfaces. *Géotechnique* **75(2)**:278-290, https://doi.org/10.1680/jgeot.22.00404.

Cui, S. Q. (2023) *Thermo-mechanical behaviour of energy piles in unsaturated silt*. Ph.D. thesis, The Hong Kong Polytechnic University, HK.

Cundall, P. A. (1988) Computer simulations of dense sphere assemblies. *Studies in Applied Mechanics* **20**:113-123, https://doi.org/10.1016/B978-0-444-70523-5.50021-7.

Cundall, P. A. & Strack, O. D. L. (1979) A discrete numerical model for granular assemblies. *Géotechnique* **29(1)**:47-65, https://doi.org/10.1680/geot.1979.29.1.47.

Daiyan, N., Kenny, S., Phillips, R., *et al.* (2011) Investigating pipeline–soil interaction under axial–lateral relative movements in sand. *Canadian Geotechnical Journal* **48(11)**:1683-1695, https://doi.org/10.1139/t11-061.

DeJong, J. T., Randolph, M. F. & White, D. J. (2003) Interface load transfer degradation during cyclic Loading: A microscale investigation. *Soils and Foundations* **43(4)**:81-93, https://doi.org/10.3208/sandf.43.4_81.

DeJong, J. T. & Westgate, Z. J. (2009) Role of initial state, material properties, and confinement condition on local and global soil-structure interface behavior. *Journal of Geotechnical and Geoenvironmental Engineering* **135(11)**:1646-1660, https://doi.org/10.1061/(ASCE)1090-0241(2009)135:11(1646).

Desai, C. S., Drumm, E. C. & Zaman, M. M. (1985) Cyclic testing and modeling of interfaces. *Journal of Geotechnical Engineering* **111(6)**:793-815, https://doi.org/10.1061/(ASCE)0733-9410(1985)111:6(793).

Di Donna, A., Ferrari, A. & Laloui, L. (2016) Experimental investigations of the soil–concrete interface: physical mechanisms, cyclic mobilization, and behaviour at different temperatures. *Canadian Geotechnical Journal* **53(4)**:659-672, https://doi.org/10.1139/cgj-2015-0294.

Dong, Y., Lu, N. & McCartney, J. S. (2018) Scaling shear modulus from small to finite Strain for unsaturated soils. *Journal of Geotechnical and Geoenvironmental Engineering* **144(2)**:04017110, https://doi.org/10.1061/(asce)gt.1943-5606.0001819.

Dove, J. E. & Frost, J. D. (1999) Peak friction behavior of smooth geomembrane-particle interfaces. *Journal of Geotechnical and Geoenvironmental Engineering* **125(7)**:544-555, http://doi.org/10.1061/(ASCE)1090-0241(1999)125:7(544).

Duriez, J. & Wan, R. (2016) Stress in wet granular media with interfaces via homogenization and discrete element approaches. *Journal of Engineering Mechanics* **142(12)**:04016099, http://doi.org/10.1061/(ASCE)EM.1943-7889.0001163.

Duriez, J. & Wan, R. (2017a) Contact angle mechanical influence in wet granular soils. *Acta Geotechnica* **12(1)**:67-83, https://doi.org/10.1007/s11440-016-0500-6.

Duriez, J. & Wan, R. (2017b) Subtleties in discrete-element modelling of wet granular soils. *Géotechnique* **67(4)**:365-370, https://doi.org/10.1680/jgeot.15.P.113.

EGIG (European Gas pipeline Incident data Group) (2020) Gas pipeline incidents: 11th Report of the European Gas Pipeline Incident Data Group (period 1970 – 2019). European Gas pipeline Incident data Group, Groningen, Netherlands.

Faizal, M., Bouazza, A., Haberfield, C., *et al.* (2018) Axial and radial thermal responses of a field-scale energy pile under monotonic and cyclic temperature changes. *Journal of Geotechnical and Geoenvironmental Engineering* **144(10)**:04018072, https://doi.org/10.1061/(ASCE)GT.1943-5606.0001952.

Fakharian, K. & Evgin, E. (1997) Cyclic simple-shear behavior of sand-steel interfaces under constant normal stiffness condition. *Journal of Geotechnical and Geoenvironmental Engineering* **123(12)**:1096-1105, http://doi.org/10.1061/(ASCE)1090-0241(1997)123:12(1096).

Farhadi, B. & Lashkari, A. (2017) Influence of soil inherent anisotropy on behavior of crushed sand-steel interfaces. *Soils and Foundations* **57(1)**:111-125, https://doi.org/10.1016/j.sandf.2017.01.008.

Feng, S. J., Liu, X., Chen, H. X., *et al.* (2018) Micro-mechanical analysis of geomembrane-sand interactions using DEM. *Computers and Geotechnics* **94**:58-71, https://doi.org/10.1016/j.compgeo.2017.08.019.

Fredlund, D. G. & Rahardjo, H. (1993) *Soil Mechanics for Unsaturated Soils.* John Wiley & Sons, Inc., New York, NY, US.

Fretti, C., Lo Presti, D. C. F. & Pedroni, S. (1995) A pluvial deposition method to reconstitute well-graded sand specimens. *Geotechnical Testing Journal* **18(2)**:292-298, https://doi.org/10.1520/GTJ10330J.

Frost, J. D. & Han, J. (1999) Behavior of interfaces between fiber-reinforced polymers and sands. *Journal of Geotechnical and Geoenvironmental Engineering* **125(8)**:633-640, http://doi.org/10.1061/(ASCE)1090-0241(1999)125:8(633).

Gao, Y., Wang, Y. H. & Chow, J. K. (2017) Application of film-like sensors for K0 and pore water pressure measurement in clay during 1D consolidation. *Geotechnical Testing Journal* **40(1)**:134-143, http://doi.org/10.1520/GTJ20160008.

Geoguide 1 (2020) Guide to Retaining Wall Design. Geotechnical Engineering Office, Hong Kong SAR.

Ghanadizadeh, A., Tabatabaie Shourijeh, P. & Lashkari, A. (2022) Laboratory investigation and constitutive modeling of the mechanical behavior of sand–GRP interfaces. *Acta Geotechnica* **17(1)**:1-23, https://doi.org/10.1007/s11440-022-01533-5.

Gillis, K., Dashti, S. & Hashash, Y. M. A. (2015) Dynamic calibration of tactile sensors for measurement of soil pressures in centrifuge. *Geotechnical Testing Journal* **38(3)**:261-274, https://doi.org/10.1520/GTJ20140184.

Grabowski, A., Nitka, M. & Tejchman, J. (2020) 3D DEM simulations of monotonic interface behaviour between cohesionless sand and rigid wall of different roughness. *Acta Geotechnica* **16(4)**:1001-1026, https://doi.org/10.1007/s11440-020-01085-6.

Gu, X. Q., Chen, Y. W. & Huang, M. S. (2017) Critical state shear behavior of the soil-structure interface determined by discrete element modeling. *Particuology* **35**:68-77, https://doi.org/10.1016/j.partic.2017.02.002.

Guo, N., Liu, H. F., Li, B. J., *et al.* (2024) DEM study of the stress fields around the closed-ended displacement pile driven in sand. *Canadian Geotechnical Journal* **61(3)**:549-561, https://doi.org/10.1139/cgj-2023-0025.

Hamid, T. B. & Miller, G. A. (2009) Shear strength of unsaturated soil interfaces. *Canadian Geotechnical Journal* **46(5)**:595-606, https://doi.org/10.1139/t09-002.

Han, F., Ganju, E., Salgado, R., *et al.* (2018) Effects of interface roughness, particle geometry, and gradation on the sand–steel interface friction angle. *Journal of Geotechnical and Geoenvironmental Engineering* **144(12)**:04018096, https://doi.org/10.1061/(asce)gt.1943-5606.0001990.

Han, Z. & Vanapalli, S. K. (2016) Stiffness and shear strength of unsaturated soils in relation to soil-water characteristic curve. *Géotechnique* **66(8)**:627-647, https://doi.org/10.1680/jgeot.15.P.104.

Hardin, B. O. & Black, W. L. (1966) Sand Stiffness Under Various Triaxial Stresses. *Journal of the Soil Mechanics and Foundations Division* **92(2)**:27-42, https://doi.org/10.1061/JSFEAQ.0000865.

HKIUS (Hong Kong Institute of Utility Specialists) (2011) Guide to utility management. Hong Kong Institute of Utility Specialists and Hong Kong Utility Research Centre, Hong Kong SAR.

Hodge, A. T. (1992) *Roman Aqueducts & Water Supply* (2nd Edition). Bristol Classical Press, UK.

Hossain, M. A. & Yin, J. H. (2010) Shear strength and dilative characteristics of an unsaturated compacted completely decomposed granite soil. *Canadian Geotechnical Journal* **47(10)**:1112-1126, https://doi.org/10.1139/t10-015.

Hossain, M. A. & Yin, J. H. (2015) Dilatancy and strength of an unsaturated soil-cement interface in direct shear tests. *International Journal of Geomechanics* **15(5)**:04014081, https://doi.org/10.1061/(ASCE)GM.1943-5622.0000428.

Houlsby, G. T. & Italiana, A. D. S. (1991) How the dilatancy of soils affects their behaviour In *Proceedings of the 10th European Conference on Soil Mechanics and Foundation Engineering*. A.A. Balkema, Florence, Italy.

Huber, M. & Wijewickreme, D. (2014) Response of buried district heating pipelines under relative axial movements In *Proceedings of the 10th International Pipeline Conference*, Alberta, Canada.

Hubler, J. F., Athanasopoulos-Zekkos, A. & Zekkos, D. (2017) Monotonic, cyclic, and postcyclic simple shear response of three uniform gravels in constant volume conditions. *Journal of Geotechnical and Geoenvironmental Engineering* **143(9)**:04017043, https://doi.org/10.1061/(ASCE)GT.1943-5606.0001723.

Interlink (2023) *FSR® integration guide & evaluation parts catalog with suggested electrical interfaces*. Interlink Electronics, Camarillo, Canada, See http://www.tinyos.net.cn/datasheet/fsrguide.pdf (accessed 14/12/2023).

ISO (International Organization for Standardization) (2007) ISO 8501-1: Preparation of steel substrates before application of paints and related products - Visual assessment of surface cleanliness - Part 1: Rust grades and preparation grades of uncoated steel substrates and of steel substrates after overall removal of previous coatings. International Organization for Standardization ISO Central Secretariat, Vernier, Geneva, CH.

ISO (International Organization for Standardization) (2019) ISO 4427-1:2019: Plastics piping systems for water supply and for drainage and sewerage under pressure - Polyethylene (PE). International Organization for Standardization ISO Central Secretariat, Vernier, Geneva, CH.

Itasca, C. (2005) PFC3D (Particle flow code in three dimensions). *Minneapolis, Minnesota, USA*.

Jiang, M. J., Leroueil, S. & Konrad, J. M. (2004) Insight into shear strength functions of unsaturated granulates by DEM analyses. *Computers and Geotechnics* **31(6)**:473-489, https://doi.org/10.1016/j.compgeo.2004.07.001.

Jiang, M. J., Zhang, W. C., Wang, J. F., *et al.* (2015) DEM analyses of an uplift failure mechanism with pipe buried in cemented granular ground. *International Journal of Geomechanics* **15(5)**, https://doi.org/10.1061/(asce)gm.1943-5622.0000430.

Jing, X. Y., Zhou, W. H., Zhu, H. X., *et al.* (2017) Analysis of soil-structural interface behavior using three-dimensional DEM simulations. *International Journal for Numerical and Analytical Methods in Geomechanics* **42(2)**:339-357, https://doi.org/10.1002/nag.2745.

Jitsangiam, P., Pra-ai, S., Boulon, M., *et al.* (2021) Characterization of a soil-rough structure interface using direct shear tests with varying cyclic amplitude and loading sequences under a large cyclic testing cycle condition. *Acta Geotechnica* **17(5)**:1829-1845, https://doi.org/10.1007/s11440-021-01289-4.

Karamanos, S. A., Gresnigt, A. M. & Dijkstra, G. J. (2021) *Geoharzards and Pipelines*. Springer, Maasland, Netherlands.

Khoury, C. N. & Miller, G. A. (2012) Influence of hydraulic hysteresis on the shear strength of unsaturated soils and interfaces. *Geotechnical Testing Journal* **35(1)**:135-149, https://doi.org/10.1520/gtj103616.

Kishida, H. & Uesugi, M. (1987) Tests of the interface between sand and steel in the simple shear apparatus. *Géotechnique* **37(1)**:45-52, https://doi.org/10.1680/geot.1987.37.1.45.

Kloss, C. & Goniva, C. (2011) *LIGGGHTS – Open Source Discrete Element Simulations of Granular Materials based on Lammps*. The Minerals, Metals & Materials Society (TMS), Online.

Kootahi, K. & Leung, A. K. (2022) Effect of soil particle size on the accuracy of tactile pressure sensors. *Journal of Geotechnical and Geoenvironmental Engineering* **148(10)**:06022008, https://doi.org/10.1061/(asce)gt.1943-5606.0002899.

Kootahi, K. & Leung, A. K. (2023) Evaluating the performance of flexible piezoresistive sensors for measuring static contact stress. *Geotechnical Testing Journal* **46(1)**:68-103, https://doi.org/10.1520/GTJ20210197.

Kozicki, J. & Donzé, F. V. (2008) A new open-source software developed for numerical simulations using discrete modeling methods. *Computer Methods in Applied Mechanics and Engineering* **197(49)**:4429-4443, https://doi.org/10.1016/j.cma.2008.05.023.

Li, M. Y., Li, Y. H. & Islam, M. R. (2021) Effects of water content and interface roughness on the shear strength of silt–cement mortar interface. *Soils and Foundations* **61(6)**:1615-1629, https://doi.org/10.1016/j.sandf.2021.08.011.

Li, T., Jiang, M. J. & Thornton, C. (2018) Three-dimensional discrete element analysis of triaxial tests and wetting tests on unsaturated compacted silt. *Computers and Geotechnics* **97**:90-102, https://doi.org/10.1016/j.compgeo.2017.12.011.

Liang, H., Shen, Y., Xu, J. H., *et al.* (2021) Multiscale three-dimensional morphological characterization of calcareous sand particles using spherical harmonic analysis. *Frontiers in Physics* **9(1)**:744319, https://doi.org/10.3389/fphy.2021.744319.

Lings, M. L. & Dietz, M. S. (2005) The peak strength of sand-steel interfaces and the role of dilation. *Soils and Foundations* **45(6)**:1-14, https://doi.org/10.3208/sandf.45.1.

Liu, K. Y., Xu, C. S. & Zhang, X. L. (2021a) Measurement performance evaluation of tactile pressure sensor with different particle sizes and sensor curvatures. *Geotechnical Testing Journal* **44(4)**:1036-1054, https://doi.org/10.1520/GTJ20200028.

Liu, X., Zhou, A., Shen, S.-L., *et al.* (2021b) Modelling unsaturated soil-structure interfacial behavior by using DEM. *Computers and Geotechnics* **137**:104305, https://doi.org/10.1016/j.compgeo.2021.104305.

Liu, X., Zhou, A., Shen, S.-L., *et al.* (2020) A micro-mechanical model for unsaturated soils based on DEM. *Computer Methods in Applied Mechanics and Engineering* **368**, https://doi.org/10.1016/j.cma.2020.113183.

Lu, N. & Likos, W. J. (2004) *Unsaturated Soil Mechanics.* John Wiley & Sons, Inc., Hoboken, NJ, US.

Luo, S. Q., Tan, S. A. & Yong, K. Y. (2000) Pull-out resistance mechanism of a soil nail reinforcement in dilative soils. *Soils and Foundations* **40(1)**:47-56, https://doi.org/10.3208/sandf.40.47.

Macaro, G. (2015) *Distinct element modelling of pipe-soil interaction for offshore pipelines on granular soils*. Ph.D. thesis, University of Oxford, UK.

Macaro, G., Utili, S. & Martin, C. M. (2021) DEM simulations of transverse pipe–soil interaction on sand. *Géotechnique* **71(3)**:189-204, https://doi.org/10.1680/jgeot.18.P.133.

Madabhushi, S. S. C. & Haigh, S. K. (2019) Using tactile pressure sensors to measure dynamic earth pressures around dual-row walls. *International Journal of Physical Modelling in Geotechnics* **19(2)**:58-71, https://doi.org/10.1680/jphmg.17.00053.

Marshall, A. M., Klar, A. & Mair, R. J. (2010) Tunneling beneath buried pipes: View of soil strain and its effect on pipeline behavior. *Journal of Geotechnical and Geoenvironmental Engineering* **136(12)**:1664-1672, http://doi.org/10.1061/(ASCE)GT.1943-5606.0000390.

Martinez, A. & Frost, J. D. (2017) The influence of surface roughness form on the strength of sand–structure interfaces. *Géotechnique Letters* **7(1)**:104-111, https://doi.org/10.1680/jgele.16.00169.

Martinez, A. & Frost, J. D. (2018) Undrained behavior of sand–structure interfaces subjected to cyclic torsional shearing. *Journal of Geotechnical and Geoenvironmental Engineering* **144(9)**:04018063, https://doi.org/10.1061/(ASCE)GT.1943-5606.0001942.

Meguid, M. A. (2019) Earth pressure distribution on rigid pipes overlain by TDA inclusion In *Proceedings of GeoMEast 2018*. Springer International Publishing, Cairo, Egypt, pp. 1-13.

Meguid, M. A. & Ahmed, M. R. (2020) Earth pressure distribution on buried pipes installed with geofoam inclusion and subjected to cyclic loading. *International Journal of Geosynthetics and Ground Engineering* **6(2)**:1-8, https://doi.org/10.1007/s40891-020-0187-5.

Meidani, M., Meguid, M. A. & Chouinard, L. E. (2017) Evaluation of soil–pipe interaction under relative axial ground movement. *Journal of Pipeline Systems Engineering and Practice* **8(4)**:04017009, https://doi.org/10.1061/(asce)ps.1949-1204.0000269.

Meidani, M., Meguid, M. A. & Chouinard, L. E. (2018) Estimating earth loads on buried pipes under axial loading condition: insights from 3D discrete element analysis. *International Journal of Geo-Engineering* **9(5)**, https://doi.org/10.1186/s40703-018-0073-3.

Meidani, M., Meguid, M. A. & Chouinard, L. E. (2020a) A finite-discrete element approach for modelling polyethylene pipes subjected to axial ground movement. *International Journal of Geotechnical Engineering* **14(7)**:717-729, https://doi.org/10.1080/19386362.2018.1483812.

Meidani, M., Meguid, M. A. & Chouinard, L. E. (2020b) On the response of polyethylene pipes to lateral ground movements: Insights from finite-discrete element analysis. *International Journal of Geosynthetics and Ground Engineering* **6(2)**, https://doi.org/10.1007/s40891-020-00201-6.

Melnikov, K., Mani, R., Wittel, F. K., *et al.* (2015) Grain-scale modeling of arbitrary fluid saturation in random packings. *Physical Review E* **92(2)**:022206, https://doi.org/10.1103/PhysRevE.92.022206.

Melnikov, K., Wittel, F. K. & Herrmann, H. J. (2016) Micro-mechanical failure analysis of wet granular matter. *Acta Geotechnica* **11(3)**:539-548, https://doi.org/10.1007/s11440-016-0465-5.

Miller, G. & Hamid, T. (2007) Interface direct shear testing of unsaturated soil. *Geotechnical Testing Journal* **30(3)**:182-191, https://doi.org/10.1520/gtj13301.

Mohitpour, M., Golshan, H. & Murray, A. (2007) *Pipeline Design & Construction: a Practical Approach* (3rd Edition). ASME Press, New York, NY, US.

Mortara, G., Mangiola, A. & Ghionna, V. N. (2007) Cyclic shear stress degradation and post-cyclic behaviour from sand–steel interface direct shear tests. *Canadian Geotechnical Journal* **44(7)**:739-752, https://doi.org/10.1139/t07-019.

Moser, A. P. & Folkman, S. (2008) *Buried Pipe Design* (3rd). McGraw-Hill, Logan, UT, US.

Muntakim, A. H. & Dhar, A. S. (2021) Assessment of axial pullout force for buried medium-density polyethylene pipelines. *Journal of Pipeline Systems Engineering and Practice* **12(2)**:04020074, http://doi.org/10.1061/(ASCE)PS.1949-1204.0000531.

Murugathasan, P., Dhar, A. S. & Hawlader, B. C. (2021) An experimental and numerical investigation of pullout behavior of ductile iron water pipes buried in sand. *Canadian Journal of Civil Engineering* **48(2)**:134-143, https://doi.org/10.1139/cjce-2019-0366.

Muszynski, M. R., Olson, S. M., Hashash, Y. M. A., *et al.* (2016) Earth pressure measurements using tactile pressure sensors in a saturated sand during static and dynamic centrifuge testing. *Geotechnical Testing Journal* **39(3)**:371-390, https://doi.org/10.1520/GTJ20150049.

Nair, G. S., Dash, S. R. & Mondal, G. (2018) Review of Pipeline Performance during Earthquakes since 1906. *Journal of Performance of Constructed Facilities* **32(6)**:04018083, https://doi.org/10.1061/(asce)cf.1943-5509.0001214.

Needham, J. (1971) *Science and Civilisation in China, Vol. 4: Physics and Physical Technology, Part 3: Civil Engineering and Nautics.* Cambridge University Press, London, UK.

Ng, C. W. W., Zhou, C. & Chiu, C. F. (2020) Constitutive modelling of state-dependent behaviour of unsaturated soils: an overview. *Acta Geotechnica* **15(10)**:2705-2725, https://doi.org/10.1007/s11440-020-01014-7.

Ni, P. P. & Mangalathu, S. (2018) Simplified evaluation of pipe strains crossing a normal fault through the dissipated energy method. *Engineering Structures* **167**:393-406, https://doi.org/10.1016/j.engstruct.2018.04.047.

Ni, P. P., Mangalathu, S. & Liu, K. W. (2020) Enhanced fragility analysis of buried pipelines through Lasso regression. *Acta Geotechnica* **15(2)**:471-487, https://doi.org/10.1007/s11440-018-0719-5.

Ni, P. P., Moore, I. D. & Take, W. A. (2018a) Distributed fibre optic sensing of strains on buried full-scale PVC pipelines crossing a normal fault. *Géotechnique* **68(1)**:1-17, https://doi.org/10.1680/jgeot.16.P.161.

Ni, P. P., Qin, X. G. & Yi, Y. L. (2018b) Use of tire-derived aggregate for seismic mitigation of buried pipelines under strike-slip faults. *Soil Dynamics and Earthquake Engineering* **115**:495-506, https://doi.org/10.1016/j.soildyn.2018.09.018.

Nicot, F., Hadda, N., Guessasma, M., *et al.* (2013) On the definition of the stress tensor in granular media. *International Journal of Solids and Structures* **50(14-15)**:2508-2517, http://doi.org/10.1016/j.ijsolstr.2013.04.001.

Nyce, D. S. (2004) *Linear Position Sensors: Theory and Application.* John Wiley & Sons, Hoboken, NJ, US.

O'Rourke, T. D., Druschel, S. J. & Netravali, A. N. (1990) Shear strength characteristics of sand - polymer interfaces. *Journal of Geotechnical Engineering* **116(3)**:451-469, https://doi.org/10.1061/(ASCE)0733-9410(1990)116:3(451).

O'Sullivan, C. (2011) *Particulate Discrete Element Modelling: A Geomechanics Perspective* (1st Edition). CRC Press, London, UK.

Ooi, L. & Carter, J. (1987) A constant normal stiffness direct shear device for static and cyclic loading. *Geotechnical Testing Journal* **10(1)**:3-12, http://doi.org/10.1520/GTJ10132J.

Oswell, J. M. (2021) *Soil Mechanics for Pipeline Stress Analysis* (2nd Edition). Naviq Consulting Inc., Canada.

Oztoprak, S. & Bolton, M. D. (2013) Stiffness of sands through a laboratory test database. *Géotechnique* **63(1)**:54-70, http://doi.org/10.1680/geot.10.P.078.

Paikowsky, S. G. & Hajduk, E. L. (1997) Calibration and use of grid-based tactile pressure sensors in granular material. *Geotechnical Testing Journal* **20(2)**:218-241, https://doi.org/10.1520/GTJ10741J.

Paikowsky, S. G., Player, C. M. & Connors, P. J. (1995) A dual interface apparatus for testing unrestricted friction of soil along solid surfaces. *Geotechnical Testing Journal* **18(2)**:168-193, https://doi.org/10.1520/GTJ10320J.

Palmer, M. C., O'Rourke, T. D., Olson, N. A., *et al.* (2009) Tactile pressure sensors for soil-structure interaction assessment. *Journal of Geotechnical and Geoenvironmental Engineering* **135(11)**:1638-1645, https://doi.org/10.1061/(asce)gt.1943-5606.0000143.

Paulin, M. J., Phillips, R., Clark, J. I., *et al.* (1998) A full-scale investigation into pipeline/soil interaction In *Proceedings of the 2nd International Pipeline Conference*, Alberta, Canada.

Peattie, K. R. & Sparrow, R. W. (1954) The fundamental action of earth pressure cells. *Journal of the Mechanics and Physics of Solids* **2(3)**:141-155, https://doi.org/10.1016/0022-5096(54)90021-6.

Peng, Y., Yin, Z. Y. & Gao, F. P. (2024) Micromechanical analysis of pipeline-soil interaction in unsaturated granular soil undergoing lateral ground movement. *Computers and Geotechnics* **169**:106181, https://doi.org/10.1016/j.compgeo.2024.106181.

Peters, J., Muthuswamy, M., Wibowo, J., *et al.* (2005) Characterization of force chains in granular material. *Physical Review E* **72(4)**:041307, https://doi.org/10.1103/PhysRevE.72.041307.

Potyondy, J. G. (1961) Skin friction between various soils and construction materials. *Géotechnique* **11(4)**:339-353, https://doi.org/10.1680/geot.1961.11.4.339.

Pra-ai, S. & Boulon, M. (2016) Soil–structure cyclic direct shear tests: a new interpretation of the direct shear experiment and its application to a series of cyclic tests. *Acta Geotechnica* **12(1)**:107-127, https://doi.org/10.1007/s11440-016-0456-6.

PRCI (Pipeline Research Council International) (2009) Guidelines for constructing natural gas and liquid hydrocarbon pipelines. Design, Materials, and Construction Committee of Pipeline Research Council International, Inc, Chantilly, VA, US.

Qin, Y., Wang, Q. K., Xu, D. S., *et al.* (2022) A fiber Bragg grating based earth and water pressures transducer with three-dimensional fused deposition modeling for soil mass. *Journal of Rock Mechanics and Geotechnical Engineering* **14(2)**:663-669, https://doi.org/10.1016/j.jrmge.2021.07.009.

Reza, A. & Dhar, A. S. (2021) Axial pullout behavior of buried medium-hensity polyethylene gas distribution pipes. *International Journal of Geomechanics* **21(7)**:04021120, https://doi.org/10.1061/(ASCE)GM.1943-5622.0002101.

Rizkalla, M. & Read, R. S. (2019) *Pipeline Geohazards: Planning, Design, Construction and Operations* (2nd Edition). ASME Press, New York, NY, US.

Robert, D. J., Soga, K., O'Rourke, T. D., *et al.* (2016) Lateral load-displacement behavior of pipelines in unsaturated sands. *Journal of Geotechnical and Geoenvironmental Engineering* **142(11)**:04016060, https://doi.org/10.1061/(asce)gt.1943-5606.0001504.

Rui, S. J., Wang, L. Z., Guo, Z., *et al.* (2020a) Monotonic behavior of interface shear between carbonate sands and steel. *Acta Geotechnica* **16(1)**:167-187, https://doi.org/10.1007/s11440-020-00987-9.

Rui, S. J., Wang, L. Z., Guo, Z., *et al.* (2020b) Cyclic behavior of interface shear between carbonate sand and steel. *Acta Geotechnica* **16(1)**:189-209, https://doi.org/10.1007/s11440-020-01002-x.

Saadawi, H. (2001) Upheaval buckling of gas injection pipelines onshore Abu Dhabi - a case study In *Proceedings of SPE Middle East Oil Show*, Manama, Bahrain.

Saberi, M., Annan, C.-D. & Sheil, B. B. (2022) An efficient numerical approach for simulating soil-pipe interaction behaviour under cyclic loading. *Computers and Geotechnics* **146**:104666, https://doi.org/10.1016/j.compgeo.2022.104666.

Sadrekarimi, A. & Olson, S. M. (2010) Shear band formation observed in ring shear tests on sandy soils. *Journal of Geotechnical and Geoenvironmental Engineering* **136(2)**:366-375, https://doi.org/10.1061/(ASCE)GT.1943-5606.0000220.

Salgado, R., Bandini, P. & Karim, A. (2000) Shear strength and stiffness of silty sand. *Journal of Geotechnical and Geoenvironmental Engineering* **126(5)**:451-462, https://doi.org/10.1061/(ASCE)1090-0241(2000)126:5(451).

Sarvanisa, G. C., Karamanosa, S., Vazourasa, P., *et al.* (2018) Permanent earthquake-induced actions in buried pipelines: Numerical modeling and experimental verification. *Earthquake Engineering and Structural Dynamics* **47(4)**:966-987, https://doi.org/10.1002/eqe.3001.

Sawangsuriya, A., Edil, T. B. & Bosscher, P. J. (2009) Modulus-suction-moisture Relationship for compacted Soils in postcompaction state. *Journal of Geotechnical and Geoenvironmental Engineering* **135(10)**:1390-1403, https://doi.org/10.1061/(ASCE)GT.1943-5606.0000108.

Scarpelli, G., Sakellariadi, E. & Furlani, G. (2003) Evaluation of soil-pipeline longitudinal interaction forces. *Rivista Italiana di Geotecnica* **4(3)**:24-41.

Scholtès, L., Hicher, P. Y., Nicot, F.*, et al.* (2009) On the capillary stress tensor in wet granular materials. *International Journal for Numerical and Analytical Methods in Geomechanics* **33(10)**:1289-1313, https://doi.org/10.1002/nag.767.

Sharif, Y. U., Brown, M. J., Ciantia, M. O.*, et al.* (2021) Using discrete element method (DEM) to create a cone penetration test (CPT)-based method to estimate the installation requirements of rotary-installed piles in sand. *Canadian Geotechnical Journal* **58(7)**:919-935, https://doi.org/10.1139/cgj-2020-0017.

Sheil, B. B., Martin, C. M., Byrne, B. W.*, et al.* (2018) Full-scale laboratory testing of a buried pipeline in sand subjected to cyclic axial displacements. *Géotechnique* **68(8)**:684-698, https://doi.org/10.1680/jgeot.16.P.275.

Shen, Z. F., Jiang, M. J. & Thornton, C. (2016) Shear strength of unsaturated granular soils: three-dimensional discrete element analyses. *Granular Matter* **18(3)**:37, https://doi.org/10.1007/s10035-016-0645-x.

Šmilauer, V. & Chareyre, B. (2021) *Yade Documentation* (3rd Edition). The Yade Project, Online.

Suits, L., Sheahan, T., Labuz, J.*, et al.* (2005) Laboratory calibration of earth pressure cells. *Geotechnical Testing Journal* **28(2)**:188-196, https://doi.org/10.1520/GTJ12089.

Suleiman, M. T. & Coree, B. J. (2004) Constitutive model for high density polyethylene material: systematic approach. *Journal of Materials in Civil Engineering* **16(6)**:511-515, https://doi.org/10.1061/(ASCE)0899-1561(2004)16:6(511).

Talesnick, M. (2013) Measuring soil pressure within a soil mass. *Canadian Geotechnical Journal* **50(7)**:716-722, https://doi.org/10.1139/cgj-2012-0347.

Talesnick, M., Horany, H., Dancygier, A. N., *et al.* (2008) Measuring Soil Pressure on a Buried Model Structure for the Validation of Quantitative Frameworks. *Journal of Geotechnical and Geoenvironmental Engineering* **134(6)**:855-865, https://doi.org/10.1061/(ASCE)1090-0241(2008)134:6(855).

Talesnick, M. L., Xia, H. W. & Moore, I. D. (2011) Earth pressure measurements on buried HDPE pipe. *Géotechnique* **61(9)**:721-732, https://doi.org/10.1680/geot.8.P.048.

Tehrani, F. S., Han, F., Salgado, R., *et al.* (2016) Effect of surface roughness on the shaft resistance of non-displacement piles embedded in sand. *Géotechnique* **66(5)**:386-400, https://doi.org/10.1680/jgeot.15.P.007.

Tejchman, J. & Wu, W. (1995) Experimental and numerical study of sand–steel interfaces. *International Journal for Numerical and Analytical Methods in Geomechanics* **19(8)**:513-536, https://doi.org/10.1002/nag.1610190803.

Thomas, H. S. H. & Ward, W. H. (1969) The design, construction and performance of a vibrating-wire earth pressure cell. *Géotechnique* **19(1)**:39-51, https://doi.org/10.1680/geot.1969.19.1.39.

Tian, Y. H., Wu, W. C., Cassidy, M. J., *et al.* (2022) A complete analytical solution for axial pipeline walking considering seabed resistance as rigid plastic behaviour. *Géotechnique* **72(9)**:810-824, https://doi.org/10.1680/jgeot.20.P.135.

Tolun, M., Emirler, B., Ertugrul, O. L.*, et al.* (2022) Effect of surface roughness characteristics on the uplift capacity of piles: A physical modelling study. *Marine Georesources & Geotechnology* **41(8)**:935-947, https://doi.org/10.1080/1064119x.2022.2110025.

Tory, A. C. & Sparrow, R. W. (1967) The influence of diaphragm flexibility on the performance of an earth pressure cell. *Journal of Scientific Instruments* **44(9)**:781-785, https://doi.org/10.1088/0950-7671/44/9/333.

Trautmann, C. H. & O'Rourke, T. D. (1985) Lateral force-displacement response of buried pipe. *Journal of Geotechnical Engineering* **111(9)**:1077-1092, https://doi.org/10.1061/(ASCE)0733-9410(1985)111:9(1077).

Uesugi, M. & Kishida, H. (1986) Frictional resistance at yield between dry sand and mild steel. *Soils and Foundations* **26(4)**:139-149, https://doi.org/10.3208/sandf1972.26.4_139.

Uesugi, M., Kishida, H. & Tsubakihara, Y. (1988) Behavior of Sand Particles in Sand-Steel Friction. *Soils Found* **28(1)**:107-118, https://doi.org/10.3208/sandf1972.28.107.

Uesugi, M., Kishida, H. & Tsubakihara, Y. (1989) Friction between sand and steel under repeated loading. *Soils and Foundations* **29(3)**:127-137, https://doi.org/10.3208/sandf1972.29.3_127.

USBR (United States Department of the Interior Bureau of Reclamation) (1996) USBR 1996: Geotechnical training manual No. 7: Pipe bedding and backfill. United States Department of the Interior Bureau of Reclamation, Technical Service Center Geotechnical Services, Denver, CO, US.

van Genuchten, M. T. (1980) A closed-form equation for predicting the hydraulic conductivity of unsaturated soils. *Soil Science Society of America Journal* **44(5)**:892-898, https://doi.org/10.2136/sssaj1980.03615995004400050002x.

Vanapalli, S. K., Fredlund, D. G., Pufahl, D. E., *et al.* (1996) Model for the prediction of shear strength with respect to soil suction. *Canadian Geotechnical Journal* **33(3)**:379-392, https://doi.org/10.1139/t96-060.

Vazouras, P., Tsatsis, A. & Dakoulas, P. (2021) Thermal upheaval buckling of buried pipelines: Eexperimental behavior and numerical modeling. *Journal of Pipeline Systems Engineering and Practice* **12(1)**:04020057, https://doi.org/10.1061/(asce)ps.1949-1204.0000507.

Vennapusa, P. K. R., White, D. J., Siekmeier, J., *et al.* (2012) In situ mechanistic characterisations of granular pavement foundation layers. *International Journal of Pavement Engineering* **13(1)**:52-67, https://doi.org/10.1080/10298436.2011.564281.

Wan, R., Duriez, J. & Darve, F. (2015) A tensorial description of stresses in triphasic granular materials with interfaces. *Geomechanics for Energy and the Environment* **4**:73-87, https://doi.org/10.1016/j.gete.2015.11.004.

Wang, P., Yin, Z. Y., Zhou, W. H., *et al.* (2022) Micro-mechanical analysis of soil–structure interface behavior under constant normal stiffness condition with DEM. *Acta Geotechnica* **17(7)**:2711-2733, https://doi.org/10.1007/s11440-021-01374-8.

Wang, Y. & Ng, C. W. W. (2005) Effects of stress paths on the small-strain stiffness of completely decomposed granite. *Canadian Geotechnical Journal* **42(4)**:1200-1211, https://doi.org/10.1139/t05-009.

Wang, Y., Shi, J. W. & Ng, C. W. W. (2011) Numerical modeling of tunneling effect on buried pipelines. *Canadian Geotechnical Journal* **48(7)**:1125-1137, https://doi.org/10.1139/t11-024.

Weatherley, D. (2009) *ESyS-Particle v2. 0 User's Guide.* Earth Systems Science Computational Centre (ESSCC), The University of Queensland, Online.

Weerasekara, L. (2007) *Response of buried natural gas pipelines subjected to ground movement*. Ph.D. thesis, University of British Columbia, BC, Canada.

Weerasekara, L. & Wijewickreme, D. (2008) Mobilization of soil loads on buried, polyethylene natural gas pipelines subject to relative axial displacements. *Canadian Geotechnical Journal* **45(9)**:1237-1249, https://doi.org/10.1139/t08-043.

Weidlich, I. & Achmus, M. (2006) Reduction of friction forces between soil and buried district heating pipes due to cyclic axial displacements In *Proceedings of the 10th International Symposium on District Heating and Cooling*, Germany.

Weidlich, I. & Achmus, M. (2008) Measurement of normal pressures and friction forces acting on buried pipes subjected to cyclic axial displacements in laboratory experiments. *Geotechnical Testing Journal* **31(4)**:334-343, https://doi.org/10.1520/GTJ100804.

Whidden, W. R. (2009) *Buried Flexible Steel Pipe: Design and Structural Analysis.* American Society of Civil Engineers, US.

Wijewickreme, D., Karimian, H. & Honegger, D. (2009) Response of buried steel pipelines subjected to relative axial soil movement. *Canadian Geotechnical Journal* **46(7)**:735-752, https://doi.org/10.1139/t09-019.

Wijewickreme, D. & Weerasekara, L. (2015) Analytical modeling of field axial pullout tests performed on buried extensible pipes. *International Journal of Geomechanics* **15(2)**:04014044, https://doi.org/10.1061/(ASCE)GM.1943-5622.0000388.

WSD (Water Supplies Department) (2012) WSD 2012: Manual of mainlaying practice. Water Supplies Department, Hong Kong SAR.

WSD (Water Supplies Department) (2020) WSD 2020: Guidelines for excavation near water mains. Water Supplies Department, HK.

Wu, H. R., Wu, W., Liang, W. J., *et al.* (2023) 3D DEM modeling of biocemented sand with fines as cementing agents. *International Journal for Numerical and Analytical Methods in Geomechanics* **47(2)**:212-240, https://doi.org/10.1002/nag.3466.

Wu, W. (2000) Non-linear analysis of shear band formation in sand. *International Journal for Numerical and Analytical Methods in Geomechanics* **24(3)**:245-263, https://doi.org/10.1002/(SICI)1096-9853(200003)24:3<245::AID-NAG52>3.0.CO;2-C.

Wu, W., Lin, J. & Wang, X. T. (2017) A basic hypoplastic constitutive model for sand. *Acta Geotechnica* **12(6)**:1373-1382, https://doi.org/10.1007/s11440-017-0550-4.

Wu, W., Wang, S., Xu, G. F., *et al.* (2019) Numerical Simulation of a CAES Pile with Hypoplasticity In *Proceedings of Desiderata Geotechnica*. Springer International Publishing, Cham.

Ye, M. G., Xie, Q. W., Ni, P. P., *et al.* (2023) Improved analytical solution of lateral soil restraint for pipes buried in dry sand considering arching effects. *Canadian Geotechnical Journal* **60(6)**:802-816, https://doi.org/10.1139/cgj-2022-0320.

Yimsiri, S. & Soga, K. (2006) DEM analysis of soil-pipeline interaction in sand under lateral and upward movements at deep embedment. *Journal of the Southeast Asian Geotechnical Society* **37(2)**:83-94, http://seags.ait.asia/e-journal/1970-2012/GEJ_2006_v37n2_August.pdf.

Yimsiri, S., Soga, K., Yoshizaki, K., *et al.* (2004) Lateral and upward soil-pipeline interactions in sand for deep embedment conditions. *Journal of Geotechnical and Geoenvironmental Engineering* **130(8)**:830-842, https://doi.org/10.1061/(ASCE)1090-0241(2004)130:8(830).

Yin, J. H., Hong, C. Y. & Zhou, W. H. (2012) Simplified analytical method for calculating the maximum shear stress of nail-soil interface. *International Journal of Geomechanics* **12(3)**:309-317, https://doi.org/10.1061/(asce)gm.1943-5622.0000151.

Yin, J. H. & Su, L. J. (2006) An innovative laboratory box for testing nail pull-out resistance in soil. *Geotechnical Testing Journal* **29(6)**:451-461, https://doi.org/10.1520/GTJ100216.

Yuan, C. & Chareyre, B. (2017) A pore-scale method for hydromechanical coupling in deformable granular media. *Computer Methods in Applied Mechanics and Engineering* **318**:1066-1079, https://doi.org/10.1016/j.cma.2017.02.024.

Yuan, C., Chareyre, B. & Darve, F. (2015) A pore-scale approach of two-phase flow in granular porous media In *Proceedings of IV International Conference on Particle-Based Methods: fundamentals and applications*. CIMNE, Barcelona, Spain.

Yuan, C., Chareyre, B. & Darve, F. (2016) Pore-scale simulations of drainage in granular materials: Finite size effects and the representative elementary volume. *Advances in Water Resources* **95**:109-124, https://doi.org/10.1016/j.advwatres.2015.11.018.

Zhang, G., Liang, D. F. & Zhang, J. M. (2006) Image analysis measurement of soil particle movement during a soil–structure interface test. *Computers and Geotechnics* **33(4)**:248-259, https://doi.org/10.1016/j.compgeo.2006.05.003.

Zhang, G., Wang, L. & Zhang, J. M. (2011) Dilatancy of the interface between a structure and gravelly soil. *Géotechnique* **61(1)**:75-84, https://doi.org/10.1680/geot.9.P.051.

Zhang, G. & Zhang, J. M. (2006) Monotonic and cyclic tests of interface between structure and gravelly soil. *Soils and Foundations* **46(4)**:505-518, https://doi.org/10.3208/sandf.46.505.

Zhang, G. & Zhang, J. M. (2009) Large-scale monotonic and cyclic tests of interface between geotextile and gravelly soil. *Soils and Foundations* **49(1)**:75-84, https://doi.org/10.3208/sandf.49.75.

Zhang, Z. T. & Wang, Y. H. (2015) Three-dimensional DEM simulations of monotonic jacking in sand. *Granular Matter* **17(3)**:359-376, https://doi.org/10.1007/s10035-015-0562-4.

Zhou, C., Tai, P. & Yin, J. H. (2020) A bounding surface model for saturated and unsaturated soil-structure interfaces. *International Journal for Numerical and Analytical Methods in Geomechanics* **44(18)**:2412-2429, https://doi.org/10.1002/nag.3123.

Zhou, W. H. & Yin, J. H. (2008) A simple mathematical model for soil nail and soil interaction analysis. *Computers and Geotechnics* **35(3)**:479-488, https://doi.org/10.1016/j.compgeo.2007.07.001.

Zhu, B., Ye, Z. G., Wang, L. J.*, et al.* (2020) Hydro-mechanical behavior of unsaturated soil surrounding a heated pipeline considering moisture evaporation and condensation. *Computers and Geotechnics* **119**:103377, https://doi.org/10.1016/j.compgeo.2019.103377.

Zhu, H., Zhang, L. M., Chan, K.*, et al.* (2018) Design safe distance between a buried pipe and a soil slope. *Proceedings of the Institution of Civil Engineers - Geotechnical Engineering* **171(4)**:324-331, https://doi.org/10.1680/jgeen.17.00153.